Science

22 October 2004

Vol. 306 No. 5696
Pages 557–760 $10

AAAS

Science

Volume 306
22 October 2004
Number 5696

SPECIAL ISSUE

GENE EXPRESSION: GENES IN ACTION

A computational method enables rapid analysis of the blocklike pattern of genetic variation in the mouse genome, which can be used in analyzing mouse models of human disease (see page 690). A special section in this issue of *Science* explores new approaches to understanding how genes are expressed and how they function. [Image: Myriam Kirkman-Oh]

INTRODUCTION

NEWS

VIEWPOINTS AND REVIEW

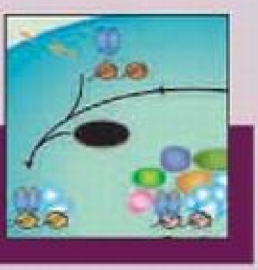

For related online content, see page 569, or go to www.sciencemag.org/sciext/genome2004

DEPARTMENTS

NEWS OF THE WEEK

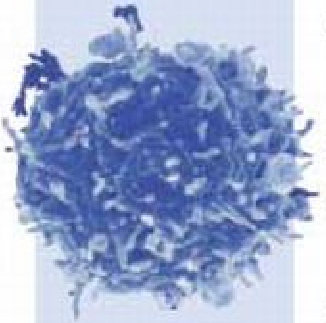

596

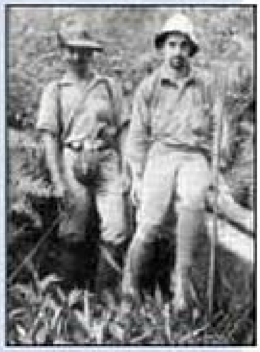

614

NEWS FOCUS

LETTERS

BOOKS *ET AL.*

POLICY FORUM

Contents continued

PERSPECTIVES

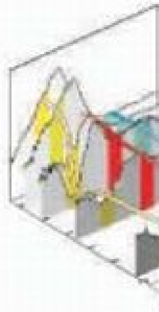

618, 669, 672, & 675

SCIENCE EXPRESS www.sciencexpress.org

TECHNICAL COMMENT ABSTRACTS

BREVIA

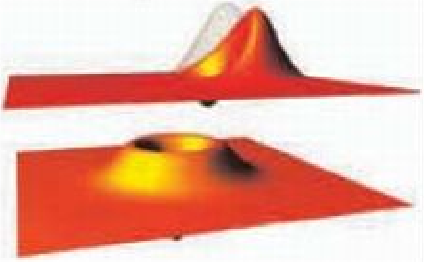

RESEARCH ARTICLE

660

REPORTS

Contents continued

REPORTS CONTINUED

666 **APPLIED PHYSICS:** Electric Field Effect in Atomically Thin Carbon Films
K. S. Novoselov, A. K. Geim, S. V. Morozov, D. Jiang, Y. Zhang, S. V. Dubonos, I. V. Grigorieva, A. A. Firsov
Exfoliating graphite yields stable carbon films just a few atoms thick, which on a silicon substrate act as a new type of strong semimetal transistor.

CHEMISTRY

669 Hydrated Electron Dynamics: From Clusters to Bulk
A. E. Bragg, J. R. R. Verlet, A. Kammrath, O. Cheshnovsky, D. M. Neumark

672 Electrons in Finite-Sized Water Cavities: Hydration Dynamics Observed in Real Time
D. H. Paik, I.-R. Lee, D.-S. Yang, J. S. Baskin, A. H. Zewail
Photoelectron spectroscopy reveals that an excited electron in a water cluster relaxes rapidly and then transfers energy to surrounding water molecules, disrupting their hydrogen bonding. *related Perspective page 618; Report page 675*

675 **CHEMISTRY:** How Do Small Water Clusters Bind an Excess Electron?
N. I. Hammer, J.-W. Shin, J. M. Headrick, E. G. Diken, J. R. Roscioli, G. H. Weddle, M. A. Johnson
An excess electron in a small water cluster mainly resides with a water molecule that accepts hydrogen bonds from two others, resolving a long-standing question. *related Perspective page 618; Reports pages 669 and 672*

679 **ATMOSPHERIC SCIENCE:** Reconstructing Past Climate from Noisy Data
H. von Storch, E. Zorita, J. M. Jones, Y. Dimitriev, F. González-Rouco, S. F. B. Tett
The climate of past centuries was more variable than is represented in regression-based reconstructions that use noisy data from climate indicators such as tree rings. *related Perspective page 621*

683 **MOLECULAR BIOLOGY:** Mycobacterial Ku and Ligase Proteins Constitute a Two-Component NHEJ Repair Machine
M. Della et al.
Prokaryotes can repair a double-stranded break in DNA with just one multipurpose and one joining enzyme, whereas mammals require numerous enzymes.

686 **MICROBIOLOGY:** Elemental and Redox Analysis of Single Bacterial Cells by X-ray Microbeam Analysis
K. M. Kemner et al.
The distribution and oxidation state of chromium and other metals important in cell metabolism can be observed in single living cells with a high-energy x-ray beam.

687 **GENETICS:** A Chromosome 21 Critical Region Does Not Cause Specific Down Syndrome Phenotypes
L. E. Olson, J. T. Richtsmeier, J. Leszl, R. H. Reeves
In a mouse version of Down syndrome, the so-called Down syndrome critical region unexpectedly fails to cause typical facial abnormalities, implying that other genes are involved. *related Perspective page 619*

690 **GENETICS:** In Silico Genetics: Identification of a Functional Element Regulating *H2-Eα* Gene Expression
G. Liao et al.
Computational analysis of genetic maps can quickly identify the genes responsible for trait variation in 16 inbred mouse strains. *related Gene Expression section page 629*

695 **CELL BIOLOGY:** The PP2A-Associated Protein α4 Is an Essential Inhibitor of Apoptosis
M. Kong, C. J. Fox, J. Mu, L. Solt, A. Xu, R. M. Cinalli, M. J. Birnbaum, T. Lindsten, C. B. Thompson
An inhibitory subunit of a phosphatase enzyme prevents it from activating the transcription factors that trigger suicide in mammalian cells.

698 **CELL SIGNALING:** A Network of Control Mediated by Regulator of Calcium/Calmodulin-Dependent Signaling
S. V. Rakhilin, P. A. Olson, A. Nishi, N. N. Starkova, A. A. Fienberg, A. C. Nairn, D. J. Surmeier, P. Greengard
A previously undescribed protein increases signals transmitted by neurons by amplifying two major signaling pathways.

702 **PLANT BIOLOGY:** Plant Cuticular Lipid Export Requires an ABC Transporter
J. A. Pighin, H. Zheng, L. J. Balakshin, I. P. Goodman, T. L. Western, R. Jetter, L. Kunst, A. L. Samuels
The waxy coating on the leaves of plants is deposited by lipid transporters similar to those found in mammals. *related Perspective page 622*

704 **MOLECULAR BIOLOGY:** Oscillations in NF-κB Signaling Control the Dynamics of Gene Expression
D. E. Nelson et al.
Nuclear-cytoplasmic oscillations of a transcription factor are required for sustained gene expression in response to a stimulus.

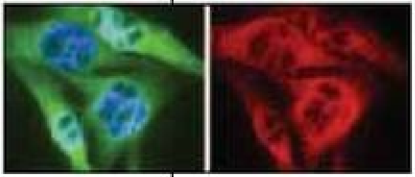

695

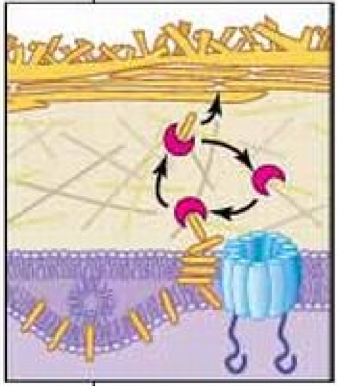

622 & 702

AAAS
ADVANCING SCIENCE, SERVING SOCIETY

SCIENCE (ISSN 0036-8075) is published weekly on Friday, except the last week in December, by the American Association for the Advancement of Science, 1200 New York Avenue, NW, Washington, DC 20005. Periodicals Mail postage (publication No. 484460) paid at Washington, DC, and additional mailing offices. Copyright © 2004 by the American Association for the Advancement of Science. The title SCIENCE is a registered trademark of the AAAS. Domestic individual membership and subscription (51 issues): $130 ($74 allocated to subscription). Domestic institutional subscription (51 issues): $500; Foreign postage extra: Mexico, Caribbean (surface mail) $55; other countries (air assist delivery) $85. First class, airmail, student, and emeritus rates on request. Canadian rates with GST available upon request, GST #1254 88122. Publications Mail Agreement Number 1069624. Printed in the U.S.A.

Change of address: allow 4 weeks, giving old and new addresses and 8-digit account number. **Postmaster:** Send change of address to Science, P.O. Box 1811, Danbury, CT 06813–1811. **Single copy sales:** $10.00 per issue prepaid includes surface postage; bulk rates on request. **Authorization to photocopy** material for internal or personal use under circumstances not falling within the fair use provisions of the Copyright Act is granted by AAAS to libraries and other users registered with the Copyright Clearance Center (CCC) Transactional Reporting Service, provided that $15.00 per article is paid directly to CCC, 222 Rosewood Drive, Danvers, MA 01923. The identification code for Science is 0036-8075/83 $15.00. Science is indexed in the *Reader's Guide to Periodical Literature* and in several specialized indexes.

Contents continued ▶

Science
www.scienceonline.org

Visit *Science* Functional Genomics for an online discussion on the future of microarrays.
www.sciencegenomics.org

sciencenow www.sciencenow.org DAILY NEWS COVERAGE

Planet Building Isn't Pretty
Infrared telescope finds signs of persistent smashups around young stars.

Giant Virus Sequenced
Surprising complexity may force researchers to reevaluate definition of life.

Centenarian Clams Cut Calories
Meager diet may have enabled ancient clams to live long lives.

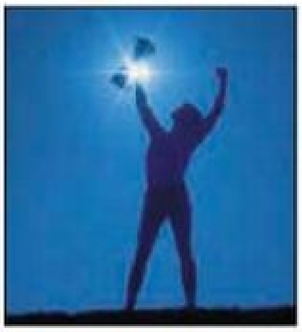

An award winner tells her story.

science's next wave www.nextwave.org CAREER RESOURCES FOR YOUNG SCIENTISTS

EUROPE: Success in Academia—Recipe From a Serial Award Winner *E. Pain*
Sheer drive and a proactive approach were key to this scientist's success.

GLOBAL/US: Funding International Collaborations *The GrantDoctor*
The GrantDoctor discusses the nuts and bolts of NSF and NIH funding for international research.

GLOBAL/GERMANY: Destination Germany? A Researchers Mobility Tool *A. Forde*
The Researcher Mobility Portal helps researchers who want to move to a state in the European Union.

NETHERLANDS: Co-tutelle de Thèse—French-Dutch Ph.D. Collaboration *M. de Bakker*
Two scientists are working toward their Ph.D.'s in both the Netherlands and France. [In Dutch]

MISCINET: Your Own "Family Values" *S. Clemmons*
A minority graduate student gets help in dealing with personal and professional isolation.

science's sage ke www.sageke.org SCIENCE OF AGING KNOWLEDGE ENVIRONMENT

Related Gene Expression section page 629

PERSPECTIVE: Aging-Related Research in the "-omics" Age *M. Kaeberlein*
Genome-wide analyses should provide insight into aging and longevity.

REVIEW: Microarrays as a Tool to Investigate the Biology of Aging—A Retrospective and a Look to the Future *S. Melov and A. Hubbard*
Microarray-based experiments present special problems and require careful design.

NEWS FOCUS: Gone to Waste *M. Leslie*
Inflammation-producing compound spurs muscle deterioration.

NEWS FOCUS: Sticky Situation *M. Beckman*
DNA landing sites for worm hibernation protein might flag aging-associated genes.

NEWS FOCUS: Wilting Weed? *R. J. Davenport*
Arabidopsis might provide new insights into workings of protein linked to a premature aging disease.

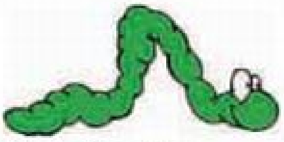

Illuminating aging.

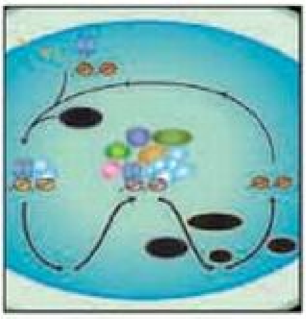

Transcription complexes assemble and disassemble.

science's stke www.stke.org SIGNAL TRANSDUCTION KNOWLEDGE ENVIRONMENT

Related Gene Expression section page 629

EDITORIAL GUIDE: Focus Issue—The Dynamics of Gene Expression *N. R. Gough*
Regulatory factors and DNA perform an intricate dance to regulate gene expression.

REVIEW: Selective Gene Expression in Multigene Families From Yeast to Mammals *J. Z. Dalgaard and S. Vengrova*
Exclusive gene expression is achieved through diverse mechanisms.

PERSPECTIVE: Dynamic Control of Nuclear Receptor Transcription *A. M. Fowler and E. T. Alarid*
Nuclear receptors and transcriptional regulators interact dynamically with DNA.

PROTOCOL: UV Laser Cross-linking—A Real Time Assay to Study Dynamic Protein/DNA Interactions During Chromatin Remodeling *A. K. Nagaich and G. L. Hager*
UV laser cross-linking can be used to study transcription factor interactions with DNA in real time.

Separate individual or institutional subscriptions to these products may be required for full-text access.

GrantsNet	**AIDScience**	**Members Only!**	**Functional Genomics**
www.grantsnet.org	www.aidscience.com	www.AAASMember.org	www.sciencegenomics.org
RESEARCH FUNDING DATABASE	HIV PREVENTION & VACCINE RESEARCH	AAAS ONLINE COMMUNITY	NEWS, RESEARCH, RESOURCES

Genomics and Drug Toxicity

As genomics has revolutionized the study of biology, so has it affected how drugs are discovered. Pharmaceutical companies have also realized another major application: how drugs are assessed for safety. The analysis of gene expression profiles is now actively used alongside conventional toxicological assays to assess drug safety. Such toxicogenomic analysis is being used to predict drug toxicities and to gain a more in-depth understanding of toxic mechanisms, so that more successful drug candidates can be selected.

The U.S. Food and Drug Adminstration (FDA) sees genomics as a beneficial aid to the drug risk assessment process primarily through its ability to identify specific patients who are either likely to benefit from a particular drug or who may experience harm. The use of toxicogenomics also has promise in proving hypotheses that support safe drug use in humans through a mechanistic understanding of toxicities found in drug-treated animals. Take the case in which rats were treated with a certain class of hypolipidemic drugs. Changes in the expression of specific liver genes were seen that have been shown to correlate with observed liver toxicity. However, when treated human and rat liver cells were compared, analogous gene expression changes were not seen in the human cells.* Thus, by gaining a better idea of the mechanisms of toxicity in an animal species, it becomes feasible to examine species-specific effects to better assess the possible relevance of animal findings to humans. After a number of conferences and workshops based on recent FDA draft guidelines, there was agreement that some standards ought to be adopted for the generation and subsequent submission of toxicogenomic data to the FDA. This would help ensure that any regulatory decisions based on an interpretation of data can be made in a consistent manner.

A number of groups are actively addressing the issues of standardization of toxicogenomic data generation and exchange. The European Bioinformatics Institute (EBI) has created Tox-MIAMExpress to incorporate toxicity and toxicogenomics data into their Array Express database.† Such efforts help identify the essential elements of a microarray experiment that are critical to interpreting a gene expression profile in the context of an associated toxicity. Some aspects of toxicogenomics experiments that are suitable for further standardization include data normalization methods, statistical assessments of gene expression, gene annotation and function, data visualization methods, and issues related to quality control of transcripts and probes.

Once a compound is selected for development by a pharmaceutical company, submission of toxicogenomic data to the FDA as part of a risk assessment package may be needed to help address safety concerns. An approach being taken by the Clinical Data Interchange Standards Consortium (CDISC) Pharmacogenomic Standards nonclinical working group is to develop hypothetical cases in which the submission of toxicogenomic data would assist in the interpretation and determination of the relevance of specific toxicity issues. In the example of the hypolipidemic drugs mentioned above, the availability of toxicogenomic data submission standards would offer drug companies the ability to submit data at a molecular level highlighting the species-specific nature of an animal finding, thereby helping to address the safety concerns of regulators.

The development of standards for toxicogenomic data generation and interpretation will help establish toxicogenomic approaches as scientifically accepted practices in the complex process of drug risk assessment. Central to this process is the continuation of the ongoing dialogue between molecular and traditional toxicologists from drug companies, regulatory bodies, and academia. The development of a scientific consensus on toxicogenomic data standards and data interpretation would mean fewer safety concerns and fewer delays in the drug approval process, resulting in improved availability of safe and effective drugs. The development and acceptance of toxicogenomic data submission standards promise to significantly improve the drug risk assessment process, which would benefit the pharmaceutical industry and public alike.

Peter G. Lord and Thomas Papoian

Peter G. Lord is in Pharmaceutical Research and Development at Johnson & Johnson in Raritan, NJ. Thomas Papoian is at the U.S. Food and Drug Administration in Rockville, MD.

*J. W. Lawrence *et al.*, *J. Biol. Chem.* **276**, 31521 (2001). †W. B. Mattes *et al.*, *Environ. Health Perspect.* **112**, 495 (2004).

CREDITS: PHOTOS.COM; (OVERLAY) GENOME.GOV

Published by AAAS

PAGE 590
An avian flu's surprising reach

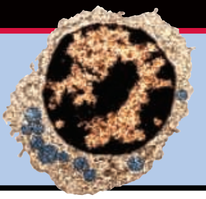

592
Mitochondrial link to metabolic syndrome

BIOETHICS

Stem Cell Researchers Mull Ideas for Self-Regulation

Scientists and ethicists gathered at a brainstorming session last week in Washington, D.C., to discuss voluntary limits on human cloning and embryonic stem (ES) cell research. The event echoed the 1975 meeting in Asilomar, California, where an earlier generation tried to establish guidelines for genetic engineering. As was the case 29 years ago, researchers are eager to move ahead: Even as the session at the National Academy of Sciences got under way, for example, Harvard University officials were announcing that diabetes researcher Douglas Melton is applying for permission to use nuclear transfer—otherwise known as research cloning—to create new human cell lines in a privately funded effort to model diseases.

In the United States, federal funds may be spent only on government-approved human ES lines, yet private funding is flowing to the field, largely without regulation. This has increased pressure on scientists to develop their own rules. To get started, the academies created an 11-member Committee on Guidelines for Human Embryonic Stem Cell Research, co-chaired by cancer researcher Richard O. Hynes of the Massachusetts Institute of Technology and Jonathan Moreno, director of the University of Virginia Center for Biomedical Ethics. Last week experts made suggestions covering all aspects of work with human ES cells, from informed-consent procedures to distribution of cell lines.

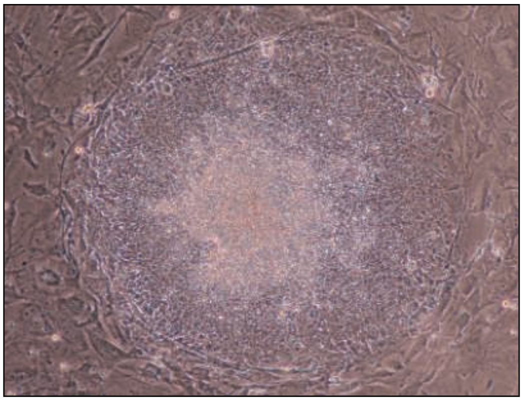

What scientists want. This colony of human ES cells was cultivated from a blastocyst that a South Korean group created using nuclear transfer.

"There's definitely a need to create standards in the field so it won't take 6 to 12 months to start work," said blood researcher Leonard Zon of Children's Hospital in Boston. He ticked off a list of offices that have to pass on any project—including administration, research, finance, legal, ethics, intellectual property, and public affairs. Researchers also must contend with a patchwork of state regulations, noted Georgetown University bioethicist LeRoy Walters, who described rules ranging from California and New Jersey's aggressive pro-research policies to nine states' bans on human embryo research. On top of this tangle of standards are dizzying moral questions, such as: If an embryo is being created for research, is it better to do it through in vitro fertilization or nuclear transfer? And what does it mean to accord an early embryo "respect"?

Leading the way. Harvard's Melton.

Much of the political debate over stem cell research in the United States has focused on the Bush Administration's prohibition on using federal funds to work with human ES cell lines other than a handful already in existence 3 years ago. All these lines were established from "spare" embryos created at fertility clinics.

More ethically charged are efforts to create new stem cell lines by transferring DNA into an enucleated egg. Many researchers are eager to get on with such studies. But speakers warned of public resistance, complicated by the fact that stem cell research is conflated with cloning in many minds. "I hate to break the news, but there really isn't much support for nuclear transfer," said Franco Furger, director of the Human Biotechnology Governance Forum at Johns Hopkins University, who cited a variety of polls to that effect. Michael Werner of the Biotech Industry Organization warned that even biotech investors "don't distinguish between stem cell research and cloning."

So far only one group—in South Korea—has successfully cloned a human embryo (*Science*, 12 March, p. 1669), but more are on the horizon. In the United Kingdom, the International Centre for Life in Newcastle last August got the first license to clone human embryonic cells for research (*Science*, 20 August, p. 1102). Another British researcher, Ian Wilmut, is applying for a license to use nuclear transfer to study amyotropic lateral sclerosis. At Harvard, Melton's proposal to use these techniques to create embryonic stem cell lines expressing the genes for diabetes and Parkinson's and Alzheimer's disease is under review, and Zon and George Daley hope to create lines expressing the genes for blood diseases. China, India, Japan, Singapore, Belgium, and Israel have sanctioned nuclear transfer; Sweden is expected to do the same.

Given the qualms over stem cell research and cloning, some participants at last week's meeting thought voluntary guidelines would be insufficient to reassure the public. Alison Murdoch of the Newcastle center said she holds the "very strong view that really strong regulation, with every embryo accounted for," is needed. Speakers also saw a need for oversight of the loosely regulated in vitro fertilization industry so that any cell line that might end up in a clinical application can be shown to have a squeaky-clean pedigree. As it stands now, said Michael Malinowski of Louisiana State University School of Law in Baton Rouge, "much assisted reproduction is human experimentation in the name of treatment."

Some called for a standing oversight body like the Recombinant DNA Advisory Committee set up after Asilomar. Leon Kass, chair of the President's Bioethics Council, noted that Asilomar led to a voluntary gene-splicing moratorium and called for a similar moratorium on nuclear transfer. "This is momentous enough that it should be decided on a national level," he said. The committee is to come up with proposed guidelines in February.

–CONSTANCE HOLDEN

CREDITS (TOP TO BOTTOM): JUSTIN IDE/HARVARD NEWS OFFICE; W. S. HWANG

Published by AAAS

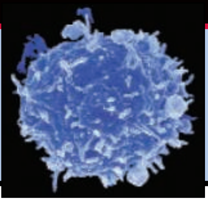

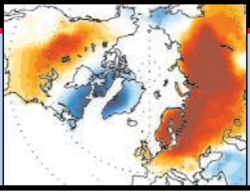

MALARIA

A Complex New Vaccine Shows Promise

After years of dashed hopes, a vaccine against malaria has shown tantalizing results in a clinical trial in Mozambique. In a study involving 2022 children between the ages of 1 and 4, the vaccine lowered a recipient's chance of developing malaria symptoms by 30%. The results are the most promising so far in the search for a vaccine against a disease that kills between 1 million and 3 million people per year. "Malaria has had a sense of hopelessness and intractability around it," says Melinda Moree of the Malaria Vaccine Initiative, an independent nonprofit group that helped fund the trial. "These results bring hope to us all that a vaccine may be possible." Even so, the approach faces several hurdles, including whether the complex vaccine would be affordable in the poor countries most affected by the disease.

A consortium led by GlaxoSmithKline (GSK) Biologicals in Rixensart, Belgium, developed the vaccine, called RTS,S/AS02A. It uses several techniques to boost the immune system's fight against the malaria parasite. Its designers engineered a hybrid protein that combines a protein fragment from the parasite, *Plasmodium falciparum*, with a piece of a protein from the hepatitis B virus. The *Plasmodium* protein is a promising target because it is present on the parasite's surface when it is first injected into the bloodstream by the bite of an infected mosquito. The hepatitis B protein is included because it is particularly effective at prompting an immune response. The vaccine also contains a powerful new adjuvant, developed by GSK Biologicals, that increases the body's production of antibodies and T cells.

The combination seemed to work, at least partially. Although it didn't prevent all children from being infected with the parasite, it did seem to keep them from becoming sick. Children who received the full three doses of the vaccine were 30% less likely to develop clinical malaria in the first 6 months following the injections, a team from GSK Biologicals and the University of Barcelona reported in the 16 October issue of *The Lancet*. Data suggest that the vaccine is considerably more effective at preventing the most dangerous form of the disease, lowering a recipient's risk of severe malaria by 58%. Among children between ages 1 and 2, the results looked even better: The vaccine seemed to reduce the chance of severe malaria by 77%, although the numbers were quite small. "These are the best results we've ever seen with a candidate malaria vaccine," says Pedro Alonso of the University of Barcelona in Spain, who led the trial.

The sheer number of malaria parasites that people in endemic areas are exposed to makes it difficult to develop a vaccine that prevents all infection, notes GSK scientist Joe Cohen. In addition, *Plasmodium* has evolved multiple ways to elude the human immune system. Cohen says scientists aren't sure exactly

▶

PLANETARY SCIENCE

Flipped Switch Sealed the Fate of Genesis Spacecraft

A design error by spacecraft contractor Lockheed Martin Astronautics Inc. caused engineers to install critical sensors upside down in the Genesis sample return capsule, dooming it to slam into the Utah desert floor last month at 360 kilometers per hour, according to the chair of the mishap investigation board. The accident, Lockheed Martin's third major incident of late, may be another reminder of an era when space missions were underfunded, too rushed, and undermanaged. Chances are good, however, that an identically equipped spacecraft, Stardust, will escape a similar fate.

According to board chair Michael Ryschkewitsch of NASA's Goddard Space Flight Center in Greenbelt, Maryland, if the two pairs of sensors had been installed right-side up, they would have triggered Genesis's parachutes. Flipped according to incorrect drawings that assemblers were following, the sensors' spring-loaded weights were already at the end of their range of possible motion as the capsule hit the upper atmosphere and began slowing, so deceleration could not drive them through the required trigger point.

CREDIT: JPL/LMA

The snafu recalls two earlier mishaps involving Denver-based Lockheed Martin as contractor and NASA's Jet Propulsion Laboratory (JPL) as spacecraft operator. In 1999, the Mars Climate Orbiter broke up as it skimmed too close to Mars. Engineers at the two organizations had misunderstood which units of thrust—English or metric—the other group was using. And in the same year, Mars Polar Lander crashed onto the surface after a software error caused its retrorockets to shut down too far above the surface.

Fateful reversal. Incorrect drawings led assemblers to install critical sensors upside down.

Before pointing fingers over Genesis, says space policy analyst John Logsdon of George Washington University in Washington, D.C., critics should consider its history. Although Genesis launched late enough to get additional reviews after the 1999 Mars losses, it was designed years earlier, at the height of the "faster, cheaper, better" era of NASA mission design. Spacecraft were being designed, built, and operated by fewer people in less time than ever before. Genesis was thus prone to the same sorts of problems as the Mars probes, although its particular problem "still should have been caught" by later reviews, says Logsdon. In its final report, due out by early December, Ryschkewitsch's board hopes to document why those reexaminations failed.

More pressing, perhaps, is the state of the Stardust spacecraft's sensors. Also a Lockheed Martin/JPL mission, Stardust will be depending on identical sensors to trigger its landing sequence in January 2006 as it returns samples of comet dust. "Preliminary indications are that the design and installation of the switches on Stardust are correct," says NASA deputy associate administrator Orlando Figueroa. Time will no doubt tell.

–RICHARD A. KERR

Published by AAAS

how the vaccine works, but they suspect that the antibodies and T cells produced may both interrupt the parasite's ability to infect liver cells and help the immune system target infected cells for destruction.

Alonso notes that even partial protection against malaria could save thousands of lives every year. Combined with techniques such as using bed nets and insecticides, "the vaccine could have a huge impact," he says. But he and others caution that the vaccine still must be tested for efficacy and safety in younger children, as large-scale immunization efforts in Africa target children younger than 1 year.

"It is a very exciting, encouraging result that establishes the feasibility of developing a malaria vaccine," says Stephen Hoffman of Sanaria, a Rockville, Maryland–based biotech company working on a different type of malaria vaccine. But questions remain about the GSK vaccine. Candidate vaccines for other diseases have seemed to protect young children only to prove ineffective in infants, he notes. It is not yet clear how long the protection lasts. And the vaccine also has to show its mettle in areas with more intense malaria transmission than Mozambique.

Another possible drawback is the vaccine's cost, which Jean Stephenne, president of GSK Biologicals, estimated at $10 to $20 per dose; multiple doses will likely be needed. Cohen acknowledges that it won't be cheap to produce. "If it gets on the market, it would be the most complex vaccine ever developed," he says. Hoffman notes that the vaccine is about as effective as bed nets and other conventional malaria prevention methods, although it would be much more expensive. (A bed net typically costs about $5.) Moree agrees: "Any vaccine that goes forward will have to be cost-effective, or it will not be used."

–Gretchen Vogel

New hope. A team member treats a child with malaria at the Manhica Health Research Center in Mozambique.

CREDIT: HOSPITAL CLINIC BARCELONA

CANADA

Martin Backs Science Academy

Ottawa—Canadian Prime Minister Paul Martin has given the green light to what one prominent scientist calls "scientific advice on a shoestring budget."

On 5 October, Martin promised that his budget next spring would include $27.6 million over 10 years for a Canadian Academies of Science (CAS). The announcement culminates a decade-long campaign by leading scientists for a national organization that would deliver independent assessments of pressing scientific questions. But its status is dependent on the survival of Martin's minority government, which narrowly avoided being toppled in a procedural vote following his speech.

CAS would be run by the Royal Society of Canada, the Canadian Academy of Engineering (CAE), and the Canadian Institute of Advanced Medicine. Officials from the three organizations have long touted the idea (*Science*, 27 October 2000, p. 685). "We're practically the only country in the world that doesn't have" such an organization, adds CAE executive director Philip Cockshutt.

Royal Society past president William Leiss estimates that CAS will carry out no more than five studies a year—compared with the 200 or so churned out annually by the U.S. National Academies, on which CAS is modeled—with help from a small CAS secretariat. A board of governors, featuring two representatives apiece from the three founding organizations and six members of the public, will choose the panelists for each study. (The board could grow if other members join CAS.)

CAS may also do a small number of self-initiated studies, Leiss said. But he expects the government to provide the bulk of the academies' support. "What they'll get is a kind of definitive resolution of some really thorny issues," says Leiss, adding that all its reports would become public.

Leiss credits Canada's new science adviser, Arthur Carty, with putting the campaign over the top. Carty will serve as the gatekeeper and conduit between the government and the new academy, submitting formal requests for the academy to undertake a study and receiving its final reports. Carty says the academy will give Canada a "voice" on the international science front and a point of entry for countries seeking its input on international projects. He also plans to consult with its members in preparing his recommendations to government.

–Wayne Kondro

ScienceScope

NSF Worries About Growing Antarctic Ice ...

National Science Foundation (NSF) officials are hoping that an unexpected increase in Antarctic sea ice won't complicate plans to resupply two U.S. research stations by ship. But just in case, they are already pondering how else to get 23 million liters of fuel and 5 million kilograms of material to the McMurdo and South Pole stations during the busy austral summer scientific season.

For the past 4 years, the Coast Guard has used both of its polar-class icebreakers to clear paths for cargo ships through the ice around McMurdo Sound and channel. Although one of the behemoths is now awaiting repairs, in July, Coast Guard officials said that going solo would be fine because the newly formed 1-meter-thick ice cover was only 40 kilometers. But by August it had grown to 200 kilometers. So next week the service's *Polar Star* will set out alone from Seattle (a 6-week trip) to battle the ice.

"We're still confident *Polar Star* can get the job done," says the Coast Guard's Capt. Dennis Holland. NSF officials hope he's right. But last week they outlined several alternatives, including renting a commercial ice breaker and offloading fuel and supplies several kilometers up the channel.

–Jeffrey Mervis

... As South Pole Research Group Aims for Fresh Start

The international body that oversees research in Antarctica hopes that an infusion of funds and ideas will rescue it from its scientific doldrums. "We need to focus on some big-issue science to raise our profile," says Colin Summerhayes, executive director of the U.K.-based Scientific Committee on Antarctic Research, a 32-nation body that earlier this month approved a new research agenda, changes to its organizational structure, and a dues increase.

The new research plan calls for Antarctic scientists to focus on five interdisciplinary themes, including Antarctica's role in global climate and ocean systems (see www.scar.org). The one-time dues increase will help erase a $100,000 shortfall in the group's $322,000 annual budget. Germany and the United Kingdom have pledged to double their contributions, to $28,000 annually through 2008. But persuading other countries to follow suit will be "a bit of a headache," predicts Chris Rapley, director of the British Antarctic Survey.

–Fiona Proffitt

Published by AAAS

BIOTERRORISM AND THE COURTS

Butler Appeals Conviction, Risking Longer Sentence

Taking a high-stakes legal gamble that could lengthen his 2-year prison term, former plague researcher Thomas Butler is appealing his conviction for mishandling bacteria samples and defrauding his university. Government prosecutors say they will respond with their own request to erase a judge's decision that cut 7 years off a possible 9-year prison term.

"Butler is taking a huge, huge risk," says former prosecutor Larry Cunningham, a law professor at Texas Tech University in Lubbock. "The judge gave him a sweet deal; this gives the government a shot at overturning it."

Butler "is willing to risk a longer sentence to fight for important principles," says Jonathan Turley, one of Butler's attorneys and a law professor at George Washington University in Washington, D.C. "The trial was rife with irregularities; the government is pursuing a longer sentence because it is embarrassed about losing its core case." Prosecutors declined comment.

Butler, 63, captured national headlines last year after he reported 30 vials of plague bacteria missing from his Texas Tech laboratory, sparking a bioterror scare (*Science*, 19 December 2003, p. 2054). The government ultimately charged him with 69 counts of lying to investigators, moving plague bacteria without proper permits, tax fraud, and stealing from his university by diverting clinical trial payments to his own use. Last December, a Texas jury acquitted him of the central lying charge and most of the plague-related allegations but convicted him on 44 financial charges and three export violations involving a mismarked Federal Express package containing bacteria.

Although government sentencing guidelines called for a 9-year sentence, federal judge Sam Cummings reduced it to 2 years, in part because Butler's research had "led to the salvage of millions of lives." Butler is currently in a Texas prison.

Prosecutors were unhappy with the sentence, say sources familiar with the case, but agreed not to challenge it unless Butler filed an appeal. He recently did just that, arguing in an 80-page brief that his trial was marred by the government's refusal to try him separately on the plague and financial charges, its use of vague university financial policies as the basis for criminal charges, and a judge's ruling that barred Butler from gaining access to university e-mails. He is asking the appeals court to strike down the convictions or at least order a new trial. Prosecutors are expected to file a response later this month, and a hearing in New Orleans, Louisiana, could come as early as January.

Butler has rolled the legal dice before. He rejected a pretrial government plea bargain offer that included 6 months in jail. Turley expects the government to ask the appeals court to impose the full 10-year sentence allowed by the export violations but says that move would be a "vindictive, gross abuse of prosecutorial discretion."

If the government wins, Butler will lose more than his argument. Because the appeal is expected to take longer than his current sentence, he could find himself back in prison after spending time as a free man.

–DAVID MALAKOFF

INFECTIOUS DISEASES

Bird Flu Infected 1000, Dutch Researchers Say

AMSTERDAM—At least 1000 people—many more than assumed—contracted an avian influenza virus during a massive poultry outbreak in the Netherlands last year, according to a new study. In another unexpected finding, those who developed symptoms after being infected passed the virus on to a whopping 59% of their household contacts, say the researchers at the National Institute for Public Health and the Environment (RIVM), whose results were published in Dutch last week.

Flu experts were cautious in discussing the findings, which they had not yet been able to read. But if correct, they are "another warning signal," says Klaus Stöhr, head of the World Health Organization's global influenza program. Every time an avian virus infects a human being, Stöhr says, the risk that it will mutate into a pandemic strain grows.

Almost 31 million poultry were culled in the Netherlands before the virus, a strain called H7N7, was contained. By the end of the outbreak, the virus had killed one veterinarian, and some 450 people had reported health complaints, mostly an eye infection called conjunctivitis. In a paper published in *The Lancet* in February, RIVM virologist Marion Koopmans and her colleagues reported that they detected the H7N7 virus—using the polymerase chain reaction or by culturing the virus—in eye swabs of 89 of them.

Take your pills. Many of those exposed to infected chickens did not take antiviral drugs, the study found.

To gauge the true reach of H7N7, Koopmans and her colleagues also tested those at risk, such as poultry farmers and those hired to cull and remove poultry, for antibodies against the virus. This test provides more definitive and longer-lasting proof of infection. They used a new variation on the classic hemagglutinin inhibition test, which the team says is better at picking up antibodies to avian flu in humans. (It uses red blood cells from horses, rather than turkeys or chickens, in a key step.)

They found antibodies in about half of 500 people who had handled infected poultry; based on the total number of poultry workers at risk, the team concludes that at least 1000 people must have become infected, most of them without symptoms. Wearing a mask and goggles did not seem to prevent infection; taking an antiviral drug called oseltamivir (Tamiflu) did, but a quarter of the cullers and half of the farmers did not use the drugs.

Among 62 household contacts of conjunctivitis patients, 33 became infected—another surprisingly high figure, Stöhr says. Having a pet bird at home increased household members' risk of becoming infected, perhaps because the birds replicated the virus too.

Detecting antibodies to avian influenza is "tricky," and the results need to be corroborated, cautions flu specialist Maria Zambon of the U.K. Health Protection Agency, whose lab may retest the Dutch samples.

Human antibody tests for H5N1, the avian flu virus currently ravaging Asian poultry, are ongoing, Stöhr says. So far, the results show that, although far more lethal to humans, the virus has caused few, if any, infections beyond the known 43 patients.

–MARTIN ENSERINK

CREDIT: MICHAEL KOOREN/REUTERS

BIOCONTAINMENT

1918 Flu Experiments Spark Concerns About Biosafety

Just days after publishing a well-received study in which they engineered the 1918 pandemic influenza virus to find out why it was so deadly, researchers are catching flak from critics who say their safety precautions were inadequate. The lead investigator, Yoshihiro Kawaoka, contends his team followed federal guidelines. But critics say these rules are out of date.

The brouhaha erupted after Kawaoka's team at the University of Wisconsin and the University of Tokyo reported in the 7 October issue of *Nature* that a normal human flu virus containing a gene for a coat protein from the 1918 flu strain is highly pathogenic to mice. An article in the *New York Times* noted that although the team began the studies in a stringent biosafety level 4 (BSL-4) lab in Canada, where workers wear "space suits," the University of Wisconsin's safety board approved moving the work to its own BSL-3 lab.

That set off alarm bells with some biosafety experts, including Karl M. Johnson, a former Centers for Disease Control and Prevention (CDC) virologist now retired in Albuquerque, New Mexico. He and several others wrote to Promed, an Internet e-mail forum widely read in the infectious-disease community, arguing that the move to a BSL-3 was dangerous.

Kawaoka responds that the critics do not know the full extent of his team's precautions. Among other steps, his workers get the regular flu vaccine, which protects mice against 1918-like flu viruses. All workers also take the antiflu drug Tamiflu prophylactically. Work by Kawaoka's group (in the BSL-4 facility) and by a federal lab has shown that the antiviral "works extremely well" at protecting mice against 1918-like flu strains, Kawaoka says. According to National Institutes of Health (NIH) guidelines for research with recombinant organisms, this puts the work in the BSL-3 category, he notes.

Kawaoka's group also beefed up its lab to what is informally known as an "enhanced" BSL-3, or BSL-3+. For example, workers wear battery-powered air purifiers with face shields and shower when they leave the lab. When Kawaoka presented the work in September to NIH's Recombinant DNA Advisory Committee (RAC), which was reviewing research with pathogenic viruses, "no member raised any concern," he says.

Johnson is partly assuaged. "I feel a bit better," he says, adding that BSL-3+ may be adequate for some experiments with engineered 1918 flu. But he still has reservations about, for instance, whether the vaccine would fully protect some individuals.

Other critics on Promed, however, such as Ronald Voorhees of the New Mexico Department of Health, argue that antiviral drugs may not eliminate the risk of a worker passing the virus to someone outside the lab, so a BSL-4 facility is needed. Biosafety expert Emmett Barkley of Howard Hughes Medical Institute suggests that if experts were polled, "half of them would call for [BSL-4]."

Safety risk? Some experts question whether BSL-3+ conditions, like the air purifier worn here, would prevent engineered 1918 pandemic flu from escaping.

CREDIT: DARRELL KAPCZYNSKI

Part of the confusion stems from another set of federal guidelines, *Biosafety in Biomedical and Microbiological Laboratories* (*BMBL*). This manual says that flu viruses require only BSL-2 facilities, and there is no mention of 1918 flu or "enhanced" BSL-3, Johnson notes. The issue is important to resolve, as Kawaoka's is not the only group working on 1918-like flu viruses. A group led by Mount Sinai School of Medicine in New York City is doing so in a BSL-3+ facility at the CDC, and the University of Washington plans to study monkeys infected with modified 1918 flu strains in a BSL-3+ lab.

Even more controversial are planned experiments that would mix pathogenic avian flu strains, such as the H5N1 strain now circulating in Asia, with human flu viruses (*Science*, 30 July, p. 594). CDC scientists have opted for BSL-3+, but flu expert Robert Webster of St. Jude Children's Research Hospital in Memphis, Tennessee, says he would do these studies in a BSL-4 facility.

Clearer guidance may emerge in the next version of *BMBL*, due out in 2005. Meanwhile, RAC expects to release "points to consider" in December.

–Jocelyn Kaiser

ScienceScope

Fly Me to the Moon?

NASA's new research plan for sending humans to the moon and Mars is a "solid beginning," says a National Academies interim report released last week. But it cautions that limited space-based studies, funding uncertainties, and NASA's failure to adequately consider radiation and psychological hazards to astronauts could hamper preparation for long-duration missions.

To gain better insight into the challenges of space living, the panel—led by anesthetist David Longnecker of the University of Pennsylvania in Philadelphia—recommends that NASA make greater use of Earth-based experiments, including trials in extreme environments such as polar bases and underwater shelters. The panel is due to release a final report next August, and Guy Fogelman, head of NASA's new human health and performance office, says the agency is likely to adopt "most or all" of the recommendations.

–Andrew Lawler

Schwarzenegger Backs Stem Cell Initiative

California's popular "Governator" has weighed in on Proposition 71, giving the state's $3 billion stem cell bond initiative a boost that supporters predict will result in a big win on election day. Republican Governor Arnold Schwarzenegger this week defied his party with a surprise endorsement of the measure, saying that "I am very much interested in stem cell research and support it 100%."

Schwarzenegger won his post with a promise to rein in the state's spiraling budget deficit. Although opponents of Proposition 71 predict that it would add to the state's debt, Schwarzenegger sided with supporters who claim it would spark a biotech boom. Initiative backers "made a compelling fiscal argument that he bought," says stem cell researcher Evan Snyder of the Burnham Institute in La Jolla, California. "We are ecstatic."

Schwarzenegger's decision could cause political ripples beyond California, says Matthew Nisbet, a communications professor at Ohio State University in Columbus who studies public opinion on the stem cell issue. He says the endorsement "will reinvigorate the issue in the [presidential] campaign too."

–Constance Holden

GENERAL RELATIVITY

Swiveling Satellites See Earth's Relativistic Wake

Curve balls. LAGEOS's laser-ranging satellites revealed a twist in spacetime.

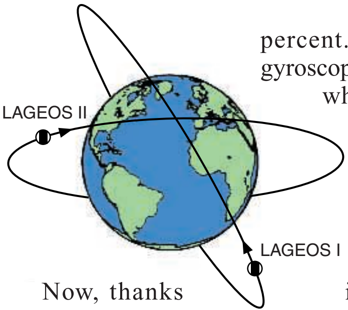

The world's a drag—and scientists have proved it. By studying the dance of two Earth-orbiting satellites, Italian physicists have detected the subtle twisting of spacetime around a massive, spinning object.

The measurement is the most convincing sighting yet of a hard-to-spot consequence of Albert Einstein's general theory of relativity, says Neil Ashby, a physicist at the University of Colorado, Boulder. "There was a lot of criticism of previous results, but this is the first reasonably accurate measurement," Ashby says. Physicists Ignazio Ciufolini of the University of Lecce, Italy, and Erricos Pavlis of Goddard Space Flight Center in Greenbelt, Maryland, describe the result this week in *Nature*.

General relativity predicts that a spinning mass drags the fabric of space and time around with it, much as a restless sleeper drags the sheets around while twisting and turning in bed. This effect, known as the Lense-Thirring or "frame dragging" effect, is difficult to detect. To spot it, one has to observe how a spinning body changes the orientations of nearby gyroscopes—much tougher than seeing, say, how a massive body bends light.

Ciufolini, Pavlis, and colleagues tried to measure the effect in 1998 by using two satellites, LAGEOS and LAGEOS II, as test gyroscopes. The satellites—half-meter-wide mirrored spheres—were launched in 1976 and 1992 as targets for laser range finders, which can track their position within a few centimeters. As the satellites spin around Earth, the Lense-Thirring effect twists the planes of their orbits slightly. The early measurements were "very rough," Ciufolini says, because the uneven distribution of Earth's mass causes similar orbital distortions thousands of times greater than those due to the Lense-Thirring effect. "[A satellite's] precession is about 2 meters per year due to frame-dragging. The precession due to the oblateness of the Earth is many thousands of kilometers per year," Ashby says.

Because the mass distribution was poorly known, Ciufolini and colleagues had to make a few controversial estimates, including one about how the satellites' perigees precess. As a result, their published value of the Lense-Thirring effect had a large error—20%—and even that was greeted with some skepticism.

Now, thanks to better gravitational maps produced by twin satellites known as GRACE, as well as improved gravitational models and other refinements, the perigee estimation is no longer needed. The result is a much firmer detection with an error of about 10%. "I believe that in a few years, more accurate gravitational field models and a longer period of observation will make it more and more accurate," says Ciufolini. "It will be at the level of a few percent." By then, physicists hope, the gyroscope-laden satellite Gravity Probe B, which was designed to detect the Lense-Thirring effect, will have produced results with an error of about 1%—far lower than the two LAGEOS satellites can achieve (*Science*, 16 April, p. 385). "I think that the biggest contribution is a validation of what, in a year or so, will be the results from Gravity Probe B," says Richard Matzner, a physicist at the University of Texas, Austin.

To keep Gravity Probe B from being the only game in town, Ciufolini and other researchers are pushing to loft another LAGEOS satellite into an orbit that would completely eliminate the effects of Earth's mass distribution. "If we had a third satellite, we could go even below the 1% limitation," says Ciufolini. Of course, getting funding for a new satellite is quite a drag—one much easier to sense than the Lense-Thirring effect.

–CHARLES SEIFE

MEDICINE

Metabolic Defects Tied to Mitochondrial Gene

Abnormally high blood pressure is bad enough by itself; it predisposes people to diseases such as kidney failure, heart attacks, and strokes. But for an estimated 47 million Americans with so-called metabolic syndrome, high blood pressure (hypertension) comes hand in hand with other cardiovascular risk factors such as diabetes and high blood concentrations of cholesterol and triglycerides. Obese people often have metabolic syndrome, but so do some nonobese people, so excess weight isn't the sole cause.

Findings published online this week by *Science* (www.sciencemag.org/cgi/content/abstract/1102521) now point to an unexpected new culprit. The work, by a team led by Richard Lifton of Yale University School of Medicine, shows that a mutation in a mitochondrial gene causes people to develop a constellation of symptoms—hypertension, high concentrations of blood cholesterol, and lower-than-normal concentrations of magnesium—similar to those of metabolic syndrome.

The mutation likely disrupts the function of mitochondria, subcellular structures that provide most of a cell's energy and have their own small genome. Despite uncertainty about how a mitochondrial DNA mutation could lead to such diverse symptoms, hypertension expert Theodore Kurtz of the University of California, San Francisco, says that the finding "could be of tremendous importance." Previously, few cardiologists looked to the mitochondria for insight into hypertension and other cardiovascular risk factors, but this, he says, "could shift the interest dramatically."

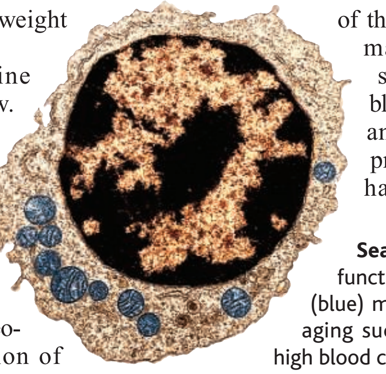

Seat of the problem? Malfunction of the mitochondria (blue) may underlie problems of aging such as hypertension and high blood cholesterol.

The new discovery grew out of the examination of a female patient who was suffering from low blood magnesium. Lifton and his colleagues had previously discovered a handful of genes that, when mutated, cause this blood condition, which is characterized by general malaise and weakness. In the course of conversations with the woman, she mentioned that several of her relatives also suffered from low blood magnesium. What's more, her family was a gene hunter's dream. It "was extremely large and ▶

CREDITS (TOP TO BOTTOM): NASA; GOPAL MURTI/VISUALS UNLIMITED

Published by AAAS

all lived close to one another," Lifton says.

Further investigation turned up 142 relatives, many of whom had low magnesium, hypertension, elevated blood cholesterol concentrations, or some combination of those problems. Even more intriguing, in all cases, the traits had been inherited from the individuals' mothers—a clear indication that the gene at fault was located in the mitochondrial genome. The genes that Lifton has previously linked to low blood magnesium had all been nuclear.

The mitochondrial location of the new gene mutation was a big advantage because that genome consists of only 16,000 base pairs as opposed to the 3 billion in the nuclear genome. Analysis of the mitochondrial genome of family members turned up one mutation found only in affected members and not detected in any of the thousands of mitochondrial genomes previously sequenced. This mutation altered one base—a thymidine was changed to a cytosine—in the gene for a mitochondrial transfer RNA (tRNA), which carries amino acids to the ribosome for protein synthesis.

Because virtually all tRNAs have a thymidine at that spot, implying that it's essential for the molecule's function, the swap likely disrupts the tRNA's structure and interferes with protein synthesis in the mitochondria. "The [thymidine] is extremely conserved," says Carlos Moraes, an expert on mitochondrial genetics at the University of Miami, Florida. "That does indicate that the mutation could cause some kind of problem."

Moraes adds that he's surprised that people with the mutation don't suffer even more serious problems. Previous mutations found in mitochondrial tRNA genes have caused, among other things, muscle and nerve degeneration, although the extent of the damage can vary.

A key question now is how the mutation produces hypertension and the other symptoms, which seem to be independent of one another. The low blood magnesium levels, which appear even in children, might be due to failure of the kidney to remove the mineral from the urine before it's excreted—a process that requires a great deal of energy.

In contrast, blood pressure and cholesterol concentrations were normal in young individuals but began increasing at about age 30. That suggests additional factors come into play with age. These might be environmental—say, a high-fat diet—or related to the declining mitochondrial function that some researchers think contributes to aging.

Another crucial unknown is whether mitochondrial dysfunction contributes to metabolic syndrome in the general population. Kurtz thinks it might. "The implications are much greater than this finding in one family," he predicts.

–JEAN MARX

PHYSICS

Researchers Build Quantum Info Bank By Writing on the Clouds

An information theorist doesn't care whether a quantum bit is stored on particles of matter or particles of light. But to an experimentalist, it's a very big deal where your qubit is stored because slow but long-lived chunks of matter have very different properties from those of quick but evanescent photons. Now, two physicists have shown how they can reliably transfer quantum information from matter to light. The procedure may soon enable scientists to exploit the advantages of both matter and light in building systems for quantum communications.

"It's a breakthrough that is needed," says Klaus Møller, a physicist at the University of Aarhus in Denmark. "It's a bridge between traveling qubits—light—and stationary ones."

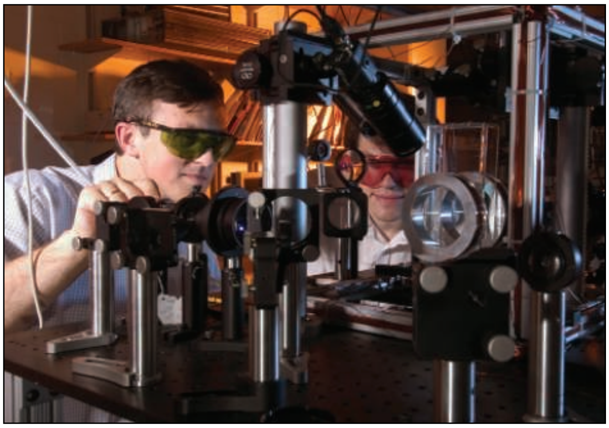

Bright bits. By routing laser beams through wisps of gas, physicists shuttled information between light and matter.

For years, physicists have been excited about using the properties of quantum theory in computing and communications. In theory, a quantum computer could solve certain problems (such as cracking a code) much faster than a classical computer can; a communications system built upon quantum-mechanical particles would be functionally immune from eavesdropping.

But quantum computers and quantum communications depend on having information stored on quantum objects like atoms and photons rather than classical ones like hunks of silicon—and quantum objects are hard to handle. Quantum bits stored on particles of light travel well—they can zip for kilometers down a fiber-optic cable—but they are tricky to store. Quantum bits stored on matter "keep" for milliseconds or longer, but they're usually confined to a trap and can't be transmitted from place to place.

In this issue (p. 663), Alexei Kuzmich and Dmitri Matsukevich of the Georgia Institute of Technology in Atlanta describe how they store a quantum bit in a cloud of rubidium atoms and induce the cloud to inscribe that information, undamaged, upon a photon. The researchers start with two clouds of rubidium gas. By shooting a laser through both clouds simultaneously, they force the clouds to emit a single photon that is quantum-mechanically entangled with both of the clouds simultaneously. (Quantum indeterminacy and the experimental setup make it impossible to say the photon came from one cloud or the other.) The entanglement links the fates of the photon and the clouds; tweaking the photon's polarization alters the quantum state of the clouds. By manipulating the photon, the physicists can inscribe a quantum bit upon the two clouds.

A few hundred nanoseconds later, the researchers read out the information by shining another laser upon the rubidium samples. The laser induces the clouds to emit another photon—a photon whose polarization contains the information that the researchers had inscribed upon the cloud. That laser-driven retrieval transfers quantum information from matter to light, Kuzmich says.

Although the procedure is beset by losses due, in part, to the inefficiency of rubidium clouds' absorption of laser light, Kuzmich believes that the method will lead to useful tools for quantum communication. "To be honest, I think that this will be a practical device eventually," he says. Indeed, he and Matsukevich are hard at work trying to hook up two of the matter-light devices to create a quantum repeater—an amplifier that reverses the inevitable loss of signal strength that occurs when light is sent down a long stretch of fiber-optic cable. Such repeaters would be essential for long-distance quantum communication.

"I firmly believe that these guys will do it," says Møller. If they do, he says, quantum communications and large-scale quantum computation will be considerably closer than before. "Everyone will benefit."

–CHARLES SEIFE

CREDIT: GARY W. MEEK/GEORGIA TECH

NATIONAL INSTITUTES OF HEALTH

Male Sweep of New Award Raises Questions of Bias

Where are the women? That's what some scientists are asking after the National Institutes of Health (NIH) picked nine men to receive the inaugural Director's Pioneer Award for innovative research (*Science*, 8 October, p. 220).

The 5-year, $500,000-a-year awards are part of NIH's "roadmap" for increasing the payoff from the agency's $28 billion budget, and Director Elias Zerhouni has compared the winners to famed U.S. explorers Merriweather Lewis and William Clark for their willingness "to explore uncharted territory." Within hours of the 29 September announcement, however, some researchers had begun to bristle at the gender imbalance in that first class of biomedical pioneers.

"It sends a message to women researchers that they are not on an even playing field," wrote Elizabeth Ivey, president of the Association for Women in Science, in a 1 October letter to Zerhouni. "I hope that you [will] make an effort to correct such a perception." The American Society for Cell Biology, in a 15 October letter to Zerhouni, commended him for creating the prize but lamented its "demoralizing effect" on the community. Critics noted that men constituted 94% (60 of 64) of the reviewers tapped to help winnow down some 1300 applications for the award and seven of the eight outside scientists on the final review panel, which grilled applicants for an hour before settling on the winners.

NIH officials estimate that women made up about 20% of the Pioneer applicants. But only about 13% of the 240 who made it through the first cut were women, and only two of the 21 finalists. (In contrast, about 25% of the applicants for NIH's bread-and-butter R01 awards to individual investigators are women, and their success rate is within a percentage point of that of their male counterparts.) "With any elite award, there are so many deserving candidates that it's easy to choose only men," says Stanford University neuroscientist Ben Barres, who says he was "outraged" by the gender imbalance. "I actually think it's more a matter of neglect than of sexism."

The gender of the final applicants did not come up during the discussion, says review panel member Judith Swain, professor of medicine at Stanford. Swain, who called the exercise "the most interesting review panel I've ever been involved in," says she saw no evidence of "active discrimination." But she concurs that the demographics of the reviewers and the winners lead to "a disturbing observation."

NIH officials are struggling to find the best way to respond to the charges of gender insensitivity. Stephen Straus, head of the National Center for Complementary and Alternative Medicine and team leader for the NIH-wide competition, told *Science* on the day of the awards that "we gave the gender issue a great deal of thought, but none of the women finalists came close to making the pay line." A week later, in the first of a series of e-mail exchanges with Barres, Straus remarked that the absence of women was "noted with some surprise" by senior NIH officials and that "we know we can do better" in subsequent rounds. In a later exchange, however, Straus wrote, "I don't believe that NIH can credibly discard its two-level peer review system when nine grants out of the many thousands awarded this year turn out differently than some might wish."

NIH is evaluating how it ran the Pioneer program—including how the award was publicized and the demographics of the applicants—before launching the next competition in January. A thorough review is essential, says Arthur Kleinman, a medical anthropologist at Harvard University and chair of the final review panel, who believes NIH needs to do more to reach several groups—minorities and social and behavioral scientists as well as women—not represented in the first batch of winners. "I agree that they need to be more sensitive to diversity," he says. "But at the same time, I think Zerhouni deserves a lot of credit for even trying something like this."

—JEFFREY MERVIS

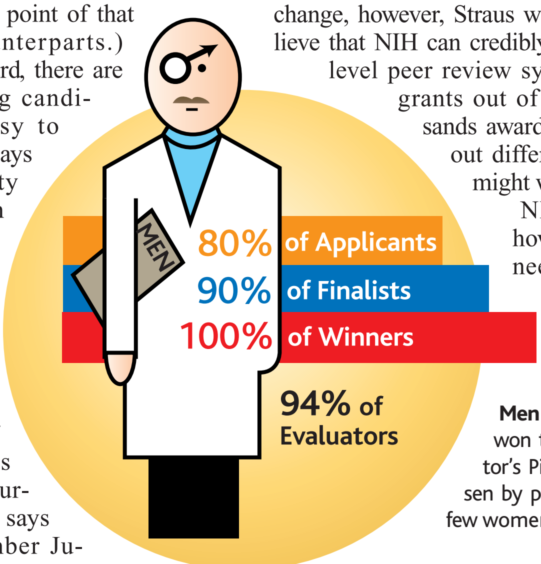

Men at work. Nine men won the first NIH Director's Pioneer Awards, chosen by panels that included few women.

SOURCE: NIH

NATIONAL SCIENCE FOUNDATION

End of Cost Sharing Could Boost Competition

The National Science Foundation (NSF) is leveling the playing field for grant seekers by removing a mandatory cost-sharing requirement for some programs. But the move is expected to result in a more crowded playing field, too, as institutions that couldn't afford the entry fee can now apply.

Last week the agency's policymaking body, the National Science Board, voted to eliminate cost-sharing rules that, in 2001, affected roughly one-sixth of NSF's 20,000 grants—in particular large centers and major instrumentation programs—and added $534 million to the agency's own spending on research. In some cases, universities had to come up with funding that matched the size of the award.

The requirements were seen as a way to stretch tax dollars and ensure that an institution's leaders were committed to a proposal, but university officials have long viewed them as a hidden tax on federally funded research. Two years ago, the board told NSF that the amount a university promises to contribute should not affect decisions on which proposals get funded. The new rule goes one step further, by banning mandatory cost-sharing entirely except for a statutory 1% fee.

"NSF's current policy represented an unfair burden on some institutions that couldn't afford to enter the competition," says Mark Wrighton, chancellor of Washington University in St. Louis, Missouri, and chair of the board committee that recommended the change. "This will give schools greater flexibility to invest their research dollars." The board also asked for a report in 2 years on any unintended consequences of the new policy.

NSF officials began cutting back on cost sharing after the board's 2002 directive, and this month a solicitation for its major research instrumentation program, written before the board's action, drops the requirement. But there's a quid pro quo: Institutions must pick up the full cost of maintenance and operations when a project starts rather than after the grant expires. Even so, Dragana Brzakovic, who manages the instrumentation program, expects success rates to drop from nearly 40% to about 30% as more institutions compete for the awards.

—JEFFREY MERVIS

Published by AAAS

In hopes of finding new remedies for ills including cancer and diabetes, scientists are following a band of elusive immune-cell cops whose existence was once hotly debated

Policing the Immune System

From blood samples, pediatric immunologist Hans Ochs has diagnosed five infant boys who all had the same devastating problems. Their immune systems had gone haywire, attacking their gastrointestinal tracts within a few weeks of birth and causing severe, intractable diarrhea. Wayward immune cells also laid siege to each boy's pancreas, producing diabetes around 3 months of age. Within months of their births, several of the infants became depleted of red and white blood cells from the immune onslaught.

No cure exists for this rare and frequently deadly immune disease dubbed immune dysregulation, polyendocrinopathy, enteropathy, X-linked syndrome (IPEX). But thanks in large part to recent work by Ochs at the University of Washington School of Medicine in Seattle and his colleagues, its cause in most cases is now known. A genetic defect severely impairs, if not abolishes, the body's ability to produce regulatory T cells, a mysterious class of immune cells apparently designed to squelch dangerous immune responses.

Once dismissed as artifacts of misguided research, regulatory T cells—originally called suppressor T cells—are now white hot among immunologists, thanks to a body of research that over the past 8 years clarified their existence. Hundreds of researchers are flocking to the field, which could lead to novel treatments for an array of immune disorders, such as type I diabetes, multiple sclerosis, graft-versus-host disease, and allergy, that are far more common than IPEX. Studying regulatory T cells may also provide clues to the treatment of cancer; the cells actually seem to protect tumors against immune attack.

"All anyone is talking about these days is regulatory T cells," says Ethan Shevach, a cellular immunologist at the National Institute of Allergy and Infectious Diseases (NIAID) in Bethesda, Maryland. Nevertheless, fundamental mysteries remain about this newfound class of immune cells. Their mechanism of action is almost totally opaque. Also unclear is to what extent they play roles in more ordinary human autoimmune diseases that develop later in life, such as diabetes and multiple sclerosis. "Regulatory T cell research is very intriguing but is not yet ready for mass consumption," Ochs says. "There are still a lot of puzzles."

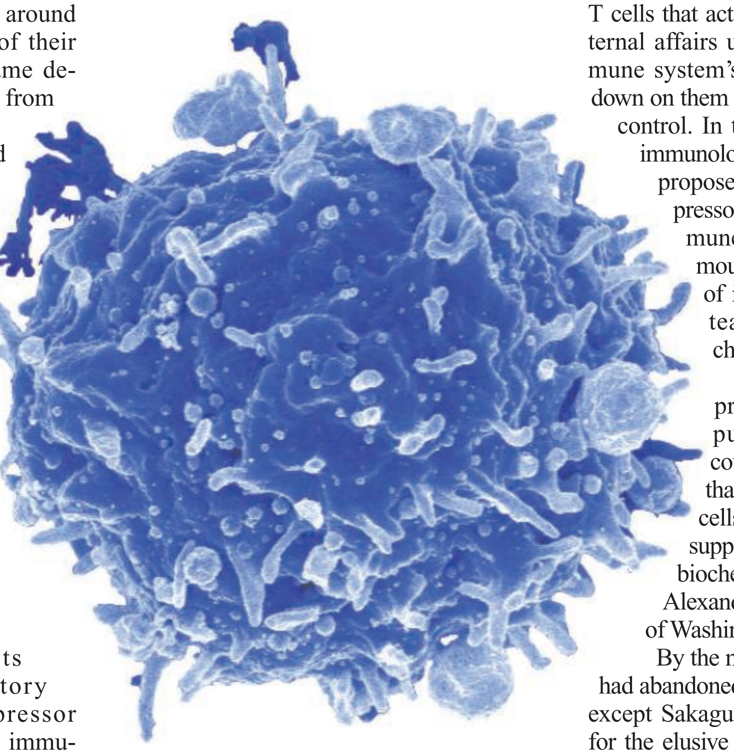

Caught. Scientists have finally nabbed the elusive regulatory T cell.

CREDIT: K. HASENKRUG AND D. DORWARD

Even so, many researchers are optimistic that studying regulatory T cells will lead to new therapies. Drugs that seem to target these cells are already being tested in people with cancer and diabetes, and pharmaceutical companies are trying to develop drugs that augment or suppress regulatory T cells for other disorders. "Within 5 years, some clinical application of these cells will be here," predicts Shimon Sakaguchi, an immunologist at Kyoto University in Japan and a pioneer in the field.

From fantasy to reality

The human body makes several types of T cells, including killer T cells, which eradicate infected cells, and helper T cells, which arouse killer T cells and various other immune cells to fight invaders. And for decades, researchers have kicked around the idea that the body also makes a class of T cells that act like a police department's internal affairs unit, keeping tabs on the immune system's cellular cops and cracking down on them if they threaten to spiral out of control. In the early 1970s, the late Yale immunologist Richard Gershon formally proposed the existence of these suppressor cells to explain a form of immune tolerance he observed in a mouse. The idea caught the fancy of immunologists, and numerous teams rushed to identify and characterize these cells.

The entire concept of suppressor T cells fell into disrepute, however, when no one could verify reports of molecules that supposedly characterized the cells. "It was a kind of fantasy not supported by modern genetics and biochemistry," recalls immunologist Alexander Rudensky of the University of Washington, Seattle.

By the mid-1980s, virtually everybody had abandoned the idea of suppressor T cells except Sakaguchi, who continued his quest for the elusive cells. Extending earlier work, Sakaguchi and his colleagues showed, in the 1980s, that removing the thymus of a mouse on day 3 of its life—which depletes the animal of most of its T cells—causes various autoimmune diseases to develop. Inoculating the thymus-free mice with a mixed population of T cells from another mouse prevents those diseases, the researchers found.

Sakaguchi felt that the autoimmune diseases resulted from a deficit in putative suppressor T cells that were made in the thymus on or after day 3; their absence left unchecked any T cells that had developed earlier. But critics contended that infections could have triggered the autoimmune reaction. Without pinpointing the suppressors, the Kyoto team could not prove its case.

Published by AAAS

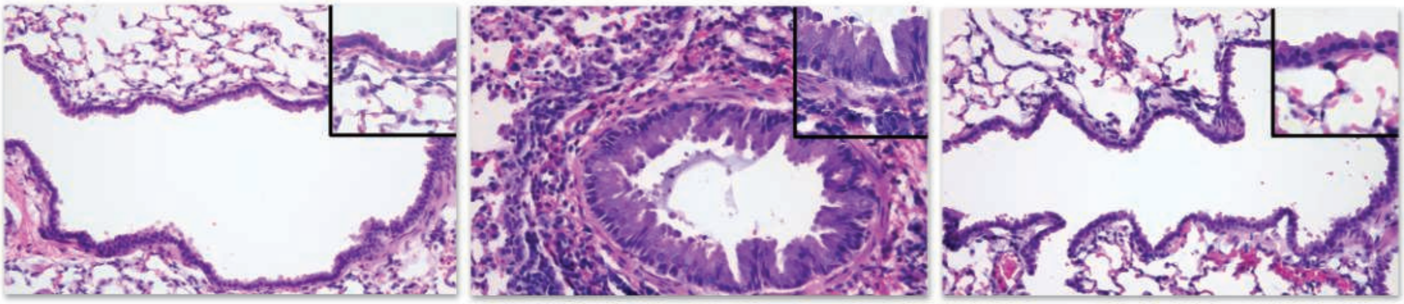

Fighting asthma. Compared to the clear lungs of a normal mouse (left), the lungs of an egg-white-allergic mouse become inflamed when exposed to the allergen (middle). Infusing such a mouse with regulatory T cells before exposure blocks the inflammation (right).

Finally, in 1995, Sakaguchi and his colleagues reported that they had identified suppressor T cells by the presence on them of a newly identified cell surface protein called CD25 as well as the more ubiquitous surface protein CD4. When they infused a batch of T cells devoid of ones with these markers into mice that lacked their own T cells, the mice developed autoimmune disease. But if they infused the suppressors along with the other T cells, no autoimmune disease appeared. These experiments convincingly showed that a small, specific population of T cells worked to dampen autoimmune reactions.

Virtually no immunologists read the paper, however, because hardly anybody was interested in suppressor T cells anymore. But NIAID's Shevach did. He was so struck by the finding that he rushed to repeat it in his own laboratory—and succeeded. "I had a religious conversion to believe in regulatory T cells," he says. That brought others into the fold, as Shevach had been an outspoken skeptic of the idea. Rudensky credits Sakaguchi's 1995 paper as the turning point: "The field took off."

In 1998, Shevach's and Sakaguchi's groups independently developed cell culture systems that enabled others to study the suppressive activity of the rodent cells in dishes. In 2001, several research teams, including Don Mason and Fiona Powry's at the University of Oxford, plucked out CD4$^+$ CD25$^+$ cells in human blood and determined that they halted the proliferation of other T cells, showing that the rodent data had some relevance to humans.

"Within 5 years, some clinical application of these cells will be here." —Shimon Sakaguchi, an immunologist at Kyoto University in Japan

And last year, the cells were shown to underlie human disease. Three teams of investigators reported that Foxp3, the protein that Ochs and others found to be missing or defective in IPEX patients in 2001, is specifically expressed in regulatory T cells and is essential to their development.

Mice engineered with a defective *Foxp3* gene have a deficit in CD4$^+$ CD25$^+$ T cells and suffer from an IPEX-like disease called scurfy that can be blocked by treatment with regulatory T cells at 1 day old, Rudensky and his colleagues revealed in *Nature Immunology*. In the same journal, a team led by Fred Ramsdell, formerly at Celltech Research & Development in Bothell, Washington, reported that the expression of Foxp3 by T cells in mice correlates with their ability to suppress immune responses. And transferring Foxp3 into naïve T cells converts them into regulatory cells, the Sakaguchi group showed the same year (*Science*, 14 February 2003, p. 1057). Together, the studies indicated that a deficiency of regulatory T cells in humans can lead to severe immune dysfunction.

How suppressor T cells do their job remains a mystery, however. In the test tube, natural regulatory T cells—the type that express CD25 and are made during immune system development—seem to suppress other T cells through direct contact. In living animals, they also may release anti-inflammatory cytokines such as interleukin-10 or transforming growth factor β. So-called adaptive regulatory T cells, which become regulatory only after being stimulated by an antigen and respond only to immune cells targeting that antigen, seem to exert their influence solely by means of cytokines. If that's not complicated enough, Shevach recently reported that regulatory T cells may directly kill the B cells that generate antibodies (*Science*, 6 August, p. 772).

Good cop, bad cop

Despite basic gaps in their understanding of regulatory T cells, researchers are tracking down potential roles for the cells in human disease. David Hafler and his team at Harvard Medical School in Boston reported in April in the *Journal of Experimental Medicine* that patients with multiple sclerosis seem to have defective regulatory T cells.

Impotent regulatory T cells may also play a role in allergy and asthma. Allergist Douglas Robinson of Imperial College London and his colleagues isolated natural regulatory T cells from the blood of people with and without allergies. They then exposed the remaining T cells to an allergen. In all of the samples, the allergen (from grass pollen) triggered T cell proliferation and a release of inflammatory molecules, or cytokines, from immune cells. Adding back regulatory T cells from the nonallergic people completely suppressed this inflammatory response, whereas the regulatory T cells from the allergic individuals were far less effective in doing so. The suppression was weaker still from regulatory T cells from patients with hay fever during the pollen season, the researchers reported in February in *The Lancet.*

"One implication is that people who get allergic disease do so because their regulatory T cells don't respond," Robinson says. Boosting the response of these cells, he adds, might help prevent or treat their disease. Boosting the adaptive class of regulatory T cells may also be important. Two years ago, for example, Stanford's Dale Umetsu and his colleagues identified adaptive regulatory T cells that protect against asthma and also inhibit allergic airway inflammation in mice.

Although regulatory T cells seem to be protective in autoimmune disorders and allergy, they may have a darker side. In the March issue of *Immunity*, a team led by immunologist Kim Hasenkrug of NIAID's Rocky Mountain Laboratories in Hamilton, Montana, suggests that some viruses, such as those that cause hepatitis and AIDS, may exploit regulatory T cells to

CREDITS (TOP TO BOTTOM): D. UMETSU, *NATURE MED.* **8** (2002); COURTESY OF SHIMON SAKAGUCHI

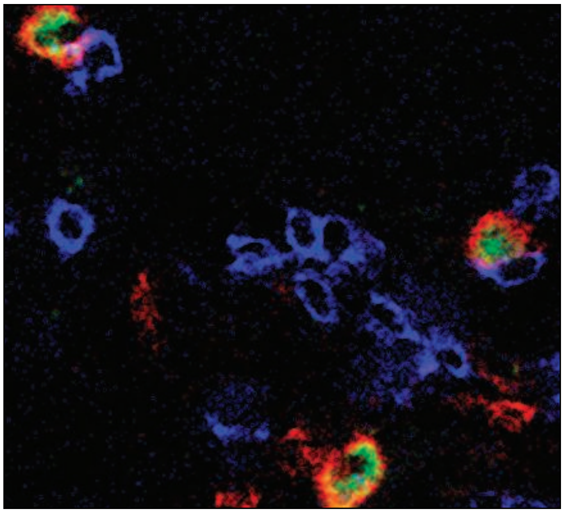

Tumor bodyguards. Regulatory T cells (red and green) interact with tumor-killing T cells (blue) in ovarian tumor tissue.

CREDIT: P. MOTTRAM AND W. ZOU/TULANE UNIVERSITY

dampen the body's antiviral response and allow chronic infections.

Similarly, regulatory T cells may protect tumors from immune attack. Researchers have shown, for example, that removing such T cells from a cancer-afflicted mouse can cause the rodent to reject a tumor. High levels of regulatory T cells have also been found in samples from several types of human tumors. More recently, tumor immunologist Weiping Zou of Tulane University Health Science Center in New Orleans, Louisiana, and his colleagues linked the quantity of regulatory T cells associated with a tumor to disease severity in cancer patients.

Zou's team isolated and counted the T cells in tumor tissue from 104 ovarian cancer patients and noted that the higher the ratio of regulatory T cells to total T cells in the tumor, the farther the cancer had progressed. Regulatory T cells were also associated with a higher risk of death: The more tumor-associated regulatory T cells, the worse the prognosis. Zou and his colleagues further showed that the regulatory cells recovered from tumor tissue protected tumors in a mouse model of ovarian cancer by inhibiting both the proliferation and potency of tumor-attacking T cells.

Zou's team also discovered that, as the cancer progressed, a patient's regulatory T cells appeared to migrate progressively away from their normal home in the lymph nodes to the tumor. The investigators determined that tumor cells secrete a chemical, dubbed CCL22, that attracts regulatory T cells. Blocking CCL22 with an antibody stopped regulatory T cells from migrating to the tumor in the mouse model, the team reported in the September 2004 issue of *Nature Medicine.*

"All anyone is talking about these days is regulatory T cells."

—Ethan Shevach, a cellular immunologist at the National Institute of Allergy and Infectious Diseases

By extension, disarming these regulatory cells or preventing their migration to the tumor could leave the tumor vulnerable to immune destruction. The Tulane researchers and others are testing a regulatory T cell–killer called Ontak in advanced cancer patients. The drug binds to CD25 and kills the cells with diphtheria toxin. The results so far, Zou says, are "encouraging."

Immunologist Steven Rosenberg of the National Cancer Institute in Bethesda has tested another regulatory T cell–blocker in patients with metastatic melanoma. The treatment—an antibody to an essential molecule on the surface of regulatory T cells, called cytotoxic T lymphocyte–associated antigen 4—induced cancer remission in three of 14 treated patients who had end-stage cancer, Rosenberg's team reported last year. More than 2 years later, the patients are still in remission, and Rosenberg's team has now seen a similar remission rate among almost 100 patients.

"The fact that inhibiting regulatory T cells enabled three patients to undergo cancer regression was very strong evidence that regulatory T cells are inhibiting the immune response against tumors," says Rosenberg. "This is the first time that getting rid of this brake on the immune system has been shown to have any impact in humans."

The study also suggests how tricky it may be to interfere safely with the regulatory T cell system, however. Six of the initial 14 cancer patients, including the three who went into remission, developed autoimmune diseases affecting the intestines, liver, skin, or pituitary gland, although these were all reversible with short-term steroid treatment.

Expansion plans

Even in disorders such as type I diabetes, in which regulatory T cells have not been consistently shown to be abnormal in function or number, researchers are exploring them as potential therapy. "Traditionally, immunotherapy is designed to block effector cells or their activities. Now there is the entirely new possibility that we could treat the disease by expanding suppressors," says Ralph Steinman, an immunologist at Rockefeller University in New York City.

In June, Steinman's team and, separately, a team led by Jeffrey Bluestone at the University of California, San Francisco (UCSF), reported mouse studies in the *Journal of Experimental Medicine* that illustrated how this might work. Both research teams plucked out natural regulatory T cells from diabetes-prone mice that made only one type of T cell, one that responds to an antigen on the islet cells of the pancreas. Each team then used different methods to expand the mouse regulatory T cells in lab dishes and found that they could prevent or reverse diabetes when infused into other diabetes-prone mice.

A diabetes treatment that is thought to boost T cell regulation has already reached human trials. The treatment is an antibody to CD3, a cell-surface protein tightly associated with the T cell receptor. The antibody was first found to induce long-term remission of diabetes in mice a decade ago. That surprising result contradicted the idea that the CD3 antibody—which was then used to treat organ rejection—worked by inactivating destructive T cells, because the treatment's effects far outlasted the depletion of activated T cells.

Last year, immunologists Jean-François Bach and Lucienne Chatenoud and their colleagues at Necker Hospital in Paris, along with UCSF's Bluestone, reported in *Nature Medicine* that the antibody appeared to activate natural regulatory T cells in mice. When diabetes-prone mice were treated with the antibody a month after diabetes onset, they became nondiabetic. But if the mice were also treated with drugs that block regulatory T cells, the diabetes remained. "It's a nice story indicating that, in the mouse, immunoregulation explains the long-term effect of the antibody," Bach says.

After initial tests of this antibody approach proved encouraging in a small number of diabetics, Kevan Herold, an endocrinologist at Columbia University School of Medicine in New York City, and his colleagues recently launched a six-center trial of the therapy in 81 diabetic patients. Meanwhile, Chatenoud and her colleagues are about to unveil the results of a multicenter, 80-patient, placebo-controlled trial of the CD3-targeting antibody conducted in Belgium and Germany.

Boosting regulatory T cell activity might someday also induce drug-free immune tolerance to donor organs. In July, Sakaguchi's team reported removing natural regulatory T cells from a normal mouse and expanding them in cell culture with interleukin-2, a growth promoter, along with an antigen from a donor mouse of a

Published by AAAS

“Regulatory T cell research is very intriguing but is not yet ready for mass consumption. There are still a lot of puzzles.” —Hans Ochs, pediatric immunologist, University of Washington

different strain. This generated a population of antigen-specific regulatory cells, which they then infused into so-called nude mice, which lack T cells. The regulatory cell infusion enabled those rodents to accept skin grafts from the donor strain even though they were simultaneously infused with killer and helper T cells. By contrast, nude mice that received only killer and helper T cells—but no regulatory cells—quickly rejected the grafts. “With just a one-time injection of regulatory T cells, we can induce graft-specific tolerance without drugs,” Sakaguchi says.

In cases in which organ donors—such as living donors—are known in advance, Sakaguchi envisions generating antigen-specific regulatory T cells prior to transplantation of human organs. If the therapy works, he says, it could replace the use of immunosuppressive drugs, which come with a significant risk of infection and cancer.

A boost from bugs

The growing understanding of regulatory T cells may eventually shed some light on an immunology-based theory called the hygiene hypothesis. According to this controversial idea, the rise in allergic disorders in recent decades in developed countries results from those countries’ increasing cleanliness, which reduces children’s exposure to protective microbes. A number of researchers have shown that exposure to parasitic worms called helminths may protect against allergy and asthma, among other immune disorders, largely through the induction of regulatory T cells (*Science*, 9 July, p. 170).

Some strains of bacteria have also been shown to be protective—and again regulatory T cells may be involved. Immunologist Christoph Walker of the Novartis Institutes for Biomedical Research in Horsham, U.K., and his colleagues demonstrated that treating mice with killed *Mycobacterium vaccae* before sensitizing them to egg-white allergen significantly reduced the rodents’ inflammatory responses to the allergen, as compared to mice that did not receive the bacteria. Regulatory T cells isolated from bacteria-treated mice could transfer the protection to untreated mice sensitized to the same allergen, demonstrating that the cells mediated the bacteria’s protective effects, the team reported in 2002.

The suppressive response was allergen-specific: The regulatory T cells generated in the egg white–sensitized mice could not dampen the response to cockroach allergen in mice made allergic to cockroaches. “Regulatory T cells generated by mycobacteria treatment may have an essential role in restoring the balance of the immune system to prevent and treat allergic diseases,” the authors wrote in *Nature Medicine.* Walker’s team is now trying to mimic the bacteria’s effects with a chemical that stimulates the same receptors on regulatory T cells that the bacteria stimulate.

But some researchers note that opportunities for rational drug design may be limited by the paucity of knowledge about how regulatory T cells suppress their immune system colleagues. Says Shevach: “We won’t know how to enhance the response until we know what it is.”

Nevertheless, he, Sakaguchi, and others have succeeded in a vital first step. They’ve at long last convinced fellow immunologists that regulatory T cells exist and are important. “So many people are working on regulatory T cells,” Sakaguchi says. “It’s been a pleasant surprise.”

–INGRID WICKELGREN

Climate Change

A Few Good Climate Shifters

Meteorologists probing a dauntingly complex atmosphere have found patterns of natural climate change that offer hope for making regional climate predictions

Look more than a week or two into the future, and none of the atmosphere’s detailed behavior—the weather—can be predicted. Climate, on the other hand, is less capricious. All of northern Europe, for example, warms or cools for years or decades at a time. The shifts in atmospheric circulation behind such relative climatic stability once seemed likely to provide a way to predict patterns of regional climate change around the world. But a profusion of patterns discerned by applying different analytical techniques to different data sets—think dozens of blind men and an elephant—soon threatened to swamp the promising field.

Researchers are now managing to stem the tide. “When I was a graduate student in the late ’80s, there were a zillion” patterns of variability, says climate modeler John Fyfe of the University of Victoria, British Columbia. “Of those, only a handful have survived.” Three new studies show that almost all proposed patterns fit into one of three or four globally prominent patterns: the El Niño pattern tied to the tropical Pacific Ocean; two great rings of climate variability, each circling a pole at high latitudes; and a last pattern across much of the northern mid-latitudes. “At one point, it looked like there might be an infinite number” of patterns, says meteorologist Kevin Trenberth of the National Center for Atmospheric Research (NCAR) in Boulder, Colorado. “Well, actually, there are relatively few.”

This emerging simplification of meteorologists’ view of atmospheric dynamics “provides a basis to move forward on regional climate change,” says Trenberth. That ability will become increasingly important as the greenhouse intensifies: Policymakers want to know what’s going to happen regionally, not just on the global average.

Oops. When Siberian permafrost thaws, buildings can lose their footing and slowly crumble.

CREDIT: ALEXANDER SHIKLOMANOV/UNIVERSITY OF NEW HAMPSHIRE

Until recently, natural climate variations were beginning to look as complex and indecipherable as next month’s weather. “The climate dynamics literature abounds with patterns of variability,” note meteorologists Roberta Quadrelli and Michael Wallace of the University of Washington, Seattle, in their October *Journal of Cli-*

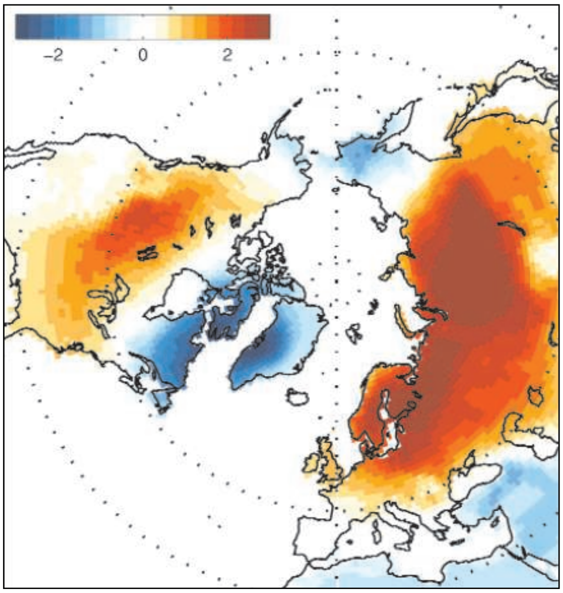

Change in the air. Wind shifts—perhaps induced by rising greenhouse gases—brought 40 years of warming (oranges) and cooling (blues) to high latitudes.

CREDIT: R. QUADRELLI AND J. M. WALLACE, *JOURNAL OF CLIMATE* **17** (2004)

mate paper. The Northern Hemisphere alone has had at least 17 patterns proposed for it, variously termed teleconnection patterns, oscillations, clusters, seesaws, circulation regimes, and modes. Quadrelli and Wallace believe they've narrowed it down to two "principal patterns of variability," or more informally, modes.

Quadrelli and Wallace tried to get as comprehensive a feel for the elephant as they could. They considered the entire Northern Hemisphere outside the tropics during the 4 months of winter, when atmospheric circulation is strongest. They analyzed the longest, most thoroughly vetted data set available, which runs from 1958 to 1999. They started with atmospheric pressure at sea level, but also included a measure of atmospheric pressure up through the lower atmosphere as well as surface air temperature. And they employed a statistical method that is widely used to identify the most common patterns of atmospheric behavior.

The results were just two patterns in the Northern Hemisphere. One is the previously recognized Arctic Oscillation, now termed the Northern Annular Mode (NAM). The second is a pattern strongly resembling the long-established Pacific–North American (PNA) pattern. The NAM is an erratic pressure seesaw that raises pressures alternately over the pole and in a ring passing over southern Alaska and central Europe (*Science*, 9 April 1999, p. 241). These pressure shifts in turn weaken and strengthen the westerly winds there. The fluctuations in the NAM can favor cold outbreaks down through Canada into the lower 48 states, for example.

The PNA is a pattern of alternating centers of high and low pressure arcing across the North Pacific and North America; in part, it is set up by the Tibetan Plateau and Rocky Mountains jutting into the atmosphere's westerly flow. Its oscillations can shift warmth into Alaska and cool, wet weather into the southeastern United States. These two patterns subsume many of the previously proposed leading modes of the Northern Hemisphere, say Quadrelli and Wallace, including the North Pacific Index, the cold ocean–warm land pattern, the Aleutian-Icelandic seesaw, and the North Atlantic Oscillation.

Between them, the two modes account for about half the variability of sea level pressure from year to year and on longer time scales, Quadrelli and Wallace find. Half is a lot for meteorologists, who eagerly pursue anything accounting for 10% or more of atmospheric behavior. But the two modes by themselves explain "virtually all" of the broad trends over the 42-year period, they say. There's no need for any others over the long haul.

In another upcoming paper in the *Journal of Climate*, meteorologists Monika Rauthe of the Institute for Atmospheric Physics in Kühlungsborn, Germany, and Heiko Paeth of the University of Bonn, Germany, report that these two major modes of pressure variation in turn account for much of regional variability of winter temperature. Shifting pressure patterns produce wind shifts that pick up heat from the oceans and carry it to new regions. Rauthe and Paeth find that their rendition of the NAM and PNA account for 30% to 75% of temperature variations from year to year within swaths of the Northern Hemisphere that are each several thousand kilometers across. The regions include northwestern North America, northern Europe, and north-central Siberia. Precipitation can vary just as much, but over fewer and smaller regions.

South of northern mid-latitudes, Trenberth, David Stepaniak, and Lesley Smith of NCAR find only two more modes, they will report in *Journal of Climate*. In their analysis of global, year-round variations of atmospheric mass—a more fundamental measure than pressure—there is no true Southern Hemisphere equivalent of the PNA. The Southern Hemisphere has nothing quite like the towering Tibetan Plateau and Rocky Mountains to create such a pattern. And the Southern Annular Mode presents a far more continual and symmetrical ring than its northern sibling, thanks to a dearth of those disruptive influences that distort the NAM.

And then there is the tropical Pacific's El Niño. Meteorologists call it the El Niño–Southern Oscillation (ENSO) to include the interaction of atmosphere and ocean that produces cyclic ocean warming (El Niño) and cooling (La Niña) as well as the atmospheric circulation changes that accompany them. Trenberth and his colleagues find that ENSO dominates year-to-year variability in the tropics and mid-latitudes around the globe. It even seems to take such a strong hand in North Pacific variability that—at least on year-to-year and longer time scales—it dominates Quadrelli and Wallace's PNA-like pattern. Over years, decades, and presumably centuries, that would make ENSO and the two annular modes the rulers of the climate change roost. "A very large fraction of large-scale atmospheric variation can be explained by a few basic patterns," says meteorologist Timothy Palmer of the European Center for Medium-Range Weather Forecasts in Reading, U.K.

Climate researchers would now like to use these basic patterns to help predict how regional climate will change under the intensifying greenhouse. In their paper, Rauthe and Paeth report that hot spots of particularly intense warming seen in climate model simulations of greenhouse warming are due in large part to the circulation changes of modes. If the greenhouse caused modes to shift their behavior—spending more time at one extreme of a pressure seesaw than the other—that wouldn't by itself amplify global warming. However, the resulting circulation changes might redistribute heat, intensifying warming in some places and moderating it elsewhere, or it could shift storm tracks and redistribute precipitation.

Rauthe and Paeth find that in an ensemble of seven models, changes in the intensity of modes under rising greenhouse gases account for almost 60% of temperature changes over Northern Hemisphere land. Northwestern North America and northern Siberia would experience the most added warming, whereas northern Africa, the southeastern United States, and far northeastern Canada/western Greenland would warm less than the global average. Smaller regions would see precipitation changes, notably enhanced dyring across southern Europe. Given the apparent utility of modes, "there will be more pressure on modelers to look at things from this standpoint," says Trenberth. "This is the wave of the future."

–Richard A. Kerr

NIMH Takes a New Tack, Upsetting Behavioral Researchers

Basic behavioral scientists are feeling the squeeze as Thomas Insel makes a top priority of "translational" research

When Thomas Insel took over as head of the National Institute of Mental Health (NIMH) in November 2002, he was seen as a reassuring choice to succeed psychiatrist Steven Hyman, who beefed up basic science and promoted large-scale clinical trials. A former NIMH researcher, Insel had sterling credentials, with groundbreaking work on the neurobiology of attachment in voles. But reassuring demeanor aside, he's now rocking the NIMH boat in a way that has some basic researchers sending out SOS signals.


Narrowed focus. Insel says others should pick up research NIMH no longer funds.

Early this month Insel put into effect a reorganization, in the works for the past 6 months, intended to move the institute closer to the front lines in battling mental illness through "translational" research—in other words, bringing the fruits of new knowledge to people with disorders such as depression and schizophrenia. Practically, it means that the agency is lowering the priority of basic cognitive or behavioral research unless it has a strong disease component.

The original Basic Behavioral and Social Science Branch has been broken up: Research that can be tied with brain science is in a new Behavioral Science and Integrative Neuroscience branch. And some nonbiological research—including studies in cognitive science and social psychology—has been parceled out to NIMH divisions with clinical portfolios. But the welcome mat is no longer out for grant applications in some areas of personality, social psychology, animal behavior, theoretical modeling, language, and perception. When Mark Seidenberg of the University of Wisconsin, Madison, applied for funds to continue his research on models of language learning, he says, "I was told the agency no longer supported basic research on language."

NIMH has traditionally been the federal agency that supports such research. Alan Kraut of the American Psychological Society (APS) guesses that perhaps $400 million of the institute's $1.4 billion budget is devoted to it. But with budget growth slowing, Insel says he wants to tighten the focus on NIMH's mission. "We're one of the disease-specific institutes," he asserts, arguing that other institutes should pick up some areas of research NIMH is downgrading.

The move is welcomed by advocates for mentally ill people. The National Alliance for the Mentally Ill (NAMI), which has long pressed for NIMH to keep its eye on major mental illness, is delighted. "It's a start in the right direction," says former NIMH psychiatrist E. Fuller Torrey, who runs NAMI's research arm, the Stanley Foundation. "They're shifting away from studying how pigeons think." It's "a real quantum leap," says James McNulty, former NAMI head and a member of the NIMH advisory council, applauding the agency's transition to "an applied research institute."

But among researchers, "there's a lot of angst and anxiety," says Steven Breckler, executive director for science at the American Psychological Association. Cognitive psychologist Richard Shiffrin of the University of Indiana, Bloomington, argues that translational research is all very well, but there is still not much to translate, and "gains produced by a few extra dollars for translational research will be far outweighed by the harm it will do to basic research."

One researcher whose grant NIMH failed to renew this year is Mahzarin Banaji, a Harvard University social psychologist who examines unconscious mental processes in stereotyping and discrimination. She decries the timing—when "clinical psychologists are uncovering new mental-health uses" of a scale she and her colleagues developed. The scale can aid in studying phobias or probing attitudes of people with depression, she says. Terminating support for this work, says a National Institutes of Health (NIH) official who asked not to be quoted, "means unfortunately, for a topic of grave social importance, no one in the federal government will fund it."

Some animal studies are also being deemphasized. Robert Seyfarth, a well-known psychologist at the University of Pennsylvania in Philadelphia, says his grant almost wasn't renewed, and when it was, funding was drastically cut, just as his team was moving beyond basic research on social behavior in nonhuman primates to research linking social behavior and stress.

"Some people think I'm out to kill basic behavioral science," concedes Insel, who says that view is all wrong. Instead, he says he wants basic behavioral scientists to be more aware of the problems NIMH needs to solve. For example, he says, cognitive deficits are a major part of schizophrenia, so "if someone's on the track of an important piece of cognitive science using healthy undergraduate [subjects], we might work with them to begin to study people with schizophrenia."

Insel wants to redirect some behavioral research to institutes dealing with relevant issues such as child development, aging, and communication. Others agree with him that NIMH has been carrying more than its share of the burden. The larger issue, they say, is which federal agency should be taking it on. The National Science Foundation doesn't spend much on that type of research, says Kraut of APS. And although some NIH institutes have big behavioral components—for example, on how to get people to stop smoking—Kraut says, "I can't tell you how hard it has been to convey the importance of basic behavioral science in any sophisticated sense." Kraut and several members of Congress are pushing for the National Institute of General Medical Sciences to take up the slack.

Basic behavioral research will not be abandoned, Insel hopes. Last March, NIH director Elias Zerhouni set up a working group, chaired by sociologist Linda Waite of the University of Chicago, which is pondering the role of social and behavioral science at NIH. And Insel himself heads another group, under the White House Office of Science and Technology Policy, that is looking at investments in social, behavioral, and economic research throughout the federal government. The NIH body is scheduled to make recommendations in December; Insel's group will weigh in later.

–CONSTANCE HOLDEN

CREDIT: COURTESY OF NIMH

Published by AAAS

Hawaii Girds Itself for Arrival of West Nile Virus

Health officials and wildlife biologists hope vigilant surveillance and rapid response will prevent infected mosquitoes from establishing a beachhead

No barriers. Mosquitoes hitching a ride inside airplanes could bring West Nile virus to Hawaii, threatening honeycreepers and other native birds.

CREDITS (TOP TO BOTTOM): ROBERT Y. ONO/CORBIS; D. LAPOINTE/USGS

On 24 September, officials at the Hawaii Department of Health (DOH) got the news that they'd been dreading for several years: An island bird had tested positive for West Nile virus. Although infected birds are now routine across the continental United States, Hawaii has so far been spared. And it is fighting to stay that way. Immediately after the discovery, the health department launched an assault; all night long a truck fogged the Kahului Airport on Maui, where the bird had been caught, with insecticide. Additional crews with backpack sprayers doused off-road sites to kill any potentially infected mosquitoes.

State officials breathed a sigh of relief the following week when the case turned out to be a false positive. But they aren't letting down their guard. Should West Nile become established on the islands, virus-ridden mosquitoes could spread the disease year round. And many of the state's remaining endemic birds, already hammered by avian malaria and pox, might go extinct. "The effects could be disastrous," says ornithologist Peter Marra of the Smithsonian Environmental Research Center in Edgewater, Maryland.

To avert such a catastrophe, researchers have been scrambling to improve surveillance and eradication plans. Observers on other Pacific islands, which also face a similar threat, are hoping to learn from Hawaii's efforts to stamp out the virus as soon as it enters. "We're not just throwing our hands up in the air," says epidemiologist Shokufeh Ramirez, who coordinates West Nile prevention efforts for the Hawaii DOH.

On the mainland, West Nile virus has proved unstoppable. After first appearing on the East Coast, in New York in 1999, West Nile virus marched steadily across the country. The virus is transmitted by mosquitoes, which pass it on to birds and humans. Although infection is rarely deadly to people, it kills some bird species such as crows with a vengeance; other infected birds remain healthy enough to fly and spread the virus. Last year, it reached California.

But Hawaii has a chance, if not to keep West Nile virus out, at least to stop it upon arrival. That's because researchers know how it's likely to get there. Rather than infected humans or migratory birds, the most probable culprits are mosquitoes in the cargo holds of planes, concluded A. Marm Kilpatrick of the Consortium for Conservation Medicine at Wildlife Trust in Palisades, New York, and others in a paper published in *EcoHealth* in May. Based on previous research, they estimated that seven to 70 infected mosquitoes probably reach Hawaii each year. Far less is known about the risks of introduction via shipping containers, some 1200 of which arrive in Hawaiian harbors each day. The number of overseas flights—about 80 a day—also makes prevention difficult. Moreover, airlines have balked at treating their cargo holds with insecticides that kill mosquitoes on contact. The state has made progress on another front: preventing infected poultry and pet birds from entering by mail. In 2002, the U.S. Postal Service prohibited the mailing of most live birds to Hawaii. Quarantine regulations have also been strengthened.

The health department has focused primarily on monitoring 11 airports and harbors. In 2002, they began checking dead birds by polymerase chain reaction (PCR) for West Nile virus. Last year, they added mosquito traps that are sampled each week and also examined by PCR for the virus.

At the same time, researchers are trying to figure out just what might happen if West Nile virus manages to evade detection. "Bird biodiversity will probably be severely impacted," says Jeff Burgett of the U.S. Fish and Wildlife Service in Honolulu, who heads an interagency task force. One reason is that Hawaii's endemic birds have not had a chance to build resistance to West Nile through exposure to related viruses, such as St. Louis encephalitis, that are not present on the islands. Those species that survive only in captive breeding programs, such as the Hawaiian crow, might never be able to return to the wild.

As a first step to gauge the consequences, biologists with the U.S. Geological Survey (USGS) have sent 20 native Hawaiian honeycreepers (*Hemignathus virens*) to the survey's National Wildlife Health Center in Madison, Wisconsin. There, veterinarian Erik Hofmeister has injected some of the birds with West Nile virus and is following their health and ability to serve as reservoirs for the virus. He also plans to investigate how efficiently the primary vector in Hawaii, the mosquito *Culex quinquefasciatus*, can infect these birds.

A similar experiment should help solve a problem that hampers the effort to spot the virus in dead birds. Hawaii doesn't have the North American birds—crows, magpies, jays—that provide the most obvious warning of the virus. So Hofmeister plans in December to examine which introduced birds in Hawaii, such as minahs, might be most susceptible to the virus. This will assist efforts to model potential spread of the virus. "It will also tell you which species might be amplifying the virus, and which species you may want to control," says ecologist Dennis LaPointe of USGS.

While the health department waits for these results, it is trying to speed its lab testing and streamline the response plan. Meanwhile, DOH and wildlife biologists have their fingers crossed that Hawaii's defenses will be adequate to stave off the virus—forever. "Every year it's going to be knocking on Hawaii's door," says Peter Daszak of the Consortium for Conservation Medicine at Wildlife Trust.

–Erik Stokstad

Letters to the Editor

Letters (~300 words) discuss material published in *Science* in the previous 6 months or issues of general interest. They can be submitted through the Web (www.submit2science.org) or by regular mail (1200 New York Ave., NW, Washington, DC 20005, USA). Letters are not acknowledged upon receipt, nor are authors generally consulted before publication. Whether published in full or in part, letters are subject to editing for clarity and space.

Another Question for Bush and Kerry

THE ARTICLE "BUSH AND KERRY OFFER THEIR views on science" (1 Oct., p. 46) raises an important question. Is it known for certain that Bush and Kerry actually took the time to read the campaign responses before they were returned to *Science*, or were the responses stock answers handled by staff? If it is not known, then in future campaigns, it might be wise to include a final question: "Mr. Candidate, did you personally read and approve of the responses to our questions?" The answer, or lack thereof, might say more about the priority of science to the candidate than any other question you ask.

SOL MICHAEL GRUNER
Cornell University, 518 Clark Hall, Ithaca, NY 14850, USA.

Struggling to Attend U.S. Meetings

THE FREE EXCHANGE OF KNOWLEDGE AND ideas is a defining feature of science and the driving force of its progress. In their Editorial "International science meetings" (10 Sept., p. 1531), J. Lubchenco and G. Mehta address some recent challenges to the freedom of scientific communication. Perhaps one of the most formidable for those wishing to share information at conferences in the United States is the "visa wall." Faced by relentless new security regulations, scientists wishing to visit the United States to meet with colleagues have become victims of the "war on terror." As repeatedly highlighted in recent years (*1*–*3*), this problem has reached a level where researchers from certain regions of the globe are effectively blocked from attending U.S. meetings, and even keynote speakers are unable to get past the immigration bureaucracy, despite the lack of a reasonable explanation of why several-days-long visits by established scientists pose such a threat to the security of the United States. Pledges (*2*, *4*) by renowned academics and international bodies to ease the visa restrictions for scientists have elicited various promises (*5*, *6*), but have yet to translate into tangible improvements. Because of these circumstances, major international societies have expressed reservations about sponsoring conferences in the United States, and certain meetings there have been postponed or simply cancelled (*1*, *7*). As things stand, the willingness of scientists or scientific organizations to overcome political prejudices will be of little relevance as long as the leading scientific nation ignores the principles of scientific universality.

> **"[R]esearchers from certain regions of the globe are effectively blocked from attending U.S. meetings..."**
>
> –GARVALOV

BOYAN K. GARVALOV
Max Planck Institute of Neurobiology, Am Klopferspitz 18, 82152 Martinsried, Germany

References
1. J. Schultz, *J. Natl. Cancer Inst.* **95**, 579 (2003).
2. G. Brumfiel *et al.*, *Nature* **427**, 190 (2004).
3. I. Verma, *Mol. Ther.* **9**, 767 (2004).
4. Y. Bhattacharjee, *Science* **304**, 943 (2004).
5. Y. Bhattacharjee, *Science* **305**, 1222 (2004).
6. *Nature* **431**, 238 (2004).
7. J. Lubchenco, letter from the ICSU President to Dr. George H. Atkinson, Science and Technology Advisor to the U.S. Department of State, 10 June 2004 (available at www.icsu.org/5_abouticsu/Visa_Restrictions.pdf).

Is Bedout an Impact Crater? Take 1

L. BECKER *ET AL.*'S RECENT PROPOSAL THAT the Bedout structure off northwestern Australia is a giant bolide impact crater of Permian-Triassic (P-Tr) boundary age ("Bedout: a possible end-Permian impact crater offshore of northwestern Australia," Research Article, 4 June, p. 1469; published online 13 May; 10.1126/science.1093925) provides many readily testable hypotheses, not least of which is that there should be some evidence of the impact in the sedimentary record of the surrounding area. The Bedout structure is located in the Roebuck Basin, which is part of a 2000-km extent of Late Palaeozoic-Mesozoic rift basins developed from Perth to Darwin. Marine conditions during the latest Permian and Early Triassic are recorded by the Kockatea Shale in the Perth Basin and equivalents in other basins.

We have examined core material from the Kockatea Shale in the Hovea-3 borehole, located around 1000 km south of the Bedout structure (*1*, *2*). This reveals a P-Tr transition in which bioturbated mudstones with a diverse latest Permian fauna, dominated by brachiopods, are replaced by laminated, anoxic shales with earliest Triassic bivalves. At no level in the core, which spans a Wuchiapingian-to-Dienerian interval, is there evidence for a layer of impact ejecta or a tsunamite. A trace metal assay also failed to find evidence for iridium enrichment. Core material is not available from sites nearer to Bedout, but mudlog data and wireline logs from boreholes as close as 400 to 500 km from Bedout also indicate a shale-on-shale transition across the P-Tr boundary. It is significant that the Hovea-3 core is substantially closer to the proposed impact site than the celebrated K-T impact sites in northeastern Mexico are to the Chicxulub Crater. For example, the famous Mimbral site, with its spherule layers and thick tsunamite record, is over 1500 km distant from Chicxulub.

We suggest that either the impact did not occur in the late Permian to Early Triassic interval (and therefore it has no relevance to the P-Tr mass extinction event), or it is not an impact crater and is more likely to be a volcanic structure.

PAUL WIGNALL,[1] BRUCE THOMAS,[2] ROBBERT WILLINK,[2] JOHN WATLING[3]
[1]School of Earth Sciences, University of Leeds, Leeds LS2 9JT, UK. [2]Origin Energy Limited, 34 Colin Street, West Perth 6005, Western Australia. [3]Department of Applied Chemistry, Curtin University, Bentley 6102, Western Australia.
*To whom correspondence should be addressed. E-mail: wignall@earth.leeds.ac.uk

References
1. B. M. Thomas *et al.*, *Austr. J. Earth Sci.*, in press.
2. B. M. Thomas, C. J. Barber, *APPEA J.* **44**, 59 (2004).

Response

WE AGREE WITH WIGNALL *ET AL.* THAT THE study of cores from Permian-Triassic (P-Tr) sections in western Australia potentially provides a valuable test of the hypothesis that Bedout is a large P-Tr boundary crater. What is at issue is whether any of the existing cores or well logs, including Hovea-3, contain a complete record across the boundary. In many of the onshore basins that are proximal to Bedout, much of the Permian and Early Triassic section is missing (up to 2 km in some basins). Wignall *et al.* also state that Hovea-3 is closer to Bedout than some K-T impact sites (e.g., northeastern Mexico) are to the Chicxulub crater, and, thus, Hovea-3 should have some preservation of an impact ejecta layer. The distance between Hovea-3

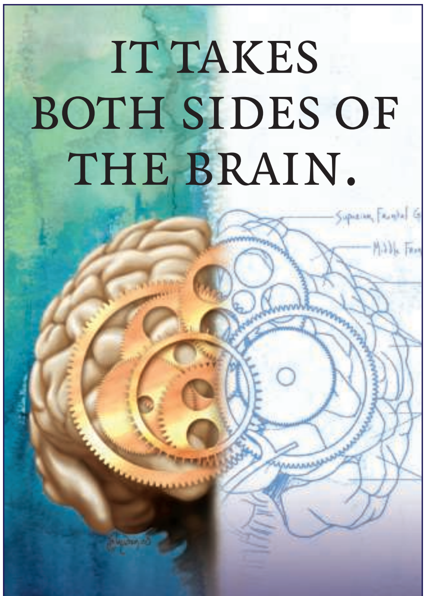

and Bedout (1000 km) is about the same (not closer) as that between Chicxulub and the northeastern Mexico sections such as El Mimbral. These Mexican sections, and even closer (to Chicxulub) ones in Haiti, contain less than 1 m of ejecta; thus, even minor erosion at the boundary could erase the record.

Wignall *et al.* rely on biostratrigraphy to determine the P-Tr boundary in Hovea-3. As shown elsewhere for the P-Tr, biostratigraphy alone is not a reliable indicator of the completeness of the boundary layer (*1*, *2*). However, if it can be further demonstrated (e.g., by isotope dating) that Hovea-3 does indeed represent a record of continuous sedimentation across the P-Tr boundary, and it contains no ejecta, then this would argue against Bedout being a large P-Tr boundary crater.

Finally, the absence of iridium in Hovea-3 is consistent with other P-Tr sections worldwide. This may reflect, again, upon the completeness of the P-Tr boundary, the type of section (marine versus continental), or the actual impacting body (e.g., asteroid versus comet). Several impact tracers (see our Research Article) occur in P-Tr boundary sections worldwide, none of which contains elevated iridium. Thus, we await full documentation and future investigations of impact tracers in Hovea-3 and other onshore cores that may include the P-Tr boundary.

L. BECKER,[1] R. J. POREDA,[2] K. O. POPE[3]

[1]Institute for Crustal Studies, Department of Geological Sciences, University of California, Santa Barbara 93106, USA. [2]Department of Earth and Environmental Sciences, University of Rochester, Rochester, NY, USA. [3]Geo Eco Arc Research, Aquasco, MD 20608, USA.

References

1. S. A. Bowring *et al.*, *Science* **280**, 1039 (1998).
2. Y. G. Jin *et al.*, *Science* **289**, 432 (2000).

Is Bedout an Impact Crater? Take 2

IN THEIR RESEARCH ARTICLE "BEDOUT: A possible end-Permian impact crater offshore of northwestern Australia," L. Becker *et al.* report having identified a buried impact structure, which they link to the Permian-Triassic mass extinction (4 June, p. 1469; published online 13 May; 10.1126/science.1093925). Becker *et al.* have scarcely extended the suggestion made by Australian petroleum workers (in industry trade journals) (*1*). Our scrutiny of the alleged evidence indicates that there is no substantiation that this alleged structure is an impact crater. The gravity map (fig. 11) actually highlights the differences between Bedout and confirmed impact structures. There is actually no crater defined by the geophysical data, only a noncircular high in the seismic data, claimed to be a "central uplift." In comparison, the central uplift feature of a large impact structure, such as the 250- to 300-km-diameter Vredefort Structure, would reveal a significant central positive gravity anomaly due to the uplift of relatively denser mid- to lower crustal material. The highly altered rocks described by Becker *et al.* as impact products strongly resemble volcanic breccias and lack impact diagnostic textures. No true shock features are described from any of the samples. No mineralogical or geochemical evidence is provided that the purported "diaplectic glass" or "maskelynite" are indeed glasses, and mineral chemical information is missing. The "shock features" claimed to be presented in quartz grains from "ejecta horizons" (which remain of uncertain stratigraphic relation either to the alleged Bedout feature or to the end-Permian extinction) do not show any of the characteristics of unambiguous shocked minerals.

The 250 Ma "age" interpreted from argon isotope data by Becker *et al.*, which presents the entire basis for the sensationalistic claim of a relationship between Bedout and the P/Tr boundary, has no objective basis. Their data present no consistent indication of the presence of a 250-million-year component in the sample analyzed. Results from only one sample, a concentrate of unknown lithologic and stratigraphic relation to the Bedout geophysical feature, were reported. The data do not define a plateau, and only two of twelve steps purportedly defining a plateau actually encompass the ad hoc "plateau age" within analytical errors. Even allowing an exceptionally generous definition of a plateau, the reported "plateau age" does not follow from the isotope data using any combinatoric method of which we are aware. Yet this putative 250 Ma "age" (with its alleged uncertainty of 4.5 million years deduced by unstated and indeed cryptic means) will inevitably be cited in the literature by uninformed nonspecialists as evidence for a causal relationship to the extinction. Consequently, the report of a Bedout impact structure of P-Tr boundary age must be considered with utmost caution.

See related Technical Comment Abstracts on page 613

PAUL R. RENNE,[1] H. JAY MELOSH,[2]
KENNETH A. FARLEY,[3] W. UWE REIMOLD,[4]
CHRISTIAN KOEBERL,[5] MICHAEL R. RAMPINO,[6]
SIMON P. KELLY,[7] BORIS A. IVANOV[8]

[1]Berkeley Geochronology Center, 2455 Ridge Road, Berkeley, CA 94709, USA, and Department of Earth and Planetary Science, University of California, Berkeley, CA 94720, USA. [2]Lunar and Planetary Laboratory, University of Arizona, 935 Gould/Simpson Building, Tucson, AZ 85721–0092, USA. [3]Division of Geological and Planetary Sciences, California Institute of Technology, MS 170-25, Pasadena, CA 91125, USA. [4]Impact Cratering Research Group, School of Geosciences, University of the Witwatersrand, Johannesburg, Private Bag 3, P.O. Wits 205, South Africa. [5]Institute of Geochemistry, University of Vienna, Althanstrasse 14, Vienna A-1090, Austria. [6]Earth and Environmental Science Program, New York University, 100 Washington Square East, New York, NY 10003, USA. [7]Department of Earth Sciences, The Open University, Milton Keynes MK7 6AA, UK. [8]Institute for Dynamics of Geospheres, Russian Academy of Science, 38-6 Leninsky Prospect, Moscow 11797, Russia.

Reference

1. J. Gorter, *Pet. Explor. Soc. Aust. News* **1996**, 33 (1996).

Response

ALTHOUGH WE FEEL THAT THERE ARE ISSUES that could use clarification in our recent Research Article, we found the general tone of the Renne *et al*. Letter to be out of balance with the specific objections. Renne *et al.* take exception to each line of evidence we presented, but they offer no plausible alternative explanation for these data. We considered a number of possible explanations for the nature of the Bedout structure, including a volcanic origin. However, we could find no other examples of an isolated volcano the size of Bedout (40 to 60 km in diameter and 3 to 4 km in height) forming along a passive continental margin. We also could find no known terrestrial volcanic sample(s) that exhibit the unusual melt chemistry and shock features (maskelynite) observed in the Bedout core. When Renne *et al.* claim that we describe no true shock features, nor present mineralogical or geochemical evidence for glass, they ignore the petrographic and chemical evidence we provided (see tables S-1 and S-2 and figs. S-4 to S-8 in the Supporting Online Material in our paper). Moreover, the shocked quartz and other impact debris (fullerenes, meteoritic fragments, Fe-Ni metal grains, and chromium isotopes) from Graphite Peak (Antarctica), Frasier Park (Australia), and Meishan (China) are all clearly associated with end-Permian sediments (e.g., marked by stratigraphy, biostratigraphy, carbon isotopes, ^{40}Ar/^{39}Ar, and U-Pb dating), regardless of Renne *et al.*'s unsubstantiated and undocumented claims to the contrary (see our paper and references therein). We note with irony the objection of Renne *et al.* to our use of industry publications that suggested an impact origin for the Bedout structure, given that industry data identifying the Chicxulub crater were essentially ignored by academia for over a decade.

The comments by Renne *et al.* pertaining to crater morphology imply that all large impact craters should have a clear, quasicircular, central gravity high, but we note that the ~200-km Sudbury crater in Canada does not. The gravity expression of the central uplift at Vredefort is especially clear because that crater is exposed by erosion and not tectonically deformed. The Bedout structure is deeply buried and deformed, and although the existing geophysical data are of low resolution, they do show a central uplifted core of denser rock surrounded by an annular depression, similar to the gravity and seismic signature of Chicxulub. Better geophysical data are needed, however, to clearly define the geometry of the entire Bedout structure.

Renne *et al.* make the remarkable statement that our $^{40}\text{Ar}/^{39}\text{Ar}$ age has "no objective basis." The integrated age of steps 5 to 13 of the Lagrange (LG-1) plagioclase is 250.6 ± 4.3 Ma (1σ; steps 1 to 4 reflect Ar loss, step 14 contains no radiogenic signal, and step 15 reflects degassing of the crucible slag). This is in agreement with the previous independently determined K-Ar date of 253 ± 5 Ma [(*20*, *30*) in our paper] and is consistent with the stratigraphic position of the Bedout breccia at the top of the Permian. Clearly, there is inhomogeneity in the $^{40}\text{Ar}/^{39}\text{Ar}$ release from LG-1, but this has been observed previously in samples inferred to be closed systems (*1*). Although there is no universally accepted definition of a plateau [(*1*), p. 111], we would have been better served not to have used the term "plateau," which is a much-abused concept. For example, the plateau method has been applied on occasion to slowly cooled minerals that manifestly contain heterogeneous $^{40}\text{Ar}/^{39}\text{Ar}$ ages [e.g., (*2*, *3*)], a view for which there is truly no objective basis. Improved dating for Bedout awaits future drilling of the structure or an onshore coring project in adjacent basins where late Permian volcanics and basement may be preserved.

Our goal was to draw attention to the various lines of evidence—none of which individually are definitive—that support an impact origin for Bedout. We stand by our conclusion that the data we present are consistent with an impact origin for Bedout and that the current best estimate of the age of the structure is within error of the age of the P-Tr boundary.

L. BECKER,[1]* R. J. POREDA,[2] A. R. BASU,[2] K. O. POPE,[3] T. M. HARRISON,[4] C. NICHOLSON,[1] R. IASKY[5]

[1]Institute for Crustal Studies, Department of Geological Sciences, University of California, Santa Barbara, CA 93106, USA. [2]Department of Earth and Environmental Sciences, University of Rochester, Rochester, NY 14627, USA. [3]Geo Eco Arc Research, Aquasco, MD 20608, USA. [4]Australian National University, Canberra, Australia. [5]Geological Survey Western Australia, Perth, Australia.

*To whom correspondence should be addressed. E-mail: lbecker@crustal.ucsb.edu

References

1. I. McDougall, T. M. Harrison, *Geochronology and Thermochronology by the ^{40}Ar/^{39}Ar Method* (Oxford Univ. Press, New York, ed. 2, 1999).
2. P. R. Renne, O. T. Tobisch, J. B. Saleeby, *Geology* **21**, 331 (1993).
3. W. D. Sharp, O. T. Tobisch, P. R. Renne, *GSA Bull.* **112**, 1059 (2000).

The Next Step for Kennewick Man

THE PENULTIMATE PARAGRAPH OF C. HOLDEN'S news report (News of the Week, 30 July, p. 591) on the Kennewick Man case, "Court battle ends, bones still off-limits," includes a statement by Alan Schneider, head of the legal team representing the Bonnichsen plaintiffs in the case, attributing to me a notion that is incorrect. Schneider questions concerns that I have expressed about further study of the Kennewick remains. He seems to infer that I might object to any future study because the government already has conducted similar studies of the remains.

However, my concern, expressed to

Holden and reported in her article, about future investigations of the Kennewick Man skeleton is not whether additional studies may be undertaken. That new studies will be allowed has been determined by the outcome of a 2-year legal struggle in federal courts. However, it is essential that any additional studies build on the substantial amount of scientific investigation already conducted by the Department of the Interior and the Corps of Engineers as part of their efforts to resolve the Kennewick Man case (*1*). Like any good scientific investigation, new studies should use the results of past studies, drawing fully upon what already has been learned.

Throughout the legal contest just concluded, the plaintiffs' legal team, led by Schneider, routinely disparaged the scientific investigations undertaken by the government. Now that the case has been resolved, such legal maneuvering and tactics should be set aside. The government agencies responsible for the Kennewick Man skeletal remains conducted a number of standard and detailed scientific investigations. Over 20 scientists from nationally recognized academic, laboratory, and museum departments were involved. The research design for further study of the Kennewick remains needs to take account of the methods, techniques, and conclusions of the earlier government studies.

FRANCIS P. MCMANAMON*

Archeology and Ethnography Program, National Park Service, 1849 C Street NW, Washington, DC 20240, USA.

*Chief Archeologist for the National Park Service and Departmental Consulting Archeologist for the Department of the Interior

Reference

1. The government studies are available at www.cr.nps.gov/aad/kennewick.

TECHNICAL COMMENT ABSTRACTS

COMMENT ON "Bedout: A Possible End-Permian Impact Crater Offshore of Northwestern Australia"

Andrew Glikson

A petrological–geochemical study of breccia cored at a depth of about 3040 meters over the Bedout basement high identifies a hydromagmatic hyaloclastic volcanic breccia consisting of fragments of basalt and dolerite retaining igneous textures, mineralogy, and chemistry, and set in a mafic mesostasis. Alteration by cryptocrystalline albite and microcrystalline albite-chlorite assemblages is widespread. No evidence is observed for impact-induced shock metamorphism in these rocks, as suggested by Becker *et al.* (Research Articles, 4 June 2004, p. 1469).

Full text at www.sciencemag.org/cgi/content/full/306/5696/613b

RESPONSE TO COMMENT ON "Bedout: A Possible End-Permian Impact Crater Offshore of Northwestern Australia"

L. Becker, R. J. Poreda, A. R. Basu, K. O. Pope, T. M. Harrison, C. Nicholson, R. Iasky

Many of the observations of texture, mineral chemistry, and high-silica glass composition, as well as the presence of maskelynite, in the lowermost section of the Bedout core are incompatible with an ordinary magmatic origin. These observations are consistent, however, with an impact-induced origin for the Bedout structure.

Full text at www.sciencemag.org/cgi/content/full/306/5696/613c

CORRECTIONS AND CLARIFICATIONS

Special Section on Testing Human Limits: News: "A race to the starting line" by G. Vogel (30 July, p. 632). The article stated incorrectly that "[p]eople living at high altitudes produce more EPO naturally to compensate for the lower oxygen concentration in the air." The concentration of oxygen in air does not change at high altitudes, but the partial pressure drops.

TECHNICAL COMMENT

Comment on "Bedout: A Possible End-Permian Impact Crater Offshore of Northwestern Australia"

Nearly a decade ago, Gorter (*1*) suggested that the Bedout basement high, offshore Western Australia, might represent an impact structure, in view of the site's well-defined circular Bouguer anomaly and seismic reflection data indicating a possible ring syncline. Recently, Becker *et al*. (*2*), as part of the search for the cause or causes of the mass extinction that marks the Permian-Triassic (P-T) boundary (*3*), examined the P-T boundary breccia cored at a depth of 3044 m in the Bedout-1 well and with an age (using plagioclase $^{40}\text{Ar}/^{39}\text{Ar}$ dating) of 250.7 ± 4.3 million years (My)—within experimental error from the age of the P-T extinction event (251.4 ± 0.4 My) and Siberian Norlisk volcanism [251.7 ± 0.4 to 251.1 ± 0.3 Ma (*4*)]. Becker *et al*. (*2*) suggested the presence in the Bedout breccia of shocked mineral grains, diaplectic plagioclase glass (maskelynite), and impact melt glass. Drawing an analogy between the Bedout breccia and the suevite melt breccia at Chicxulub and Sudbury, they attributed the origin of the breccia to the melting of Mg-rich sedimentary materials, although they noted the presence of some basalt in the target material (*2*).

The diagnostic hallmarks of extraterrestrial impacts (*5*, *6*) include (i) shocked minerals displaying planar deformation features (PDFs)—for example, in quartz, feldspar, and zircon; (ii) the presence of high-pressure mineral polymorphs such as coesite, stishovite, and diamond; (iii) megascopic shock structures (for example, shatter cones and melt breccia); and (iv) chondritic chemical signatures—in particular, platinum group elements and other siderophile elements (Ni, Co) (*7*). A study by the author of this comment (*8*) suggested that the volcanic breccia samples in the interval from 3035.8 to 3044.95 m in the Bedout-1 core meet none of these criteria. The rocks consist of metaglass-bearing hydromagmatic mafic volcanic breccia dominated by fragments of basalt and dolerite set in mafic pyroclastic matrix (Fig. 1), including vesicular volcanic lapilli, closely akin to hydromagmatic spilites described in detail by Amstutz (*9*).

The figures presented by Becker *et al*. (*2*) provided no suggestion of intracrystalline PDF elements, nor are measurements of crystal orientations reported. Instead, the principal argument presented by Becker *et al*. for impact effects hinges on the suggested existence of diaplectic feldspar glass (maskelynite) around and within plagioclase [figures 6 and 8 in (*2*)]. No criteria allowing discrimination between maskelynite and volcanic glasses are indicated. Because the plagioclase-to-maskelynite transformation occurs at a pressure of 35 to 45 GPa (*5*, *6*)—after the development of PDFs, which occurs at 10 to 35 GPa—identification of maskelynite is closely related to the presence of PDFs, which Becker *et al*. have not documented. Nor do these authors offer any criteria for discrimination between volcanic metaglass and maskelynite. Any presence of pristine unaltered glass, a highly metastable component under hydrous conditions, requires tests by transmission electron microscopy and infrared spectroscopy. The intercrystaline near-isotropic regions shown by Becker *et al*. [figure 6 in (*2*)] compare well with the cryptocrystalline chlorite/albite–dominated alteration zones (*7*) common in hydromagmatic altered spilites (*9*). The intracrystalline near-isotropic regions within calcic plagioclase [figure 8 in (*2*)] correspond to recrystallization and alteration of internal euhedral crystal sectors of oscillatory reverse-zoned magmatic plagioclase, under high water pressures associated with hydromagmatic processes (*9*). By contrast, in impact-related rocks, maskelynite irregularly overprints PDF-bearing crystalline relics [see, for example, figure 4.31 in (*5*)].

The excellent preservation in the Bedout-1 rocks of igneous ophitic and microlitic textures in little-deformed dolerite and basalt fragments, and of calcic plagioclase that retains primary prismatic (euhedral) crystals and albite twinning (Fig. 1), is hardly consistent with the combination of deformation and the hydrothermal effects that commonly accompany impact (*5*). The presence of euhedral chlorite pseudomorphs after ophitically enclosed mafic phases and euhe-

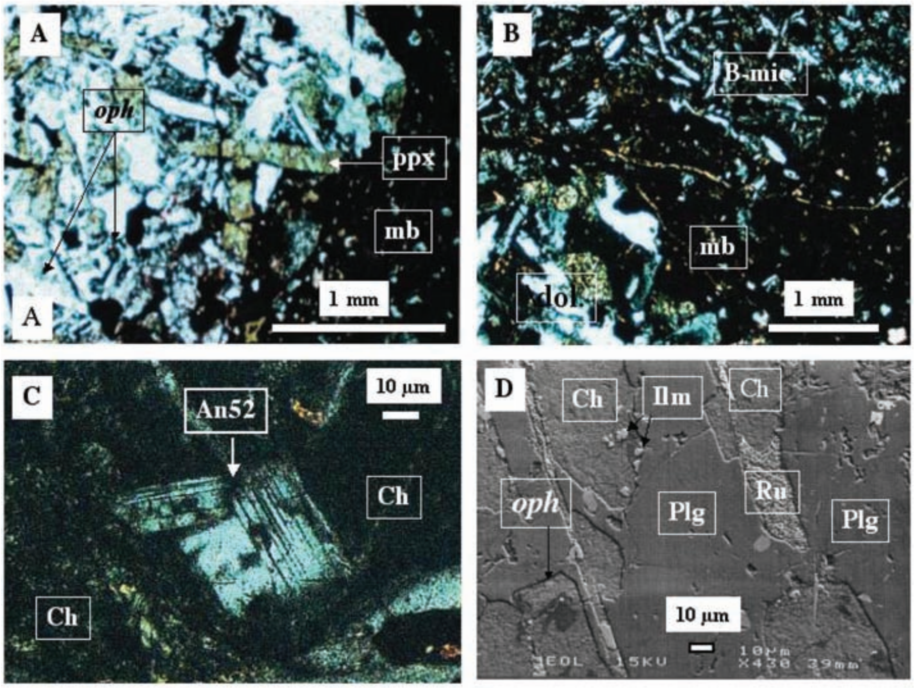

Fig. 1. (**A**) Ophitic-textured dolerite fragment in Bedout-1 breccia, showing lath-like calcic plagioclase and pseudomorphs of chlorite after pyroxene (pyx) protruding into feldspar in an ophitic texture (oph). The fragment is enveloped and injected by microbreccia (mb). Crossed nicols. (**B**) Microlite-rich basalt fragment (B-mic) and dolerite fragment (dol) separated by microbreccia (mb). Crossed nicols. (**C**) Plagioclase (An 52) microphenocryst in chlorite-dominated basalt fragment. Crossed nicols. (**D**) Backscattered scanning electron microscope image of ophitic dolerite fragment with plagioclase enveloping pseudomorphs of chlorite after pyroxene and accessory rutile. White arrows denote relic ophitic crystal structure (oph) of mafic pseudomorph within calcic plagioclase.

dral Ti-magnetite and ilmenite typical of mafic volcanic rocks (*10*) are all consistent with burial metamorphism of mafic volcanic breccia, but distinct from features diagnostic of suevite shock-melt breccia (*5*). The Ries suevite includes shocked PDF-bearing granite clasts and carbonate sediment-derived clasts that display extensive heat-induced plastic deformation of fragments intermeshed with flow-banded melt components [figures 5.9 to 5.15 in (*5*)], clearly distinct from the angular to subrounded breccia at Bedout.

High degrees of impact melting may result in magmatic-type rocks, for example in the Mistasin and Dellen craters [figures 6.12 to 6.21] and in Vredefort granophyre veins (*5*). However, these processes commonly result in coarse-grained quench crystallization, not seen in the Bedout breccia.

In the absence of the unique criteria of shock metamorphism, Becker *et al*. (*2*) invoke novel petrologic and geochemical arguments for an impact connection for the Bedout breccia, including high-silica glass, spherulitic glass, feldspar compositions, presence of Mg-ilmenite, carbonate clasts with fragmented ooids, and coexistence of Ti-rich silica glass with Ti-poor aluminous silica glass. They describe the mineral parageneses of the breccia as "compositions . . . unknown and unlikely to exist in terrestrial volcanic agglomerates, lava flows, and intrusive pipes" (*2*). However, the spherulitic-textured particles [figure 5 and figure 7, A and B, in (*2*)] are identical to vesicular lapilli fragments in spilitic pyroclastics [pp. 24 and 26 in (*9*)]. High-silica cryptocrystalline veins form under hydromagmatic conditions, hydrothermal conditions, or both. Mg-ilmenite is known in ultrabasic and alkaline xenoliths (*11*) and is no criterion for impactites. Likewise, liquid immiscibilities, which are observed in heterogeneous volcanic magmas (*12*), offer no criterion for impact melting.

Becker *et al*. (2004) refer to the breccia in part as product of Mg-rich sediments (e.g., dolomites). However, apart from the pristine igneous textures of the breccia, the transition element levels (chlorite in dolerite fragment—Ni 97 to 160 ppm, Co 75 to 152 ppm, Cu 69 to 204 ppm; interfragmental mesostasis—Ni 29 to 45 ppm, Co 18 to 52 ppm, Cu 26 to 110 ppm) are consistent with Fe-rich basalts but exceed common abundances in carbonates and marls (*13*).

Becker *et al*. (*2*) thus have identified no impact effects at Bedout. The circular gravity structure and the presence of flanking rim synclines around the Bedout High (*1*) justify drilling into the basement that underlies the breccia at Bedout-1 and Legrange-1 to test the origin of this important structure.

Andrew Glikson
Research School of Earth Science
Australian National University
Canberra, A.C.T. 0200, Australia
andrew.glikson@anu.edu.au

References

1. J. Gorter, *PESA News* **October-November 1996**, 32 (1996).
2. L. Becker *et al.*, *Science* **304**, 1469 (2004).
3. P. B. Wignall *et al.*, in *Catastrophic Events and Mass Extinctions: Impact and Beyond*, C. Koeberl, K. C. McLeod, Eds., *Geol. Soc. Am. Spec. Pap.* **356**, 395 (2003).
4. S. A. Bowring *et al.*, *Science* **280**, 1039 (1998).
5. B. M. French, *Traces of Catastrophe: Lunar Planetary Science Contribution* **954** (1998).
6. D. Stoffler, F. Langenhorst, *Meteoritics* **29**, 155 (1994).
7. F. T. Kyte, *Geol. Soc. Am. Spec. Pap.* **356**, 21 (2002).
8. A. Y. Glikson, unpublished data.
9. G. C. Amstutz, *Spilites and Spilitic Rocks* (Springer-Verlag, Berlin, 1974).
10. T. R. McGetchin, R. O. Pepin, R. J. Phillips, *Basaltic Volcanism on the Terrestrial Planets* (Pergamon, New York, 1981).
11. W. A. Deer, R. A. Howie, J. Zussman, *Rock Forming Minerals* (Longman, New York, 1972).
12. J. Ferguson, K. L. Currie, *Nature* **235**, 86 (1972).
13. K. H. Wedepohl, *Handbook of Geochemistry* (Springer-Verlag, 1978).

17 May 2004; accepted 30 August 2004

Response to Comment on "Bedout: A Possible End-Permian Impact Crater Offshore of Northwestern Australia"

Glikson (*1*) suggests that any "true" extraterrestrial impact structure should include shocked minerals (for example, quartz with planar deformation features, or PDFs), high-pressure polymorphs (for example, coesite or diamond), shatter cones, and chondritic chemical signatures of platinum group elements (PGEs). He ignores the criteria we present (shocked glass or maskelynite) and later dismisses the data as being indicative of a volcanic breccia. Moreover, his suggestion that the identification of maskelynite in an impact breccia necessitates the presence of PDFs is incorrect. As stated in (*2*), the shock pressures for the formation of maskelynite (35 to 45 GPa) and silica glass (>45 to 65 GPa) that characterize the Bedout core are well above the shock pressures for preserved PDFs. In addition, some researchers (*3*) now distinguish between "plagioclase diaplectic glass" and "maskelynite," with the latter forming without being initiated in PDFs as suggested by Glikson. Chen and El Goresy (*3*) recently described maskelynite grains in several SNC martian meteorites as smooth with no cleavage, no contraction cracks, and no shock-induced fractures, which is what we see in the Bedout core [see, for example, figure 6 in (*2*)]. Thus, the notion that the presence of preserved PDFs is required to interpret maskelynite in a melt breccia core—especially one that is 250 million years old and highly altered—is overstated. The petrology and geochemistry of this "volcanic breccia," as interpreted by Glikson, are unlike those of any volcanic rock in the world. It is not surprising that, as Glikson notes, some of the clasts resemble altered basalts; as we stated in (*2*), the target rocks likely contained basalts, and unmelted basalt clasts are among the more noticeable features of the Bedout-1 core.

The evidence for impact glass that we presented in (*2*) comes from the lowermost section (3044 m) of the Bedout core, where many of the observed features are completely at odds with a magmatic origin and are most consistent with impact-induced melting. At that depth, large plagioclase crystals (An 50) have transformed to glass [figures 6 and 8 in (*2*)]; the shocked grains are isotropic but maintain the perfect outline of a plagioclase lath [figure 6 in (*2*)]. They do not even remotely resemble nearby grains of crystalline plagioclase, as suggested by Glikson. Instead, the texture indicates shock-induced melting and quenching of the dense melt at high pressure, which erased the inherited shock-induced fractures but retained the morphology of the plagioclase lath (*3*). The chemistry of this isotropic region is exactly that of plagioclase with <0.1% TiO_2 and <1% Fe and Mg; no volcanic glass in existence resembles that composition.

Could the isotropic regions result from alteration or spilitization, as suggested by Glikson? It is unlikely that it could, and still retain the isotropic optical character and the exact chemical signature of An 50 plagioclase. The altered region within the core of the plagioclase [table S1, no. 21 in the supporting online material in (*2*)] shows the changes in chemistry that occur during alteration (loss of Na and Ca and addition of Mg and Fe; addition of H_2O). Conversely, the unaltered isotropic core [table S1, no. 4 in the supporting online material in (*2*)] and the crystalline rim of the plagioclase [table S1, no. 3 in the supporting online material in (*2*)] have identical "plagioclase" chemistry (within error). There is no core-rim zonation that would typify plagioclase zoning or "overgrowth," as Glikson would assert. The only logical conclusion is that the core of the plagioclase was shock-melted and quenched at high pressure. Both figures 6 and 8 in (*2*) show large feldspar laths (300 to 500 μm) that have begun to alter over 250 million years of burial, and there is clear evidence of maskelynite in fresh plagioclase laths [figures S4 and S5 in the supporting online material in (*2*)]. There is no visible evidence of alteration in plane polarized light, yet the core of the feldspars is isotropic; it is not even remotely "cryptocrystalline," as suggested by Glikson.

As noted in (*2*), the high-silica glass that we described cannot be a magmatic product. We agree with Glikson that silica does exist in ancient volcanic rocks, precipitated as veins during hydrothermal circulation. However, the high-silica glass in Bedout differs from vein filling in several important respects: (i) The rare occurrences of silica have the shape of "relict quartz grains" and do not resemble a vein. (ii) There are no silica veins in this core; all veins examined in the Bedout core [see, for example, figure S11 in the supporting online material in (*2*)] are filled with lower temperature carbonates. (iii) The high-silica glass contains substantial amounts of TiO_2 (~5%), which is not an element commonly associated with veins of opal or chert but which does occur as rutile inclusions in quartz. Glikson also notes that some of the glass that we describe in (*2*) resembles volcanic lapilli. The glass photomicrographs in figure 7, A and B, in (*2*) do resemble volcanic lapilli in gross texture, because they both formed in explosive, high-energy events. However, the chemistry of the altered glass in figure 7B in (*2*) resembles no known volcanic product. In particular, the glass contains background levels of TiO_2 in a composition that would otherwise be considered basaltic. Overall, the textures and chemical compositions that we described in the Bedout core require a wide range of bulk rock compositions, from acid to ultrabasic, in the same thin section—a paradoxical situation that can only be explained by a process such as impact.

Perhaps the most troubling aspect of Glikson's interpretation of Bedout as volcanic in origin is that he cites no examples or analogs of a comparable volcanic product—nor does he attempt to explain how Bedout, as a volcano, would have formed. We looked at a number of possible explanations for the nature of Bedout, including a volcanic origin. However, we could find no explanation for an isolated volcano the size of Bedout (40 to 60 km in diameter and 3 to 4 km in height) forming along a passive continental margin. This has been grossly overlooked by Glikson and others (*4*). The discovery of the Chicxulub crater prompted a similar set of arguments pertaining to interpreting its origin. For example, the Yucatan-6 core was originally interpreted as being from a "volcanic dome" based on the presence of "andesite" in the basement rocks, even though such a large feature was clearly inconsistent with the region's passive-margin geology. More work is needed to confirm that the Bedout structure is consistent with an impact origin. For example, we agree with Glikson that the presence of PGEs (for example, iridium or chromium) in the melt breccia would strengthen our interpretation. However, we remain confident that the data we present in (*2*) are most consistent with an impact origin for Bedout.

L. Becker
Institute for Crustal Studies
Department of Geological Sciences
University of California
Santa Barbara, CA 93106, USA
E-mail: lbecker@crustal.ucsb.edu

R. J. Poreda
A. R. Basu
Department of Earth and
Environmental Sciences
University of Rochester
Rochester, NY 14627, USA

K. O. Pope
Geo Eco Arc Research
Aquasco, MD 20608, USA

T. M. Harrison
Australian National University
Canberra, Australia

C. Nicholson
Institute for Crustal Studies
Department of Geological Sciences
University of California
Santa Barbara, CA 93106, USA

R. Iasky
Geological Survey Western Australia
Perth, Australia.

References

1. A. Glikson, *Science* **306**, 613 (2004); www.sciencemag.org/cgi/content/full/306/5696/613b.
2. L. Becker *et al.*, *Science* **304**, 1469 (2004).
3. M. Chen, A. El Goresy, *Earth Planet. Sci. Lett.* **179**, 489 (2000).
4. R. A. Kerr, *Science* **304**, 941 (2004).

10 August 2004; accepted 23 September 2004

PHILOSOPHY OF BIOLOGY

A Centenarian's Summary

Matthias Glaubrecht

When, in February 1928, the 23-year-old German ornithologist Ernst Mayr left Berlin for an adventurous one-man expedition as a naturalist-explorer in New Guinea, he took only two books with him: Hans Driesch's *Philosophie des Organischen* (1899) and Henri Bergson's *L'Evolution Créatrice* (1911). These were surprising choices for a young systematist, because both authors were prominent early-20th-century vitalists. More than two years later, Mayr returned from the tropics having collected thousands of specimens (mostly birds, but also mammals, reptiles, butterflies, and shells). He also brought back important observations on the geographical variation of species, observations that in the 1940s he would use to implement the notion of speciation by geographical isolation, or the origin of biological diversity, as an integral part of the modern evolutionary synthesis. In contrast, he was quite disappointed with his two "travel books," because the philosophers had little to offer that would account for the phenomena of the living world.

What Makes Biology Unique? Considerations on the Autonomy of a Scientific Discipline

by Ernst Mayr

Cambridge University Press, New York, 2004. 246 pp. $30, £25. ISBN 0-521-84114-3.

Mayr later concluded that not only vitalism in particular, but traditional philosophy in general—based on logic, mathematics, and the physical sciences—could not satisfy his search for the genuine essence of biology. The organisms he had studied in the field in New Guinea were certainly more than mere machines in Descartes's sense. He remains convinced that basic problems in biology cannot be solved by either Cartesian or vitalistic philosophy. In the 1970s, Mayr devoted considerable attention to topics in the history and philosophy of science, and he began to work out his own philosophy of biology, one based on a lifetime of empirical research in evolutionary biology. Now, early in what is being hailed as the century of biology, Mayr offers his latest—and, as he notes in the first lines of his preface, final—survey of controversial concepts in biology, *What Makes Biology Unique?*

After productive observations but disappointing reading. Mayr (right) and his field assistant Sario in 1928, after two months of collecting birds in the interior mountains of New Guinea.

CREDIT: ERNST MAYR LIBRARY OF THE MUSEUM OF COMPARATIVE ZOOLOGY/HARVARD UNIVERSITY

In the book, his 25th, Mayr again presents a critique of philosophy's contributions to the science of biology. The book comprises 12 essays. Four are newly written, and the other eight chapters are revised versions of articles formerly scattered (thus being rather inaccessible) in journals and symposium volumes. The collection could be considered to serve as the author's personal festschrift in celebration of his 100th birthday. As Mayr confessed in a recent essay (*1*), he finds evolutionary biology to be an "endless frontier" where "there is still plenty to be discovered."

Those unacquainted with Mayr's thinking will find the book an excellent firsthand overview of his philosophy of biology, while those who have read previous books and articles by Mayr will find themselves on familiar ground. The essays present perspectives that are based on ideas Mayr has expounded upon in several previous accounts, including an earlier collection of essays (*2*) and an accessible introduction to biology's place among the sciences (*3*). The book covers several interrelated themes, such as determinism and teleology (a progressive tendency toward ever-increasing perfection), reductionism versus analysis, populational thinking versus typology or essentialism, emergence (the idea of systems that possess properties not present in their individual components), the importance of species, and the differences between species concepts and the delineation of species taxa. Although the topics are treated in a somewhat abbreviated manner, the essays are intended to offer "a revised, more mature" version of Mayr's thoughts.

Physicists, Mayr complains, still arrogantly believe that there is only one true science and that it is physics. And most philosophers, if they do not completely ignore biology, persist in viewing it as a second physics; they are still busy with what Kant or Hegel wrote. In contrast, Mayr the biologist insists that his discipline, which deals with living organisms and vital processes, is not subsumed by physics but remains an autonomous science. Mayr argues that none of the theories in physics, no matter how revolutionary they may be considered, had any effect in changing biology or how biologists view the world. He maintains that reductionism is an ill-fated attempt to seek explanations only at the lowest levels of organization, an attempt that, in part, stems from confusing reductionism with analysis as scientific methodology. He also holds that Thomas Kuhn's theory of scientific revolutions does not apply to changes in the theoretical framework of biology, preferring instead an evolutionary epistemology.

Once more, Mayr compares and contrasts approaches in biology (e.g., historical-narrative explanations) with those used in physical sciences. He notes that variability and the genetic program combine to impart a fundamental difference between the organic and inorganic worlds. Whereas an electron remains an electron, of Earth's six billion humans, no two are identical.

For Mayr, evolution is the most revolutionary idea ever formulated, and Darwin the greatest philosopher. But he stresses that Darwin actually advocated five independent theories about evolution—not just one, as Darwin himself insisted and many after him have claimed. Two of the five (transformation in time and common descent) were readily accepted, while gradualism, the multiplication of species, and natural selection only gained approval in the mid-20th century. Many controversies have been caused by confounding these five theories into a single composite.

The reviewer is in the Department of Malacology, Institute of Systematic Zoology, Museum of Natural History, Humboldt University, Invalidenstrasse 43, D-10115 Berlin, Germany. E-mail: matthias.glaubrecht@rz.hu-Berlin.de

As an evolutionary biologist—who, incidentally, works in the Natural History Museum in Berlin, where Mayr began his scientific career—I admire his clear and elegant writing as well as his insights into biology and philosophy. His book offers the biologist exactly the answers that he sought during his exploration of New Guinea. His earliest experience with philosophy reminded me of my own frustration when, as a biology student, I took seminars in philosophy. I was puzzled by how completely disconnected from biology the philosophers were and how at a loss they left those of us eager to understand the living world. Therefore, I am convinced that *What Makes Biology Unique?* will be loved by those who are curious about biology and used to empirical approaches—not the least because Mayr's style lacks the unintelligible meandering that often detracts from philosophical writing. I assume, however, that many philosophers of science will not have such a positive response. (For one thing, Mayr holds that their belief that their problems can be solved by logic alone has led them to miss the importance and implications of biology.) I only regret not having had this excellent introduction to the philosophy of biology in my pocket during my first research in the tropics.

References

1. E. Mayr, *Science* **305**, 46 (2004).
2. E. Mayr, *Toward a New Philosophy of Biology: Observations of an Evolutionist* (Harvard Univ. Press, Cambridge, MA, 1988).
3. E. Mayr, *This Is Biology: The Science of the Living World* (Harvard Univ. Press, Cambridge, MA, 1997).

FICTION

Of Politics and Particle Physics

Jay M. Pasachoff

How wonderful to encounter a novel that presents a scientist as a popular and engaging principal character. *A Hole in Texas* offers a refreshing contrast with the treatments of mad scientists that are so abundant in literature and popular culture. Add to the cauldron some significant physics and astrophysics, mix with an analysis of scientific politics and the U.S. Congress's effects on major scientific research, and the brew is a delightful tale, one that should be of interest to most readers of this magazine.

A Hole in Texas
A Novel
by Herman Wouk

Little, Brown, New York, 2004. 279 pp. $25, C$35. ISBN 0-316-52590-1.

Herman Wouk's previous novels have covered a wide range of topics, from life on a mismanaged warship in *The Caine Mutiny* (1951), through coming of age in New York City and suburban Mamaroneck in *Marjorie Morningstar* (1955), to the global epic of World War II in *The Winds of War* (1971) and *War and Remembrance* (1978). In his most recent work, the Pulitzer Prize–winning author (now 89 years old) takes up modern particle physics and the politics of big science. We learn what has happened to physicist Guy Carpenter since Congress terminated the Superconducting Super Collider (SSC) in 1993.

Through the stories of Carpenter and the other characters, Wouk has managed to create an exciting plot that involves the Higgs boson. His scientific thriller deals with the prospective political fallout should that elusive particle be discovered by the Chinese. Could a "boson bomb" result? Whose fault is it that America has fallen behind? The consequences are assessed at the highest levels of government, and we are treated to the tense, behind-the-scenes view of a congressional hearing on the subject.

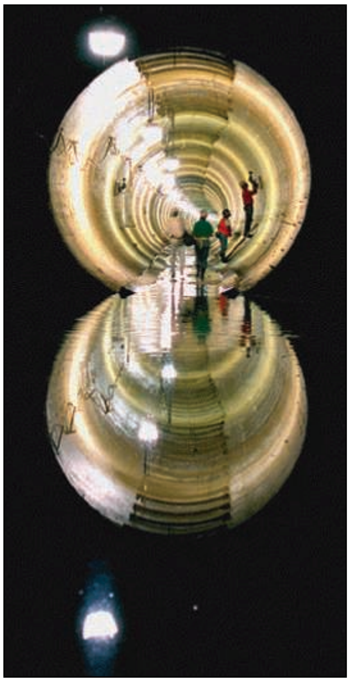

Terminated Texas tunnel. The SSC was abandoned after about 25% of the tunnel for the 87-kilometer-circumference large collider ring had been bored.

CREDIT: SUPERCONDUCTING SUPER COLLIDER PICTURE ARCHIVES

The author gives us a good idea of the size and scale of the "hole in Texas" (the partially excavated tunnel left behind when Congress canned the SSC after spending more than $2 billion on it) and of the devastating personal consequences of so many physicists being laid off at the same time. He suggests that the budgetary decision a decade ago reflected a choice between the SSC and the space station, with the latter winning. I look forward to seeing Hollywood's helicopter views over Waxahachie, Texas.

Readers will find many links to headlines from our daily newspapers. For example, there are bits about the role of secrecy in government and the media backlash over the treatment of a Chinese scientist at Los Alamos National Laboratory. (Indeed, the beautiful physicist who leads the Chinese program, and whom Carpenter loved when they were in graduate school together, is named Wen Mei Li—a possible reference to Wen Ho Lee, especially given the mention of the latter's unfortunate treatment at Los Alamos.)

In a pleasant change from the stories of lone geniuses familiar from much popular writing on science (fiction and nonfiction), Wouk accurately depicts science as an often interactive and collegial enterprise. His storytelling skill highlights the interplay among scientists as well as researchers' relations with outsiders. He shows how bonds among fellow graduate students can last lifetimes, on both personal and scientific bases. We hear Carpenter explain how his career interests moved from philosophy to physics to astrophysics as well as the heroine's response to his description: "Her eyes shone at him. 'A seeker after truth, then.'"

I am not giving away too much plot, I hope, to thrill at how astrophysics comes to the rescue. Here, as throughout the book, the science is presented fairly accurately (though one almost never sees solar flares during a total eclipse). The novel is especially timely given the award of the 2004 Nobel Prize in physics for work on quantum chromodynamics.

One of the book's heroes explains that the "discovery of the Higgs boson goes to the fundamental mystery of mass," and perhaps some readers will go on to deeper studies of the nature of matter. In any case, they will learn about many scientific-political choices that our society confronts. By offering readers a sympathetic physicist with whom they can identify, Wouk may lead them to recall past times when the public unabashedly admired researchers' abilities and their scientific results.

Leon Lederman, the nonfictional Nobelist particle physicist, has devoted much of his recent years to outreach and education. He has valiantly encouraged the presentation of favorable images of scientists in television and movies, and Wouk's novel provides an excellent opportunity for developing such a script. I hope that this engaging novel continues Wouk's string of characters who become fixed in the public mind, and the physicist Carpenter is surely a more pleasant person than the *U.S.S. Caine*'s Captain Queeg.

The author is in the Department of Astronomy, Williams College, Williamstown, MA 01267, USA. E-mail: Jay.M.Pasachoff@williams.edu

NUCLEAR SAFETY

Brazil's Nuclear Puzzle

Liz Palmer* and Gary Milhollin

Brazil is planning to commission later this year a uranium enrichment plant that, if configured to do so, could fuel several nuclear weapons annually. As a member of the Nuclear Nonproliferation Treaty (NPT), Brazil has promised not to make such weapons and is obliged to allow the International Atomic Energy Agency (IAEA) to ensure this is the case. But this spring Brazil took the extraordinary step of barring the plant's doors to the IAEA's inspectors.

Brazil and the IAEA are now negotiating how much access the IAEA will have. The outcome will set a precedent for Iran and any other country that builds an enrichment plant while a member of the treaty.

At its announced capacity, Brazil's new facility at Resende will have the potential to produce enough ^{235}U to make five to six implosion-type warheads per year (*1*, *2*). By 2010, as capacity rises, it could make enough every year for 26 to 31 (*3*) and by 2014 enough for 53 to 63 (*4*).

Brazil has pledged that to enrich uranium to only 3.5% ^{235}U, the concentration required by its two power reactors. This would be too weak to fuel a bomb, which typically requires a concentration of 90% or above. If Brazil should change its mind, its stockpile of uranium already enriched to 3.5 or 5% will have received more than half the work needed to bring it to weapon grade (*5*, *6*). This confers what is known as "breakout capability"—the power to make nuclear weapons before the world can react. Such a power is what the United States and some European countries fear Iran is aiming at.

Iran, too, plans to field thousands of centrifuges at a new enrichment facility at Natanz and claims that its sole purpose is to produce low-enriched reactor fuel. If Brazil succeeds in denying the IAEA access to its centrifuges, Iran can demand the same treatment. Under the NPT, there is no legal ground for treating the two countries differently.

There is little evidence that Brazil actually intends to become a nuclear weapon power. Brazil's science and technology minister Eduardo Campos, declared earlier this year that "the Brazilian nuclear project is intended exclusively for peaceful purposes" (*7*). He pointed out that Brazil has joined the Treaty of Tlatelolco, as well as the NPT, both of which forbid Brazil to make nuclear weapons. Brazil has also adopted a new constitution that does the same.

These statements, however, must be seen in light of Brazil's nuclear history. During the 1980s, Brazil ran a secret effort to build an atomic bomb that ran in parallel with the public program to make electricity. It was administered by the military and hidden from the IAEA. In 1990, the program was openly repudiated by Brazil's newly elected president, Fernando Collor de Mello (*8*). Brazil then joined the NPT and accepted international inspection.

But now, Brazil has built a physical screen around its centrifuges at Resende for the express purpose of preventing inspectors from seeing them. Brazil says it has done this to protect its advanced technology from leaking out to competitors (*9*). The IAEA, however, has a long history of protecting commercial secrets. Brazil is thus a serious challenge to the IAEA's authority.

The real effect of the screen will be to make it harder—if not impossible—for the IAEA to do its job. The IAEA must account for all the enriched uranium the plant makes and must ensure that it is used only to fuel peaceful power reactors. Brazil contends that the inspectors will be allowed to see everything going into Resende and everything coming out and that that should be sufficient. But with a screen in place, it will be difficult to be sure the centrifuges are not hooked up to a hidden supply and outlet of uranium. Such a hookup would allow Brazil to stockpile enriched material while inspectors believe that the facility is less efficient than it really is. And since there is no requirement that Brazil enrich a certain amount of uranium, no one would be the wiser. Unfortunately, the IAEA has already allowed the Brazilian Navy to shield a group of centrifuges for several years at a pilot plant, where uranium was enriched. Thus, Brazil can argue that if the IAEA could certify for years that the pilot-scale plant was not siphoning off any uranium, and could do so without seeing the centrifuges, the same should be possible at Resende.

One response to this argument is that the throughput of the plants is different. Resende will have the capacity to enrich enough uranium for dozens of bombs per year. If the machines are shielded, the inspectors can only measure input and output and then calculate the "material unaccounted for." This is the amount of uranium assumed to be hung up somewhere in the system. Every plant has some. The question is whether the amount makes sense. At Resende, the amount could be considerable, whereas the amount at the pilot plant, given the limited number of centrifuges there, was fairly small.

It seems unlikely that Brazil is really concerned that the IAEA will illegally reveal industrial secrets. More likely, Brazil is trying to hide the origin of the centrifuges. In December 1996, Brazil arrested Karl-Heinz Schaab, a former employee of Germany's MAN Technologie AG, a firm that developed centrifuges for the European enrichment consortium called Urenco (*10*, *11*). German authorities wanted Schaab extradited to prosecute him for selling centrifuge blueprints to Iraq. There is evidence that Schaab and other experts were helping Brazil as well (*12*). It follows that, if the IAEA inspectors were to see the Brazilian centrifuges, they might discover that Urenco's design data had been transferred.

The United States has decided not to challenge Brazil's new status and instead has tried to persuade Brazil to cooperate with the IAEA. Its inspectors were to arrive in Brazil 15 October to pursue a solution to the inspection dispute. The rest of the world should help the United States convince Brazil to put these concerns to rest and to be a good nuclear citizen.

The authors are with the Wisconsin Project on Nuclear Arms Control, Washington, DC 20006, USA.

*To whom correspondence should be addressed. E-mail: liz@wisconsinproject.org

References and Notes

1. If one assumes that the plant's first cascade will produce 20,000 SWU/year and that 16 kg of uranium enriched to 93.5% U-235 are needed for an implosion device. For SWU capacity, see (*2*).
2. M. Hibbs, *Nuclear Fuel*, **7** July 2000.
3. If one assumes 100,000 SWU/year.
4. If one assumes 200,000 SWU/year.
5. About 3000 kg of uranium feed requires ~3500 SWU to make one implosion bomb. The same feed needs more than 2000 SWU to enrich to 3.5%. See (*6*).
6. T. B. Cochran *et al.*, *Nuclear Weapons Databook*, vol. 2, *U.S. Nuclear Warhead Production* (Natural Resources Defense Council, Washington, DC, 1987), Table 5.1, p. 127.
7. "Brazil refuses to let UN inspectors into nuclear facility," Agence France-Presse, 5 April 2004.
8. J. Brooke, *New York Times*, 9 October 1990, p. A1.
9. "Brazil's commitment to nonproliferation under suspicion," CNN.com, 4 April 2004.
10. M. Hibbs, *Nucleonics Week* **37** (51), 19 December 1996, p. 1.
11. M. Hibbs, *Nucleonics Week* **38** (12), 20 March 1997, p. 17.
12. M. Hibbs, *NuclearFuel* **23** (6), 23 March 1998, p. 5.

CHEMISTRY

A Fresh Look at Electron Hydration

Kenneth D. Jordan

When an extra electron is added to water, a hydrated electron is formed. First discovered in 1962 (*1*), this fascinating species is of fundamental importance in radiation chemistry and in electron transfer processes in water, and has therefore been studied widely (*2*, *3*). It remains unclear, however, how the hydrated electron moves through water and how the water molecules are arranged in its vicinity. Three reports in this issue describe experimental studies of negatively charged water clusters that shed light on these questions.

In bulk water, the hydrated electron is believed to be confined in a roughly spherical cavity with a radius of 0.22 to 0.24 nanometers (1 nm = 10^{-9} m), and to occupy an *s*-type ground electronic state. It is characterized by a broad electronic absorption near 1.7 eV, which can be thought of as a transition from the *s* state to an excited *p* state (*1*–*3*). Spectroscopic studies of hydrated electrons have revealed transient absorption on time scales of 50 femtoseconds (fs), (1 fs = 10^{-15} s) 200 to 300 fs, and 1 picosecond (ps) (1 ps = 10^{-3} fs) after excitation to the *p* state (*4*, *5*). These time scales are typical for molecular motions. Some researchers have attributed the 50-fs process to hindered rotational motion of water molecules in the excited state and the 200- to 300-fs process to nonradiative decay of the *p* to the *s* state (*4*). Others have attributed the 50-fs process to *p* → *s* decay and the 200- to 300-fs process to subsequent relaxation of the solvent in the *s* state (*5*). In these scenarios, the 1-picosecond time scale corresponds to long-time relaxation on the *s* state.

Bragg *et al.* (page 669) and Paik *et al.* (page 672) use pump-probe photoelectron spectroscopy to follow the dynamics of photoexcited clusters containing 15 to 50 water molecules and one excess electron (*6*, *7*). Hammer *et al.* (page 675) use vibrational predissociation spectroscopy to elucidate the structures of smaller clusters with just four to six water molecules and one excess electron (*8*). All three studies are motivated by the fact that measurements of clusters can provide a level of detail that is difficult to achieve in studies of the bulk.

Bragg *et al.* (*6*) and Paik *et al.* (*7*) both provide evidence of fast (130 to 250 fs) dynamics associated with the decay of the *p* state to the *s* state of their clusters. Very short lifetimes have previously been reported for the excited states of such clusters (*9*). Bragg *et al.* find that the excited-state lifetimes decrease with increasing cluster size. They extrapolate to a value of 50 fs for bulk water and conclude that the 50-fs process observed in bulk water containing hydrated electrons is due to nonradiative conversion from the *p* to the *s* state, as suggested previously in (*5*).

Paik *et al.* investigate the fate of the *s* state after *p* → *s* decay by selecting the energy of the electron that is ejected as a result of photoexcitation. Their experiments provide insights into the solvent dynamics in clusters of different sizes. The solvation dynamics are found to occur on a time scale of 300 to 450 fs, depending on cluster size. Because this time scale is similar to that of solvation dynamics in bulk water, Paik *et al.* conclude that the local solvent structure is critical for electron solvation. They also observe dynamics on a much longer time scale of 2 to 10 ps, which they ascribe to the breakage of hydrogen bonds followed by evaporation of a water monomer.

These measurements (*6*, *7*) provide new insights into the dynamics of an excess electron interacting with hydrogen-bonded networks. However, the relevance of the new data for hydrated electron dynamics in the bulk depends on whether the excess electron is bound to the cluster surface or resides in its interior (*10*). Paik *et al.* do not reach a conclusion on this issue, whereas Bragg *et al.* argue that they are probing an interior-bound electron. If this is indeed the case, then Paik *et al.* probably also probe an interior-bound electron. Both studies would then be directly relevant to the dynamics of hydrated electrons.

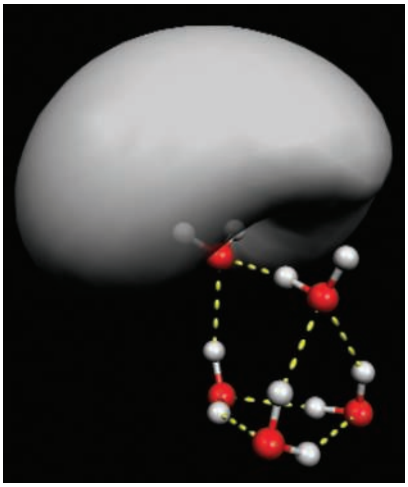

An excess electron binds to a cluster of five water molecules. The water molecule closest to the diffuse excess electron (gray area) is in a double-acceptor hydrogen-bonding environment. Data from electronic structure calculations reported in (*8*).

Aside from the issue of interior versus surface binding, there is the question how the water molecules are arranged in the vicinity of the excess electron. This problem is addressed by Hammer *et al.* (*8*).

With the exception of the negatively charged water dimer, the geometrical structures of negatively charged water clusters have proven elusive. The report by Hammer *et al.* represents a major advance in establishing some of these structures (*8*). By clever use of mixed complexes of water and argon, the authors have been able to synthesize the elusive tetramer, either with normal or with deuterated water, as well as the pentamer and the hexamer. Their vibrational spectra show conclusively that in all three clusters, the excess electron binds in the vicinity of a water molecule that accepts two hydrogen bonds from adjacent molecules but does not itself donate any hydrogen bonds to the hydrogen-bonding network (see the figure). This arrangement is energetically unfavorable in neutral clusters. Its predominance in the negatively charged clusters shows how the excess electron disrupts the hydrogen-bonding network.

The importance of the geometries with double-acceptor waters for the binding of excess electrons to water clusters was first proposed by Lee *et al.* (*11*) on the basis of electronic structure calculations for the negatively charged hexamer. Furthermore, Hammer *et al.* find that vibrational excitation of the OH stretch associated with the double-acceptor water molecule of the negatively charged tetramer and pentamer leads to rapid (50 to 300 fs) ejection of the excess electron.

In the small clusters studied by Hammer *et al.*, the excess electron is surface-bound.

The author is in the Department of Chemistry, University of Pittsburgh, Pittsburgh, PA 15260, USA. E-mail: jordan@pitt.edu

In the interior of larger clusters and in bulk water, the hydrated electron may not be bound in the vicinity of double-acceptor water molecules. However, this type of arrangement could very well occur on ice surfaces or at the surface of large water clusters. The application of the vibrational predissociation technique of Hammer *et al.* to larger clusters may elucidate the location (surface or interior) of the excess electron.

These new experimental results for negatively charged water clusters are important benchmarks for theoretical studies of the structure and dynamics of excess electrons in aqueous environments. Recent theoretical studies have shown that dispersion interactions between the excess electron and the electrons of the water molecules make an important contribution to the binding energy of the former (*12*). Such interactions could play a role in determining whether the excess electron is surface- or interior-bound and could also affect its dynamics.

References

1. E. J. Hart, J. W. Boag, *J. Am. Chem. Soc.* **84**, 4090 (1962).
2. P. J. Rossky, J. Schnitker, *J. Phys. Chem.* **92**, 4277 (1988).
3. L. Turi, D. Borgis, *J. Chem. Phys.* **117**, 6186 (2002).
4. K. Yokoyama, C. Silva, D. H. Son, P. K. Walhout, P. F. Barbara, *J. Phys. Chem. A* **102**, 6957 (1998).
5. M. S. Pshenichnikov, A. Baltuska, D. A. Wiersma, *Chem. Phys. Lett.* **389**, 171 (2004).
6. A. E. Bragg, J. R. R. Verlet, A. Kammrath, O. Cheshnovsky, D. M. Neumark, *Science* **306**, 669 (2004); published online 16 September 2004 (10.1126/science.1103527).
7. D. H. Paik, I.-R. Lee, D.-S. Yang, J. S. Baskin, A. H. Zewail, *Science* **306**, 672 (2004); published online 16 September 2004 (10.1126/science.1102827).
8. N. I. Hammer *et al.*, *Science* **306**, 675 (2004); published online 16 September 2004 (10.1126/science.1102792).
9. J. M. Weber *et al.*, *Chem. Phys. Lett.* **339**, 337 (2001).
10. J. V. Coe *et al.*, *J. Chem. Phys.* **107**, 6023 (1997).
11. H. M. Lee, S. Lee, K. S. Kim, *J. Chem. Phys.* **119**, 187 (2003).
12. F. Wang, K. D. Jordan, *Annu. Rev. Phys. Chem.* **54**, 367 (2003).

GENETICS

The Critical Region in Trisomy 21

David L. Nelson and Richard A. Gibbs

Manipulating mice to model human genetic disorders has become routine since the development of methods to introduce targeted mutations by homologous recombination. Although excellent mouse models exist for many human single-gene disorders such as hemophilia or Zellweger syndrome, mouse models for other diseases only partially mimic or sometimes fail to recapitulate any aspect of the human syndrome. It is therefore surprising that some mouse models of human conditions that are caused by chromosome-scale anomalies have proved valuable. Perhaps the most ambitious of these efforts is the creation of mouse models for Down syndrome (DS), a developmental abnormality characterized by trisomy of human chromosome 21. It has been presumed that several dosage-sensitive genes in a section of human chromosome 21 called the Down syndrome critical region (DSCR) are responsible for many of the features of this disease, including craniofacial abnormalities. On page 687 of this issue, Olson *et al.* (*1*) put this theory to the test with their study of mice engineered to be trisomic but only for those sections of the mouse genome that are orthologous to the human DSCR. In this way, the investigators hoped to more closely model the effect of carrying three copies of genes in this region in an intact animal. Surprisingly, they discovered that three copies of the DSCR genes are not sufficient to cause the cranial anomalies characteristic of Down syndrome. These findings allow a firm refutation of the notion that trisomy of the DSCR is the sole cause of the craniofacial aspect of the Down syndrome phenotype.

Down syndrome, or trisomy 21, is the most common genetic cause of mental retardation, with a worldwide frequency of 1 in 700 births. Trisomy results from sporadic nondisjunction of chromosome 21 leading to three copies of the smallest human chromosome. Although the vast majority of individuals with Down syndrome have three copies of the entire chromosome (and all of the genes it contains), rare individuals with Down syndrome have smaller portions triplicated because of unbalanced translocations. Comparison of the chromosome anomalies and physical characteristics shared among these patients has led to the concept of a critical region for certain features of Down syndrome (*2*). Although controversial, the idea of a DSCR implies that much of Down syndrome could be caused by extra copies of one or a small number of genes in this region (*3*). The notion that a few genes might be of critical importance in this syndrome is particularly attractive because such a simple model would bode well for possible therapeutic intervention.

The development of a mouse model for Down syndrome has not been easy. Human chromosome 21 carries about 231 defined genes across the 33.5 million bases (Mb) of its long arm. The orthologous genes in the mouse are distributed across three chromosomes: 10, 16, and 17. Mouse chromosome 16 contains orthologs of most of the human chromosome 21–linked genes, but it also carries orthologs of genes found on three other human chromosomes. Presumably as a result of these additional genes, mice with trisomy 16 are not viable postnatally. This has necessitated the development of segmental trisomy mouse models of Down syndrome. The Ts65Dn mouse—derived by Davisson and colleagues using translocation chromosomes—exhibits segmental trisomy for orthologs of 104 human chromosome 21–linked genes, and this mouse remains viable into adulthood (*4*). A second partial trisomy mouse model, Ts1Cje, carries a smaller segment containing 81 genes in 10.3 million bases (*5*). Although neither mouse perfectly models human trisomy 21, there are substantial similarities in phenotype, notably craniofacial changes that mimic the human condition, along with electrophysiological differences in brain activity and altered behavior.

Olson *et al.* (*1*) exploited the ability to create defined deletions and duplications in mouse chromosomes by introduction of *Cre* recombinase recognition sequences through homologous recombination in mouse embryonic stem cells. Pioneered by Bradley's group, this method enables the generation of specific deletions and duplications spanning tens of millions of bases (*6*). A particularly successful application of this technique by Baldini and colleagues led to the creation of mouse deletions similar to those found in human DiGeorge syndrome (*7*). However, so far, these methods have not been widely applied to creating mouse models of human diseases, although this may change with the recent description by Adams *et al.* of a new resource to facilitate manipulation of the mouse genome (*8*).

In the new work, Olson and co-workers engineered mice to carry either a duplication or deletion of a 3.9-Mb segment of mouse chromosome 16 containing the 33 orthologs of genes found in the human DSCR. The authors analyzed the phenotype of these mice. They then bred animals with the deleted chromosome segment with those carrying existing segmental trisomies (the Ts65Dn and Ts1Cje mice). This enabled analysis of animals that were trisomic for most of the genes in the Ts65Dn or Ts1Cje mice, but disomic for the 33 DSCR genes. They found that three copies of these 33 genes alone were not

---

The authors are in the Department of Molecular and Human Genetics and the Human Genome Sequencing Center, Baylor College of Medicine, Houston, TX 77030, USA. E-mail: nelson@bcm.tmc.edu

Published by AAAS

In the interior of larger clusters and in bulk water, the hydrated electron may not be bound in the vicinity of double-acceptor water molecules. However, this type of arrangement could very well occur on ice surfaces or at the surface of large water clusters. The application of the vibrational predissociation technique of Hammer *et al.* to larger clusters may elucidate the location (surface or interior) of the excess electron.

These new experimental results for negatively charged water clusters are important benchmarks for theoretical studies of the structure and dynamics of excess electrons in aqueous environments. Recent theoretical studies have shown that dispersion interactions between the excess electron and the electrons of the water molecules make an important contribution to the binding energy of the former (*12*). Such interactions could play a role in determining whether the excess electron is surface- or interior-bound and could also affect its dynamics.

References

1. E. J. Hart, J. W. Boag, *J. Am. Chem. Soc.* **84**, 4090 (1962).
2. P. J. Rossky, J. Schnitker, *J. Phys. Chem.* **92**, 4277 (1988).
3. L. Turi, D. Borgis, *J. Chem. Phys.* **117**, 6186 (2002).
4. K. Yokoyama, C. Silva, D. H. Son, P. K. Walhout, P. F. Barbara, *J. Phys. Chem. A* **102**, 6957 (1998).
5. M. S. Pshenichnikov, A. Baltuska, D. A. Wiersma, *Chem. Phys. Lett.* **389**, 171 (2004).
6. A. E. Bragg, J. R. R. Verlet, A. Kammrath, O. Cheshnovsky, D. M. Neumark, *Science* **306**, 669 (2004); published online 16 September 2004 (10.1126/science.1103527).
7. D. H. Paik, I.-R. Lee, D.-S. Yang, J. S. Baskin, A. H. Zewail, *Science* **306**, 672 (2004); published online 16 September 2004 (10.1126/science.1102827).
8. N. I. Hammer *et al.*, *Science* **306**, 675 (2004); published online 16 September 2004 (10.1126/science.1102792).
9. J. M. Weber *et al.*, *Chem. Phys. Lett.* **339**, 337 (2001).
10. J. V. Coe *et al.*, *J. Chem. Phys.* **107**, 6023 (1997).
11. H. M. Lee, S. Lee, K. S. Kim, *J. Chem. Phys.* **119**, 187 (2003).
12. F. Wang, K. D. Jordan, *Annu. Rev. Phys. Chem.* **54**, 367 (2003).

GENETICS

The Critical Region in Trisomy 21

David L. Nelson and Richard A. Gibbs

Manipulating mice to model human genetic disorders has become routine since the development of methods to introduce targeted mutations by homologous recombination. Although excellent mouse models exist for many human single-gene disorders such as hemophilia or Zellweger syndrome, mouse models for other diseases only partially mimic or sometimes fail to recapitulate any aspect of the human syndrome. It is therefore surprising that some mouse models of human conditions that are caused by chromosome-scale anomalies have proved valuable. Perhaps the most ambitious of these efforts is the creation of mouse models for Down syndrome (DS), a developmental abnormality characterized by trisomy of human chromosome 21. It has been presumed that several dosage-sensitive genes in a section of human chromosome 21 called the Down syndrome critical region (DSCR) are responsible for many of the features of this disease, including craniofacial abnormalities. On page 687 of this issue, Olson *et al.* (*1*) put this theory to the test with their study of mice engineered to be trisomic but only for those sections of the mouse genome that are orthologous to the human DSCR. In this way, the investigators hoped to more closely model the effect of carrying three copies of genes in this region in an intact animal. Surprisingly, they discovered that three copies of the DSCR genes are not sufficient to cause the cranial anomalies characteristic of Down syndrome. These findings allow a firm refutation of the notion that trisomy of the DSCR is the sole cause of the craniofacial aspect of the Down syndrome phenotype.

Down syndrome, or trisomy 21, is the most common genetic cause of mental retardation, with a worldwide frequency of 1 in 700 births. Trisomy results from sporadic nondisjunction of chromosome 21 leading to three copies of the smallest human chromosome. Although the vast majority of individuals with Down syndrome have three copies of the entire chromosome (and all of the genes it contains), rare individuals with Down syndrome have smaller portions triplicated because of unbalanced translocations. Comparison of the chromosome anomalies and physical characteristics shared among these patients has led to the concept of a critical region for certain features of Down syndrome (*2*). Although controversial, the idea of a DSCR implies that much of Down syndrome could be caused by extra copies of one or a small number of genes in this region (*3*). The notion that a few genes might be of critical importance in this syndrome is particularly attractive because such a simple model would bode well for possible therapeutic intervention.

The development of a mouse model for Down syndrome has not been easy. Human chromosome 21 carries about 231 defined genes across the 33.5 million bases (Mb) of its long arm. The orthologous genes in the mouse are distributed across three chromosomes: 10, 16, and 17. Mouse chromosome 16 contains orthologs of most of the human chromosome 21–linked genes, but it also carries orthologs of genes found on three other human chromosomes. Presumably as a result of these additional genes, mice with trisomy 16 are not viable postnatally. This has necessitated the development of segmental trisomy mouse models of Down syndrome. The Ts65Dn mouse—derived by Davisson and colleagues using translocation chromosomes—exhibits segmental trisomy for orthologs of 104 human chromosome 21–linked genes, and this mouse remains viable into adulthood (*4*). A second partial trisomy mouse model, Ts1Cje, carries a smaller segment containing 81 genes in 10.3 million bases (*5*). Although neither mouse perfectly models human trisomy 21, there are substantial similarities in phenotype, notably craniofacial changes that mimic the human condition, along with electrophysiological differences in brain activity and altered behavior.

Olson *et al.* (*1*) exploited the ability to create defined deletions and duplications in mouse chromosomes by introduction of *Cre* recombinase recognition sequences through homologous recombination in mouse embryonic stem cells. Pioneered by Bradley's group, this method enables the generation of specific deletions and duplications spanning tens of millions of bases (*6*). A particularly successful application of this technique by Baldini and colleagues led to the creation of mouse deletions similar to those found in human DiGeorge syndrome (*7*). However, so far, these methods have not been widely applied to creating mouse models of human diseases, although this may change with the recent description by Adams *et al.* of a new resource to facilitate manipulation of the mouse genome (*8*).

In the new work, Olson and co-workers engineered mice to carry either a duplication or deletion of a 3.9-Mb segment of mouse chromosome 16 containing the 33 orthologs of genes found in the human DSCR. The authors analyzed the phenotype of these mice. They then bred animals with the deleted chromosome segment with those carrying existing segmental trisomies (the Ts65Dn and Ts1Cje mice). This enabled analysis of animals that were trisomic for most of the genes in the Ts65Dn or Ts1Cje mice, but disomic for the 33 DSCR genes. They found that three copies of these 33 genes alone were not

---

The authors are in the Department of Molecular and Human Genetics and the Human Genome Sequencing Center, Baylor College of Medicine, Houston, TX 77030, USA. E-mail: nelson@bcm.tmc.edu

sufficient to generate the cranial changes found in mouse models of Down syndrome with larger numbers of triplicated genes. Furthermore, reducing trisomy of these 33 genes to disomy in the Ts65Dn mouse did not eliminate the phenotype.

Breeding mice with the deleted chromosome segment with trisomy mouse models is a particularly elegant approach to testing the role of the DSCR segment in Down syndrome. It would appear that triplication of the 33 DSCR genes is not necessary at least for the craniofacial alterations characteristic of the disease, thus reducing the likelihood of a contiguous critical region for this aspect of Down syndrome. The authors favor a model in which individual or small numbers of genes can make a "critical" contribution to Down syndrome, but where the effect is highly contextual, depending on the combined effects of altering the dosage of other genes.

The generation of these new mouse models will allow additional study of the association of these 33 genes with other Down syndrome abnormalities associated with behavior, electrophysiology, and loss of cerebellar granule cells (*9*). It will also be interesting to increase the size of the duplicated chromosome segments to more closely mimic the human disorder, although if Olson *et al*. are correct that combinations of genes of small (or no) individual effect can contribute to the overall phenotype, the numbers of permutations are daunting.

Mice remain our most useful genetic relative for modeling human disorders, despite numerous differences that complicate analysis. For diseases involving mental retardation, this is a particularly acute problem, as alterations in behavior and learned tasks must suffice to flag differences in mental acuity between mutant mice and their normal counterparts (*10*). Another challenge is the difference in colinearity of the human and mouse genomes, and the lack of conservation of gene order. Even though we now have complete genome sequences for both species, there are still many sequences not currently recognized as genes that could prove to be of great importance when designing mouse models of human disorders. Mouse models such as those described here may offer one of the best ways to understand whether such sequences contribute to phenotype.

References

1. L. E. Olson, J. T. Richtsmeier, J. Leszl, R. H. Reeves, *Science* **306**, 687 (2004).
2. M. K. McCormick *et al.*, *Genomics* **5**, 325 (1989).
3. J. R. Korenberg *et al.*, *Proc. Natl. Acad. Sci. U.S.A.* **91**, 4997 (1994).
4. R. H. Reeves *et al.*, *Nature Genet.* **11**, 177 (1995).
5. H. Sago *et al.*, *Proc. Natl. Acad. Sci. U.S.A.* **95**, 6256 (1998).
6. R. Ramirez-Solis *et al.*, *Nature* **378**, 720 (1995).
7. E. A. Lindsay *et al.*, *Nature* **401**, 379 (1999).
8. D. J. Adams *et al.*, *Nature Genet.* **36**, 867 (2004).
9. L. L. Baxter *et al.*, *Hum. Mol. Genet.* **9**, 195 (2000).
10. M. E. Coussons-Read, L. S. Crnic, *Behav. Genet.* **26**, 7 (1996).

CLIMATE

The Real Color of Climate Change?

Timothy J. Osborn and Keith R. Briffa

How sensitive is the climate to changes in solar irradiance, atmospheric aerosols, greenhouse gases, and other climate forcings? To answer this question, we first need to know the true extent of past climate fluctuations. The changing temperatures over past centuries and millennia have been reconstructed by regressing annually resolved climate proxy records—for example, from ice cores and tree rings—against recent thermometer measurements. On page 679 of this issue, von Storch *et al.* (*1*) investigate whether climate changes over decades and longer are likely to have been captured realistically in such reconstructions of Northern Hemisphere (NH) mean temperature.

The likelihood that reconstructions of this kind represent accurate "hindcasts" of past climate is usually assessed by verification against a short period of independent thermometer data. Such verification is only possible for short-term (annual to decadal) climate variability, because the instrumental climate record is too short to sample longer (decadal to centennial) time scales adequately.

To overcome this limitation, von Storch *et al.* use a 1000-year simulation from a coupled ocean-atmosphere model as a testbed in which the (simulated) NH temperature is known. They then generate pseudoproxy records by sampling a small selection of the model's simulated grid-box temperatures (replicating the spatial distribution of existing proxy records) and degrading them with statistical noise.

The authors show that most of their attempts to reconstruct the model's NH temperature with the pseudo-proxies result in significant underestimates of the amplitude of fluctuations over the last millennium. Published temperature reconstructions for the real world, based on similar calibration methods, may suffer from the same limitation.

Although von Storch *et al.* focus their discussion on the reconstruction method of Mann *et al.* (*2*), their conclusions are relevant to other attempts to reconstruct NH temperature history. They demonstrate even greater loss of long-term variations with a simple regression-and-averaging method [this observation was also made in (*3*)]. The results may apply to all regression-based methods. Accepting von Storch *et al.*'s results does not mean that we must also accept that their simulated temperature history is close to reality—merely that it is a reasonable representation of climate behavior for which any valid reconstruction method should perform adequately.

The underestimated long-term variability obtained by von Storch *et al.* is not a result of problems with proxy data or the ability of the proxies to retain information on these time scales (*4*), because the pseudo-proxies were generated free from such biases. Neither is it simply due to the usual loss of variance associated with any regression-based prediction (this loss already forms the basis for published estimates of reconstruction error). This usual loss of variance is often modeled as a random error, and although a reconstruction may not be perfect, it cannot be scaled by a simple multiplier to achieve a better fit (that is, the reconstruction and its error are uncorrelated) during the calibration period. It is clear from figure 1 of (*1*) that the underestimation of long-term temperature variability is systematic rather than random: At these time scales, a better fit to the actual NH temperature can be achieved by scaling a reconstruction by a simple multiplier (>1), because the reconstruction and its error are correlated. Such error is not incorporated in the uncertainties associated with any published NH temperature reconstruction.

The source of this systematic error can be traced to differing shapes of the variance spectra of the NH temperature and of the pseudo-proxy data. The authors constructed pseudo-proxies by adding white noise to the simulated temperatures. Doing so alters the variance spectra and leads to a deficiency in variance at longer time scales, even after calibration (see the figure). Hence, for climate reconstructions to be optimal on all time scales, proxy data must have variance spectra that are similar to those of the climate data that they are presumed to represent. It is not only through the noise inherent in proxy records that this requirement may be violated. Using

---

The authors are with the Climatic Research Unit, University of East Anglia, Norwich NR4 7TJ, UK. E-mail: t.osborn@uea.ac.uk; k.briffa@uea.ac.uk

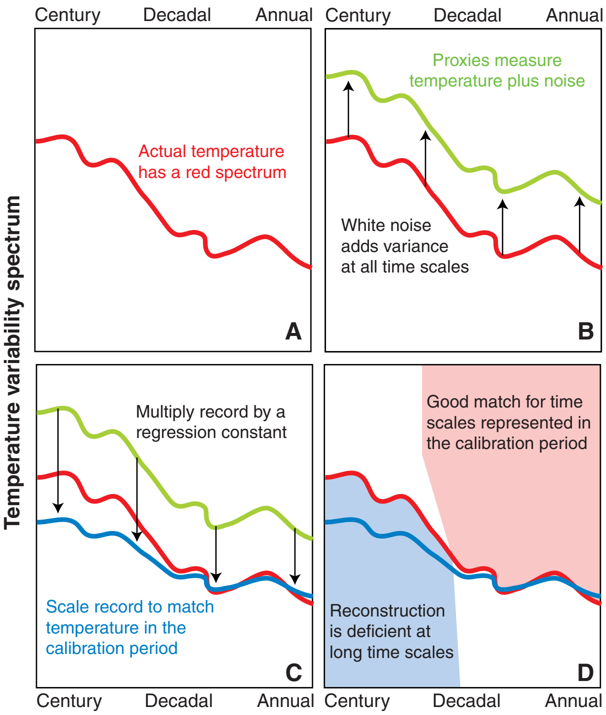

Incompatible colors of climate variability. (**A**) A variance spectrum expresses the amount of variance in a time series that occurs at different frequencies or time scales. A white spectrum has equal variance at all time scales, whereas a red spectrum has greater variance at longer time scales than at shorter time scales. A typical temperature record has a "red" variance spectrum. (**B**) Pseudo-proxies constructed by adding white noise to a simulated temperature record have variance that is increased equally at all time scales, reducing the "redness" of the spectrum (the ratio of long–time scale to short–time scale variance). (**C**) Regression-based calibration approaches scale the pseudo-proxy records by constant multipliers, leaving their redness unchanged (and thus still lower than the redness of the actual temperature spectrum). (**D**) It is not possible, therefore, for any linearly scaled proxy record to match the actual temperature spectrum at all time scales, and the fit tends to be optimized to the time scales represented in the calibration period (typically the last 100 years or less, and dominated by annual to decadal variability), resulting in a deficiency in variance at longer time scales.

just a few proxy records to represent a well-sampled NH average temperature, land-based temperature proxies to reconstruct marine temperatures, and precipitation-sensitive proxies to reconstruct past temperatures might all result in reconstructions that are insufficiently "red" (see the figure caption), that is, lacking in variance at longer time scales.

The message of the study by von Storch *et al.* is that existing reconstructions of the NH temperature of recent centuries may systematically underestimate the true centennial variability of climate. The factor of 2 or more suggested by their study is uncertain because the extent of the problem may depend on the shape of the real climate spectrum. Of course, we do not know the true shape of the spectrum of NH temperature for recent millennia. Nor do we know whether the 1000-year climate simulation used by von Storch *et al.* is closer to the real world than any of the various proxy-based reconstructions. Other model simulations of the climate of the past 1000 years (*5*) may be less "red," implying that the underestimation of long-term climate change could be less pronounced.

If the true natural variability of NH temperature is indeed greater than is currently accepted, the extent to which recent warming can be viewed as "unusual" would need to be reassessed. Systematic errors in existing climate reconstructions will also complicate the evaluation of climate model simulations of past variability. Achieving consistency between our knowledge of past climate and model simulations of that climate is crucial for building confidence in our ability to simulate future climate.

The most important ramification of the report of von Storch *et al.* (*1*) is that greater long-term climate variability is likely to imply greater sensitivity of climate to radiative forcings such as greenhouse gases. Improved climate reconstructions, further model simulations, and a methodology that takes account of all sources of error are needed to determine whether the widely cited range of a 1.5 to 4.5 K increase in average global temperature for a doubling in CO_2 (*6*) is compatible with evidence from the past. It is already clear, however, that greater past climate variations imply greater future climate change.

References and Notes

1. H. von Storch *et al.*, *Science* **306**, 679 (2004); published online 30 September 2004 (10.1126/science.1096109).
2. M. E. Mann, R. S. Bradley, M. K. Hughes, *Nature* **392**, 779 (1998).
3. T. J. Osborn, K. R. Briffa, F. H. Schweingruber, P. D. Jones, www.cru.uea.ac.uk/~timo/p/a/.
4. K. R. Briffa *et al.*, *J. Geophys. Res.* **106**, 2929 (2001).
5. P. D. Jones, M. E. Mann, *Rev. Geophys.* **42**, 2003RG000143 (2004).
6. J. T. Houghton *et al.*, *Climate Change 2001: The Scientific Basis* (Cambridge Univ. Press, Cambridge, 2001).
7. Supported by the UK Natural Environment Research Council (NER/T/S/2002/00440).

PLANT BIOLOGY

A Plant ABC Transporter Takes the Lotus Seat

Burkhard Schulz and Wolf B. Frommer

When plants moved from water to land 450 million years ago, they needed to develop a sealed surface to protect themselves against water loss in the "dry" air environment. To solve this problem, plants invented an epicuticular wax layer that covers the entire surface of the plant that is exposed to air. This protective wax cuticle also serves a multitude of other functions. Its elaborate micro- and nanostructure prevents water and other particles from sticking to the surface of leaves, keeping them clean and so enhancing their ability to trap light for photosynthesis. Adhering water droplets and other particles are washed away in a self-cleaning process called the lotus effect (*1*). The wax layer also filters out damaging ultraviolet rays, prevents volatile chemicals and pollutants from sticking to leaves and stems, and protects plants against attack by microbes and herbivores.

The plant cuticle is composed of a mixture of cutins and polysaccharides, an intracuticular wax layer, and an epicuticular surface layer of wax crystals (see the figure). The wax layer is formed from wax precursor molecules—very long chain fatty acids (VLCFAs) and their derivatives—that are synthesized by plant epidermal cells. But how is such an elaborate structure constructed on the surface of plants? How do the highly hydrophobic wax precursor molecules get to the construction site outside of the plant cell? And what were the evolutionary steps that led to this innovation? On page 702 of this issue, Pighin *et al.* (*2*) provide crucial in-

---

B. Schulz is in the Department of Horticulture and Landscape Architecture, Purdue University, West Lafayette, IN 47907, USA. W. B. Frommer is in the Department of Plant Biology, Carnegie Institution, Stanford, CA 94305, USA. E-mail: wfrommer@stanford.edu

formation on the mechanism by which wax precursor molecules are exported to the plant surface. They show that plant cells use an ABC (ATP-binding cassette) transporter protein similar to the ABC transporters found in mammalian cells for this purpose.

Traditionally, VLCFAs were thought to be exported by a vesicular pathway from their site of synthesis in the endoplasmic reticulum to their destination at the plant surface (see the figure). Sequestration in vesicles would keep these potentially harmful wax precursor molecules in a hydrophobic compartment inside the cell in the same way as plant triglycerides are stored in oleosin-coated vesicular oil bodies (*3*, *4*). Given the difficulty in analyzing the export of wax precursors biochemically, Pighin *et al*. chose a genetic approach. They exploited a large collection of *Arabidopsis* mutants with visibly altered wax cuticles on the surface of their inflorescence stems. In these so-called *cer* or eceriferum (not wax-carrying) mutants (*5*), VLCFA biosynthesis is affected. Through careful characterization of the *cer5 Arabidopsis* mutant, Pighin *et al*. identified an interesting candidate protein for VLCFA export. They show that this CER5 protein is an ABC transporter expressed in plant epidermal cells that, when defective, results in reduced wax on the surface of the *cer5* plant stem. Fluorescence imaging revealed that CER5 resides close to or at the plasma membrane of the plant cell. Intriguingly, the total VLCFA content in epidermal cells from mutant and wild-type *Arabidopsis* is comparable. This can be explained by the intracellular accumulation of VLCFAs in trilamellar inclusions in the mutant plant cells. The inclusions might be modified vesicles that contain large amounts of wax precursor molecules that are either destined for export or need to be stored in a separate compartment to protect cell membranes from accumulating too many VLCFAs.

Members of the ABC transporter family transport a wide variety of substrates including hydrophilic molecules, drugs, and lipids across the membranes of mammalian cells. Some cancer cells are able to survive despite treatment with multiple antitumor drugs because they are induced to express multidrug resistance (MDR) ABC transporters that pump out the drugs faster than they can accumulate inside the cancer cells. Transporters of this kind also export hydrophobic substrates such as platelet-activating factor (PAF), glycerophospholipids, and sphingolipids. The predicted transport activity of the plant CER5 ABC transporter resembles that of three other ABC lipid transporters: MsbA, a recently crystallized bacterial protein involved in export of lipophilic molecules (*6*); TDG1, which transports fatty acids across the chloroplast envelope (*7*); and ALDP, an ABC transporter that is mutated in the neurological disease adrenoleukodystrophy. ALDP and its plant counterpart PXA1/comatose (*8*) are found in peroxisomes, and both are crucial for VLCFA degradation inside these organelles. Mammalian cells expressing the mutant ALDP transporter also exhibit the trilamellar inclusions seen in *cer5* mutant plant cells (*9*).

A seemingly simple hypothesis is that CER5, a half-size ABC transporter, forms a homo- or heterodimeric pore through which VLCFAs are actively transported across the plasma membrane (see the figure). This hypothesis seems to rule out a vesicular pathway of export. Given the near-insolubility of the substrate and the difficulty in setting up an export assay for the CER5 transporter, it is not easy to directly determine transport activity and substrate specificity. But the identification of CER5 does not absolutely rule out a vesicular pathway. Because fluorescence imaging has limited resolution, it remains possible that CER5 is localized in a subapical compartment involved in secretion. Another possibility is that CER5 acts as a "flippase" (*6*), flipping VLCFAs from the inner to the outer leaflet of the plant cell plasma membrane. Whether bacterial MsbA acts as a pore-like transporter or as a flippase also remains a matter of debate (*10*, *11*). CER5, like MsbA, may have a side port that permits lipids to enter or exit the pore.

No matter how the lipid transporters work, the low solubility of the VLCFAs implicates fatty acid–binding proteins in all of these models. Such proteins would be analogous to serum albumin, which binds fatty acids in serum, and to other fatty acid–binding proteins of the mammalian cell cytosol. These proteins need to be identified to clarify further the export pathway for wax precursors in plants. An orphan gene in the *Arabidopsis* genome encoding protein At5g58070 and extracellular lipid-transfer proteins (LTPs) are solid candidates. Independent of the actual

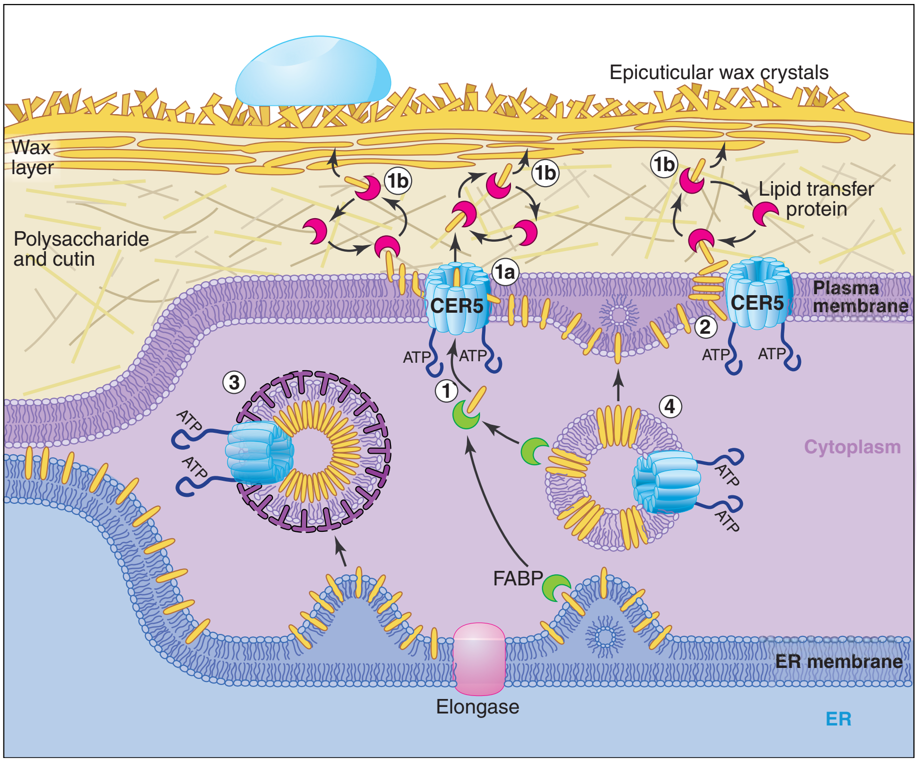

Waxing its own surface. Different models for the transport of wax precursor molecules (VLCFAs) from their site of synthesis in the endoplasmic reticulum (ER) to their site of deposition on the outer surface of plant cells. VLCFAs (orange) synthesized by ER-localized elongases (pink) may be transported to the cell surface by several routes. (**1**) They may be picked up by fatty-acid binding proteins (FABPs; green moons) and transported to the ABC transporter CER5 (pale blue) localized in the plasma membrane. CER5 may actively expel VLCFAs into the cell wall space in an ATP-dependent process. (**1a**) In a variation on this model, VLCFAs could be transported through a side port of CER5 into the upper leaflet of the plasma membrane bilayer. (**2**) Alternatively, the CER5 transporter may act as a flippase, flipping VLCFAs from the inner to the outer leaflet of the plasma membrane. (**1b**) In all cases, extracellular lipid-transfer proteins (dark pink moons) will be required to facilitate transport of VLCFAs to destinations outside the cell. Current data (*2*) are also compatible with vesicular transport of VLCFAs in either (**3**) oleosome bodies covered by oleosin-like proteins (purple) or (**4**) uncoated vesicles that contain the VLCFAs in lipid rafts. Available CER5 localization data do not exclude the possibility that CER5 loads intracellular vesicles with VLCFAs by direct transport or through a flippase mechanism.

CREDIT: ILLUSTRATION ADAPTED BY KATHARINE SUTLIFF/*SCIENCE*

transport mechanism, the identification of CER5 sheds light on wax secretion in plants and may help to elucidate how the elaborate micro- and nanostructure of the wax layer is constructed. How did land plants invent wax secretion? The genomes of living land plants contain more than 100 ABC transporter genes (*12*). Because transporters seem to be sloppy with respect to their substrate specificity (*13*, *14*), it is feasible that when plants crept out of the water, they turned a member of the ABC transporter family into a lipid exporter by ensuring that it became localized to a different cellular compartment. Perhaps this is an example of an evolutionary principle in which sloppiness is transformed into flexibility.

Obviously, there is more work to be done to identify other components of the lipid export machinery. We need to define the exact export pathway and its components. The remaining *Arabidopsis cer* mutants provide an outstanding resource with which to fill in the gaps to obtain a more complete picture. Given that the reduced-wax phenotype of the *cer5* mutant is restricted to stems, the transporters involved in wax deposition on leaves and pollen will need to be identified. A comparative analysis of fatty acid transport in bacteria, plants, and animals, although likely to reveal variations as well as commonalities, will cross-fertilize research in these respective fields. Such an analysis will help to answer crucial questions, including whether the fatty acid substrates are free or bound and how the trilamellar inclusions form. The new insight provided by Pighin and colleagues into the ABC lipid transporter of plants has implications beyond understanding the lotus effect—given the multifunctional role of the wax cuticle, the new findings will be a boon to agriculture.

References

1. W. Barthlott, C. Neinhuis, *Planta* **202**, 1 (1997).
2. J. A. Pighin *et al.*, *Science* **306**, 702 (2004).
3. L. Kunst, A. L. Samuels, *Prog. Lipid Res.* **42**, 51 (2003).
4. L. L. Listenberger *et al.*, *Proc. Natl. Acad. Sci. U.S.A.* **100**, 3077 (2003).
5. A. M. Rashotte *et al.*, *Planta* **219**, 5 (2004).
6. C. F. Higgins, K. J. Linton, *Science* **293**, 1782 (2001).
7. C. Xu *et al.*, *EMBO J.* **22**, 2370 (2003).
8. B. K. Zolman *et al.*, *Plant Physiol.* **127**, 1266 (2001).
9. D. Valle, J. Gärtner, *Nature* **361**, 682 (1993).
10. M. A. Kol *et al.*, *J. Biol. Chem.* **278**, 24586 (2003).
11. W. T. Doerrler *et al.*, *J. Biol. Chem.*, in press; published online 10 August 2004 (10.1074/jbc.M408106200).
12. E. Martinoia *et al.*, *Planta* **214**, 345 (2002).
13. G. Reuter *et al.*, *J. Biol. Chem.* **278**, 35193 (2003).
14. A. Schmidt *et al.*, *J. Biol. Chem.*, in press; published online 11 August 2004 (10.1074/jbc.M405433200).

CHEMISTRY

Redesigning Genetics

Steven A. Benner

Enhanced online at www.sciencemag.org/cgi/content/full/306/5696/625

A year has passed since the celebration of the 50th anniversary of the Watson-Crick model for the double-helical structure of DNA (*1*). Much of the celebration looked back at the marvelous advances that have emerged as genetics has come to resemble organic chemistry. Largely overlooked, however, is a new frontier in organic chemistry that has the goal of redesigning DNA to create artificial genetic systems. These artificial DNA-like molecules are providing deeper insight into how DNA works and are opening the door onto a new world of synthetic biology (*2*). They are also proving valuable for diagnostic testing of human diseases.

According to the first-generation model of DNA, the DNA duplex is like a ladder, with the upright sections composed of pentose sugar molecules linked together by negatively charged phosphate groups (see the figure). According to the model, the uprights constrain the length of the base pairs that form the rungs of the ladder. This constraint, in turn, requires that the large purine bases, adenine (A) or guanine (G), pair with small pyrimidine bases, thymine (T) or cytosine (C)—a phenomenon known as size complementarity. According to the model, hydrogen bonds between purines and pyrimidines ensure that the correct large bases pair with the correct small bases. From this model arose the two principal rules ("A pairs with T, G pairs with C") that underlie all of molecular biology.

One motivation for redesigning DNA using organic chemistry came from a vision of therapeutic benefit. For example, an uncharged DNA analog might be able to pass through a cell membrane, bind to an unwanted RNA molecule according to Watson-Crick rules, and neutralize its activity (*3*). Many dozens of DNA analogs having uncharged scaffolds were made in pursuit of this vision (*4*). Remarkably, only one can be said to have been truly successful: the polyamide-linked nucleic acid analogs (PNA) made by Nielsen *et al*. (*5*).

We now know that the repeating negative charge of the DNA backbone is tightly tied to the rule-based molecular recognition needed for transmission of genetic information (*6*). The repeating negative charge keeps contacts between two complementary DNA strands as far away from the backbone as possible, enforcing Watson-Crick pairing. Without the repeating charge, DNA analogs bend, fold, aggregate, or precipitate. Even PNA does this, given sufficient length.

The repeating charge also dominates the physical properties of DNA. The charge allows the individual bases to be substituted by mutation to create new DNA molecules that behave physically like their parents, but carry different genetic information. The repeating negatively charged phosphates of the DNA and RNA backbone are therefore key to evolution. Hence, a repeating charge may be a universal structural feature of all molecules carrying genetic information in water, perhaps even those on alien planets circling stars in remote galaxies.

Other efforts to redesign DNA have asked simple questions about the architecture of base pairing. For example, Kool wondered how DNA might behave if one got rid of the hydrogen bonds entirely, and used size complementarity as the sole principle of pairing (*7*). Surprisingly, certain DNA polymerases are able to match size-complementary species without the benefit of hydrogen bonding. This result encouraged Goodman to comment that DNA has gone "on the wagon" to join "hydrogen bonds anonymous" (*8*). Schultz, Romesberg, and their colleagues have elaborated on Kool's general theme, generating base analogs that contact each other through unusual hydrophobic interactions (*9*). The latest products from the Kool laboratory are fluorinated bases that also pair using size complementarity in the absence of hydrogen bonds (*10*).

Things generally work out better, however, if the hydrogen bonds are retained. Hydrogen bonding might be important in size-expanded base pairs (*11*), something that has been seen previously in DNA backbones with both longer and shorter rungs (*12*). Carrying the theme further, Minakawa *et al*. asked what might happen if the hydrogen-bonding pattern were to be extended into the minor groove of the DNA backbone (*13*). With four hydrogen-bonding opportunities, we can imagine 16 different hydrogen-bonding patterns supporting 32 different nucleotide letters in an expanded genetic alphabet based on this architecture. The expanded scaffolding works well, and a new class of designer DNA molecules may emerge from this architecture.

The author is in the Department of Chemistry, University of Florida, Gainesville, FL 32611, USA. E-mail: benner@chem.ufl.edu

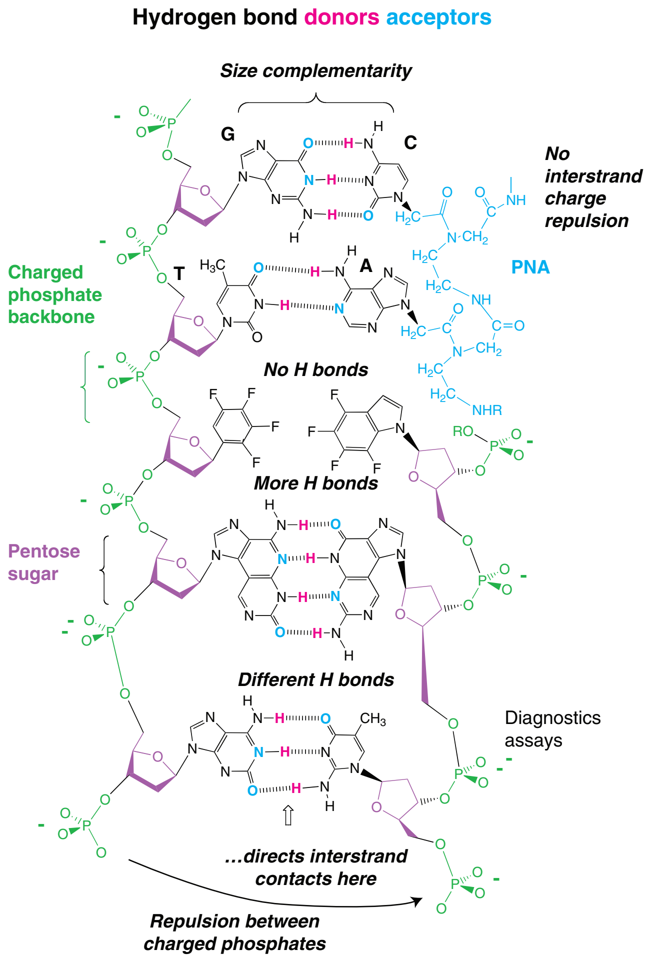

Tinkering with DNA. The standard DNA double helix has a scaffold of repeating negatively charged phosphate groups (green) that link together ribose sugars (purple). This scaffold supports size-complementary pyrimidine and purine bases (black) that present hydrogen bond donor (pink) and acceptor (blue) groups. Each nucleotide (sugar, phosphate, base) plays a role in transmitting genetic information. Attempts are under way to redesign DNA using organic chemistry for a variety of uses including diagnostic testing. For example, DNA molecules have been engineered to lack negatively charged phosphate groups (**upper right**) or hydrogen-bonding groups (**middle**), or have been made with an increased number of hydrogen bonds or rearrangements of these bonds (**bottom**). Redesigned DNA containing rearranged hydrogen bonds (branched DNA) enhances the medical care of about 400,000 patients annually through its use in diagnostic tests such as those detecting human immunodeficiency virus and human hepatitis C virus.

One need not extend the scaffold of the bases into the minor groove, however, to get extra bases (letters) into the genetic alphabet. More than a decade ago, Switzer *et al*. (*14*) and Piccirilli *et al*. (*15*) found that an additional eight letters can be added to the DNA alphabet if one simply shuffles the arrangement of hydrogen bond donating and accepting groups (see the figure). The physical properties of nonstandard bases have now been optimized. For example, tautomerism (unwanted movement of hydrogen atoms) that causes nonstandard bases to be lost during repeated copying has been fixed, undesirable acid-base properties of the artificial genetic components have been changed, and an annoying epimerization (unwanted change in the geometry of the molecule) displayed by some nonstandard nucleotides has been corrected (*16*).

The architecture of this artificially expanded information system is so reminiscent of the Watson-Crick architecture, and its properties are so similar to those found in standard DNA, that one may wonder why nature has not already exploited these extra DNA letters. Recent advances in our understanding of how the ribose sugar might have arisen prebiotically on early Earth (*17*) offer a clue. Ribose is stabilized by minerals containing borate, which might have allowed ribose to accumulate on early Earth. Attaching a heterocyclic ring to a ribose via a carbon-nitrogen bond, as in standard nucleotides, requires a dehydration event, certainly conceivable (although not trivial) prebiotically. Attaching a heterocyclic ring to a ribose via a carbon-carbon bond, as in some nonstandard nucleotides, appears to be far more difficult. The structure of our DNA may therefore reflect the minerals that were present in ancient deserts on early Earth.

Luckily, prebiotic chemistry does not constrain the application of expanded genetic alphabets to human health care. For example, the U.S. Food and Drug Administration recently approved a "branched DNA" assay developed by Urdea and Horn (*18*) that exploits nonstandard nucleotides. Incorporating extra letters into DNA speeds up hybridization and allows independent binding of two rule-based molecular systems: one based on the standard letters A, T, G, and C, and the other based on an artificial genetic alphabet. Currently, each year some 400,000 patients infected with the human immunodeficiency virus or the hepatitis B and C viruses have their care enhanced through diagnostic assays based on an expanded genetic alphabet (*19*). Expanded genetic alphabets are working their way into other preclinical assays that test for cystic fibrosis, SARS, and biohazards. They are also entering research, where nonstandard nucleotides underlie a large number of emerging tools for systems biology research and genome sequencing.

So what is next on the agenda as we redesign DNA? It is hard to say. Perhaps foreshadowing the future is the discussion of recent examples where artificial genetic systems have been copied, and the copies copied, using engineered polymerases (*20*). Although most polymerases will accept many nonstandard nucleotides with some degree of efficiency when given no other choice, polymerases have evolved for billions of years to efficiently accept only A, T, G, and C. Therefore, most polymerases wean unnatural nucleotides from a DNA molecule if given the chance.

Both the structure of the nucleotide and the structure of the polymerase can be changed to obtain a pair where this does not happen. Polymerase engineering is in its infancy, however, and most attempts at site-directed mutagenesis wreak site-directed damage on the enzyme. But with the advent of selection methods for polymerases (*21*), we can expect in the not-too-distant future fully artificial genetic systems that support a synthetic biology—a set of artificial chemical systems that can direct their own replication and evolve.

References

1. J. D. Watson, F. H. C. Crick, *Nature* **171**, 737 (1953).
2. W. Gibbs, *Sci. Am.* **290**, 74 (May 2004).
3. P. S. Miller *et al.*, *Biochemistry*, **16**, 1988 (1977).
4. S. M. Freier, K. H. Altmann, *Nucleic Acids Res.* **25**, 4429 (1997).
5. P. E. Nielsen, *Mol. Biotechnol.* **26**, 233 (2004).
6. S. A. Benner, D. Hutter, *Bioorg. Chem.* **30**, 62 (2002).
7. S. Moran *et al.*, *Proc. Natl. Acad. Sci. U.S.A.* **94**, 10506 (1997).
8. M. F. Goodman, *Nature Biotechnol.* **17**, 640 (1999).
9. M. Fa, A. Radeghieri, A. A. Henry, F. E. Romesberg, *J. Am. Chem. Soc.* **126**, 1748 (2004).
10. J. S. Lai, E. T. Kool, *J. Am. Chem. Soc.* **126**, 3040 (2004).
11. H. B. Liu *et al.*, *J. Am. Chem. Soc.* **126**, 1102 (2004).
12. C. R. Geyer *et al.*, *Structure* **11**, 1485 (2003).
13. N. Minakawa *et al.*, *J. Am. Chem. Soc.* **125**, 9970 (2003).
14. C. Y. Switzer *et al.*, *J. Am. Chem. Soc.* **111**, 8322 (1989).
15. J. A. Piccirilli *et al.*, *Nature* **343**, 33 (1990).
16. T. A. Martinot, S. A. Benner. *J. Org. Chem.* **69**, 3972 (2004).
17. A. Ricardo *et al.*, *Science* **303**, 196 (2004).
18. M. A. Collins *et al. Nucleic Acids Res.* **25**, 2979 (1997).
19. T. Elbeik *et al.*, *J. Clin. Microbiol.* **42**, 563 (2004).
20. P. Ball, *Nature* **431**, 624 (2004).
21. F. J. Ghadessy *et al.*, *Proc. Natl. Acad. Sci. U.S.A.* **98**, 4552 (2001).

INTRODUCTION

Solving Gene Expression

Words are static images on a page unless you know what they mean, how their meanings change depending on the context, and what the rules are for using them. Similarly, a complex regulatory code is buried within the genome, and researchers will need to decipher it to understand how genes are expressed, what their functions are, and how normal instructions are altered in disease.

Throughout the magazine and online this week are features that describe different aspects of gene expression and its control. Kosak and Groudine (p. 644) describe how genomes may be organized (linearly and within three-dimensional space in the nucleus) for the regulation of gene expression. A News story by Pennisi (p. 632) provides a clear introduction to the world of enhancers: regulatory elements that have been a pivotal force in evolution. Pastinen and Hudson (p. 647) describe the pitfalls associated with analyses of cis-acting control mechanisms governing allele-specific differences in gene expression, some of which have been associated with disease susceptibility. At *Science*'s online Signal Transduction Knowledge Environment (STKE, www.sciencemag.org/sciext/genome2004) are features describing the dance of nuclear receptor complexes with DNA that lead to transcription (Fowler and Alaric) and approaches different organisms use to select genes within gene families for expression (Dalgaard and Vengrova).

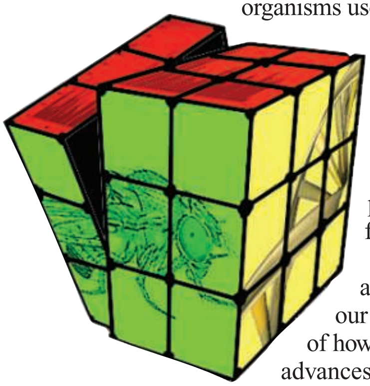

Aware of the magnitude of the challenge of developing a complete "parts list" for all of these activities, an international consortium of scientists has begun the ENCODE (ENCyclopedia Of DNA Elements) project (p. 636), whose goal is to identify all of the structural and functional elements of the human genome. In their pilot phase, researchers are comparing multiple approaches for detecting different elements on 30 Mb of DNA.

Some of the medical applications of this information are tantalizing prospects, whereas others are already at our doorstep. Hood *et al.* (p. 640) present a sweeping view of how expression patterns will be combined with technological advances to further predictive medicine. However, it is not an entirely smooth path. For instance, as the number of gene array studies proliferates, some researchers are finding that they don't necessarily lead to quick diagnosis or prognosis (see News story by Marshall on p. 630). The *Science* Functional Genomics Web site (www.sciencemag.org/feature/plus/sfg) contains additional online discussion of whether microarrays have been oversold and how they can reach their full potential. The site also has updated links to other resources. At the Science of Aging Knowledge Environment (SAGE KE, www.sciencemag.org/sciext/genome2004) are articles describing how microarrays and other genome-scale technologies are being applied to aging research (Kaeberlein; Melov and Hubbard). The Editorial by Lord and Papoian (p. 575) explores efforts to standardize microarray data so that regulatory agencies can use gene expression studies to evaluate drug safety.

In the course of their analysis of RNA expression for protein-coding and non–protein-coding sequences during the *Drosophila* life cycle (p. 655), White and his group have come to see the task of assembling the functional parts of the genome as being like a Rubik's cube. Although ~4.3×10^{19} different positions are possible, the cube can be resolved from any position by 29 or fewer manipulations. As we begin to understand biological systems through carefully designed experiments and analyses, the complexity we are seeing now may begin to resolve into simpler principles.

–BARBARA R. JASNY AND LESLIE ROBERTS

CONTENTS

NEWS

VIEWPOINTS AND REVIEW

Science

CREDIT: ADNAN LOTIA

NEWS

Getting the Noise Out of Gene Arrays

Thousands of papers have reported results obtained using gene arrays, which track the activity of multiple genes simultaneously. But are these results reproducible?

When Margaret Cam began hunting for genes that are turned up or down in stressed-out pancreas cells a couple of years ago, she wasn't looking for a scientific breakthrough. She was shopping. As director of a support lab at the National Institute of Diabetes and Digestive and Kidney Diseases (NIDDK), she wanted to test-drive manufactured devices called microarrays or gene arrays that measure gene expression; she had her eye on three different brands. These devices are hot, as they provide panoramic views of the genes that are active in a particular cell or tissue at a particular time.

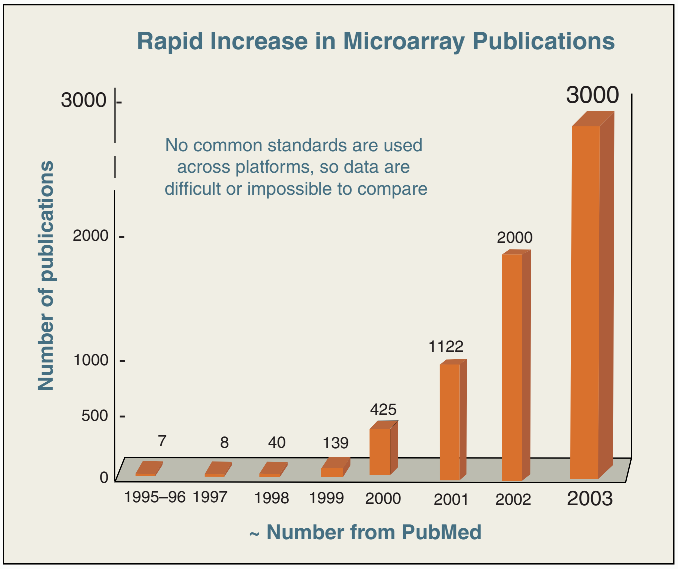

Hot technology. The number of studies using microarrays to analyze genes being turned on and off in concert has exploded in the last decade.

Gene array studies are increasingly being used to explore biological causes and effects and even to diagnose diseases. But array experiments are expensive, and Cam wanted to be sure that her colleagues would get high-quality, repeatable, credible results.

She was taken aback by what she found. Not only was she unable to pick a clear winner, but she had a hard time figuring out whether any of the arrays produced trustworthy results. As she delved deeper, she found that the devices produced wildly incompatible data, largely because they were measuring different things. Although the samples she tested were all the same—RNAs from a single batch of cells—each brand identified a different set of genes as being highly up- or down-regulated.

The disharmony appears in a striking illustration in Cam's 2003 paper in *Nucleic Acids Research*. It shows a Venn diagram of overlapping circles representing the number of genes that were the most or least active on each device. From a set of 185 common genes that Cam selected, only four behaved consistently on all three platforms—"very low concordance," she said at an August forum in Washington, D.C., run by the Cambridge Healthtech Institute, based in Newton Upper Falls, Massachusetts. Using less rigorous criteria, she found about 30% agreement—but never more than 52% between two brands. "It was nowhere near what we would expect if the probes were assaying for the same genes."

Cam's findings caused "one's jaw to drop," says Marc Salit, a physical chemist at the National Institute of Standards and Technology (NIST). This was not the first paper to highlight such inconsistencies, but Cam's little diagram had an impact: With support from commercial array makers and academics, Salit is now coordinating an effort at NIST to understand exactly what is measured by these devices.

A few ex-enthusiasts think the promise of gene arrays may have been oversold, especially for diagnostics. Take Richard Klausner, the former director of the National Cancer Institute (NCI) now at the Bill and Melinda Gates Foundation in Seattle, Washington. "We were naïve" to think that new hypotheses about disease would emerge spontaneously from huge files of gene-expression data, he says, or that "you could go quickly from this new technology to a clinical tool." His own experience with arrays indicated they were too sensitive and finicky: The more data he gathered on kidney tumor cells, the less significant it seemed.

But those who have persevered with gene expression arrays attribute such problems to early growing pains. They claim that experienced labs are already delivering useful clinical information—such as whether a breast cancer patient is likely to require strong chemotherapy—and that new analytical methods will make it possible to combine results from different experiments and devices. Francis Barany of Cornell University's Weill Medical College in New York City insists that arrays work well—if one digs deeply into the underlying biology.

Imperfections

Digging into the biology is just what Cam did after her experiments produced reams of discordant data. She and colleagues in Marvin Gershengorn's group at NIDDK wanted to pick out a set of key genes active in pancreatic tumor cells undergoing differentiation. From there, they meant to go on to examine how islet cells develop. "We were very surprised," she recalls, when they couldn't cross-validate results from studies done with Affymetrix, Agilent, and Amersham arrays. So she began pulling the machines apart.

Cam soon ran into a barrier: Manufacturers weren't eager to share information about the short DNA sequence probes each kit uses to spot gene activity. Each commercial system uses a similar approach. Short bits of DNA from known genes are printed as probes on arrays. When an experimental sample is exposed to the array, RNAs made by genes cling specifically to the probes that have a complementary sequence, triggering a fluorescent signal that can be read by an optical scanner. The more RNA on a probe, the stronger the signal. The activity of thousands of genes can be tracked simultaneously this way.

Although manufacturers identified which genes the probes targeted, they would not reveal the actual nucleotide sequence of each probe. This made it difficult to know exactly what the probes were picking up. Recalls Zoltan Szallasi of Harvard's Children's Hospital in Boston, "For the first 6 years researchers were actually flying blind." That changed in 2001, he says, when the companies began sharing data.

Cam says, "We managed to get partial sequences [of array probes] from Agilent," along with "full sequences from Affymetrix

CREDIT: ADAPTED FROM NIH

Published by AAAS

and Amersham." Her team analyzed the probe and gene matchup in detail and found that supposedly different probes were responding to pieces of the same gene. Targeting different parts can be a problem because genes often contain many components that can be spliced into variant RNA packages. The result, several experts say, is that probes can over- or underestimate gene activity.

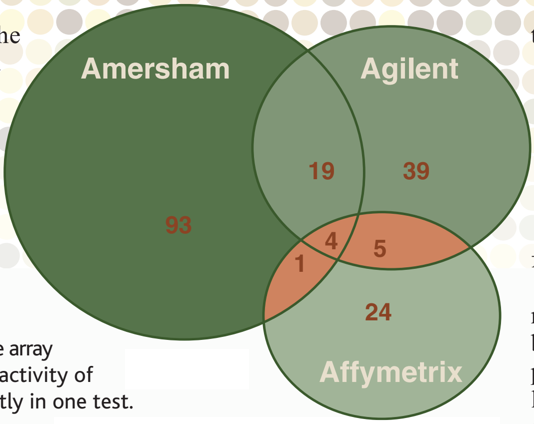

Little overlap. Three array systems rated the activity of 185 genes differently in one test.

Sorting out the confusion is tough because the probes have not been designed to be specific to gene-splice variants, and no one has even created a master list of variants. Cam is encouraged that companies are beginning to make arrays specific to different splice variants. "That should reduce the ambiguity."

Another confounding factor, Szallasi claims, is promiscuous matches: Probes often respond not only to gene products that exactly fit the sequence but also to those that "cross-hybridize" with near matches. "Every manufacturer claims to have avoided this problem, but there must be a reason why microarray probes targeting almost the same region of a given gene give wildly different intensity signals," he says.

Moreover, many probes just don't correspond to annotated sequences in the public database, RefSeq, Szallasi says; removing these problematic probes significantly improves study results. But the best way to build confidence in gene array results and novel analytical methods, he argues, is to validate probe-gene matches using the more rigorous and time-consuming polymerase chain reaction methods of sequence testing. Szallasi has been doing just that as part of an effort to help collaborators at Harvard and at Baylor College of Medicine in Houston, Texas, merge their gene expression data sets. He's also been trying to get other researchers in Boston to share information on validated matches.

Emerging proof

The difficulty in comparing gene array results, say Szallasi and others, raises questions about how much confidence to have in the thousands of papers already published and whether it will ever be possible to merge existing data and find significant results. Relatively few labs have tried to replicate large gene expression studies, even those using identical test devices, says NCI's Richard Simon, a cancer clinician who directs gene array studies. People don't want to waste hard-to-obtain tissue on such work, and they'd rather not spend money on replicating others' findings. Simon argues that the correct test of comparability in clinical medicine is not "whether you come up with the same set of genes" in two studies, but whether you come up with an accurate and consistent prediction of patient outcomes.

He and others note that gene arrays have already proved their mettle in two clinical areas: breast cancer and lymphomas. Molecular geneticist Todd Golub of the Broad Institute in Cambridge, Massachusetts, says his group has independently validated gene expression results of Louis Staudt of NCI and Pat Brown of Stanford University that identify subcategories of lymphoma that have relatively poor or good outcomes. And Lyndsay Harris, a breast cancer researcher at Harvard's Dana-Farber Cancer Institute, says many of her colleagues have confidence in gene expression data that identify a high-risk form of breast cancer associated with cells in the basal epithelium, a strategy that Charles Perou, now at the University of North Carolina, Chapel Hill, pioneered.

In basic research as well, Golub agrees with Simon that broad themes, not specific genes, should be the focus of comparison studies. He looks for a "biologically robust" response in patterns of gene activity—such as activation of coordinated cell signals—as a sign that two experiments have detected the same result. Spotting a signal in the noise is like "recognizing a face, regardless of whether you're wearing bifocals, or sunglasses, or no glasses." Eventually, Golub says, biostatistical methods can probably be used to define such "signatures" in a flexible way to recognize different expression patterns as alternative forms of the same result.

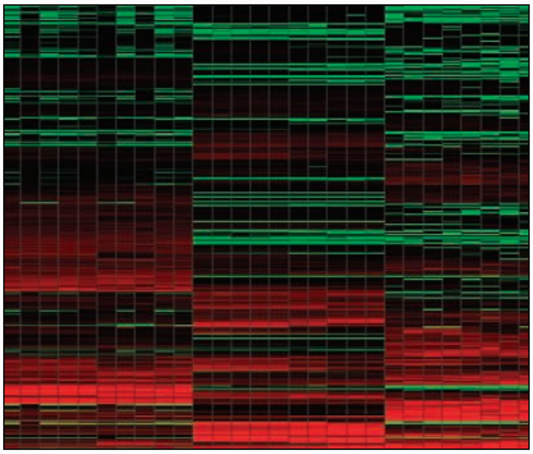

Map of discordance. An experiment at NIH found that three commercial devices rated different genes as being turned on (red) and turned off (green) in a single batch of pancreatic cells.

Trials have begun to test some of the newer interpretations of cancer pathology based on gene expression, such as efforts to profile high-risk breast cancer at the Netherlands Cancer Institute (*Science*, 19 March, p. 1754). But many champions of gene-expression tests contend that they are not yet ready for "prime-time" clinical use.

Staudt thinks the time will come when "every cancer patient gets a microarray-based diagnosis." But before then, "we still have to show how reproducible the results are." He is part of an NCI-sponsored consortium that is attempting to correlate results from his own group, obtained from one type of device (spotted arrays of lengthy cDNAs), with those from a type of mass-produced device (printed arrays of short oligonucleotides) made by Affymetrix. Already, they have achieved "very good prediction" of tumor type in retrospective studies of 500 samples. Now they plan to test the model prospectively.

Seeking harmony

Researchers have now got "all the major journals" using a single format to report array data, says Alvis Brazma of the European Bioinformatics Institute in Hinxton, UK, a co-founder of the Microarray Gene Expression Data Society. But eliminating discordance in the hardware may not be so easy, says Ernest Kawasaki, chief of NCI's microarray facility: "If I had all the money in the world, I would say the best thing is to start over from the beginning"—presumably with a set of validated gene expression probes and shared standards.

That kind of money isn't available, but Salit says NIST recently agreed to spend $1.25 million a year for 5 years to tackle the problem of "discordance." Salit is coordinating a group that includes microarray manufacturers and a coalition of academics—the External RNA Control Consortium—to develop a set of standards that can be used to calibrate gene arrays and ensure that results can be translated meaningfully from one lab to another. If it succeeds, "the pie is going to get bigger" because "everybody's results will improve."

–ELIOT MARSHALL

CREDITS (TOP): ADAPTED FROM *NUCLEIC ACIDS RESEARCH*; (BOTTOM) ADAPTED FROM *NUCLEIC ACIDS RESEARCH*

NEWS

Searching for the Genome's Second Code

The genome has more than one code for specifying life. The hunt for the various types of noncoding DNA that control gene expression is heating up

Molecular biologists may have sequenced the human genome, but it's going to take molecular cryptographers to crack its complex code. Genes, keystones to the development and functioning of all organisms, can't by themselves explain what makes cows cows and corn corn: The same genes have turned up in organisms as different as, say, mice and jellyfish. Instead, new findings from a variety of researchers have made clear that it's the genome's exquisite control of each gene's activity—and not the genes per se—that matters most.

"The evolution of the genetic diversity of animal forms is really due to differences in gene regulation," says Michael Levine, an evolutionary biologist at the University of California (UC), Berkeley. Turning on a gene at a different time, or in a new place, or under new circumstances can cause variations in, say, size, coloration, or behavior. If the outcome of that new regulatory pattern improves an organism's mating success or ability to cope with harsh conditions, then it sets the stage for long-term changes and, possibly, the evolution of new species.

Unfortunately, "people don't look to regulatory elements as the cause of the variation they see," says Stephen Proulx of the University of Oregon, Eugene. These elements are "a major part of the [evolution] story that's been overlooked," Levine says.

That neglect is now being righted. Although many biologists remain gene-centric, an increasing number are trying to factor in the effects of gene regulation. Researchers are beginning to come up with efficient ways to locate the different regulatory regions scattered along the strands of DNA. Others are piecing together the workings of transcription factors, proteins that interact with regulatory DNA and with each other to guide gene activity. They are homing in on exactly where transcription factors operate along the DNA and what they do to ensure that a gene turns on at the right time and in the right amount.

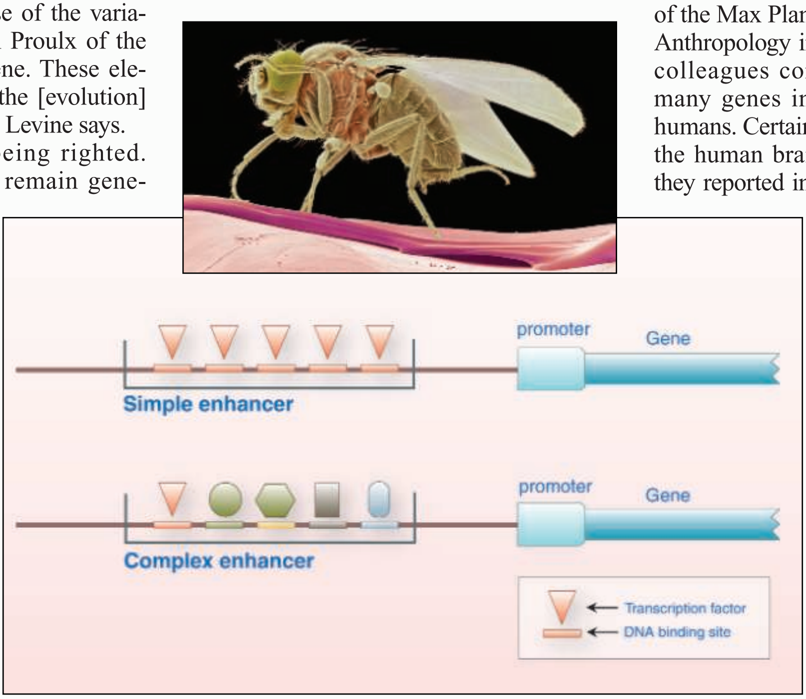

Model organism. Fruit flies have played a critical role in the search for stretches of regulatory DNA called enhancers, which control gene expression by binding to one or more transcription factors.

Most are tackling the functions of regulatory elements one at a time, although a few are taking more global and bioinformatics approaches (see sidebar on p. 635). At the California Institute of Technology (Caltech) in Pasadena, one group is trying to identify all the regulatory interactions in maturing embryos; their goal is to elucidate how genes and regulatory DNA work together to guide development and also how those interactions change over evolutionary time.

All this work is making clear that buried in DNA sequence is a regulatory code akin to the genetic code "but infinitely more complicated," says Michael Eisen, a computational biologist at Lawrence Berkeley National Laboratory in California. Researchers can predict the proteins specified by the genetic code, but, he adds, "we can't predict gene expression by simply looking at the sequence."

Manolis Dermitzakis of the Wellcome Trust Sanger Institute in Cambridge, U.K., agrees: "The complexity of the genome is much higher than we have defined for the past 20 years. We have to change our way of thinking."

From genes to regulation

At the Medical Research Council's Laboratory of Molecular Biology in Cambridge, U.K., Francis Crick—co-discoverer of DNA's structure—Sydney Brenner, and their colleagues took the first steps toward figuring out how genomes work. In 1966, they proved that genes are written in a three-unit code, each of which specifies a particular amino acid. By combining these threesomes, called codons, in different ways, the genome encodes instructions for thousands of proteins. This discovery focused the spotlight on genes themselves and the coding regions within them; for decades biologists called the intervening DNA "junk."

Consequently, the notion of gene regulation languished, even when results pointed to its importance. In the early 1970s, Allan Wilson of UC Berkeley and his student, Mary Claire King, demonstrated that humans and chimps are quite similar in their genes. The key to what makes the two species so different, they suggested, lies in where and when those genes are active.

But not until 2 years ago did experiments begin to bear out this idea. Wolfgang Enard of the Max Planck Institute for Evolutionary Anthropology in Leipzig, Germany, and his colleagues compared the expression of many genes in tissues from chimps and humans. Certain genes are far more active in the human brain than in the chimp brain, they reported in the 15 April 2002 issue of *Science* (p. 340), a finding that supports Wilson and King's ideas.

Enard's 2002 work came on the heels of dozens of other studies suggesting that gene changes are not the be-all and end-all of evolutionary innovation. Instead, researchers increasingly attribute innovation to a variety of types of regulatory DNA, some just recently detected. Certain genes code for the proteins that make up the transcription machinery, which binds to promoters, the DNA right at the beginning of a coding se-

CREDITS (TOP): PHOTO RESEARCHERS INC., 2002; (BOTTOM) N. KEVITIYAGALA/*SCIENCE*

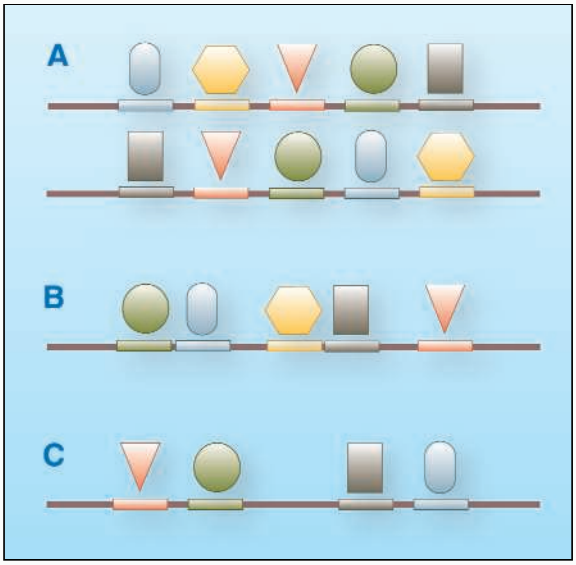

Genome cryptography. The regulatory code is encoded in the arrangement of an enhancer's DNA binding sites (A), in the spacing between binding sites (B), or by the loss or gain of one or more of these sites (C).

quence. Other genes code for transcription factors that can be located anywhere in the genome. All affect their target genes by attaching to regulatory DNA—sometimes called modules—that's usually near but not next to a gene. Protein-laden modules that stimulate gene activity are called enhancers; those that dampen activity are called silencers.

As a plethora of meetings and research reports suggests, enhancers are hot. They are small genetic command centers, consisting of stretches of 500 or so bases. Those clusters in turn are peppered with transcription factor binding sites, which can be less than 10 bases long. The target of a particular enhancer—and its effect—depends on the spacing and order of the binding sites within it.

Sometimes the enhancer simply contains multiple copies of the same binding site and therefore uses the same transcription factor throughout its length. Other times, it has multiple transcription factors, and slight differences among these proteins can cause one gene to turn on and another to turn off.

Both enhancers and silencers are especially hard to find because they are very small pieces of sequence and, unlike promoters, reside at varying distances from the gene they regulate. "We have a lot of potentially short stretches of DNA where the action is and stretches of DNA that don't matter," Patrick Phillips, an evolutionary developmental biologist at the University of Oregon, Eugene, points out. Theorists predict that humans could have as many as 100,000 enhancers and silencers, but fewer than 100 are known, says Levine.

Hot on the enhancer trail

To understand the role of enhancers in development, Levine is studying their architecture and function in the fruit fly genome. The first challenge he encountered was simply finding the elusive quarry: Several years ago he encouraged his graduate student Michele Markstein (and her computer-savvy parents) to write a computer program that could begin to do just that.

The trio worked first with a transcription factor, dorsal, which was known to affect a gene called *zen*. They already knew that the enhancer for *zen* contained four binding sites for dorsal, packed close together. The researchers used that signature sequence as a probe for finding other enhancers that also had clusters of dorsal binding sites.

The method worked. Proof positive came when the program pinpointed three previously identified enhancers that control other genes. It also turned up a dozen more clusters containing three or four of dorsal's binding sites. The researchers have since shown that at least two are definitely enhancers. Levine is encouraged: "Sometimes the clustering of a single factor's binding sites is sufficient to find new enhancers," he says. Indeed, using a similar strategy, Eisen identified a set of enhancers responsible for anterior-posterior development in the fruit fly. The groups published their results 2 years ago.

That same year, Eisen, Levine, and UC Berkeley's Benjamin Berman teamed up to use this approach, along with other bioinformatics tools, to look for more complex enhancers. Instead of containing repeated binding sites for the same transcription factor, complex enhancers contain binding sites for several different factors, thereby providing precise regulation of gene expression.

To find these sequences, Berman and his colleagues looked for pieces of DNA with binding sites for five transcription factors. They didn't have a specific enhancer in mind but sought out DNA with those binding sites sitting close enough together to suggest they formed an enhancer.

The five transcription factors all affect embryonic genes. Initially, Berman's program found several dozen of what seem to be complex enhancers; recently the count has more than doubled. And in pinning down these enhancers, the researchers uncovered almost 50 genes that seem to be controlled by this same set of transcription factors and thus are likely to work together to guide early development

So far, the researchers have confirmed that at least some of these newly identified clusters really are enhancers by testing their activity in transgenic fruit flies. They add DNA consisting of the putative enhancer and a marker gene. If the marker gene shows up in the same place as the enhancer's target gene, then the researchers know they have got what they want. These data are showing that when several enhancers have a similar binding site composition, they tend to work together and coordinate the expression of sets of genes.

Enhancer encryption

With the first enhancers in hand, Levine and his colleagues were ready to take the next step: to figure out how enhancers orchestrate development and effect the changes underlying evolution. They began to dissect the architecture of these bits of sequence, determining exactly where the transcription factor dorsal attached and whether those locations had anything to do with the enhancer's function. They also tracked down transcription factors that interacted with the same enhancers as dorsal.

Through these efforts, Levine and UC Berkeley collaborator Albert Erives have been able to decipher another layer of "code" scattered in the arrangement of binding sites within the enhancer. This code

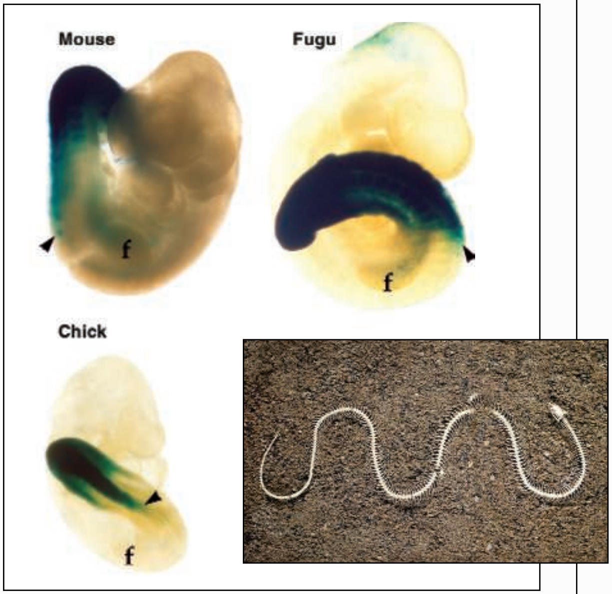

One gene, many sizes. Enhancers from different species alter the extent of a *Hox* gene's expression (dark stain), variation that leads to species-specific numbers of thoracic vertebrae.

CREDITS: (TOP) N. KEVITIYAGALA/*SCIENCE*; (BOTTOM MAIN BOX) ANAND & BELTING/*PNAS*; (BOX WITHIN) PHOTO RESEARCHERS INC., 2002

is critical to directing patterns of differentiation in embryonic tissue, they reported in the 16 March *Proceedings of the National Academy of Sciences*.

Dorsal, whose concentration in the embryo is highest on the ventral side and decreases toward the dorsal, is key in defining these regions. Gene activity varies along the dorsal-ventral axis, leading to the differentiation of tissue types. High amounts of dorsal lead to mesoderm, a precursor to muscle; low amounts stimulate the development of precursor nervous system tissue.

When the researchers probed more closely into the enhancer, they found that a binding site for dorsal was always next to the binding site for a transcription factor called twist. Levine found that the close proximity and specific order of the binding sites were conserved in an equivalent enhancer in mosquito and a different fruit fly: “They were not randomly arranged,” Levine says.

These results suggested that the effect of an enhancer on a gene is determined not just by the combination of transcription factors but also by the spacing between the binding sites. Levine thinks that dorsal and twist have to be quite close together for the enhancer to work dorsally, where concentrations of dorsal are low; when far apart, much more dorsal is needed. Thus it seems that the genome can use the same subset of transcription factors to regulate different genes simply by changing the order or spacing of those proteins, or where they bind along the enhancer. With this work, “Levine has gotten inside the mind of enhancers,” says Eisen.

Enhancers and evolution

Alterations in the order and spacing of binding sites can also affect how the same gene works across several species, new research is finding, suggesting that it might take only a relatively simple rearrangement to change an enhancer and affect evolution. At a meeting on developmental diversity held in April in Cold Spring Harbor, New York, developmental biologist Cooduvalli Shashikant of Pennsylvania State University, University Park, described his survey of enhancer effects on a gene called *Hoxc8*. This gene, found in many organisms, helps define the number and shape of thoracic vertebrae. Shashikant suspected that the enhancer, rather than the gene alone, plays a pivotal role in delineating different vertebrae configurations among species. To find out, he and his colleagues analyzed the sequence of the 200-base-pair enhancer that lays just upstream of *Hoxc8* in zebrafish, puffer fish, and mice.

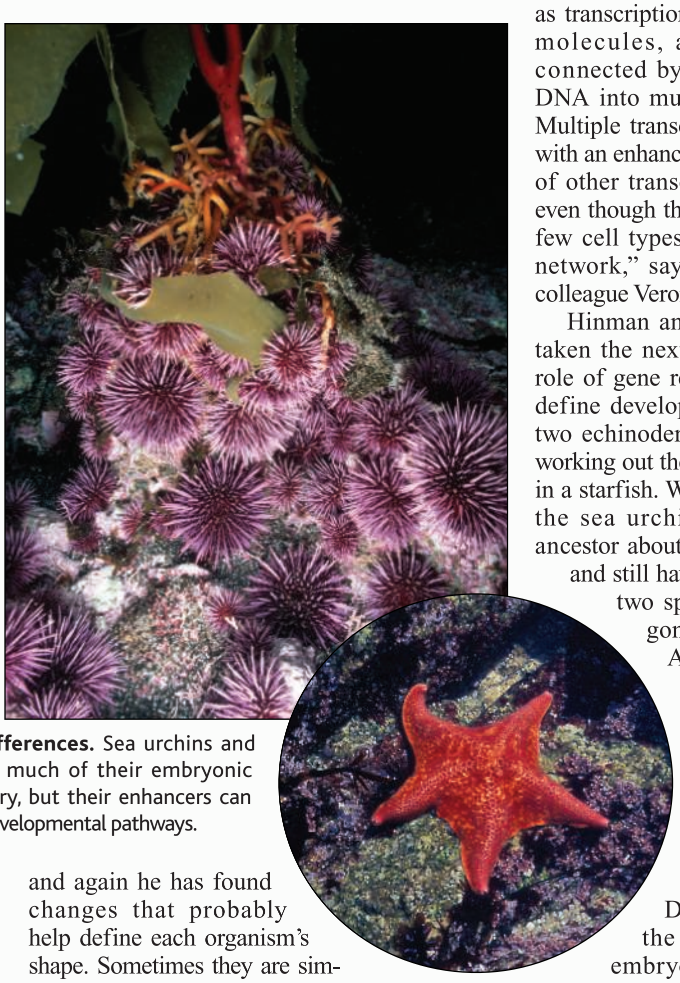

Enhancing differences. Sea urchins and starfish share much of their embryonic genetic circuitry, but their enhancers can vary, altering developmental pathways.

CREDITS: (TOP) PHILLIP COLLA, OCEANLIGHT.COM; (BOTTOM) JOSEPH DOUGHERTY/ECOLOGY.ORG

After adding a reporter gene to each enhancer so they could see where it was active, Shashikant’s group inserted the combination into mouse embryos. Then they compared the pattern of expression generated with the zebrafish and puffer fish enhancers to that of the mouse enhancer. In all three cases, the activity of the gene was restricted to the back part of the developing spine.

Shashikant suspects that the subtle differences among the enhancers in each species changes the physical boundaries of *Hoxc8* expression within the embryo, thereby helping explain why chickens wind up with seven thoracic vertebrae and snakes about 200, he says. Shashikant is also looking at the sequences of this enhancer in other species, including whales and coelacanths, and again he has found changes that probably help define each organism’s shape. Sometimes they are simple sequence changes. Other times, missing or additional DNA alters the mix of transcription factors involved. Through evolution, “a lot of tinkering has gone on at the enhancer level,” Shashikant says.

Evolving embryonic differences

Similarly, Eric Davidson, a developmental gene regulation biologist at Caltech, has found that a small change in one enhancer’s structure, and likely many alterations in all sorts of enhancers, pave the way to the different developmental pathways that make each species distinctive. Five years ago, he and his colleagues embarked on an ambitious project to map all the genetic interactions necessary to build the embryonic sea urchin’s endomesoderm, cells that are precursors to the skeleton, gut, and other tissues. They worked gene by gene, determining the expression pattern of each and deducing their functions by knocking them out in developing embryos. From these data and more, they pieced together a computer model of the 50-gene circuitry controlling the embryo’s first 30 hours as an initial glob of cells began to differentiate into endomesoderm.

The circuit is a hairball of proteins such as transcription factors and signaling molecules, and their genes, all connected by means of regulatory DNA into multiple feedback loops. Multiple transcription factors partner with an enhancer to control the activity of other transcription factors. Thus, even though the circuit involves just a few cell types, “it’s a very complex network,” says Davidson’s Caltech colleague Veronica Hinman.

Hinman and Davidson have now taken the next step: elucidating the role of gene regulation in helping to define developmental differences in two echinoderms. Hinman has been working out the same genetic circuitry in a starfish. Whereas the starfish and the sea urchin shared a common ancestor about 500 million years ago and still have similar embryos, the two species have long since gone their separate ways. Adult sea urchins look like pincushions, with rounded exoskeletons; starfish are flat, with arms protruding from a central cavity. Hinman has focused on the earliest moments of the starfish’s life. Despite the differences in the adults, much of the embryonic genetic circuitry studied so far is almost identical in both species, she reported in 2003.

Yet subtle variations have had a big impact. For example, there’s a five-gene circuit both species share. A key gene in this pathway is *otx*, and it sets off the circuit in the sea urchin and the starfish. Hinman has found a tiny change in this enhancer: Between the two species, this enhancer varies by just one binding site, for a transcription factor called t-brain.

A Fast and Furious Hunt for Gene Regulators

Genes may be essential, but researchers increasingly recognize the pivotal role that another element of the genome—regulatory DNA—plays in human disease, speciation, and evolution. In many labs, the search to find where these regions are buried is intensifying (see main text). While some researchers are tackling these regions one at a time, others are experimenting with high-speed methods to detect regulatory regions, such as enhancers, en masse and determine what each one does.

At the Whitehead Institute for Biomedical Research in Cambridge, Massachusetts, Richard Young and Ernest Fraenkel are using microarrays to analyze yeast in an effort to turn up all its promoters, the sites at the beginning of a gene that bind to activating proteins. The team starts by treating a cell and one of its transcription factors so that the factor permanently sticks to its DNA-binding sites, thereby tagging all the promoters that use this factor. Then they use that transcription factor to isolate these sequences from the rest of the genome. After filling a microarray with pieces of yeast DNA whose positions on the genome are known, they add the tagged DNA, which then links to its matching sequence in the microarray, revealing the approximate location of each piece.

The computer program takes over from there, says Fraenkel, refining the location of the binding sites using similar DNA from other organisms as a guide. In this way the team has been able to pinpoint the promoter-binding sites for each individual transcription factor in yeast simultaneously. Now, Young and Fraenkel are using this technique to find enhancers and regulatory DNA in organisms that have more complex genomes than yeast's. Already they have cornered enhancers on both human liver and pancreatic cells.

Others are also using comparative genomics techniques to fish out regulatory regions. The idea is straightforward enough: Compare two or more sequenced genomes to identify those places where DNA outside genes is highly similar and presumably functional. The challenge lies in deciding which genomes to compare, explains postdoc Marcelo Nobrega of Lawrence Berkeley National Laboratory (LBNL) in California. If the animals are too closely related, their genomes will share many noncoding sequences that have no connection to regulation. If the organisms are too distant, then even functional regions, including regulatory regions, will be too different to detect.

Nobrega's LBNL colleague Len Pennacchio thinks he has the answer. When his team compared the human genome to that of a puffer fish, they came up with a whopping 2500 potential enhancers. To test the effectiveness of this method, the LBNL team has been inserting 100 of the putative enhancers, identified on human chromosome 16, into transgenic mouse embryos, which they then analyze for signs of regulatory activity. At a meeting in Cold Spring Harbor, New York, in May, Pennacchio reported that 48 of the 60 enhancers tested to date were real.

Testing, testing. High-throughput screens for enhancers can turn up false positives, which can be excluded by looking for enhancer function in mouse embryos.

But Ewan Birney and his colleagues at the European Bioinformatics Institute (EBI) in Hinxton, U.K., and the European Molecular Biology Laboratory in Heidelberg, Germany, worry that comparisons alone will yield spurious matches as well as valid ones. "If you look at conservation itself, it doesn't tell you a great deal," says Birney.

To refine the comparative approach, his team has written a program that considers only short sequences that are conserved between human and mouse—and only when they are present in higher than usual densities in front of a gene. EBI's computers divide human and mouse genomes into small pieces, say, six or eight bases, then compare them.

In the initial experiments, the researchers asked their computers to pick out a well-known piece of regulatory DNA called the TATA box, which is required for the activation of many genes. The program did just fine, says Birney, which gives him hope that it will also be able to pin down other regulatory regions elsewhere in the genome.

Birney eventually hopes to tie these data in with forthcoming results from other labs suggesting that gene regulation is controlled by other aspects of the genome as well—such as how chromosomes are twisted around various proteins. And that, he hopes, will enable him to begin to address "how all this is put together as a code" that researchers can use to decipher the true workings of the genome.

–E.P.

CREDIT: MALAK SHOUKRY/LAWRENCE BERKELEY NATIONAL LABORATORY

The starfish has this binding site; the sea urchin does not. In the sea urchin, t-brain works in concert with other regulatory genes and sets off the embryo's skeleton-forming circuitry, a genetic pathway absent in the starfish embryo. But because the *otx* enhancer is missing t-brain, the sea urchin must also rely on a different transcription factor to get the *otx* gene in the five-gene circuitry to kick in.

Meanwhile the t-brain binding site on the starfish's *otx* enhancer keeps *otx* focused on genes for the incipient gut. Davidson thinks that ancestral echinoderms had a t-brain site on the enhancer for *otx*, one that disappeared from that enhancer in the sea urchin. "This looks like species-specific jury-rigging," he points out. "The evolution of body plans happens by changes in the network architecture."

Enhancing genome studies

Through these kinds of studies, researchers are beginning to decode the regulatory genome. If this code can be made clear, they should be able to piece together how organisms diversify, says Nipam Patel, a biologist at UC Berkeley. For example, through Davidson and his colleagues' thorough descriptions of the gene pathways guiding development, they can pin down where enhancer modules have been added or lost. That understanding, in turn, is changing how some researchers make sense of evolution, adds Michael Ludwig of the University of Chicago. It's a vision in which regulatory elements, including enhancers and silencers, are as important, if not more important, than gene mutations in introducing genetic innovations that may set the stage for speciation. Changes in one type of regulatory element, the transcription factors, can be quite detrimental, as each influences many genes. By contrast, enhancer mutations work locally, affecting just their target genes, and so are less likely to have deleterious effects on the rest of the genome.

Yet Ludwig and others are the first to admit that they have not cracked this regulatory code. "We need to learn what it is and how this information is written in these sequences," says Eisen. "At this moment, we still do not have that ability."

–ELIZABETH PENNISI

Published by AAAS

VIEWPOINT

The ENCODE (ENCyclopedia Of DNA Elements) Project

The ENCODE Project Consortium*†

The ENCyclopedia Of DNA Elements (ENCODE) Project aims to identify all functional elements in the human genome sequence. The pilot phase of the Project is focused on a specified 30 megabases (∼1%) of the human genome sequence and is organized as an international consortium of computational and laboratory-based scientists working to develop and apply high-throughput approaches for detecting all sequence elements that confer biological function. The results of this pilot phase will guide future efforts to analyze the entire human genome.

With the complete human genome sequence now in hand (*1*–*3*), we face the enormous challenge of interpreting it and learning how to use that information to understand the biology of human health and disease. The ENCyclopedia Of DNA Elements (ENCODE) Project is predicated on the belief that a comprehensive catalog of the structural and functional components encoded in the human genome sequence will be critical for understanding human biology well enough to address those fundamental aims of biomedical research. Such a complete catalog, or "parts list," would include protein-coding genes, non–protein-coding genes, transcriptional regulatory elements, and sequences that mediate chromosome structure and dynamics; undoubtedly, additional, yet-to-be-defined types of functional sequences will also need to be included.

To illustrate the magnitude of the challenge involved, it only needs to be pointed out that an inventory of the best-defined functional components in the human genome—the protein-coding sequences—is still incomplete for a number of reasons, including the fragmented nature of human genes. Even with essentially all of the human genome sequence in hand, the number of protein-coding genes can still only be estimated (currently 20,000 to 25,000) (*3*). Non–protein-coding genes are much less well defined. Some, such as the ribosomal RNA and tRNA genes, were identified several decades ago, but more recent approaches, such as cDNA-cloning efforts (*4*, *5*) and chip-based transcriptome analyses (*6*, *7*), have revealed the existence of many transcribed sequences of unknown function. As a reflection of this complexity, about 5% of the human genome is evolutionarily conserved with respect to rodent genomic sequences, and therefore is inferred to be functionally important (*8*, *9*). Yet only about one-third of the sequence under such selection is predicted to encode proteins (*1*, *2*). Our collective knowledge about putative functional, noncoding elements, which represent the majority of the remaining functional sequences in the human genome, is remarkably underdeveloped at the present time.

An added level of complexity is that many functional genomic elements are only active or expressed in a restricted fashion—for example, in certain cell types or at particular developmental stages. Thus, one could envision that a truly comprehensive inventory of functional elements might require high-throughput analyses of every human cell type at all developmental stages. The path toward executing such a comprehensive study is not clear and, thus, a major effort to determine how to conduct such studies is warranted.

To complement ongoing large-scale projects that are contributing to the identification of conserved elements in the human genome (*10*) (www.intlgenome.org) and to the isolation and characterization of human full-length cDNAs (*11*), the ENCODE Project (www.genome.gov/ENCODE) was launched to develop and implement high-throughput methods for identifying functional elements in the human genome. ENCODE is being implemented in three phases—a pilot phase, a technology development phase, and a production phase. In the pilot phase, the ENCODE Consortium (see below) is evaluating strategies for identifying various types of genomic elements. The goal of the pilot phase is to identify a set of procedures that, in combination, can be applied cost-effectively and at high-throughput to accurately and comprehensively characterize large regions of the human genome. The pilot phase will undoubtedly reveal gaps in the current set of tools for detecting functional sequences, and may reveal that some methods being used are inefficient or unsuitable for large-scale utilization. Some of these problems should be addressed in

---

*Affiliations for all members of the ENCODE Consortium can be found on *Science* Online at www.sciencemag.org/cgi/content/full/306/5696/636/DC1.

†To whom correspondence should be addressed. E-mail: elise_feingold@nih.gov

ENCODE Project Scientific Management:
National Human Genome Research Institute (E. A. Feingold, P. J. Good, M. S. Guyer, S. Kamholz, L. Liefer, K. Wetterstrand, F. S. Collins).

Initial ENCODE Pilot Phase Participants:
Affymetrix, Inc. (T. R. Gingeras, D. Kampa, E. A. Sekinger, J. Cheng, H. Hirsch, S. Ghosh, Z. Zhu, S. Patel, A. Piccolboni, A. Yang, H. Tammana, S. Bekiranov, P. Kapranov, R. Harrison, G. Church, K. Struhl); Ludwig Institute for Cancer Research (B. Ren, T. H. Kim, L. O. Barrera, C. Qu, S. Van Calcar, R. Luna, C. K. Glass, M. G. Rosenfeld); Municipal Institute of Medical Research (R. Guigo, S. E. Antonarakis, E. Birney, M. Brent, L. Pachter, A. Reymond, E. T. Dermitzakis, C. Dewey, D. Keefe, F. Denoeud, J. Lagarde, J. Ashurst, T. Hubbard, J. J. Wesselink, R. Castelo, E. Eyras); Stanford University (R. M. Myers, A. Sidow, S. Batzoglou, N. D. Trinklein, S. J. Hartman, S. F. Aldred, E. Anton, D. I. Schroeder, S. S. Marticke, L. Nguyen, J. Schmutz, J. Grimwood, M. Dickson, G. M. Cooper, E. A. Stone, G. Asimenos, M. Brudno); University of Virginia (A. Dutta, N. Karnani, C. M. Taylor, H. K. Kim, G. Robins); University of Washington (G. Stamatoyannopoulos, J. A. Stamatoyannopoulos, M. Dorschner, P. Sabo, M. Hawrylycz, R. Humbert, J. Wallace, M. Yu, P. A. Navas, M. McArthur, W. S. Noble); Wellcome Trust Sanger Institute (I. Dunham, C. M. Koch, R. M. Andrews, G. K. Clelland, S. Wilcox, J. C. Fowler, K. D. James, P. Groth, O. M. Dovey, P. D. Ellis, V. L. Wraight, A. J. Mungall, P. Dhami, H. Fiegler, C. F. Langford, N. P. Carter, D. Vetrie); Yale University (M. Snyder, G. Euskirchen, A. E. Urban, U. Nagalakshmi, J. Rinn, G. Popescu, P. Bertone, S. Hartman, J. Rozowsky, O. Emanuelsson, T. Royce, S. Chung, M. Gerstein, Z. Lian, J. Lian, Y. Nakayama, S. Weissman, V. Stolc, W. Tongprasit, H. Sethi).

Additional ENCODE Pilot Phase Participants:
British Columbia Cancer Agency Genome Sciences Centre (S. Jones, M. Marra, H. Shin, J. Schein); Broad Institute (M. Clamp, K. Lindblad-Toh, J. Chang, D. B. Jaffe, M. Kamal, E. S. Lander, T. S. Mikkelsen, J. Vinson, M. C. Zody); Children's Hospital Oakland Research Institute (P. J. de Jong, K. Osoegawa, M. Nefedov, B. Zhu); National Human Genome Research Institute/Computational Genomics Unit (A. D. Baxevanis, T. G. Wolfsberg); National Human Genome Research Institute/Molecular Genetics Section (F. S. Collins, G. E. Crawford, J. Whittle, I. E. Holt, T. J. Vasicek, D. Zhou, S. Luo); NIH Intramural Sequencing Center/National Human Genome Research Institute (E. D. Green, G. G. Bouffard, E. H. Margulies, M. E. Portnoy, N. F. Hansen, P. J. Thomas, J. C. McDowell, B. Maskeri, A. C. Young, J. R. Idol, R. W. Blakesley); National Library of Medicine (G. Schuler); Pennsylvania State University (W. Miller, R. Hardison, L. Elnitski, P. Shah); The Institute for Genomic Research (S. L. Salzberg, M. Pertea, W. H. Majoros); University of California, Santa Cruz (D. Haussler, D. Thomas, K. R. Rosenbloom, H. Clawson, A. Siepel, W. J. Kent).

ENCODE Technology Development Phase Participants:
Boston University (Z. Weng, S. Jin, A. Halees, H. Burden, U. Karaoz, Y. Fu, Y. Yu, C. Ding, C. R. Cantor); Massachusetts General Hospital (R. E. Kingston, J. Dennis); NimbleGen Systems, Inc. (R. D. Green, M. A. Singer, T. A. Richmond, J. E. Norton, P. J Farnham, M. J. Oberley, D. R. Inman); NimbleGen Systems, Inc. (M. R. McCormick, H. Kim, C. L. Middle, M. C. Pirrung); University of California, San Diego (X. D. Fu, Y. S. Kwon, Z. Ye); University of Massachusetts Medical School (J. Dekker, T. M. Tabuchi, N. Gheldof, J. Dostie, S. C. Harvey).

the ENCODE technology development phase (being executed concurrently with the pilot phase), which aims to devise new laboratory and computational methods that improve our ability to identify known functional sequences or to discover new functional genomic elements. The results of the first two phases will be used to determine the best path forward for analyzing the remaining 99% of the human genome in a cost-effective and comprehensive production phase.

ENCODE Targets

The defining feature of the ENCODE pilot phase is the uniform focus on a selected 30 Mb of the human genome. Each pilot-phase participant will study the entire set of ENCODE targets—44 discrete regions that together encompass ~1% of the human genome. All approaches will thus be tested on a relatively large amount of genomic sequence, allowing an assessment of the ability of each to be applied at large scale. The use of a single target set will allow the results of different approaches to be directly compared with one another.

The set of ENCODE targets was chosen to represent a range of genomic features (www.genome.gov/10005115). It was first decided that a number of smaller regions (0.5 to 2 Mb) distributed across many different chromosomes should be chosen, as opposed to (for example) a single 30-Mb region. To ensure that existing data sets and knowledge would be effectively utilized, roughly half of the 30 Mb was selected manually. The two main criteria used for the manual selection were as follows: (i) the presence of extensively characterized genes and/or other functional elements; and (ii) the availability of a substantial amount of comparative sequence data. For example, the genomic segments containing the α- and β-globin gene clusters were chosen because of the wealth of data available for these loci (*12*). On the other hand, the region encompassing the *CFTR* (cystic fibrosis transmembrane conductance regulator) gene was selected because of the extensive amount of multispecies sequence data available (*13*). Once the manual selections had been made, the remaining targets were chosen at random by means of an algorithm that ensured that the complete set of targets represented the range of gene content and level of nonexonic conservation (relative to mouse) found in the human genome. The locations and characteristics of the 44 ENCODE target regions (along with additional details about their selection) are available at the UCSC ENCODE Genome Browser (www.genome.ucsc.edu/ENCODE/regions_build34.html).

The ENCODE Consortium

The pilot phase is being undertaken by a group of investigators, the ENCODE Consortium, who are working in a highly collaborative way to implement and evaluate a set of computational and experimental approaches for identifying functional elements. The pilot phase began in September 2003 with the funding of eight projects (table S1) that involve the application of existing technologies to the large-scale identification of a variety of functional elements in the ENCODE targets, specifically genes, promoters, enhancers, repressors/silencers, exons, origins of replication, sites of replication termination, transcription factor binding sites, methylation sites, deoxyribonuclease I (DNase I) hypersensitive sites, chromatin modifications, and multispecies conserved sequences of yet unknown function (Fig. 1). Genetic variation within the conserved sequences is also being determined. The methodological approaches being employed in the pilot phase include transcript and chromatin immunoprecipitation–microarray hybridization (ChIP-chip; see below) analyses with different microarray platforms, computational methods for finding genes and for identifying highly conserved sequences, and expression reporter assays.

In addition to the initial eight, other groups have since joined the ENCODE Consortium. These include groups doing comparative sequencing specifically for ENCODE, groups coordinating databases for sequence-related and other types of ENCODE data, and groups conducting studies on specific sequence elements (table S1). Beyond these current

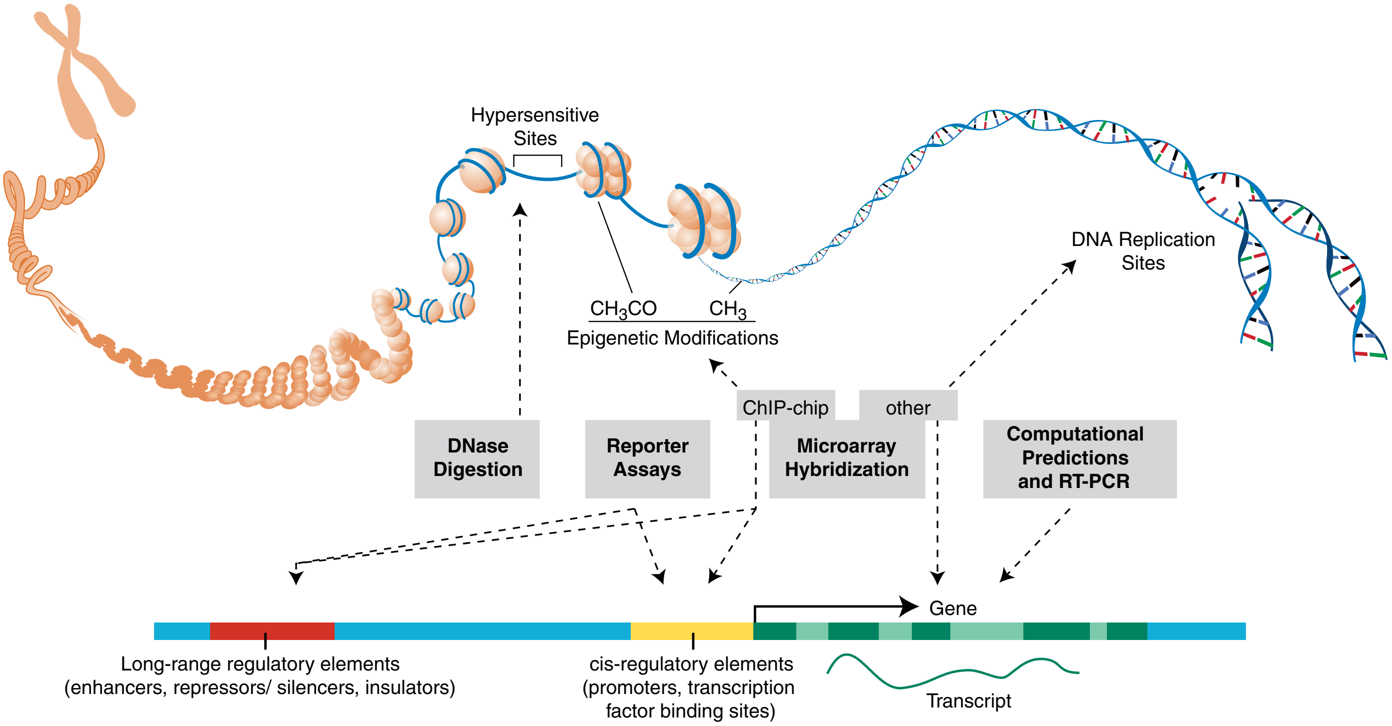

Fig. 1. Functional genomic elements being identified by the ENCODE pilot phase. The indicated methods are being used to identify different types of functional elements in the human genome.

participants, the ENCODE Consortium is open to all interested academic, government, and private-sector investigators, as long as they abide by established Consortium guidelines (www.genome.gov/10006162), which require the commitment to work on the entire set of ENCODE targets, to participate in all Consortium activities, to make a significant intellectual contribution, and to release data in accordance with the policies specifically established for the project (see below).

The parallel technology development phase (table S2) is intended to expand the ''tool box'' available for high-throughput identification of functional genomic elements, and includes projects to develop new methods both for more efficient identification of known elements and for identification of heretofore unknown elements.

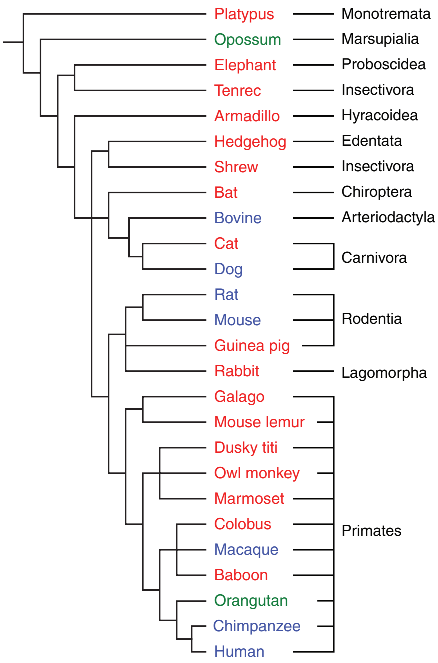

Fig. 2. Mammals for which genomic sequence is being generated for regions orthologous to the ENCODE targets. Genomic sequences of the ENCODE targets are being generated for the indicated mammalian species. The current plans are to produce high-quality finished (blue), comparative-grade finished (red), or assembled whole-genome shotgun (green) sequence, as indicated. High-quality finished reflects highly accurate and contiguous sequence, with a best-faith effort used to resolve all difficult regions (*26*). Comparative-grade finished reflects sequence with greater than eightfold coverage that has been subjected to additional manual refinement to ensure accurate order and orientation of all sequence contigs (*16*). In the case of whole-genome shotgun sequence, the actual coverage and quality may vary. Other vertebrate species for which sequences orthologous to the ENCODE targets are being generated include chicken, frog, and zebrafish (not shown). A complete list of the ENCODE comparative sequencing efforts is provided in table S3.

Research Plans

Each group is using one or more high-throughput approaches to detect a specific genomic element(s). In some cases, multiple platforms are being evaluated in comparable experiments. For example, several types of microarrays [e.g., oligonucleotide arrays made by different technologies, polymerase chain reaction (PCR)–amplicon arrays] are being used to identify transcribed regions. The pilot project participants are primarily using a restricted number of cell lines to identify functional elements. This approach is being taken for practical purposes, but it has the limitation that not all cell types will be surveyed, and therefore some elements with tissue-restricted function may not be identified in the pilot phase. To facilitate comparison of data generated on different platforms and by different approaches, a common set of reagents is being included whenever appropriate. So far, the common reagents chosen include two cell lines (HeLa S3, a cervical adenocarcinoma, and GM06990, an Epstein-Barr virus–transformed B-lymphocyte) and two antibodies [one for the general transcription factor $\text{TAF}_{\text{II}}250$ (*14*) and another for the inducible transcription factor STAT-1 (*15*)].

The ENCODE pilot phase also includes a component that is generating sequences of the genomic regions that are orthologous to the ENCODE target regions from a large set of nonhuman vertebrates (www.nisc.nih.gov/open_page.html?/projects/encode/index.cgi) (*16*). This will allow ENCODE to identify the quality and amount of comparative sequence data necessary to accurately identify evolutionarily conserved elements, and to develop more powerful computational tools for using comparative sequence data to infer biological function. An initial set of 10 vertebrates have been selected for targeted sequencing on the basis of multiple factors, including phylogenetic position (Fig. 2 and table S3) and the availability of a bacterial artificial chromosome (BAC) library. In addition to this ENCODE-specific effort, comparative sequence data are also being captured from ongoing whole-genome sequencing projects, including those for mouse, rat, dog, chicken, cow, chimpanzee, macaque, frog, and zebrafish. A unique RefSeq accession number (*17*) is being assigned for the sequence of each ENCODE-orthologous target region in each species, with periodic data freezes.

A feature of the evolutionarily conserved elements to be assayed is sequence variation. This will be accomplished by resequencing PCR-amplified fragments from genomic DNA of 48 individuals, the same samples being used by the HapMap Consortium to determine common patterns of genetic variation (*18*). This will result in a quantitative view of the evolutionary constraints on conserved regions.

Data Management and Analysis

Capturing, storing, integrating, and displaying the diverse data generated will be challenging. Data that can be directly linked to genomic sequence will be managed at the UCSC Genome Browser (www.genome.ucsc.edu/ENCODE) (*19*). Other data types will be stored either at available public databases [e.g., the GEO (Gene Expression Omnibus) (www.ncbi.nlm.nih.gov/geo) and ArrayExpress (www.ebi.ac.uk/arrayexpress) sites for microarray data] or on publicly accessible Web sites specifically developed by ENCODE Consortium participants. An ENCODE portal will also be established to index these data, allowing users to query different data types regardless of location. Access to metadata associated with each experiment will be provided. The ENCODE pilot phase will make use of the MAGE standard for representing microarray data (*20*), and data standards for other data types will be developed as needed.

Figure 3 uses the early pilot-phase data for one of the ENCODE target regions (ENr231) to illustrate how the ENCODE data will be presented in a way that will capture the innovation of the ENCODE Project's goal of developing a full representation of functional genomic elements. The results of the different analyses are presented as parallel tracks aligned with the genomic sequence. For example, the gene structures for known genes are shown; future ENCODE data will include the precise locations of 5′ transcription start sites, intron/exon boundaries, and 3′ polyadenylation sites for each gene in the ENCODE targets. In addition, efforts will be made to confirm all gene predictions in these regions. Positions of the evolutionarily conserved regions, as detected by analyzing sequences from several organisms, are shown and can be correlated with results of other studies. This presentation will allow a comprehensive depiction of the results from all of the ENCODE components, enabling both comparisons of different methods and of the reproducibility of the data from different laboratories. The former is illustrated by comparison of two different methods for localizing promoter regions, one based on reporter constructs containing sequences around putative transcription initiation sites (*21*) and the other involving chromatin immunoprecipitation (ChIP) with an antibody to RNA polymerase (RNAP) and hybridization to DNA microarrays (chip) (*22*) (so-called ChIP-chip) to identify sequences bound by components of the transcriptional machinery. Reproducibility is illustrated by the comparison of

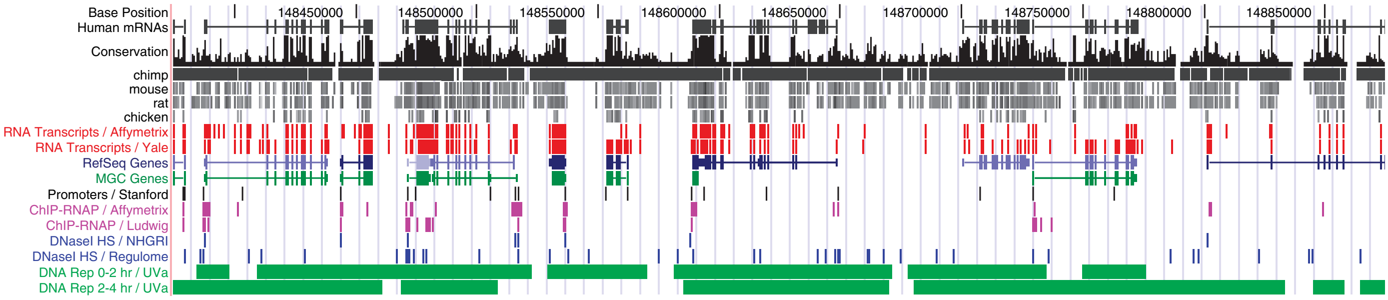

Fig. 3. UCSC Genome Browser display of representative ENCODE data. The genomic coordinates for ENCODE target ENr231 on chromosome 1 are indicated along the top. The different tracks are labeled at the left with the source of the data. The Conservation track shows a measure of evolutionary conservation based on a phylogenetic hidden Markov model (phylo-HMM) (*27*). Multiz (*28*) alignments of the human, chimpanzee, mouse, rat, and chicken assemblies were used to generate the species tracks. RefSeq Genes, MGC Genes indicate the mapping of mRNA transcripts from RefSeq (*17*) and MGC (*24*) projects, respectively, whereas the track labeled Human mRNAs represents all mRNAs in GenBank. Other tracks represent verified data from the ENCODE Consortium (*23*). The track with the location of sequences tested for promoter activity in a reporter assay is labeled as Promoters/Stanford. The positions of transcripts identified by oligonucleotide microarray hybridization (RNA Transcripts/Affymetrix and RNA Transcripts/Yale) and sequences detected by ChIP/chip analysis (ChIP-RNAP/Ludwig and ChIP-RNAP/Affymetrix) are indicated. The DNA replication tracks show segments that are detected to replicate during specified intervals of S phase in synchronized HeLa cells. The 0-2 hours and 2-4 hours tracks show segments that replicate during the first and second 2 hours periods of S phase. The DNA fragments released by DNase I cleavage were identified either from $CD4^+$ cells (DNaseI HS/NHGRI) or from K562 cells (DNaseI HS/Regulome).

studies conducted by two laboratories within the ENCODE Consortium, which analyzed different biological starting materials using the ChIP-chip approach and found an 83% concordance in the identified RNAP-binding sites in the region (*23*). Representation of the ENCODE data in this manner will afford a synthetic and integrative view of the functional structure of each of the target regions and, ultimately, the entire human genome.

Each research group will analyze and publish its own data to evaluate the experimental methods it is using and to elucidate new information about the biological function of the identified sequence elements. In addition, the Consortium will organize, analyze, and publish on all ENCODE data available on specific subjects, such as multiple sequence alignments, gene models, and comparison of different technological platforms to identify specific functional elements. At the conclusion of the pilot phase, the ENCODE Consortium expects to compare different methods used by the Consortium members and to recommend a set of methods to use for expanding this project into a full production phase on the entire genome.

Data Release and Accessibility

The National Human Genome Research Institute (NHGRI) has identified ENCODE as a ''community resource project'' as defined at an international meeting held in Fort Lauderdale in January 2003 (www.wellcome.ac.uk/doc_WTD003208.html). Accordingly, the ENCODE data-release policy (www.genome.gov/ENCODE) stipulates that data, once verified, will be deposited into public databases and made available for all to use without restriction.

Two concepts associated with this data-release policy deserve additional discussion. First, ''data verification'' refers to the assessment of the reproducibility of an experiment; ENCODE data will be released once they have been experimentally shown to be reliable. Because different types of experimental data will require different means of demonstrating such reliability, the Consortium will identify a minimal verification standard necessary for public release of each data type. These standards will be posted on the ENCODE Web site. Subsequently, ENCODE pilot-phase participants will use other experimental approaches to ''validate'' the initial experimental conclusion. This enriched information will also be deposited in the public databases.

Second, the report of the Fort Lauderdale meeting recognized that deposition in a public database is not equivalent to publication in a peer-reviewed journal. Thus, the NHGRI and ENCODE participants respectfully request that, until ENCODE data are published, users adhere to normal scientific etiquette for the use of unpublished data. Specifically, data users are requested to cite the source of the data (referencing this paper) and to acknowledge the ENCODE Consortium as the data producers. Data users are also asked to voluntarily recognize the interests of the ENCODE Consortium and its members to publish initial reports on the generation and analyses of their data as previously described. Along with these publications, the complete annotations of the functional elements in the initial ENCODE targets will be made available at both the UCSC ENCODE Genome Browser and the ENSEMBL Browser (www.ensembl.org).

Conclusion

ENCODE will play a critical role in the next phase of genomic research by defining the best path forward for the identification of functional elements in the human genome. By the conclusion of the pilot phase, the 44 ENCODE targets will inevitably be the most well-characterized regions in the human genome and will likely be the basis of many future genome studies. For example, other large genomics efforts, such as the Mammalian Gene Collection (MGC) program (*24*) and the International HapMap Project (*25*), are already coordinating their efforts to ensure effective synergy with ENCODE activities. Although the identification of all functional genomic elements remains the goal of the ENCODE project, attaining such comprehensiveness will be challenging, especially in the short term. For example, not all types of elements, such as centromeres, telomeres, and other yet-to-be defined elements, will be surveyed in the pilot project. Nonetheless, this project will bring together scientists with diverse interests and expertise, who are now focused on assembling the functional catalog of the human genome.

References and Notes

1. International Human Genome Sequencing Consortium, *Nature* **409**, 860 (2001).
2. J. C. Venter *et al.*, *Science* **291**, 1304 (2001).
3. International Human Genome Sequencing Consortium, *Nature*, in press.
4. Y. Okazaki *et al.*, *Nature* **420**, 563 (2002).
5. T. Ota *et al.*, *Nat. Genet.* **36**, 40 (2004).
6. J. L. Rinn *et al.*, *Genes Dev.* **17**, 529 (2003).
7. P. Kapranov, V. I. Sementchenko, T. R. Gingeras, *Brief Funct. Genomic Proteomic* **2**, 47 (2003).
8. International Rat Sequencing Consortium, *Nature* **428**, 493 (2004).
9. International Mouse Sequencing Consortium, *Nature* **420**, 520 (2002).
10. D. Boffelli, M. A. Nobrega, E. M. Rubin, *Nat. Rev. Genet.* **5**, 456 (2004).
11. T. Imanishi *et al.*, *PLoS Biol.* **2**, 856 (2004).
12. T. Evans, G. Felsenfeld, M. Reitman, *Annu. Rev. Cell Biol.* **6**, 95 (1990).
13. J. W. Thomas *et al.*, *Nature* **424**, 788 (2003).
14. S. Ruppert, E. H. Wang, R. Tjian, *Nature* **362**, 175 (1993).

15. K. Shuai, C. Schindler, V. R. Prezioso, J. E. Darnell Jr., *Science* **258**, 1808 (1992).
16. R. W. Blakesley *et al.*, *Genome Res.* **14**, 2235 (2004).
17. K. D. Pruitt, T. Tatusova, D. R. Maglott, *Nucleic Acids Res.* **31**, 34 (2003).
18. International HapMap Consortium, *Nat. Rev. Genet.* **5**, 467 (2004).
19. W. J. Kent *et al.*, *Genome Res.* **12**, 996 (2002).
20. P. T. Spellman *et al.*, *Genome Biol* **3**, RESEARCH0046 (2002).
21. N. D. Trinklein *et al.*, *Genome Res.* **14**, 62 (2004).
22. B. Ren, B. D. Dynlacht, *Methods Enzymol.* **376**, 304 (2004).
23. ENCODE Consortium, unpublished data.
24. Mammalian Gene Collection (MGC) Project Team, *Genome Res.***14**, 2121 (2004).
25. International HapMap Consortium, *Nature* **426**, 789 (2003).
26. A. Felsenfeld, J. Peterson, J. Schloss, M. Guyer, *Genome Res.* **9**, 1 (1999).
27. A. Siepel, D. Haussler, in *Statistical Methods in Molecular Evolution*, R. Nielsen, Ed. (Springer, New York, in press).
28. M. Blanchette *et al.*, *Genome Res.* **14**, 708 (2004).
29. The Consortium thanks the ENCODE Scientific Advisory Panel for their helpful advice on the project: G. Weinstock, G. Churchill, M. Eisen, S. Elgin, S. Elledge, J. Rine, and M. Vidal. We thank D. Leja, and M. Cichanowski for their work in creating figures for this paper. Supported by the National Human Genome Research Institute, the National Library of Medicine, the Wellcome Trust, and the Howard Hughes Medical Institute.

Supporting Online Material
www.sciencemag.org/cgi/content/full/306/5696/636/DC2
Tables S1 to S3

VIEWPOINT

Systems Biology and New Technologies Enable Predictive and Preventative Medicine

Leroy Hood,[1]* James R. Heath,[2,3] Michael E. Phelps,[3] Biaoyang Lin[1]

Systems approaches to disease are grounded in the idea that disease-perturbed protein and gene regulatory networks differ from their normal counterparts; we have been pursuing the possibility that these differences may be reflected by multiparameter measurements of the blood. Such concepts are transforming current diagnostic and therapeutic approaches to medicine and, together with new technologies, will enable a predictive and preventive medicine that will lead to personalized medicine.

Biological information is divided into the digital information of the genome and the environmental cues that arise outside the genome. Integration of these types of information leads to the dynamic execution of instructions associated with the development of organisms and their physiological responses to their environments. The digital information of the genome is ultimately completely knowable, implying that biology is unique among the sciences, in that biologists start their quest for understanding systems with a knowable core of information. Systems biology is a scientific discipline that endeavors to quantify all of the molecular elements of a biological system to assess their interactions and to integrate that information into graphical network models (*1–4*) that serve as predictive hypotheses to explain emergent behaviors.

The genome encodes two major types of information: (i) genes whose proteins execute the functions of life and (ii) cis control elements. Proteins may function alone, in complexes, or in networks that arise from protein interactions or from proteins that are interconnected functionally through small molecules (such as signal transduction or metabolic networks). The cis control elements, together with transcription factors, regulate the levels of expression of individual genes. They also form the linkages and architectures of the gene regulatory networks that integrate dynamically changing inputs from signal transduction pathways and provide dynamically changing outputs to the batteries of genes mediating physiological and developmental responses (*5*, *6*). The hypothesis that is beginning to revolutionize medicine is that disease may perturb the normal network structures of a system through genetic perturbations and/or by pathological environmental cues, such as infectious agents or chemical carcinogens.

Systems Approaches to Model Systems and Implications for Disease

A model of a metabolic process (galactose utilization) in yeast was developed from existing literature data to formulate a network hypothesis that was tested and refined through a series of genetic knockouts and environmental perturbations (*7*). Messenger RNA (mRNA) concentrations were monitored for all 6000 genes in the genome, and these data were integrated with protein/protein and protein/DNA interaction data from the literature by a graphical network program (Fig. 1).

The model provided new insights into the control of a metabolic process and its interactions with other cellular processes. It also suggested several concepts for systems approaches to human disease. Each genetic knockout strain had a distinct pattern of perturbed gene expression, with hundreds of mRNAs changing per knockout. About 15% of the perturbed mRNAs potentially encoded secreted proteins (*8*). If gene expression in diseased tissues also reveals patterns characteristic of pathologic, genetic, or environmental changes that are, in turn, reflected in the pattern of secreted proteins in the blood, then perhaps blood could serve as a diagnostic window for disease analysis. Furthermore, protein and gene regulatory networks dynamically changed upon exposure of yeast to an environmental perturbation (*9*). The dynamic progression of disease should similarly be reflected in temporal change(s) from the normal state to the various stages of disease-perturbed networks.

Systems Approaches to Prostate Cancer

Cancer arises from multiple spontaneous and/or inherited mutations functioning in networks that control central cellular events (*10–12*). It is becoming clear from our research that the evolving states of prostate cancer are reflected in dynamically changing expression patterns of the genes and proteins within the diseased cells.

A first step toward constructing a systems biology network model is to build a comprehensive expressed-mRNA database on the cell type of interest. We have used a technology called multiple parallel signature sequencing (MPSS) (*13*) to sequence a complementary DNA (cDNA) library at a rate of a million sequences in a single run and to detect mRNA transcripts down to one or a few copies per cell. A database containing more than 20 million mRNA signatures was constructed for normal prostate tissues and an androgen-sensitive prostate cancer cell line, LNCaP, in four states: androgen-starved,

---

[1]Institute for Systems Biology, Seattle, WA, USA. [2]Department of Chemistry, California Institute of Technology, Pasadena, CA, USA. [3]Department of Molecular and Medical Pharmacology, The David Geffen School of Medicine at the University of California Los Angeles, Los Angeles, CA, USA.

*To whom correspondence should be addressed. E-mail: lhood@systemsbiology.org

androgen-stimulated, normal conditions, and an androgen-insensitive variant. In comparing the androgen-sensitive (typical of early-stage cancer) and androgen-insensitive (typical of late-stage cancer) stages (*14*, *15*), thousands of changes in mRNA expression were identified but, out of 554 expressed transcription factors, 112 changed between the early- and late-stage cell lines (80% of which were missed when cDNA arrays were used), and a similar number changed between the cancerous cells and normal tissue. By comparing the prostate database with a tissue-wide database of 58 million MPSS signatures from 29 normal tissues from Lynx Therapeutics, about 300 prostate-specific genes (Fig. 2) were identified, approximately 60 of which possessed signal peptides, suggesting that they may be secreted (*8*). Antibodies to one of these proteins recognized, by blood analyses, 5 out of 10 early and 5 out of 10 late prostate cancers (*16*). In contrast, the standard prostate cancer blood marker, PSA, recognized no early cancers but many of the late prostate cancers, including all of those missed by our marker. Thus, two markers are better than one, and by extension a panel of multiple markers might recognize most early and late prostate cancers.

Several groups have documented the fact that (unidentified) molecules in blood serum, detected by mass spectrometry, reflect various stages of cancer (*17–20*). Aebersold's group has succeeded in identifying many of these biomarkers through the use of a glycoprotein capture method, coupled with isotopic labeling and analyses by mass spectrometry (*21*, *22*). Molecular diagnostics will increasingly play a key role in providing direct measures of disease biology for selecting and following therapeutic responses.

Given enough measurements, one can presumably identify distinct patterns for each of the distinct types of a particular cancer, the various stages in the progression of each disease type, the partition of the disease into categories defined by critical therapeutic targets, and the measurement of how drugs alter the disease patterns. The fascinating question is how many parameters need to be measured in order to stratify and follow the progression of various prostate cancers, or to stratify and follow the progression of the most frequent 20 or 30 cancers, or eventually the most common diseases. Finally, changes in the tissue-specific markers might identify critical points within the network. It is the key nodal points within these perturbed networks that may be affected by drugs, either to convert the diseased network back toward normalcy or to permit the specific killing of the diseased cells. Thus, multiparameter blood measurements will not only be invaluable for diagnostics but also for rationalizing the discovery of appropriate drug targets. In this scenario, molecular diagnostics will become an invaluable tool for molecular therapeutics.

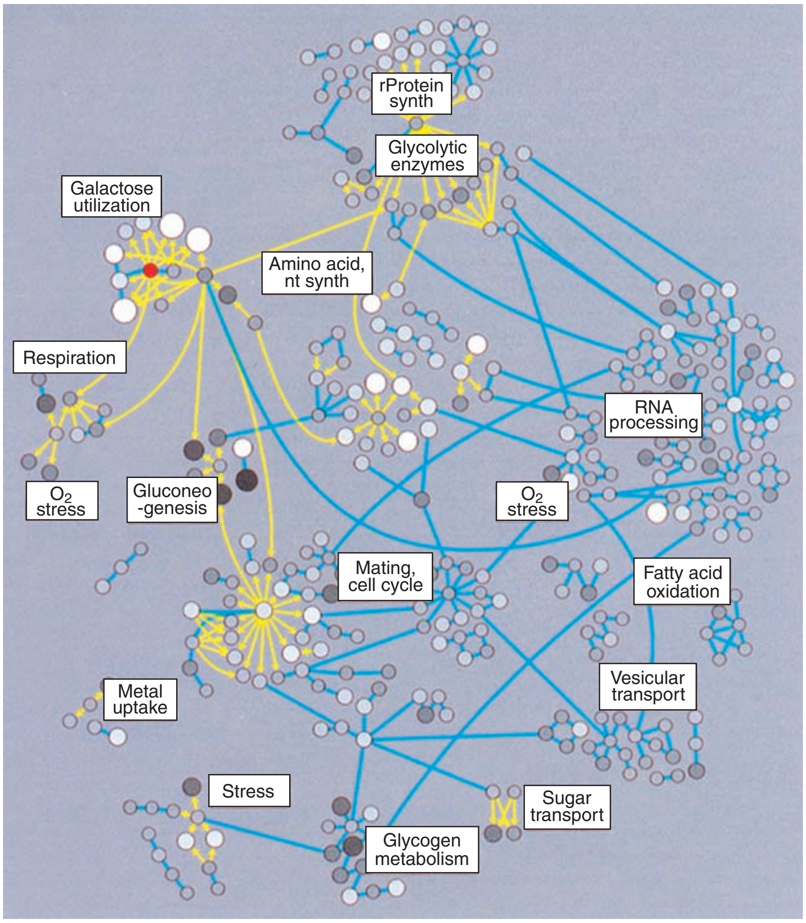

Fig. 1. A network perturbation model of galactose utilization in yeast. This model reflects the integration of mRNA levels for the 6000 yeast genes in each of 20 different genetic and environmental perturbations, as well as thousands of protein/protein and protein/DNA interactions from the literature. The software program Cytoscape (*54*) integrated these data into a network where the nodes represent proteins (encoded by genes) and the lines represent interactions (blue straight lines, protein/protein interactions; yellow lines with arrows, protein/DNA interactions). A gray scale represents the levels of mRNA, with black being abundant levels and white very low levels. The red node indicates that this network model reflects the knockout of the corresponding gene (and protein) *gal 4*—a key transcription factor. rProtein, ribosomal protein; nt, nucleotide; synth, synthesis.

Toward Analyses of Single Cells and Single Molecules

The systems biology approach toward constructing a predictive network model of a metabolic process in yeast required ~10^5 measurements. For the prostate cancer example, roughly 10^8 measurements were sufficient to begin constructing a large set of cancer markers that could be correlated back to the digital code of the genome. However, for constructing a predictive model of human disease, methods that can address the heterogeneity that characterizes biology—from the differences in how individual cells respond to environmental perturbations, to the diversity of cell types and environments within real tissues—will be critical.

In the prostate, there are neuroepithelial cells, various stromal cells, endothelial cells, and epithelial cells (from which 95% of cancers arise), each of which exhibits a continuous developmental cycle. One cannot reliably generate information for networks from mixed populations of cells. Various investigators have used cell sorting (*23*), manual dissection (*24*), or laser capture microdissection (LCM) (*25*) to obtain relatively homogeneous populations of cells. However, cell sorting and LCM themselves may cause processing-induced changes in gene expression (*26*, *27*), and manual microdissection rarely provides completely homogeneous cell types. Furthermore, even cells of one type typically represent different stages of a developmental or physiological process. Biologists would like to analyze individual cells for the key measurements of systems biology, so that network hypotheses could be generated from individual cells. The mRNAs from single cells have been analyzed after polymerase

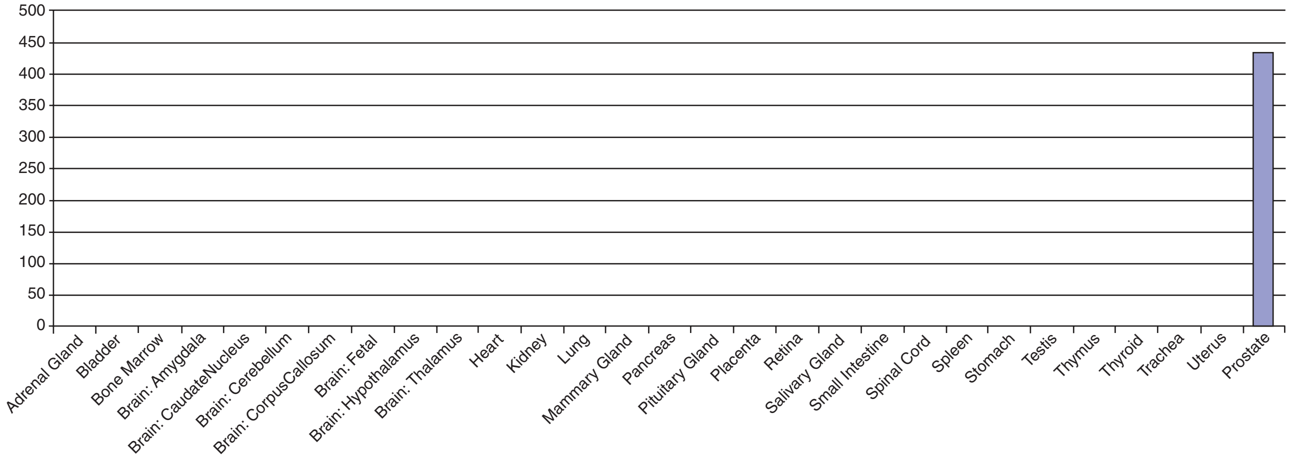

Fig. 2. A prostate-specific marker identified through quantitative profiling of all mRNAs across all 29 major organs in the human body. The gene *HOXB13* is expressed at 432 transcripts per million in the prostate tissue but is not expressed in the other 28 normal tissues. This method has been used to identify approximately 50 potential serum-based protein biomarkers for prostate cancer.

chain reaction (PCR) amplification, but there is no similar amplification technique for proteins. Thus, techniques are needed that are highly parallel, allow for multiple types of measurements (genes and proteins) and operations (such as cell sorting) to be integrated, are miniaturized (to analyze single cells and single molecules), and are automated. Here we highlight just a few of the technologies that are being driven by the needs of systems biology.

Microfluidics has existed as a useful biotechnology for some time (*28–30*). However, multilayer elastomer microfluidics (Fig. 3) is a powerful new technology that allows for the integration of many pumps, valves, and channels within an easily fabricated microchip. This means that multiple operations, such as cell sorting (*31*, *32*), DNA purification, and single-cell gene expression profiling (*33*), can be executed in parallel. This technology provides a bridge between biological materials and systems biology through large-scale multiparameter analysis, with applications ranging from molecular dissections of single cells (for example, from needle biopsies) and very small cell populations to multiparameter disease diagnostics from cells and blood.

Nanomechanical (*34*) and nanoelectronic (*35*, *36*) devices are emerging as highly sensitive, label-free, and real-time detectors of genes, mRNAs, and proteins. To date, demonstrations of these nanotechnologies have been at the single- or few-device level, but the reported detection sensitivities and dynamic ranges (*37*, *38*) have been spectacular. Nanofabrication methods for constructing large libraries of these devices (*39–43*) and integrating nanotechnologies with elastomer microfluidics (*44*) are moving forward. It is likely that within the next couple of years, miniaturized and automated microfluidics/nanotech platforms that integrate operations such as cell sorting and serum purification with measurements of 5 to 10 biomarkers from single cells or very small fluid volumes will emerge. New measurement types, such as quantifying the forces associated with protein/protein, protein/DNA, and protein/drug interactions, are possible. Other emerging nanotechnologies include tools for the

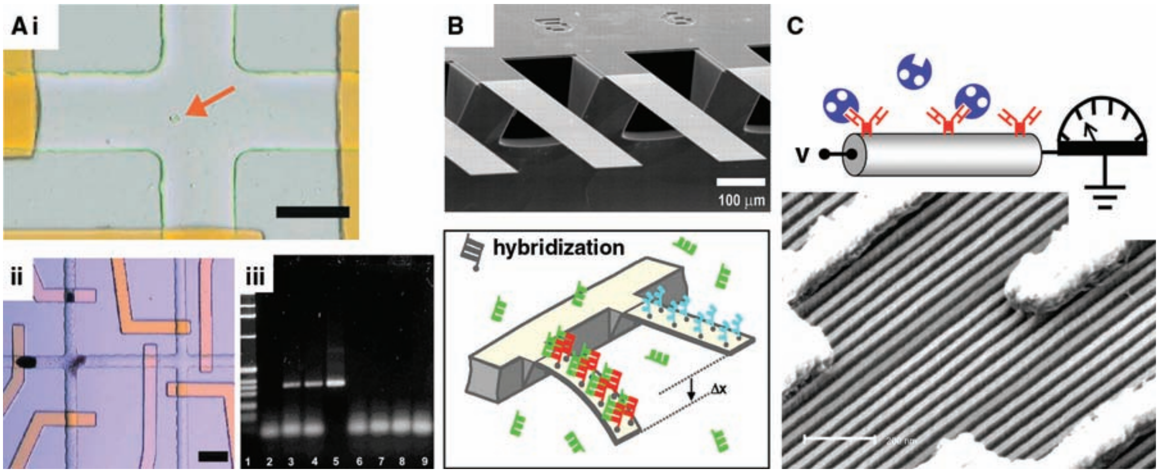

Fig. 3. Microfluidic and nanotechnology platforms. (**A**) An integrated microfluidics environment for single-cell gene expression studies. A single cell is introduced (**i**) into a 100-µm-wide channel. Before the cell is introduced, an affinity column (beads covered with oligo dT) is loaded [dark regions in (**ii**)]. The orange-colored regions in (ii) are valves that separate, for example, the empty chamber at the right from the region in which the column is being constructed. Three such valves constitute a peristaltic pump (not shown). Data from a real-time PCR analysis of the isolated mRNA (**iii**) illustrate the power of this integrated microfluidics approach. Lanes 3 and 4 correspond to one and nine cells, respectively, whereas the other lanes correspond to various controls [adapted from (*33*)]. (**B**) Array of nanomechanical biomolecular sensors. The cantilevers are fabricated to be only a few nanometers thick, with a molecular probe (such as single-stranded DNA) bonded to their top surface. DNA hybridization leads to steric crowding that forces the cantilever to bend. The bending can be detected optically or electronically [adapted from (*34*)]. (**C**) An electron micrograph showing a library of 16-nm-wide silicon nanowire biomolecular sensors. The scale bar is 200 nm, and the structures on top of the nanowires are electrical contacts. Nanowire sensors operate by binding molecular probes (such as antibodies) to the surface of a semiconducting nanowire. When the target protein binds to the probe, the conductivity properties of the nanowire are altered, and so the binding event is electronically detected. Both nanocantilevers and nanowires are capable of real-time biomolecular detection [adapted from (*55*)].

rapid sequence analysis of individual DNA molecules (*45*) and even nanoparticle-based in vivo cancer imaging probes (*46*).

These various technologies will be harnessed to generate preliminary network hypotheses for analyzing human diseases within the next few years. Those hypotheses must ultimately be tested in vivo. Such testing typically means molecular imaging, which encompasses methods ranging from bioluminescence and fluorescence (*47–50*) to positron emission tomography (PET) (*49–52*) and magnetic resonance imaging (MRI) (*48*). The challenge is to reduce the large numbers of elements delineated in the network analyses to one of a few targets of molecular imaging biomarkers that can provide critical tests of the network. For example, specific metabolic enzymes that are selectively expressed in prostate cancer cells would constitute such a target. We searched the genes that were differentially expressed between early- and late-stage prostate cancer cell lines (*15*) and determined that L-lactate dehydrogenase A, which catalyzes the formation of pyruvate from (S)-lactase, was only expressed, and at a high level, in the late-stage cancer cells. A specific PET tracer based on this reaction would serve to validate this finding and might also allow the identification of prostate cancer metastases. Molecular imaging is already being aligned with molecular therapeutics in the use of labeled drug candidates to provide direct measurements in patients by imaging pharmacokinetics of the drug throughout the body, titration of drugs to their disease targets, and measuring therapeutic effects on the biological processes of disease (*49–53*).

The Future

The medicine of today is reactive, with a focus on developing therapies for preexisting diseases, typically late in their progression. Over the next 10 to 20 years, medicine will move toward predictive and preventive modes. New technologies will allow individuals to have the relevant portions of their genomes sequenced, and multiparameter informative molecular diagnostics via blood analysis will become a routine procedure for assessing health and disease status. During this period, there will also be extensive correlations of genetic variations with disease, and this combination of advances will allow for the determination of a probabilistic future health history for each individual.

Preventive medicine will follow as disease-perturbed networks can be used to identify drug targets—first for therapy and later for prevention. Pharmacological intervention will focus on preventing disease-mediated transitions, as well as reversing or terminating those that have occurred. This will require building a fundamental understanding of the systems biology that underlies normal biological and pathological processes, and the development of new technologies that will be required to achieve this goal.

Predictive and preventative medicine will lead naturally to a personalized medicine that will revolutionize health care. Drug companies will have the opportunity for more effective means of drug discovery guided by molecular diagnostics, although the paradigm will shift to partitioning patients with a particular disease into a series of therapeutic windows, each with smaller patient populations but higher therapeutic effectiveness. Health care providers will move from dealing with disease to also promoting wellness (prevention). Finally, the public must be educated as to their roles in a very different type of medicine, as must the physicians who practice it. There will be enormous scientific and engineering challenges to achieve this vision—far greater than those associated with the Human Genome Project. Predictive, preventive, and personalized medicine will transform science, industry, education, and society in ways that we are only beginning to imagine.

References and Notes

1. E. H. Davidson *et al.*, *Science* **295**, 1669 (2002).
2. E. H. Davidson, D. R. McClay, L. Hood, *Proc. Natl. Acad. Sci. U.S.A.* **100**, 1475 (2003).
3. H. Kitano, *Science* **295**, 1662 (2002).
4. U. Alon, *Science* **301**, 1866 (2003).
5. E. V. Rothenberg, E. H. Davidson, in *Innate Immunity*, R. A. B. Ezekowitz, J. A. Hoffman, Eds. (Humana, Totowa, NJ, 2003), pp. 61–88.
6. D. T. Odom *et al.*, *Science* **303**, 1378 (2004).
7. T. Ideker *et al.*, *Science* **292**, 929 (2001).
8. The prediction of classical secretory proteins was based on the existence of signal peptides and the number and position of transmembrane domains in a protein. The prediction of nonclassical secretory proteins (proteins without an N-terminal signal peptide) was based on the algorithm developed by J. D. Bendtsen *et al*. (http://www.cbs.dtu.dk/services/SecretomeP-1.0/).
9. A. D. Weston, N. S. Baliga, R. Bonneau, L. Hood, *Cold Spring Harbor Symp. Quant. Biol.* **68**, 345 (2003).
10. C. A. Klein, *Cell Cycle* **3**, 29 (2004).
11. P. A. Covitz, *Pharmacogenomics J.* **3**, 257 (2003).
12. D. Hanahan, R. A. Weinberg, *Cell* **100**, 57 (2000).
13. S. Brenner *et al.*, *Nature Biotechnol.* **18**, 630 (2000).
14. B. Lin *et al.*, in preparation.
15. B. Lin *et al.*, in preparation.
16. A. G. Utleg *et al.*, in preparation.
17. E. F. Petricoin 3rd *et al.*, *J. Natl. Cancer Inst.* **94**, 1576 (2002).
18. B. L. Adam *et al.*, *Cancer Res.* **62**, 3609 (2002).
19. E. P. Diamandis, *Clin. Chem.* **49**, 1272 (2003).
20. Y. Qu *et al.*, *Clin. Chem.* **48**, 1835 (2002).
21. H. Zhang, X. J. Li, D. B. Martin, R. Aebersold, *Nature Biotechnol.* **21**, 660 (2003).
22. Using this method, Aebersold's group was able to identify 100 peptides in sera that were strongly associated with cancer status in a mouse model for chemically induced skin cancer.
23. J. G. Church, E. A. Stapleton, B. D. Reilly, *Cytometry* **14**, 271 (1993).
24. L. Whetsell, G. Maw, N. Nadon, D. P. Ringer, F. V. Schaefer, *Oncogene* **7**, 2355 (1992).
25. N. L. Simone, R. F. Bonner, J. W. Gillespie, M. R. Emmert-Buck, L. A. Liotta, *Trends Genet.* **14**, 272 (1998).
26. A. Y. Liu *et al.*, *Proc. Natl. Acad. Sci. U.S.A.* **94**, 10705 (1997).
27. R. A. Craven, R. E. Banks, *Proteomics* **1**, 1200 (2001).
28. A. G. Hadd, D. E. Raymond, J. W. Halliwell, S. C. Jacobson, J. M. Ramsey, *Anal. Chem.* **69**, 3407 (1997).
29. I. Karube, K. Ikebukuro, Y. Murakami, K. Yokoyama, *Ann. N.Y. Acad. Sci.* **750**, 101 (1995).
30. L. C. Waters *et al.*, *Anal. Chem.* **70**, 158 (1998).
31. R. H. Carlson, C. V. Gabel, S. S. Chan, R. H. Austin, J. P. Brody, *Phys. Rev. Lett.* **79**, 2149 (1997).
32. A. Y. Fu, H. P. Chou, C. Spence, F. H. Arnold, S. R. Quake, *Anal. Chem.* **74**, 2451 (2002).
33. J. W. Hong, V. Studer, G. Hang, W. F. Anderson, S. R. Quake, *Nature Biotechnol.* **22**, 435 (2004).
34. J. Fritz *et al.*, *Science* **288**, 316 (2000).
35. Y. Cui, Q. Wei, H. Park, C. M. Lieber, *Science* **293**, 1289 (2001).
36. R. J. Chen *et al.*, *Proc. Natl. Acad. Sci. U.S.A.* **100**, 4984 (2003).
37. G. Wu *et al.*, *Nature Biotechnol.* **19**, 856 (2001).
38. J. Hahm, C. M. Lieber, *Nano Lett.* **4**, 51 (2004).
39. R. McKendry *et al.*, *Proc. Natl. Acad. Sci. U.S.A.* **99**, 9783 (2002).
40. Y. Arntz *et al.*, *Nanotechnology* **14**, 86 (2003).
41. N. A. Melosh *et al.*, *Science* **300**, 112 (2003).
42. Y. Bunimovich *et al.*, *Langmuir*, in press.
43. K. B. Lee, S. J. Park, C. A. Mirkin, J. C. Smith, M. Mrksich, *Science* **295**, 1702 (2002).
44. R. Pantoja *et al.*, *Biosensors and Bioelectronics*, in press; published online 6 May 2004; doi.10.1016/j.bios.2004.02.020 (http://dx.doi.org/10.1016/j.bios.2004.02.020).
45. I. Braslavsky, B. Hebert, E. Kartalov, S. R. Quake, *Proc. Natl. Acad. Sci. U.S.A.* **100**, 3960 (2003).
46. S. A. Wickline, G. M. Lanza, *Circulation* **107**, 1092 (2003).
47. G. Choy *et al.*, *Biotechniques* **35**, 1022 (2003).
48. R. Weissleder, U. Mahmood, *Radiology* **219**, 316 (2001).
49. H. R. Herschman, *Science* **302**, 605 (2003).
50. T. F. Massoud, S. S. Gambhir, *Genes Dev.* **17**, 545 (2003).
51. M. E. Phelps, *Proc. Natl. Acad. Sci. U.S.A.* **97**, 9226 (2000).
52. M. E. Phelps, *PET: Molecular Imaging and Biological Applications* (Springer, New York, 2004).
53. K. Shah, A. Jacobs, X. O. Breakefield, R. Weissleder, *Gene Ther.* **11**, 1175 (2004).
54. P. Shannon *et al.*, *Genome Res.* **13**, 2498 (2003).
55. E. Johnston-Halperin *et al.*, *J. Appl. Phys.*, in press.

56. We thank all the members of the NanoSystems Biology Alliance for their insights, expertise, and encouragement. We acknowledge support from the National Cancer Institute, the Army Research Office, and the Department of Energy.

VIEWPOINT

Gene Order and Dynamic Domains

Steven T. Kosak[1] and Mark Groudine[1,2]*

When considering the daunting complexity of eukaryotic genomes, some comfort can be found in the fact that the human genome may contain only 30,000 to 40,000 genes. Moreover, growing evidence suggests that genomes may be organized in such a way as to take advantage of space. A gene's location in the linear DNA sequence and its position in the three-dimensional nucleus can both be important in its regulation. Contrary to prevailing notions in this postgenomic era, the bacteriophage λ, a paragon of simplicity, may still have a few things to teach us with respect to these facets of nonrandom genomes.

Nearly 40 years have passed since Jacob and Monod received the Nobel Prize for their contributions to elucidating the transcriptional regulation of the bacteriophage λ. The paradigm of gene regulation offered by λ stresses the importance of gene proximity (in the form of operons), gene order, and competitive DNA binding by regulatory factors, largely dictated by their effective concentrations (*1*). These strategies used by the phage during the switch between lysogeny and lysis may seem to have little bearing in this postgenomic age. Yet the basic principles of phage λ regulation appear to be taking shape at the level of the coordinated regulation of transcriptomes—gene networks dedicated to eukaryotic cell fates such as death, division, and differentiation. Emerging evidence indicates that eukaryotic genes may be organized in the form of genomic domains that allow for their coexpression through mechanisms both similar to and different from λ.

Tandem Gene Arrays

Size has always seemed to matter for molecular biologists attempting to understand the coordinated regulation of eukaryotic genes. Given the vast difference in relative length, eukaryotic genomes have long been thought to operate under a set of principles different from lower organisms, such as phage λ. However, analysis of the growing list of sequenced eukaryotic genomes is beginning to yield commonalities in gene regulation regardless of genome size (*2*). Even before the availability of whole genome sequences, experimental evidence suggested that the first principle of λ regulation, gene proximity, plays an important role in the regulation of tandem gene arrays, colinear series of individual genes often formed through duplication events. Tandem gene arrays are common features of eukaryotic genomes, and they are both ubiquitously expressed [e.g., small nuclear RNA, histones, ribosomal DNA (rDNA), major histocompatibility complex (MHC), etc.] and tissue specific [e.g., Hox, immunoglobulin (Ig), T cell receptor (TCR), β-globin, cadherin, olfactory, etc.]. The size of tandem gene arrays varies—for example, the mouse Ig heavy chain (IgH) contains ~3 Mb, whereas β-globin contains ~120 kb (λ itself is 48 kb)—but the prevalence of these loci suggests that proximity in the linear gene order is important in coordinate gene regulation. The actual role that linear proximity plays in transcriptional regulation is still being established. The rDNA arrays may represent one potential mechanism in that a shared linear position facilitates the nucleolar localization of the relevant ribosomal genes (*3*). Additionally, the Ig and β-globin loci, as shown by fluorescence in situ hybridization (FISH), are specifically positioned in the nucleus during cellular differentiation, and their nuclear localization has been correlated with their state of activity (*4*, *5*). The clustering of genes in arrays may therefore allow the simultaneous localization of genes to compartments of the nucleus important in their regulation.

Tandem gene arrays also demonstrate the second principle of λ regulation: the activation of genes according to their linear order in the genome. With phage λ, the position of the *cI* gene (the repressor) to the left of the operator and of the *cro* gene (Cro) to the right are requisite features of the genetic switch that determines the choice between lysogenic and lytic cell fates (*1*). Similarly, the β-globin, Hox, and Ig gene arrays demonstrate a sequential and developmentally regulated activation of genes according to their order. Not unlike phage λ, the sequential activation of these tandem gene arrays may be due to the proximity of the "early" genes to the dominant regulatory element of a given loci. The β-globin locus undergoes sequential activation of globin genes during embryogenesis, with those genes closest to the locus control region (LCR) being up-regulated first (*6*). With the Ig heavy chain locus (IgH), the genes first to undergo germline transcription are those closest to the intronic and 3′ enhancers (*7*). For the Ig and TCR gene arrays, this type of consecutive activation is correlated with the sequential events of V-D-J recombination. The vertebrate Hox gene clusters, however, uniquely illustrate this phenomenon with linear gene order. In addition to the chronological activation of vertebrate Hox genes, the proteins themselves demonstrate a corresponding activity along the anteroposterior axis (*8*). These genes are therefore uniquely linked in their order, activation, and function.

The third property of λ regulation is the competitive binding of operator sequences by either the repressor or Cro (*1*). The cooperative binding of the dimerized repressor protein ensures transcription of the *cI* gene and continuation of the lysogenic cell fate. In the event of external influences (such as irradiation), the effective concentration of the repressor is diminished, allowing for the up-regulation of *cro* and the subsequent activation of λ early genes. Although they have not been elucidated in such regulatory detail, tandem gene arrays also demonstrate sensitivity to both protein availability and concentration, and in some cases are involved in an autoregulatory feedback mechanism like phage λ. For example, the Hox gene clusters encode homeodomain transcription factors critical in decisions of cell fate during metazoan development, and in vertebrates some of these same proteins also contribute to the regulation of the clusters themselves (*8*).

With the β-globin locus, an exchange in heterodimerization partners of a small Maf protein, MafK, leads to the switch from repression of the locus in committed but undifferentiated erythroid cells to activation of transcription in differentiated cells (*9*). Before differentiation, a heterodimer composed of MafK and the repressor Bach1 recruits transcriptional corepressor complexes to the locus, resulting in repression of globin gene expression. Upon induction of erythroid differentiation, an exchange of MafK-binding partners occurs: Bach 1 is replaced by the transcriptional activator p45. This, in turn, leads to displacement of corepressor complexes from the locus and recruitment of coactivators, resulting in globin gene expression. The mechanism behind

---

[1] Division of Basic Sciences, Fred Hutchinson Cancer Research Center, 1100 Fairview Avenue North, Seattle, WA 98109, USA. [2] Department of Radiation Oncology, University of Washington School of Medicine, Seattle, WA 98195, USA.

*To whom correspondence should be addressed. E-mail: markg@fhcrc.org

this exchange involves the relocation of MafK in the nucleus (*10*). Before the induction of differentiation, MafK colocalizes with centromeric heterochromatin, whereas p45 is restricted to euchromatic nuclear compartments. Terminal differentiation is accompanied by the relocation of MafK (and the β-globin locus) to euchromatic regions and formation of the MafK/p45 heterodimer (*10*). Differentiation is also associated with a relative increase in p45 and a decrease in Bach1 (*11*). Thus, similar to phage λ, the availability and concentration of transcription factors play a key role in effecting a switch between repressed and activated states.

Gene Clusters

The availability of genomic sequences has now allowed researchers to determine whether, beyond tandem gene arrays, eukaryotes possess clusters of coexpressed genes that are related in cellular function or fate. That is, do genomes show a level of organization in which genes that are part of a transcriptome are also proximal in the linear genome? Given the examples of tandem gene arrays, it is perhaps not surprising that all eukaryotic genomes examined to date display a tendency for the organization of coexpressed genes, often related in function, to be linearly clustered (*2*). Therefore, as opposed to displaying a homogenous distribution of genes along chromosomes, genomes appear to be specifically organized for gene regulation.

The nonrandom nature of gene distribution along chromosomes is pronounced in vertebrate genomes. By integrating the human genomic sequence with SAGE (serial analysis of gene expression) data for genome-wide mRNA expression patterns from 12 tissue types, a human transcriptome map has been determined (*12*). The linear distribution of expression along chromosomes depicted in this map reveals that the human genome is organized into regions of high and low levels of gene activity. The highly active regions, RIDGEs (regions of increased gene expression), are separated by large regions of low activity, anti-RIDGEs.

RIDGEs and anti-RIDGEs coincide with gene-dense and gene-poor chromosomal domains, respectively. Therefore, gene activity is inherently compartmentalized along the chromosome, which may indicate a higher order genomic structure. A more recent analysis of SAGE data suggests that RIDGEs form because they may be composed of ubiquitously and highly expressed housekeeping genes (*13*). Nonetheless, it is interesting to consider these highly expressed regions in light of the synteny between the genomes of human and mouse. The syntenic blocks of DNA, which constitute ~90% of both genomes, vary in length, but half are ~20 Mb, similar to the size of RIDGEs (*14*). It may be that evolution deals with a currency much larger than a single gene; evolutionary forces may impinge on genomic domains because of the importance of proximity in gene regulation.

Beyond the organization at the level of RIDGEs, genomic approaches have uncovered clusters of coregulated genes encompassing 2 to 30 genes. In the budding yeast *Saccharomyces cerevisiae*, chromosome correlation maps, which plot the expression patterns from various conditions or cell stages along the linear gene order of the chromosomes, reveal that genes from transcriptomes dedicated to cell cycle phases, sporulation, and the pheromone response are found in pairs throughout the genome (*15*). These pairs of genes are often functionally related as well. Similarly, in *Caenorhabditis elegans*, mRNA-tagging and microarray approaches have uncovered clusters of two to five genes that are coregulated in specific cell lineages, including muscle, sperm, oocytes, and the germ line (*16*). An analysis of gene expression in *Drosophila*, using microarray data determined under 80 different experimental conditions, has revealed an organization of coexpressed genes in groups of 10 to 30, covering 20 to 200 kb (*17*). The clustering of genes within the *Drosophila* genome has also been demonstrated by expressed sequence tag (EST) database analyses of tissue-specific expression from the testis, head region, and embryo. In each cell type, coregulated genes are organized into clusters of three or more genes, with a trend toward large groupings (*18*). In humans, several metabolic pathways are also shown to have their protein components encoded in genes that are proximal in the genome (*19*). Therefore, the clustering of coregulated, lineage-restricted genes indicates a functional organization of transcriptomes that define a given cell type.

The regulatory mechanisms that govern the expression of the tandem gene arrays described above offer an attractive model for the tissue-specific coregulation of gene clusters. Like phage λ, the gene arrays use shared regulatory elements and fluctuating regulatory protein concentrations to ensure their proper expression patterns. In large part these tools are successful because of the proximity of the tandem genes. Gene clusters that are involved in the differentiation or maintenance of a cell type may therefore be selected for the same regulatory purposes. In *S. cerevisiae*, for example, several of the tandem genes observed in the chromosome correlation maps share a common upstream activating sequence (*15*). Whether all of the gene clusters identified have a shared enhancer seems unlikely. However, a universal property that proximity bestows is an increased local concentration of the pools of regulatory proteins that coexpressed genes likely have in common. Specifically, because of the number of binding sites for regulatory proteins in colinear genes, gene proximity may ensure an effective concentration of these proteins, creating a localized transcriptional center or ''expression hub'' (*2*). This idea is supported by examples of definitive nuclear subcompartments with increased localized protein concentrations that a given gene cluster may associate with (or, indeed, may help to form) to direct its regulation. The nucleolus represents a paradigm of this phenomenon, being essentially a concentration of proteins that guarantees ribosomal biogenesis as well as regulation of other genes required for protein translation (*3*, *20*).

On the basis of the evidence presented above, it is attractive to consider lineage-specific transcription not as the coregulation of hundreds of disparate genes, but rather as the coordinated regulation of various gene domains. Beyond the examples of tandem gene arrays and gene clusters, genomic approaches have yielded evidence for another feature of domain-based genomes. Analysis of the histone modifications associated with active and inactive genes indicates that related modifications are shared by neighboring genes. For example, in *Drosophila*, a very tight correlation between gene expression and five different euchromatic histone modifications was observed (*21*). The pattern of euchromatic histone modification is ''binary,'' with active genes showing all such marks and inactive genes lacking such marks. These modifications are restricted to the transcribed region, and the degree of the euchromatic histone marks correlates with transcript abundance, suggesting a process of chromatin modification that is intrinsically coupled to transcription. Regardless of the basis of these marks, however, genes with these histone modifications exist in neighborhoods of two to three, similar to coexpressed gene clusters of the same size. A genomic analysis of repressive markers such as heterochromatin protein 1 (HP1) has revealed a similar association with sets of coregulated genes (*22*). Therefore, the organization of the genome into expression hubs enriched (or depleted) in such modifications and chromatin-binding proteins may facilitate the formation of nuclear subcompartments.

Dynamic Domains

The nucleus is a dynamic organelle, embodied in its great Houdini act of mitosis, in which we see the nucleus duplicate its chromosomal content, disappear, and then reappear in two places at once. In parallel, the protein content of the interphase nucleus is in constant flux (*23*). Fluorescence recovery after photobleaching (FRAP) studies have shown that regulatory proteins (such as transcription factors) have rapid diffusion rates, as do structural components of the nucleus. HP1, for example, colocalizes with constitutive heterochromatin and had long been thought to statically associate at these structures during interphase. However, FRAP analysis indicates that most of the HP1 is in fact highly diffusible (*24*).

This dynamic nature of the nucleus seems to belie the presence of nuclear bodies (such as Cajal bodies, interchromatin granule clusters, PML bodies, etc.). But these bodies are themselves dynamic (their integral components are constantly exchanged), and their structure in the nucleus is inseparable from their function: If you disturb the structure of a body you abrogate its function, and vice versa (*2*). Many genes, such as the β-globin and Ig loci, are also localized to specific nuclear compartments according to their state of transcriptional activity. Moreover, recent studies suggest that loci have the ability to mobilize to specific locations within the interphase nucleus (*25*). Although the extent to which loci can sample the nuclear environment appears to differ among organisms, evidence indicates that genes have the capacity to move beyond their segregation during mitosis.

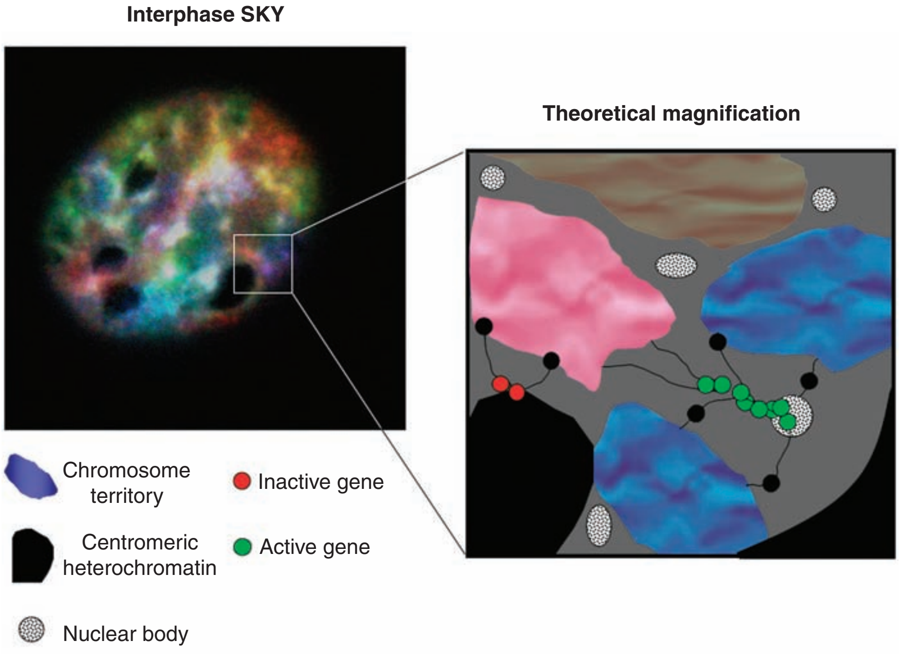

Fig. 1. What is the underlying nuclear organization of gene activity? At left is a spectral karyotype (SKY) image of an interphase nucleus from a hematopoietic progenitor. SKY allows for the simultaneous visualization of all chromosomes and is primarily applied to metaphase chromosomes to detect abnormalities. Growing evidence supports the idea that a nuclear topology exists that ensures the transcriptional program (or transcriptome) that gives rise to or maintains a given cell type. Therefore, the SKY image may represent the appropriate nuclear topology for the progenitor's transcriptome. However, the actual chromosomal organization of an entire genome has yet to be established. Nonetheless, tandem gene arrays and the linear clustering of genes that are coexpressed and dedicated to a particular cell fate argue that spatial proximity is important in coordinate gene regulation. Given the evidence for chromatin mobility and the looping of gene loci from chromosome territories, it is an attractive possibility to consider that coregulated gene clusters from different genomic regions may also be proximal in the nuclear volume, as depicted in the theoretical magnification at right. The regulation of these localized gene clusters may take advantage of protein concentrations (or may be the basis for them), as exemplified by the various types of nuclear bodies found in the nucleus.

During interphase, chromosomes are maintained as discrete structures termed chromosome territories (CTs). The majority of evidence indicates that genes are preferentially positioned at the territory surface, including contours and invaginations, of their respective chromosomes (*2*). Tandem gene arrays that are highly transcribed have been shown to loop away from their territories, as identified with whole-chromosome paints in FISH analysis. Territory looping may indicate an association of the looped gene array with the nuclear bodies that are involved in transcription and are found in the interchromatin compartment that runs among the CTs. The MHC, for example, has recently been shown to localize near PML bodies and is looped from its CT when being transcribed (*26*, *27*). For the vertebrate Hox cluster, territory looping has also been correlated with the sequential activation of particular genes (*28*). Studies of wild-type and mutant β-globin loci have helped to clarify the role of transcriptional activity in territory looping (*29*). In erythroid cells, the β-globin locus is looped away from its CT even before transcriptional induction. However, in the absence of the LCR, which is required for high-level globin gene transcription, the locus is positioned at the CT surface. Furthermore, if the β-globin LCR is replaced by elements from a B cell–specific LCR that represses transcription of reporters in erythroid cells, looping is partially restored but is now correlated with localization of the looped locus to centromeric heterochromatin of another CT. These results indicate that territory looping is not simply a consequence of activity, but may play an important role in cell type–specific transcriptional activation or repression of a locus.

Although the basis for looping of a locus from its chromosome territory has yet to be established, the β-globin locus may offer some general clues. The β-globin LCR contains several binding sites for small Maf proteins, and, as described above, the MafK/p45 heterodimer is essential for relocation and activation of the locus during differentiation. Interestingly, addition of the transactivation domain of p45 is sufficient to relocate MafK from heterochromatic to euchromatic nuclear compartments (*10*). Because the p45 activation domain interacts with coactivator complexes that also bind other erythroid-specific genes, it is tempting to speculate that such complexes comprise expression hubs to which erythroid-specific genes may relocate (via mass action, for example). A similar scenario is possible for repression of the locus by MafK/Bach1-recruited corepressor complexes before erythroid differentiation and in nonerythroid cells. Moreover, the on-off rates of chromatin-associated proteins, including the small Maf heterodimers, are likely influenced by the pattern of histone modifications (*30*).

The observations highlighted above have led many to suggest that nuclear organization may be cell type–specific: The topological organization of the interphase nucleus may be involved in the establishment and propagation of cell-specific patterns of gene expression. Dynamic domains comprising both tandem gene arrays and gene clusters may represent the means by which a nucleus is configured. Given that a transcriptome includes hundreds of genes, it may be expedient for transcriptional regulation to have these domains compartmentalized together within the nucleus. Coregulated gene clusters (including the two alleles of the same cluster) may therefore be proximally positioned to facilitate their regulation through the creation of expression hubs with shared concentrations of regulatory proteins (Fig. 1). The combined effect of the association of domains from throughout the genome would yield a cell-specific nuclear topology, resulting in definable patterns of chromosome organization.

Recent evidence has indicated that the chromosomal organization within a nucleus is maintained upon cell division. FRAP analysis with histone–fluorescent protein fusions has revealed that chromosomes appear to remain in their relative nuclear positions (*31*). It is therefore possible the nucleus of a particular cell type does have its genome specifically organized for the expression of its relevant transcriptome. The spectral karyotype (SKY, which allows the simultaneous detection of all chromosomes) (*32*) of an interphase nucleus in Fig. 1 would therefore represent the topology that ensures the overall regulation of that cell type. Evidence supports the idea that chromosomes have specific positions within the nucleus. For example, gene-dense and gene-poor chromosomes have been shown to preferentially localize to the nuclear center and periphery, respectively (*33*). Additionally, a recent study focusing on a subset of chromosomes has shown that lineage-specific associations of certain chromosomes can occur (*34*). What remains to be established, however, is the organization of an entire genome at the level of the chromosome. Furthermore, whether a given nuclear topology changes upon cell differentiation has yet to be demonstrated.

With the idea of cell-specific nuclear topology, we have clearly moved beyond the realm in which bacteriophage λ can lead by example. The dynamic regulation of hundreds to thousands of genes requires a level of coordination unnecessary for a simple phage. Still, it is important to remember that the functions of the nucleus, such as transcription, are intertwined with its structure. If the principles of eukaryotic gene regulation find basic parallels with a less complicated example, then there is hope that these principles, aided by the merging of technologies such as SKY and 3D microscopy, may allow us to fully appreciate the dynamic organization of a genome within its nucleus.

Note added in proof: A recent study has provided evidence for the colocalization of coregulated genes on the same chromosome (*35*).

References and Notes

1. M. Ptashne, *A Genetic Switch* (Cold Spring Harbor Laboratory Press, Cold Spring Harbor, NY, ed. 3, 2004).
2. S. T. Kosak, M. Groudine, *Genes Dev.* **18**, 1371 (2004).
3. A. K. Leung, A. I. Lamond, *Crit. Rev. Eukaryot. Gene Expr.* **13**, 39 (2003).
4. S. T. Kosak *et al.*, *Science* **296**, 158 (2002).
5. C. Francastel, M. C. Walters, M. Groudine, D. I. Martin, *Cell* **99**, 259 (1999).
6. M. Bulger, M. Groudine, *Genes Dev.* **13**, 2465 (1999).
7. D. Chowdhury, R. Sen, *Immunol. Rev.* **200**, 182 (2004).
8. R. S. Mann, *Bioessays* **19**, 661 (1997).
9. M. Brand *et al.*, *Nature Struct. Mol. Biol.* **11**, 73 (2004).
10. C. Francastel, W. Magis, M. Groudine, *Proc. Natl. Acad. Sci. U.S.A.* **98**, 12120 (2001).
11. M. Brand, M. Groudine, unpublished data.
12. H. Caron *et al.*, *Science* **291**, 1289 (2001).
13. M. J. Lercher, A. O. Urrutia, L. D. Hurst, *Nature Genet.* **31**, 180 (2002).
14. R. H. Waterston *et al.*, *Nature* **420**, 520 (2002).
15. B. A. Cohen, R. D. Mitra, J. D. Hughes, G. M. Church, *Nature Genet.* **26**, 183 (2000).
16. P. J. Roy, J. M. Stuart, J. Lund, S. K. Kim, *Nature* **418**, 975 (2002).
17. P. T. Spellman, G. M. Rubin, *J. Biol.* **1**, 5 (2002).
18. A. M. Boutanaev, A. I. Kalmykova, Y. Y. Shevelyov, D. I. Nurminsky, *Nature* **420**, 666 (2002).
19. L. D. Hurst, C. Pal, M. J. Lercher, *Nature Rev. Genet.* **5**, 299 (2004).
20. M. Thompson, R. A. Haeusler, P. D. Good, D. R. Engelke, *Science* **302**, 1399 (2003).
21. D. Schübeler *et al.*, *Genes Dev.* **18**, 1263 (2004).
22. F. Greil *et al.*, *Genes Dev.* **17**, 2825 (2003).
23. T. Misteli, *Science* **291**, 843 (2001).
24. T. Cheutin *et al.*, *Science* **299**, 721 (2003).
25. A. Belmont, *Curr. Opin. Cell Biol.* **15**, 304 (2003).
26. E. V. Volpi *et al.*, *J. Cell Sci.* **113**, 1565 (2000).
27. J. Wang *et al.*, *J. Cell Biol.* **164**, 515 (2004).
28. S. Chambeyron, W. A. Bickmore, *Genes Dev.* **18**, 1119 (2004).
29. T. Ragoczy, A. Telling, T. Sawado, M. Groudine, S. T. Kosak, *Chromosome Res.* **11**, 513 (2003).
30. G. Felsenfeld, M. Groudine, *Nature* **421**, 448 (2004).
31. D. Gerlich *et al.*, *Cell* **112**, 751 (2003).
32. E. Schröck *et al.*, *Science* **273**, 494 (1996).
33. S. Boyle *et al.*, *Hum. Mol. Genet.* **10**, 211 (2001).
34. L. A. Parada, P. G. McQueen, T. Misteli, *Genome Biol.* **5**, R44 (2004).
35. C. S. Osborne *et al.*, *Nature Genet.* **36**, 1065 (2004).

REVIEW

Cis-Acting Regulatory Variation in the Human Genome

Tomi Pastinen and Thomas J. Hudson*

The systematic screening of the human genome for genetic variants that affect gene regulation should advance our fundamental understanding of phenotypic diversity and lead to the identification of alleles that modify disease risk. There are several challenges in localizing regulatory polymorphisms, including the wide spectrum of cis-acting regulatory mechanisms, the inconsistent effects of regulatory variants in different tissues, and the difficulty in isolating the causal variants that are in linkage disequilibrium with many other variants. We discuss the current state of knowledge and technologies used for mapping and characterizing genetic variation controlling human gene expression.

Expression profiling and genome-wide mapping studies have shown that strong heritable factors govern differences in gene expression levels within mammalian species such as the mouse and human (*1*, *2*). The concentration of a given mRNA allele is controlled both by cis-acting factors (such as DNA polymorphisms and methylation) in the flanking DNA sequence of the gene and trans-acting modulators (such as transcription factors) that are themselves regulated by other genetic and environmental characteristics of the cell. Whereas heritable expression differences resulting from trans-acting mechanisms appear to be quantitatively more important, cis-acting variation may explain up to 25 to 35% of interindividual differences in gene expression. This is likely an underestimate, as physiological feedback mechanisms can mask the impact of subtle cis-acting variants on expression levels. Evidence for the medical importance of cis-acting polymorphisms has been provided by recent positional cloning of susceptibility genes that are not associated with protein coding or splice-site polymorphisms for common diseases such as stroke and type 2 diabetes (*3*, *4*).

Regulatory polymorphisms are DNA elements that modify the expression level of a transcript or its isoforms. Current techniques can detect expression differences as low as 1.2-fold between samples or alleles; the phenotypic consequences (if any) of such small differences are likely to depend on the function of the gene in question. Most known regulatory polymorphisms are located in gene promoter regions and function by altering gene transcription. Coding polymorphisms are also known to affect the

---

McGill University and Genome Quebec Innovation Centre, 740 Drive Penfield Avenue, Montreal, Quebec H3A 1A4, Canada.

*To whom correspondence should be addressed. E-mail: tom.hudson@mcgill.ca

expression of alleles, as in the case of the nonsense-mediated mRNA decay of transcripts harboring early stop codons (*5*). The emerging picture of regulatory sequences distributed over long distances upstream and downstream of a gene, including introns as well as the 5′ and 3′ untranslated regions, has led to the discovery of regulatory variants located outside promoter regions that can alter mRNA stability (*6*), mRNA processing efficiency (*7*), or mRNA isoform expression (*4*, *8*) or induce epigenetic changes (*9*). However, association of allelic expression with heritable regulatory polymorphisms or epigenetic mechanisms may not be straightforward. For example, different mechanisms have been suggested to underlie allelic expression of the human *TP73* gene in noncancerous cells and tissues ranging from heritable polymorphisms (*10*) to tissue-specific monoallelic expression (*11*).

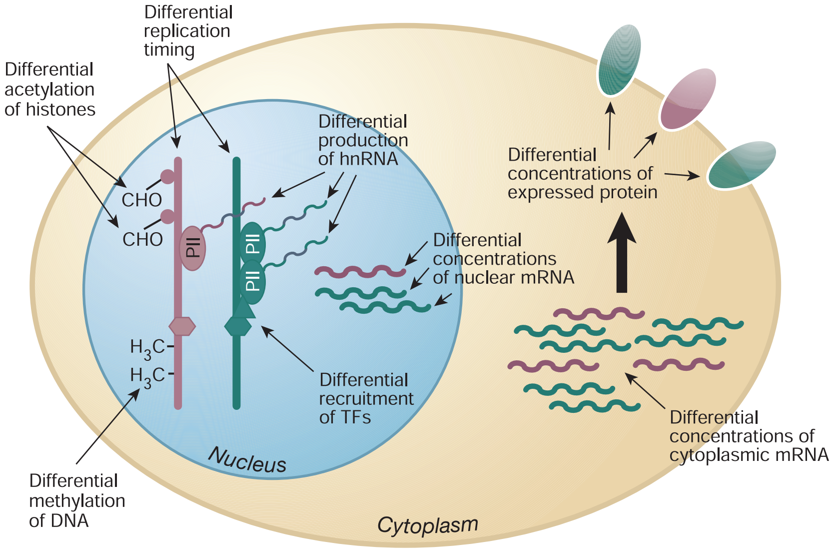

Fig. 1. Cellular phenomena associated with and measured in allele-specific expression studies. PII, RNA polymerase II.

Perils and Pitfalls in the Identification of Cis-Acting Variation

Isolating a true regulatory variant is complicated by linkage disequilibrium (LD) in the human genome. This is highlighted by studies of the lactase (LCT) persistence phenotype, a common monogenic trait caused by cis-acting regulatory variants. Genetic studies in the Finnish population have shown a perfect correlation between LCT persistence and the T allele in a single-nucleotide polymorphism (SNP) approximately 14 kb upstream of the *LCT* gene (*12*). Whereas these findings were supported by in vitro studies showing functional differences between the alleles (*13*), subsequent studies have identified individuals who are heterozygous for the persistence allele but show equal expression of *LCT* alleles (*14*). In addition, the –14-kb SNP is not associated with LCT persistence in some non-Caucasian populations (*15*); this SNP shows very high LD with other variants contained in a 1-Mb flanking region (*16*), suggesting that it may be in LD with the causative regulatory variant.

The modulation of gene expression caused by epigenetic mechanisms can be misconstrued to be due to regulatory polymorphisms. Classically imprinted autosomal loci display preferential expression of a single allele (monoallelic expression) that is independent of sequence variation. This unequal expression of transcripts, which is often transmitted according to the allele's parent of origin, is usually accompanied by different patterns of cytosine methylation or posttranslational histone modifications. This phenomenon has been best studied in mice, in which nearly 50 imprinted genes localized to 15 genomic regions have been characterized (*17*). For some genes, only one allele of a gene is arbitrarily expressed in each cell: This process is called random monoallelic expression and is reminiscent of X-chromosome inactivation in females (*18*). Other naturally occurring epigenetic mechanisms, which do not follow strictly parent-of-origin or random patterns, have also been described in mammals (*19*). Interindividual variability in levels of allele silencing in imprinted genes can be observed in normal controls (*20*), and it has been suggested that diet may influence DNA methylation and allelic expression of epigenetically regulated loci (*21*). Epigenetic alterations are common in neoplastic cells, which may even be detected in peripheral blood samples as demonstrated in colon cancer patients showing increased biallelic expression of insulin-like growth factor 2 (*IGF2*) in comparison to that of healthy controls (*22*).

Detecting Allele-Specific Expression

Allele-specific expression of a transcript can be detected by in vitro and in vivo methods that measure the cumulative effects on a number of cellular processes (Fig. 1).

In vitro approaches. In vitro methods (most commonly involving transient transfection assays) monitor the transcriptional activity of a synthetic reporter construct and are best suited for testing whether a candidate regulatory polymorphism affects gene expression (*23*). Most current studies target putative promoter or upstream flanking regions; these regions are often poorly characterized and frequently do not represent the complete promoter that is active in the cell line of interest. Although experimentally validated promoters can be found in the Eukaryotic Promoter Database (www.epd.isb-sib.ch), these comprise less than 10% of human genes. The initial choice of allele-specific constructs for transfection studies can be refined by deletion experiments to delineate the most important 5′ regulatory sequences. Alternatively, information from long-range regulatory sequences can be studied to use constructs containing proximal promoter regions and enhancer elements (*24*). More faithful reproduction of natural gene regulation can be achieved by cloning whole human genes in bacterial artificial chromosomes (*25*). Such studies are technically challenging and relatively uncommon; most published studies have used relatively small promoter constructs (<1 kb) or oligonucleotide fragments studied in the context of heterotypic minimal promoters.

Transient transfection studies may be complicated by trans-acting influences on allelic expression. Studies are often performed in preexisting animal or human lines, but there are concerns about whether the observed data can be extrapolated to the human tissues of interest. Even small trans-acting differences resulting from other genetic variants in the host may be important, as shown by the quantitative variation of allele-specific responses in fibroblasts obtained from unrelated individuals (*26*).

Transient transfection assays were recently applied in a systematic, stringent survey to study proximal promoter (–0.5 kb) haplotypes from 38 human genes. Significant allele-specific expression could be reproduced in 13 out of 17 (75%) cases when independent clones were used, suggesting that >30% of proximal promoters may harbor cis-acting variants (*27*).

In vivo approaches. In vivo monitoring of allelic RNA transcripts (*28*) is possible in tissues or cells of individuals heterozygous for an informative marker within the locus. There are several advantages to observing relative expression of the two alleles within the same tissue sample: (i) Alleles are expressed in their normal environment including genomic and chromatin context; (ii) comparison of alleles is made within rather than between samples, maximizing the sensitivity of detecting cis-acting effects; (iii) the developmental and physiologic history of the tissue is unlikely to be perturbed by the presence of two low- or two high-expressing alleles; and (iv) population-based studies allow sampling of haplotype diversity within each locus.

The approach has been applied in the context of rare monogenic diseases to demonstrate underexpression of the disease allele (*29*). Similarly, underexpression of the wild-type allele may explain variable penetrance in dominantly inherited Mendelian traits (*30*). Evidence for cis-acting regulatory polymorphisms in candidate genes for complex diseases has also been sought by allelic expression measurements (*8*). Demonstration of parent-of-origin specific expression in tissues (or cells) (*31*) and monoallelic expression in cells (*32*) provide commonly used assays to establish imprinting and random monoallelic expression, respectively.

Direct methods of visualizing allelic expression are challenging, thus measurements are commonly performed with amplified cDNA [reverse transcription polymerase chain reaction (RT-PCR)] from tissues or cell lines of interest and require the presence of an informative polymorphism in the processed transcript. Increased informativity can be achieved with the use of nuclear pre-mRNA [heteronuclear RNA (hnRNA)] (*33*). In our experience, assays performed with hnRNA have slightly higher variability and failure rates as compared with those that use mRNA, likely reflecting the lower concentration of hnRNA in total RNA preparations. Successful hnRNA assays not only increase the informativity of the allelic expression measurements but also provide evidence for transcriptional causes of allelic expression, because RNA processing differences (such as alternate splicing) can be excluded. The role of transcription in causing allele-specific expression can also be determined by the recently introduced polymerase loading assay [haplotype-specific chromatin immunoprecipitation (''HaploChIP'')] (*34*), which is based on isolating transcriptionally active DNA fragments by immunoprecipitation DNA bound to RNA polymerase II enzyme. The isolated DNA fragments can be assessed for polymorphisms in heterozygous samples to determine relative transcriptional activity of the alleles as a surrogate for relative allelic expression.

Allelic expression studies also require quantitative genotyping assays and most commonly primer extension methods have been employed for relative allelic quantitation. Imbalanced allelic expression is detected when the heterozygote allele ratio in RNA (cDNA) differs from the corresponding 1:1 ratio in genomic DNA. The cut-off for calling allelic imbalance would optimally be based on the variability of cDNA heterozygote ratios in samples known to express the alleles in equal proportions; in practice, such information is not available and thresholds are commonly derived from the analysis of variability in heterozygote genomic DNA samples. The potential biases introduced by the application of genomic standards are far less serious than the artefactual allelic imbalance caused by stochastic RT-PCR amplification of one allele in low copy number targets. Stochastic effects are a particular concern in single-cell studies (*32*).

Recent in vivo screening studies of relative allelic expression in normal tissues or cell lines for hundreds of human genes suggest that 25 to 50% of genes and 5 to 25% of heterozygotes show evidence of unequally expressed alleles (*10*, *33*, *35*). The abundance of allele-specific differences in expression is notable, though variable study designs preclude consensus estimates of its prevalence in the human genome. Furthermore, the allelic expression demonstrated in informative heterozygotes has not been correlated with total expression levels across all genotypic groups; some allelic differences could be compensated if the expression of the gene were under direct negative feedback control.

Genetic Mapping Combined with Expression Profiling

Genome-wide expression profiling technology has developed to a level at which even routine clinical applications have been contemplated. This, along with improved genotyping technologies, would allow large-scale correlations of marker genotypes to gene expression levels modeled as quantitative traits (eQTLs). When genetic linkage of the eQTL coincides with the genomic location of the gene, the presence of cis-acting regulatory variants can be deduced (*1*, *2*). Alternatively, panels of moderate sample size may have sufficient power to permit whole-genome association studies with eQTLs. The drawbacks of both approaches are that the detection of subtle cis-acting effects may require large sample sizes (i.e., thousands of RNA samples from different individuals) and that epigenetic variation is not assessed. Furthermore, without direct allele-specific expression measurements, the correlation of a marker genotype with gene expression level does not guarantee that the effect is cis-acting; a polymorphism in a trans-acting regulator in linkage disequilibrium with the marker genotype can explain the association. This may prove to be important even with high-density mapping, because antisense transcription may be a common regulatory mechanism of human gene expression (*36*).

Elucidating the Causal Mechanism of an Allelic Imbalance

Heritable cis-acting effects can be demonstrated by cosegregation of unequal allelic expression with marker genotypes in pedigrees (*10*, *29*). The lack of Mendelian inheritance of an allelic imbalance phenotype may point toward epigenetic mechanisms (*33*). Measurable phenomena associated with epigenetic allele-specific expression include replication asynchrony (*32*), differential methylation of the genomic loci (*37*), and allele-specific posttranslational histone modification (*37*). Common heritable allelic imbalance phenotypes can be mapped in unrelated individuals to establish regulatory haplotypes (*34*). For example, we demonstrated a strong regulatory haplotype in the human *BTN3A2* locus, which spanned at least 15 kb flanking the gene (*33*).

A tempting approach is to use existing bioinformatic tools to identify functional regulatory variants, but despite advances in the field (*38*), these computer predictions have relatively poor specificity. In vitro methods may also help find the functional SNP(s); however, their role is restricted by the inability of plasmid constructs to mimic the role of the natural genomic context in establishing allele-specific expression. Most of the transient transfection studies to date have been corroborated with other in vitro assays. For example, allele-specific DNA-protein interaction assays have been used to demonstrate that the putative regulatory polymorphism shows allele-specific differences in recruiting nuclear transcriptional activators or repressors. Similarly, indirect support for the functionality of the putative regulatory polymorphism may be sought by correlating genotypes with altered protein activity. Finally, the direct observation of cis-acting effects in vivo, as demonstrated for the human *LTA* gene with the use of the HaploChIP technology, provides corroboration of transcriptional events mediating allele-specific gene expression (*34*, *39*).

Allelic Expression: Next Steps

The rapidly evolving data sets, technologies, and knowledge of regulatory variation portend the generation of genome-wide mapping and characterization of allelic variants affecting gene expression. The large-scale in vivo screening studies carried out to date are generally limited to descriptions of allele-specific differences in expression, leaving the underlying mechanisms largely unexplored.

A more complete picture will require genome-wide in vivo allelic expression analyses followed by a systematic classification into probable genetic or epigenetic mechanisms with the use of family-based samples. The genetic basis of allele-specific expression phenotypes can subsequently be mapped to regulatory haplotypes. The most limiting factor for such a study is the lack of suitable panels of human tissues. In the short term, existing collections of immortalized cell lines can provide useful starting material, although these cells may express the genes of interest at low level or under abnormal transcriptional control.

Alternatively, genome-wide assessment of DNA protein interaction for transcriptionally active genes in vivo combined with allele quantitation of the protein-bound genomic fragments (*34*, *39*) could be used to determine cis-acting polymorphisms underlying interindividual differences in response to key transcriptional regulators. The latter approach may provide a short-cut to the identification of the causative regulatory polymorphism and shift the focus to cellular processes of interest. The intersection of multidisciplinary efforts to develop tools and characterize the regulatory component of the human genome [such as the ENCODE project (*40*)] with genome-wide allelic expression studies and regulatory haplotype characterization will provide a wealth of data for understanding cis-acting variation affecting the regulation of human genes and its contribution to phenotypic variance.

References and Notes

1. E. E. Schadt *et al.*, *Nature* **422**, 297 (2003).
2. M. Morley *et al.*, *Nature* **430**, 743 (2004).
3. Y. Horikawa *et al.*, *Nature Genet.* **26**, 163 (2000).
4. S. Gretarsdottir *et al.*, *Nature Genet.* **35**, 131 (2003).
5. M. C. Willing, S. P. Deschenes, R. L. Slayton, E. J. Roberts, *Am. J. Hum. Genet.* **59**, 799 (1996).
6. A. M. Carter, M. Sachchithananthan, S. Stasinopoulos, F. Maurer, R. L. Medcalf, *Thromb. Haemostasis* **87**, 846 (2002).
7. N. H. Gehring *et al.*, *Nature Genet.* **28**, 389 (2001).
8. H. Ueda *et al.*, *Nature* **423**, 506 (2003).
9. C. Ober *et al.*, *Am. J. Hum. Genet.* **72**, 1425 (2003).
10. H. Yan, W. Yuan, V. E. Velculescu, B. Vogelstein, K. W. Kinzler, *Science* **297**, 1143 (2002).
11. J. F. Hu *et al.*, *Biochim. Biophys. Acta* **1491**, 49 (2000).
12. N. S. Enattah *et al.*, *Nature Genet.* **30**, 233 (2002).
13. L. C. Olds, E. Sibley, *Hum. Mol. Genet.* **12**, 2333 (2003).
14. M. Poulter *et al.*, *Ann. Hum. Genet.* **67**, 298 (2003).
15. C. A. Mulcare *et al.*, *Am. J. Hum. Genet.* **74**, 1102 (2004).
16. T. Bersaglieri *et al.*, *Am. J. Hum. Genet.* **74**, 1111 (2004).
17. A. Ferguson-Smith, S. P. Lin, C. E. Tsai, N. Youngson, M. Tevendale, *Semin. Cell Dev. Biol.* **14**, 43 (2003).
18. R. Ohlsson, B. Tycko, C. Sapienza, *Trends Genet.* **14**, 435 (1998).
19. Z. Lin, J. Floros, *Physiol. Genomics* **11**, 235 (2002).
20. T. Sakatani *et al.*, *Biochem. Biophys. Res. Commun.* **283**, 1124 (2001).
21. D. Ingrosso *et al.*, *Lancet* **361**, 1693 (2003).
22. H. Cui *et al.*, *Science* **299**, 1753 (2003).
23. M. V. Rockman, G. A. Wray, *Mol. Biol. Evol.* **19**, 1991 (2002).
24. Y. Xu *et al.*, *J. Lipid Res.* **40**, 50 (1999).
25. R. Wade-Martins, Y. Saeki, E. A. Chiocca, *Mol. Ther.* **7**, 604 (2003).
26. J. L. Rutter *et al.*, *Cancer Res.* **58**, 5321 (1998).
27. B. Hoogendoorn *et al.*, *Hum. Mol. Genet.* **12**, 2249 (2003).
28. J. Singer-Sam, J. M. LeBon, A. Dai, A. D. Riggs, *PCR Methods Appl.* **1**, 160 (1992).
29. D. Hewett, J. Lynch, A. Child, H. Firth, B. Sykes, *Am. J. Hum. Genet.* **55**, 447 (1994).
30. S. Hutchinson *et al.*, *Hum. Mol. Genet.* **12**, 2269 (2003).
31. J. Li *et al.*, *Proc. Natl. Acad. Sci. U.S.A.* **101**, 7341 (2004).
32. A. Chess, I. Simon, H. Cedar, R. Axel, *Cell* **78**, 823 (1994).
33. T. Pastinen *et al.*, *Physiol. Genomics* **16**, 184 (2004).
34. J. C. Knight, B. J. Keating, K. A. Rockett, D. P. Kwiatkowski, *Nature Genet.* **33**, 469 (2003).
35. H. S. Lo *et al.*, *Genome Res.* **13**, 1855 (2003).
36. O. Rosok, M. Sioud, *Nature Biotechnol.* **22**, 104 (2004).
37. R. Jaenisch, A. Bird, *Nature Genet.* **33** (Suppl), 245 (2003).
38. W. W. Wasserman, A. Sandelin, *Nature Rev. Genet.* **5**, 276 (2004).
39. J. C. Knight, B. J. Keating, D. P. Kwiatkowski, *Nature Genet.* **36**, 394 (2004).
40. The ENCODE Project Consortium, *Science* **306**, 647 (2004).
41. We thank E. Harmsen, J. Engert, and R. Sladek for their advice. T.J.H. and T.P. are supported by Genome Quebec and Genome Canada. T.J.H. is the recipient of a Clinician-Scientist Award in Translational Research by the Burroughs Wellcome Fund and an Investigator Award from the Canadian Institutes of Health Research.

A Precocial Avian Embryo from the Lower Cretaceous of China

Zhonghe Zhou* and Fucheng Zhang

An avian embryo was collected from Lower Cretaceous lacustrine shale in Liaoning, in northeast China (fig. S1). It was in the final stage of development and represents an early precocial bird.

The embryo is enclosed in an oval ~35 mm by 20 mm. No evidence of eggshell was recognized. During incubation, bird embryos shift into a tucking position shortly before hatching and occupy most of the egg. The tucked posture of the Liaoning fossil is consistent with a late-stage embryo rather than with a hatchling, in which case the head would have raised beyond the vicinity of the feet.

The skeletal elements are nearly intact in articulation, with a complete skull and nearly complete postcranial bones (Fig. 1, A and B). The skull is large, with toothed jaws and an expanded braincase. The vertebral column is strongly curved. Both hindlimbs are folded and in tight contact with the skull and other postcranial bones. The long bones have obvious striations and less ossified epiphyses. The unguals of the pedal digits are large and curved, indicating that the adult would be an arboreal bird.

Extant bird embryos have a special structure on the top of the bill, the egg tooth. This tooth is used for breaking eggs before hatching and drops off soon after hatching. Such a structure is absent in the Liaoning embryo, although true teeth are still present as in most other Mesozoic birds. The egg tooth probably represents a novel feature that arose later.

The embryo has several enantiornithine apomorphies such as a strutlike coracoid with a convex lateral margin, a V-shaped furcula, metacarpal III extending well past metacarpal II distally, and metatarsal IV being more slender than metatarsals II or III.

Several avian embryos have been reported from the Upper Cretaceous, but none with feathers (*1*, *2*). The Liaoning embryo has a well-ossified skeleton with well-grown feather sheets. The jaws lie below the wing as a result of the rotation of the skull. The distal elements of the wing are well ossified, suggesting that it was in the final stage of embryological development (*3*, *4*). The embryo also preserves imprints of wing and tail feather anlagen enclosed in the feather sheets (Fig. 1, B and C). The presence of long feather sheets with no open vanes is further evidence that the fossil is an embryo.

Altricial birds are naked and helpless when they hatch, whereas precocial birds are covered with natal down and can move and feed independently. Precocial birds hatch with relatively large brains. The presence of well-developed feather sheets and the large brain indicates that the Liaoning embryo is a precocial or even a superprecocial bird. It is generally believed that precociality is ancient and altriciality is derived. All exclusively precocial bird orders have been phylogenetically arranged in the infraclass Eoaves (*5*) and placed at the basal node of the cladogram (*3*). The recognition of a Lower Cretaceous precocial avian embryo supports this phylogeny. It has been suggested that the dinosaur *Troodon* developed precocially (*6*), and the Late Cretaceous oviraptorid dinosaurs may also be precocial (*7*). Because these are close relatives of birds, the precociality of birds might represent a feature derived from their dinosaurian ancestor.

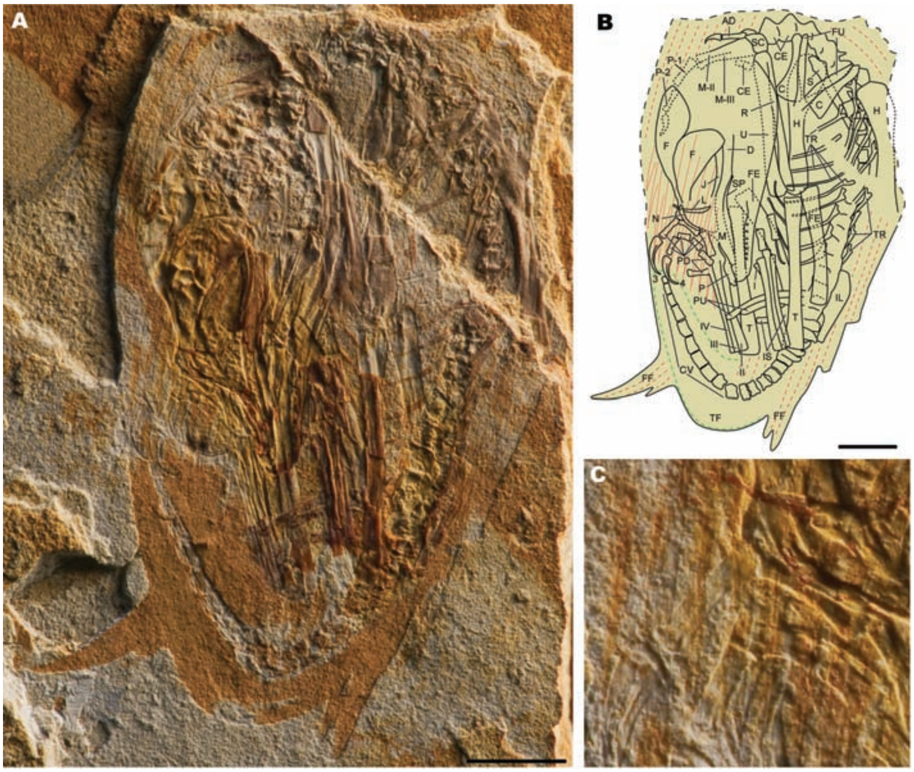

Fig. 1. (**A**) Photograph of a Lower Cretaceous avian embryo from Liaoning, China (Institute of Vertebrate Paleontology and Paleoanthropology no. V14238). (**B**) A line drawing of the fossil shown in (A). Red lines indicate wing feather sheets, and the green line shows imprints of tail feather anlagen. (**C**) A close-up view of long wing feather sheets near the pedal claws. Scale bars, 5 mm. AD, alular digit; C, coracoid; CE, cervical vertebra; CV, caudal vertebra; D, dentary; F, frontal; FE, femur; FF, wing feather sheets; FU, furcula; H, humerus; IL, ilium; IS, ischium; J, jugal; L, lachrymal; M, maxilla; M-II, metacarpal II; M-III, metacarpal III; N, nasal; PD, pedal digits; P, premaxilla; PU, pubis; P-1, first phalanx of the major digit; P-2, second phalanx of the major digit; R, radius; S; scapula; SC, semilunate carpal; SP, splenial; T, tibia; TF, tail feather sheets; TR, thoracic rib; U, ulna; 3 and 4, pedal digits III and IV; and I to IV, metatarsals I to IV.

References and Notes

1. E. Elzanowski, *Palaeont. Polon.* **42**, 148 (1981).
2. H. Schweitzer *et al.*, *J. Vert. Paleont.* **2**, 191 (2002).
3. J. M. Starck, in *Current Ornithology*, D. M. Power, Ed. (Plenum, New York, 1993), vol. 10, pp. 275–366.
4. R. E. Ricklefs, J. M. Starck, in *Avian Growth and Development*, J. M. Starck, R. E. Ricklefs, Eds. (Oxford Univ. Press, Oxford, 1998), pp. 31–58.
5. C. G. Sibley, J. E. Ahlquist, *Phylogeny and Classification of Birds* (Yale Univ. Press, New Haven, CT, 1990).
6. J. R. Horner, D. B. Weishampel, *Nature* **383**, 103 (1996).
7. M. A. Norell, J. M. Clark, L. M. Chiappe, *Am. Mus. Novit.* **3315**, 1 (2001).
8. We thank X. Wang and D. Miao for help. Supported by the National Natural Science Foundation of China (grant no. 40121202) and Special Funds for Major State Basic Research Projects of China (grant no. TG2000077700).

Supporting Online Material
www.sciencemag.org/cgi/content/full/306/5696/653/DC1
Fig. S1

6 May 2004; accepted 18 August 2004

Institute of Vertebrate Paleontology and Paleoanthropology, Chinese Academy of Sciences, Post Office Box 643, Beijing 100044, China.

*To whom correspondence should be addressed. E-mail: zhonghe@yeah.net

RESEARCH ARTICLE

A Gene Expression Map for the Euchromatic Genome of *Drosophila melanogaster*

Viktor Stolc,[1,5]* Zareen Gauhar,[1,2]* Christopher Mason,[2]*
Gabor Halasz,[7] Marinus F. van Batenburg,[7,9] Scott A. Rifkin,[2,3]
Sujun Hua,[2] Tine Herreman,[2] Waraporn Tongprasit,[6]
Paolo Emilio Barbano,[2,4] Harmen J. Bussemaker,[7,8]
Kevin P. White[2,3]†

We used a maskless photolithography method to produce DNA oligonucleotide microarrays with unique probe sequences tiled throughout the genome of *Drosophila melanogaster* and across predicted splice junctions. RNA expression of protein coding and nonprotein coding sequences was determined for each major stage of the life cycle, including adult males and females. We detected transcriptional activity for 93% of annotated genes and RNA expression for 41% of the probes in intronic and intergenic sequences. Comparison to genome-wide RNA interference data and to gene annotations revealed distinguishable levels of expression for different classes of genes and higher levels of expression for genes with essential cellular functions. Differential splicing was observed in about 40% of predicted genes, and 5440 previously unknown splice forms were detected. Genes within conserved regions of synteny with *D. pseudoobscura* had highly correlated expression; these regions ranged in length from 10 to 900 kilobase pairs. The expressed intergenic and intronic sequences are more likely to be evolutionarily conserved than nonexpressed ones, and about 15% of them appear to be developmentally regulated. Our results provide a draft expression map for the entire nonrepetitive genome, which reveals a much more extensive and diverse set of expressed sequences than was previously predicted.

Characterization of the complete expressed set of RNA sequences is central to the functional interpretation of each genome. For almost 3 decades, the analysis of the *Drosophila* genome has served as an important model for studying the relationship between gene expression and development. In recent years, *Drosophila* provided the initial demonstration that DNA microarrays could be used to study gene expression during development (*1*), and subsequent large-scale studies of gene expression in this and other developmental model organisms have given new insights into how organisms implement their developmental plan (*2*). Additional studies in *Drosophila* have addressed questions in diverse biological processes, including metamorphosis, aging, innate immune response, and sexual dimorphism, and in evolutionary patterns of gene expression (*3*–*9*). The cumulative data from such microarray studies are valuable for functional annotation of the genome. However, all microarray studies of gene expression in *Drosophila* have been restricted to fragments of genes from predicted gene sets and thus are subject to the limitations of gene prediction algorithms. Large-scale expressed sequence tag (EST) sequencing has also been extremely valuable for annotation of the *Drosophila* genome (*10*), but this approach is limited by biases due to 5′ or 3′ end DNA sequencing, the extent to which transcripts are represented in cDNA libraries, and the number of EST sequences generated. A nonbiased approach is necessary for the determination of the entire catalog of expressed sequences in the genome. Genomic "tiling" DNA arrays, which use oligonucleotides or polymerase chain reaction (PCR) products corresponding to chromosomal sequences as probes, have been used to create transcript activity catalogs for portions of the human genome and for *Arabidopsis* (*11*–*13*). Microarrays have also recently been used to characterize the great diversity of RNA transcripts brought about by differential splicing in human tissues (*14*). We used both types of approaches to characterize the *Drosophila* genome.

Experimental design. To determine the expressed portion of the *Drosophila* genome, we designed high-density oligonucleotide microarrays with probes for each predicted exon and probes tiled throughout the predicted intronic and intergenic regions of the genome. We used maskless array synthesizer (MAS) technology (*15*, *16*) to synthesize custom microarrays containing 179,972 unique 36-nucleotide (nt) probes (*17*). Of these, 61,371 exon probes (EPs) assayed 52,888 exons from 13,197 predicted genes, 87,814 nonexon probes (NEPs) assayed expression from intronic and intergenic regions, and 30,787 splice junction probes (SJPs) assayed potential exon junctions for a test subset of 3955 genes. For the SJPs, we used 36-nt probes spanning each predicted splice junction, with 18 nt corresponding to each exon (*14*). RNA from six developmental stages during the *Drosophila* life cycle (early embryos, late embryos, larvae, pupae, and male and female adults) was isolated and reverse-transcribed in the presence of oligodeoxythymidine and random hexamers, and the labeled cDNA was hybridized to these arrays. The stages were chosen to maximize the number of transcripts that would be differentially expressed between samples on the basis of previous results (*3*, *7*). Each sample was hybridized four times, twice with Cy5 labeling and twice with Cy3 labeling (fig. S1).

Genomic and chromosomal expression patterns. We determined which exon or nonexon probes correspond to genomic regions that are transcribed at any stage during development (*18*). We used a negative control probe (NCP) distribution (fig. S3) to score the statistical significance of the EP or NEP signal intensities for each of the 24 unique combinations of stage, dye, and array, correcting for probe sequence bias (*17*, *19*). These results were combined into a single expression-level estimate (*19*), a threshold for which was determined by requiring a false discovery rate of 5% (*20*). This threshold shows 47,419 of 61,371 EPs (77%) and 35,985 out of 87,814 NEPs (41%) were significantly expressed at some point during the fly life cycle. Significantly expressed EPs correspond to 79% (41,559/52,888) of all exons probed and 93% (12,305/13,197) of all probed gene annotations. Our results confirmed 2426 annotated genes not yet validated through an EST sequence (Fig. 1A). Out of 10,280 genes represented by EST sequences,

---

[1] Department of Molecular, Cellular, and Developmental Biology, [2] Department of Genetics, [3] Department of Ecology and Evolutionary Biology, [4] Department of Mathematics, Yale University, New Haven, CT 06520, USA. [5] Genome Research Facility, NASA Ames Research Center, Mail Stop 239-11, Moffett Field, CA 94035, USA. [6] Eloret Corporation, Sunnyvale, CA 94087, USA. [7] Department of Biological Sciences, [8] Center for Computational Biology and Bioinformatics, Columbia University, New York, NY 10027, USA. [9] Bioinformatics Laboratory, Academic Medical Center, University of Amsterdam, 1100 DE Amsterdam, Netherlands.

*These authors contributed equally to this work.

†To whom correspondence should be addressed. E-mail: kevin.white@yale.edu

only 401 (3.0%) were not detected in these microarray experiments. Our finding that a large fraction of intergenic and intronic regions (NEPs) is expressed in *D. melanogaster* mirrors similar observations for chromosomes 21 and 22 in humans (*16*) and for *Arabidopsis* (*14*). These results support the conclusion that extensive expression of intergenic and intronic sequences occurs in the major evolutionary lineages of animals (deuterostomes and protostomes) and in plants.

We noted that mRNA expression levels for protein-encoding genes varied with the protein function assigned in the *Drosophila* Gene Ontology (fig. S2) (*21*). For example, genes encoding G protein receptors were expressed at relatively low levels, whereas genes encoding ribosomal proteins were highly expressed. A gene's expression level was also associated with cellular compartmentalization and the biological process it mediates (fig. S2). For example, genes encoding cytosolic and cytoskeletal factors were more highly expressed than those predicted to function within organelles such as the endoplasmic reticulum, Golgi, and peroxisome. To determine whether a high level of gene expression was associated with essential genetic functions, we examined the expression levels of genes recently shown to be required for cell viability (Fig. 1B) in a genome-wide RNA interference (RNAi) screen in *Drosophila* (*22*). Compared to the rest of the genome, the genes identified as essential by RNAi showed a significant increase in expression during all stages of development (P = 0.0009, t test), even when the highly expressed ribosomal protein genes were omitted (P = 0.0005, t test). This result is also consistent with the observation that genes with mutant phenotypes from the 3-Mbase Adh genomic region are overrepresented in EST libraries (*23*). High levels of essential gene expression may in part reflect widespread expression in cells throughout the animal, and the relative RNA expression level may serve as a rough predictor of essential cellular function.

We also examined changes in gene expression during the fly life cycle to determine what fraction of the entire genome is differentially expressed between developmental stages. Figure 2A shows the expression signal intensities of transcripts from a typical 50–kilobase pair (kbp) region of the *Drosophila* genome during each major developmental stage. Stage-specific variation in expression is observed not only for exon probes, as expected, but also for intergenic and intronic probes. We used analysis of variance (ANOVA) (*24*) to systematically identify probes as differentially expressed at a false discovery rate of 5% (*16*). As expected, the majority of probes detecting differentially expressed sequences are also expressed above background noise level (89% of EPs and 81% of NEPs) (*17*) (Table 1). We found 27,176 EPs to be differentially expressed, corresponding to 76% of annotated genes, and even more when we applied a less conservative background model (fig. S4). The fact that the majority of genes are developmentally regulated is consistent with previous results obtained with cDNA microarrays (*3*). In intergenic and intronic regions, we detected differential expression for 15% (5508/35,985) of significantly expressed NEPs, indicating that many of the putative noncoding expressed transcripts are also developmentally regulated.

By examining gene expression levels along chromosomes, we discovered that genes that have remained linked during evolution are correlated with one another in expression levels. We considered the genes inside 827 syntenic blocks identified between *D. melanogaster* and *D. pseudoobscura* (*25*), whose expression varies substantially during development (Fig. 2A). We computed the average pairwise expression correlation between genes within each syntenic block and compared with the correlations among nonsyntenic genes. Average correlations among genes within 729 (88%) of these syntenic blocks showed a positive value (Fig. 2B), and genes within 369 syntenic blocks (45%) across all chromosomes showed positive correlations that were significant ($P < 0.05$) (Fig. 2C). Larger blocks show higher significance of correlated gene expression levels than smaller ones (Fig. 2D). Expression correlations for 104 out of 108 syntenic blocks greater than 300 kbp in length were statistically significant, and all expression level correlations among genes in blocks greater than 650 kbp were significant (fig. S5). These results indicate that chromatin domains

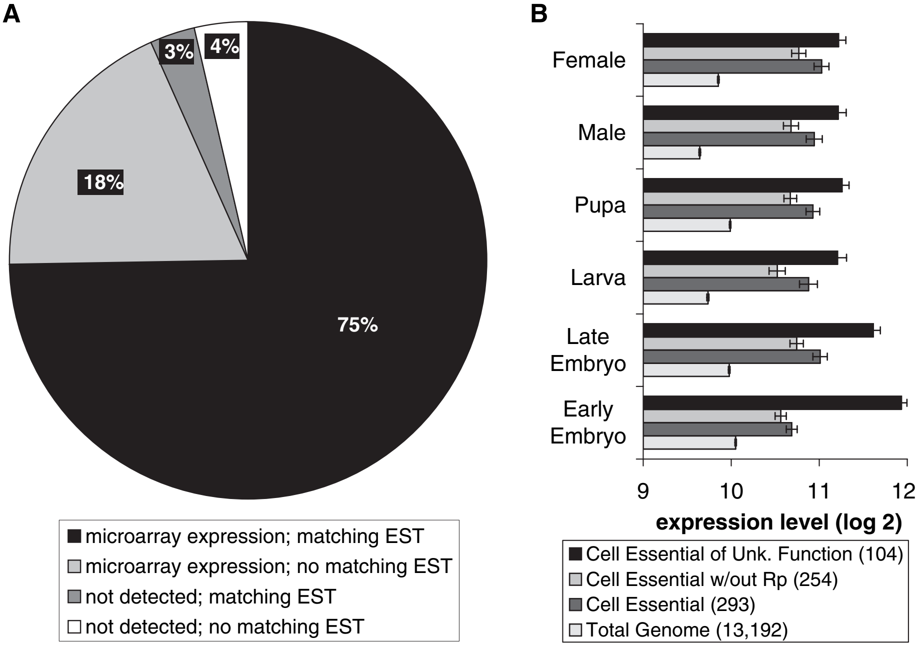

Fig. 1. Characterization of microarray probes by global expression levels can predict biological function. (**A**) Annotation confirmation. Each probe was compared to the *Drosophila* genome annotation version 3.1 (v3.1) and to cDNA/EST sequences produced by the Berkeley *Drosophila* Genome Project. 74.9% of v3.1 genes were confirmed by cDNA/EST sequencing and by this microarray analysis, 18.4% were confirmed solely by this study, 3.0% were confirmed solely by cDNA/EST sequencing, and 3.7% were unconfirmed by either method. (**B**) Cell-essential genes are expressed at higher-than-average levels. Compared to the average genome-wide, the 293 known genes identified as essential by Boutros *et al*. (*23*) showed significantly higher levels of expression during all stages of development (P = 0.0009, t test). A similar result was obtained when the highly expressed ribosomal protein (Rp) genes are omitted (P = 0.0005, t test) or when only the 104 cell-essential genes of unknown function (P = 0.004, t test) were examined. Error bars indicate ±1 SE.

Table 1. Genome-wide statistics for expressed probes. We compiled lists of probes that show significant expression on the basis of two distinct criteria: (i) absolute probe expression above background (PEAB) noise level in one or more stages based on comparison with negative control probes and (ii) differential expression between stages based on ANOVA (*16*). FDR, false discovery rate.

Probe type	Total probes	Significant probes (FDR = 0.05)		Overlap: ANOVA and PEAB
		PEAB	ANOVA	
NEPs	87,814	35,985	6789	5508 (81%)
EPs	61,371	47,419	27,176	24,062 (89%)

or long-range enhancers act across wide genomic regions and that genomic rearrangements in these regions have been constrained during the evolutionary lineages leading to these two species, thereby maintaining these blocks of synteny. Natural selection may therefore act to maintain genes within neighborhoods where expression is coordinately regulated.

Exon expression and splicing. Within each gene, expression levels of exon pairs were typically highly correlated, and the distribution of these correlations was significantly shifted relative to that of exon pairs from different genes (Fig. 3A). A pattern separation algorithm was used to determine the patterns of expression for exons within each gene during development (*17*). We found three major trends (Fig. 3, B to D): 53% of genes showed uniform or highly correlated ($r > 0.8$) expression (Fig. 3B), 46% of genes showed multiple patterns of exon expression suggesting alternative promoter usage or splicing (Fig. 3C), and 1% of genes showed multiple patterns with at least one exon pair showing strong anticorrelation during the life cycle (Fig. 3D). These strong anticorrelations suggest exclusivity in the use of one exon or another for this small subset of genes. Together, this initial analysis indicated that a vast amount of gene expression variation is missed in previous microarray studies that have used cDNAs or that assay only a subset of exons from each gene.

However, although these initial analyses allowed identification of exons that are differentially expressed during development, they did not reveal precisely which exons are spliced to one another during posttranscriptional RNA processing. To estimate the extent of splicing in the *Drosophila* genome during development, we used SJPs to directly assay spliced exons and differential use of splice isoforms. We focused on a subset of 3955 predicted genes that included genes with as few as 2 and as many as 54 exons. For these genes, we designed SJPs for all theoretically possible splicing combinations. Because SJPs could potentially hybridize to exons that were not spliced directly together, we used a specialized set of wrong junction probes (WJPs, splice junctions formed from exon segments but that do not match any possible transcript) as negative controls (fig. S6). These WJPs show higher hybridization signal than the NCPs we used as a reference distribution to detect absolute expression because of partial hybridization. We find that 28% (8732) of the 30,787 SJPs are expressed at a level above the background level defined by the WJPs.

By examining the ratio of significantly expressed, sequentially spliced exons and significantly expressed exons that are noncontiguous, we were able to determine the proportion of exons and genes that are alternatively spliced during development. The ratio of noncontiguous to contiguous splicing (NC/C ratio) for exons' use of downstream exons holds near a constant 0.40 (Fig. 4A), indicating an average of 2.5 contiguous splice events for every exon skipping (i.e., alternative) splice form. Also, these SJP data show that 53% (1374 of 2606) of expressed *Drosophila* genes from multiexon genes exhibit exon skipping (*18*).

To determine the extent of splicing that is captured by large-scale EST sequencing, we used BLASTn to align sequences from the junctions' probes to known EST and cDNA databases (Fig. 4B). We identified 3292 splice junctions in the databases that matched our positive hybridization results, whereas 3464 junction probes did not detect hybridization ("EST only" sequences) but did match the expression databases, providing a very high false negative rate of ~46%. Nevertheless, 5440 new splice variants were identified

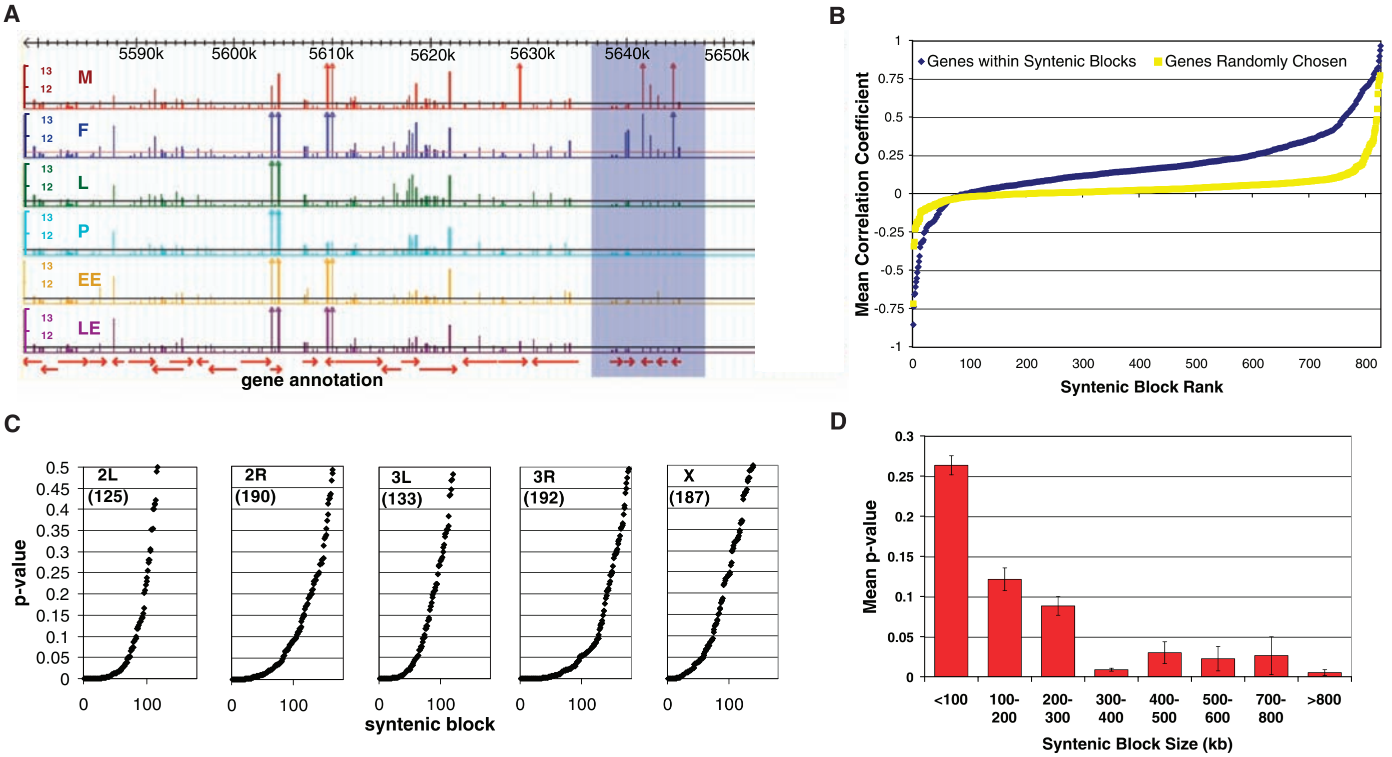

Fig. 2. Gene activity in conserved chromosomal domains. (**A**) Expression plots along chromosome 2L in the region: 5,600,000 to 5,650,000 show signal intensity of probes along the chromosome arm in six developmental stages [early embryo (EE), late embryo (LE), larva (L), pupa (P), adult male (M), and adult female (F)]. The shaded region shows a syntenic block where expression levels of transcripts encoded by genes within the block are highly correlated across development. (**B**) Distribution of Pearson correlation coefficients. Most syntenic blocks show positive correlations among expression levels for genes within them (blue), and the distribution of correlations differs from a control set of randomly selected gene blocks (yellow). Most correlations in the control set are near zero, as expected. (**C**) Significance of gene expression correlations within syntenic blocks. The distributions of P values are shown by chromosome, showing the significance of the correlations compared to the control set, for each syntenic block. (**D**) Significance of gene expression correlations increases with syntenic block size. The larger the size of syntenic regions, the stronger the bias for genes within the block to be significantly correlated in expression. Error bars indicate ±1 SE.

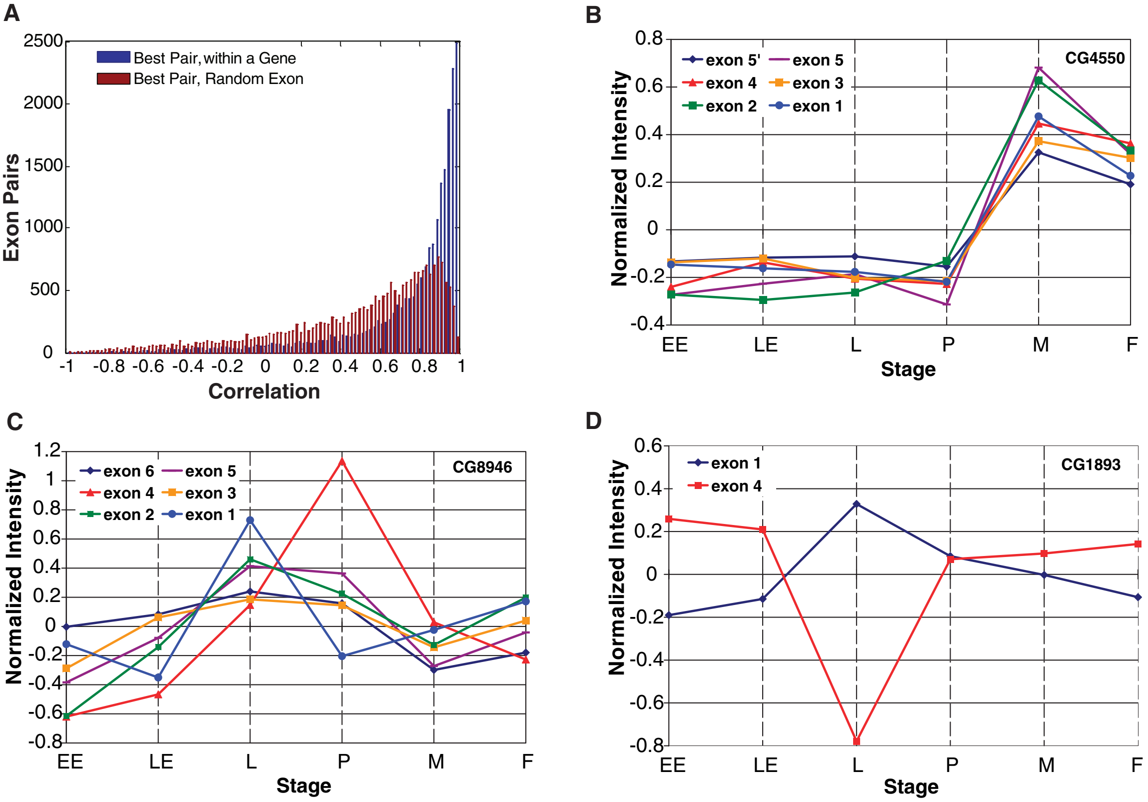

Fig. 3. Exon expression within and between genes. (**A**) Histogram of exon pairs' strongest correlation within a gene. There is a strong bias for exons expression levels within a gene (blue) to be positively correlated, compared with exons chosen at random (red). (**B**) Exon plot of the *ninaE* gene (CG4550). All exons are expressed similarly within this gene. Exon 5′ is a second probe placed within exon 5, because it is a large exon. To normalize the data from the different EPs, we show the absolute expression values minus their mean and divided by the sum of the squares. (**C**) Exon plot of gene CG8946, an example of a gene with differential exon expression during development. Exon 1 peaks in larva, whereas exon 4 peaks in pupa, but all other exons plateau at those same stages at a much lower relative level. (**D**) Two anticorrelated exons within gene CG1893.

(Fig. 4B). Most of these (4564) were alternative splice junctions, indicating that EST sequencing missed the vast majority of alternatively spliced transcripts. Taken together, the exon-specific expression patterns and the splice junction expression patterns significantly extend the functional annotation of the predicted genes in the *Drosophila* genome.

Intergenic and intronic expression. Lastly, we further examined the patterns of RNA expression from nonexonic sequences. There are several reasons to expect that a significant fraction of the annotated noncoding genome is expressed. First, previous studies performed in *Drosophila* using reverse Northern methodologies on chromosomal walks have identified multiple noncoding RNA transcripts at certain loci, such as in the bithorax complex (*26*–*28*). Second, the algorithms and experimental methods used for gene prediction and annotation may have not exhaustively identified the entire gene complement or all of the correct gene structures. Third, transcriptional analysis of a fraction of the human genome (*13*) and the *Arabidopsis* genome (*12*) has shown that about 50% of the predicted noncoding genome is expressed. Thus, we might expect this to be true for other organisms as well, although it is difficult to predict to what extent.

We examined the 41% of noncoding regions of the genome for which we detected transcriptional activity above background. Some of the NEP probes' expression may have been due to previously unannotated genes or to additional exons of already annotated genes from the current *Drosophila* genome annotation (*29*, *30*). To explore this possibility, we examined whether the expressed NEP probes corroborated computational exon predictions by Genscan (*31*). Exon predictions not in Flybase annotation (version 3.1) were divided into two groups: those bordering annotated genes and "unique" exons that did not. The latter set includes potential previously unknown genes. Genscan "unique" exons together encompassed 2045 NEP probes, 1221 (60%) of which were expressed. This represents a significant enrichment for expressed probes (compared with 41% of all NEP probes), strongly suggesting that many of these predictions represent previously unknown genes.

The overlapping NEP probes give supporting expression data for 1155 of Genscan's predicted exons. Of these, 369 represent additional exons bordering existing genes, whereas the remaining 786 exons belong to 716 putative novel genes (*18*). There were also several instances where Genscan predicted a longer upstream or downstream exon boundary relative to the current annotation. NEP probes overlapping these regions of disagreement confirmed expression of 64% (38/59) of 5′ predictions and 81% (30/37) of 3′ ones. Lastly, comparing to a recent study that identified several hundred expressed exons predicted with the Fgenesh algorithm (*32*, *33*), we found a considerable overlap of expressed NEPs within these predicted exons (61% or 477/777).

We next considered intronic expression and found that 43% of introns (6717/15,770) were expressed. There is also a relationship between the activity of an EP and its nearest intergenic NEP (and vice versa). We examined the correlations between these two classes of probes by means of a G test and a Dunn-Sidak correction for multiple testing. The nearest NEP was located on the same or opposite DNA strand in both the 5′ and 3′ direction, and for each of the 15 stage comparisons the differential expression levels of the probe pair were recorded. The stage or sex bias (e.g., transcript enrichment in males versus females) of NEPs at the 3′ end of exons is highly correlated with the stage or sex bias of the exon; similarly, the bias of exons at the 5′ end of NEPs is highly correlated with the bias of the NEP (fig. S7). These results indicate that either these expressed sequences are contained within genes whose end points have been misannotated or that they encode noncoding RNAs that are expressed in concert with nearby genes because of local chromatin or cis-regulatory effects. At least some of these transcripts are likely due to the second hypothesis, because extensive EST sequencing has failed to reveal the transcribed sequences within se-

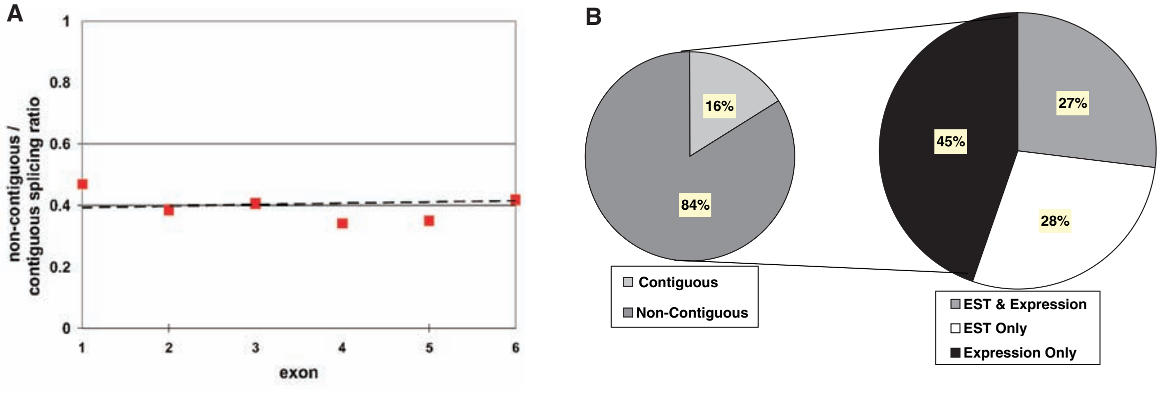

Fig. 4. Alternative and contiguous splicing patterns of the genome. (**A**) Ratios of noncontiguous to contiguous splicing. For each exon, the percentage of positives from noncontiguous or contiguous SJPs was calculated. The ratio of the percentage of contiguous SJP positives to the percentage of noncontiguous SJP positives remains near 0.4, even in larger genes (with six exons). Dotted line shows a linear regression across the data ($y = 0.0039x + 0.3904$). (**B**) Exon splicing activity above background (*16*) (fig. S6). Many of the expressed SJPs matched sequences in *Drosophila* EST databases (27%), yet a similar fraction of SJPs found within EST databases did not pass our intensity threshold criterion (28%). A substantial fraction of previously unknown splice junctions were detected (45%) as well as noncontiguous (i.e., alternative) exon splicing (84%).

quenced exons and because Northern blot analysis (fig. S8) shows that the noncoding sequences we have identified are often contained within several major and many minor polyA-RNA products that are inconsistent with expected protein-coding gene sizes. However, our analysis of the Genscan predictions suggests that many of the expressed sequences that correlate in expression with nearby annotated exons do in fact simply correspond to unannotated exons.

The extent to which these putative noncoding RNAs are functionally relevant awaits strategies for systematic characterization, but this genome-wide scan indicates that they are both abundant and developmentally regulated. The function of such extensively regulated noncoding gene expression during development is unknown. To determine whether these expressed sequences are functionally constrained at the sequence level, we used an alignment of the genomic sequences of *D. melanogaster* and *D. pseudoobscura* (*25*). Sequences corresponding to expressed NEPs were indeed more likely to be conserved than those corresponding to nonexpressed NEPs: The fraction of aligned base pairs was 68.7% for expressed probes and 59.0% for nonexpressed probes (Fig. 5) ($P = 10^{-192}$, *t* test), whereas 63.7% (expressed) and 60.9% (nonexpressed) of the base pairs in fully aligned probes were conserved between these species (*34*) ($P = 10^{-44}$, *t* test). This small but highly significant difference in conservation between expressed and nonexpressed NEPs indicates that there are evolutionary constraints on the expressed noncoding portion of the genome. The functional relevance of these sequences could potentially be further tested through methods such as large-scale RNAi screening (*22*) and systematic mutational analysis or through comparative expression analysis with additional species of *Drosophila*.

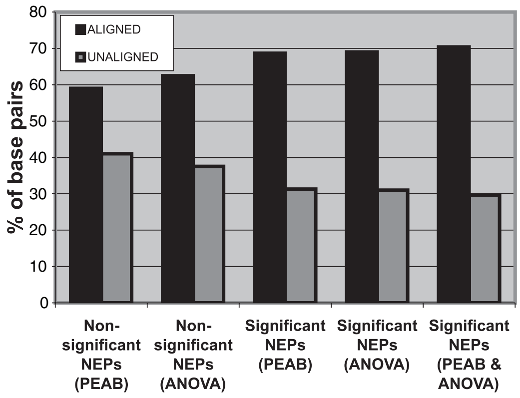

Fig. 5. NEP conservation between *D. melanogaster* and *D. pseudoobscura*. Expressed NEPs show increased sequence conservation when compared to nonexpressed NEP sequences ($P = 10^{-192}$). We used the whole-genome BLASTZ alignment between *D. melanogaster* and *D. pseudoobscura* of (*25*) to classify each base pair within our NEP probes as aligned (i.e., belonging to a chromosomal region with homology to *D. pseudoobscura*) or unaligned.

Summary. Ideally, to create a finished and fully annotated expression map of the genome, each stage and tissue would be assayed by multiple methods. Confidence measures of expression levels can have their basis in negative controls and cross-checking between data sets, such as we have presented here. It is clear that our past understanding of genome-wide RNA transcription has been very limited, because a large proportion of exons show dynamic patterns of differential splicing and noncoding activity is ubiquitous. Taken together, our results also indicate that there are thousands of uncharacterized and unannotated transcripts expressed in a developmentally coordinated manner. Systematic genetic approaches will likely be required to determine the functions of the large class of newly identified noncoding expressed sequences, which are slightly more conserved than other noncoding sequence. Additionally, the existence of evolutionarily conserved chromosomal domains of correlated gene expression indicates that these domains are also functionally important. However, the mechanisms responsible for these expression domains remain to be elucidated. This draft expression map of the *Drosophila* genome shows that there is considerably more complexity in gene and transcript regulation than was previously known, and it represents an initial step in identifying all the functional elements that ultimately control the developmental program of this organism.

References and Notes

1. K. P. White, S. A. Rifkin, P. Hurban, D. S. Hogness, *Science* **286**, 2179 (1999).
2. V. Reinke, K. P. White, *Annu. Rev. Genom. Hum. Genet.* **3**, 153 (2002).
3. M. N. Arbeitman *et al.*, *Science* **297**, 2270 (2002).
4. E. De Gregorio, P. T. Spellman, G. M. Rubin, B. Lemaitre, *Proc. Natl. Acad. Sci. U.S.A.* **98**, 12590 (2001).
5. S. A. Rifkin, J. Kim, K. P. White, *Nat. Genet.* **33**, 138 (2003).
6. T. R. Li, K. P. White, *Dev. Cell* **5**, 59 (2003).
7. J. De Vos *et al.*, *Oncogene* **21**, 6848 (2002).
8. M. Parisi *et al.*, *Science* **299**, 697 (2003); published online 2 January 2003 (10.1126/science.1079190).
9. S. D. Pletcher *et al.*, *Curr. Biol.* **12**, 712 (2002).
10. G. M. Rubin *et al.*, *Science* **287**, 2222 (2000).
11. J. L. Rinn *et al.*, *Genes Dev.* **17**, 529 (2003).
12. K. Yamada *et al.*, *Science* **302**, 842 (2003).
13. P. Kapranov *et al.*, *Science* **296**, 916 (2002).
14. J. M. Johnson *et al.*, *Science* **302**, 2141 (2003).
15. E. F. Nuwaysir *et al.*, *Genome Res.* **12**, 1749 (2002).
16. S. Singh-Gasson *et al.*, *Nature Biotechnol.* **17**, 974 (1999).
17. Materials and methods are available on *Science* Online.
18. All data are available online at http://flygenome.yale.edu. GEO submission GSE 1761.
19. R. A. Fisher, in *Statistical Methods for Research Workers*, ed. 11 (Oliver & Boyd, Edinburgh,1950), section 21.1, pp. 99.
20. Y. Benjamini, Y. Hichberg, *J. R. Stat. Soc.* **57**, 289 (1995).
21. M. Ashburner *et al.*, *Nature Genet.* **25**, 25 (2000).

22. M. Boutros *et al.*, *Science* **303**, 832 (2004).
23. M. Ashburner *et al.*, *Genetics* **153**, 179 (1999).
24. M. K. Kerr, G. A. Churchill, *Proc. Natl. Acad. Sci. U.S.A.* **98**, 8961 (2001).
25. S. Richards *et al.*, in preparation.
26. W. Bender, B. Weiffenbach, F. Karch, M. Peifer, *Cold Spring Harbor Symp. Quant. Biol.* **50**, 173 (1985).
27. W. Bender, D. P. Fitzgerald, *Development* **129**, 4923 (2002).
28. H. D. Lipshitz, D. A. Peattie, D. S. Hogness, *Genes Dev.* **1**, 307 (1987).
29. M. D. Adams *et al.*, *Science* **287**, 2185 (2000).
30. S. Misra *et al.*, *Genome Biol.* **3**, RESEARCH0083 (2002).
31. C. Burge, S. Karlin, *J. Mol. Biol.* **268**, 78 (1997).
32. A. A. Salamov, V. V. Solovyev, *Genome Res.* **10**, 516 (2000).
33. M. Hild *et al.*, *Genome Biol.* **5**, R3 (2003).
34. G. Halasz *et al.*, unpublished data.

35. V.S. was supported by NASA Center for Nanotechnology, NASA Fundamental Biology Program, and NASA Biomolecular Systems Research Program (contract NAS2-99092). H.J.B. was partly supported by grant P20LM007276-01 from NIH. M.v.B. was supported by grant BMI 050.50.201 from the Netherlands Organization for Scientific Research (NWO). G.H. was supported by NIH training grant T32GM008224-17. C.M. was supported by an NSF Graduate Student Fellowship. This work was supported by grants to K.P.W. and H.J.B. from the Human Frontier Science Program and to K.P.W. from the Yale Genomics and Proteomics Initiative, the NIH National Human Genome Research Institute, and the W. M. Keck Foundation. Thanks to S. Schaeffer for providing syntenic block coordinates and F. Aoki for help with the probe design. The GSE accession number is GSE 1761.

Supporting Online Material

www.sciencemag.org/cgi/content/full/306/5696/655/DC1
Materials and Methods
SOM Text
fig. S1

9 June 2004; accepted 20 September 2004

REPORTS

Quantum-to-Classical Transition with Single-Photon–Added Coherent States of Light

Alessandro Zavatta, Silvia Viciani, Marco Bellini*

Single-photon–added coherent states are the result of the most elementary amplification process of classical light fields by a single quantum of excitation. Being intermediate between a single-photon Fock state (fully quantum-mechanical) and a coherent (classical) one, these states offer the opportunity to closely follow the smooth transition between the particle-like and the wavelike behavior of light. We report the experimental generation of single-photon–added coherent states and their complete characterization by quantum tomography. Besides visualizing the evolution of the quantum-to-classical transition, these states allow one to witness the gradual change from the spontaneous to the stimulated regimes of light emission.

A coherent state $|\alpha\rangle$ is the closest analog to a classical light field and exhibits a Poisson photon number distribution with an average photon number $|\alpha|^2$. Coherent states have relatively well-defined amplitude and phase, with minimal fluctuations permitted by the Heisenberg uncertainty principle. On the contrary, a Fock state $|n\rangle$ is strictly quantum-mechanical and contains a precisely defined number (n) of quanta of field excitation, hence its phase is completely undefined.

Photon-added coherent states (*1*) are the result of successive elementary one-photon excitations of a classical coherent field, and they occupy an intermediate position between the Fock and the coherent states. They are obtained by repeated (m times) application of the photon creation operator $\hat{a}^\dagger$ on a coherent state ($|\alpha,m\rangle = k_{\alpha,m}\ \hat{a}^{\dagger m}|\alpha\rangle$, $k_{\alpha,m}$ being a normalization constant and m an integer) and reduce to the limit Fock or coherent states for $\alpha \rightarrow 0$ or $m \rightarrow 0$, respectively. Quite differently from the so-called displaced Fock states, where a coherent state is used to displace a number state [for example, by mixing the two fields upon a highly reflecting beam splitter (*2*)], photon-added coherent states can be roughly viewed as obtained from the displacement of a coherent state operated by a Fock state. Indeed, one easily finds that all the $|n\rangle$ terms with $n < m$ are missing in the expansion of the states $|\alpha,m\rangle$ in the Fock basis, and that all the elements of the corresponding density matrix are essentially displaced toward higher indices $\rho_{i,j} \rightarrow \rho_{i+m,j+m}$, leaving all the elements with $i,j < m$ void.

In the case of a single quantum of field excitation ($m = 1$), the single-photon–added coherent states (SPACSs) read as

$$|\alpha, 1\rangle = \frac{\hat{a}^\dagger|\alpha\rangle}{\sqrt{1+|\alpha|^2}} \tag{1}$$

Unlike the operation of photon annihilation, which maps a coherent state into another coherent state (that is, a classical field into another classical field), a single-photon excitation of a coherent state changes it into something quite different. In general, the application of the creation operator $\hat{a}^\dagger$ changes a completely classical coherent state into a quantum state with a varying degree of nonclassicality that becomes more evident the smaller the initial amplitude of the $|\alpha\rangle$ state. In the extreme case of an initial vacuum state $|0\rangle$, a single excitation event transforms it into the very nonclassical single-photon Fock state $|1\rangle$, which exhibits negative values of the Wigner function (*3*, *4*). The Wigner function is a quasi-probability distribution (*5*–*7*), which fully describes the state of a quantum system in phase space (either the position-momentum space for an harmonic oscillator or, equivalently, the space spanned by two orthogonal quadratures of the electromagnetic field for a single-mode state of light, as in this case) in the same fashion as a probability distribution (nonnegative by definition) characterizes a classical system. The negativity of the Wigner function is indeed a good indication of the highly nonclassical character of the state (Fig. 1).

We report the experimental generation of SPACSs and their complete tomographic analysis, which unveils the nonclassical features associated with the excitation of a classical coherent field by a single light quantum.

Parametric down-conversion in a nonlinear crystal is the basis for the production of the desired states (Fig. 2). Here one high-energy pump photon can annihilate into two photons that obey the global energy and momentum conservation laws and thus have lower energies and are normally emitted into symmetrically oriented directions, also called the signal and idler modes. When no other field is injected in the crystal, spontaneous parametric down-conversion takes place, starting from the input vacuum field, and pairs of entangled photons with random (but mutually correlated) phases are produced. In order to generate SPACSs, one has to inject a seed

---

Istituto Nazionale di Ottica Applicata, Largo Enrico Fermi, 6, I-50125, Florence, Italy; European Laboratory for Nonlinear Spectroscopy (LENS) and Department of Physics, University of Florence, I-50019 Sesto Fiorentino, Florence, Italy.

*To whom correspondence should be addressed. E-mail: bellini@ino.it

coherent field $|\alpha\rangle$ into the signal mode of the parametric amplifier, and the conditional preparation of the target state takes place every time that a single photon is detected in the correlated idler mode. If the parametric gain is kept sufficiently low, which is always the case in our experimental situation, the final output state can be approximated as

$$|\psi\rangle \approx (1 + g\hat{a}_s^\dagger \hat{a}_i^\dagger)|\alpha\rangle_s|0\rangle_i = |\alpha\rangle_s|0\rangle_i + g\hat{a}_s^\dagger|\alpha\rangle_s|1\rangle_i \qquad (2)$$

(where g is a gain constant with $|g| \ll 1$), and the output signal mode will contain the original coherent state most of the times, except for the few cases when the state $|1\rangle_i$ is detected in the idler output mode; these relatively rare detection events project the signal state into the SPACS $|\alpha,1\rangle_s$ (Fig. 2B), which corresponds to the stimulated emission of one photon in the same mode of $|\alpha\rangle$. The absence of a seed coherent field leaves with the usual expression for the spontaneous process, so that, by studying the evolution of the quantum state while the amplitude α gradually increases from zero, one can actually witness the smooth transition from the spontaneous to the stimulated regimes of light emission, with the transformation of an initial purely quantum state (the single-photon Fock state) into a classical coherent one. This is accompanied by the birth of a well-defined phase and can be described in more visual terms as the transition from the particlelike to the wavelike behaviors of the electromagnetic field.

The same state as described by Eq. 2 has recently been generated (*8*) to produce arbitrary superpositions of zero- and one-photon states. In that case, however, the conditioning was performed upon the detection of a single photon in the same mode $|1\rangle_s$ of the input coherent state, so that the final state was completely different from the ones investigated here and, for low α values, of the form $(\alpha|0\rangle_i + g|1\rangle_i)$. The injection of a single photon instead of a coherent state as a seed for conditional parametric amplification has also been investigated (*9*) and experimentally demonstrated (*10*, *11*) with the amplification to the $|2\rangle_s$ Fock state in the context of quantum cloning.

The primary light source for the experiment is a mode-locked laser whose pulses are frequency-doubled to become the pump for degenerate parametric down-conversion in a type-I beta-barium borate (BBO) crystal. In this configuration, the output photons share the same linear polarization and exactly the same wavelength, corresponding to twice that of the pump. In order to nonlocally select a pure state on the signal channel, idler photons undergo narrow spatial and frequency filtering before being detected by a single-photon counting module (*12*–*15*). The weak seed coherent state $|\alpha\rangle$ is obtained by controlled attenuation of a small portion of the laser emission, which is fed into the signal mode of the nonlinear crystal and is then directed to a 50% beam splitter. Here it is overlapped with a second (intense) coherent state (again obtained from a portion of the original laser pulses), which is spatially and temporally matched to the conditionally prepared SPACS and serves as the local oscillator (LO) for homodyne measurements, which are performed with a recently developed high-frequency time-domain technique (*4*, *16*, *17*).

Balanced homodyne detection (*18*–*20*) allows the measurement of the electric field quadratures of an unknown state as a function of the relative phase θ imposed between such a state and the reference LO. By performing a series of homodyne measurements on equally prepared states, it is possible to obtain the probability distributions $p(x,\theta)$ of the quadrature operator $\hat{x}_\theta = \frac{1}{2}\left(\hat{a}^\dagger e^{i\theta} + \hat{a}e^{-i\theta}\right)$ and, given a sufficient number of quadrature distributions for different values of θ, one is able to reconstruct the density matrix elements and the Wigner function of the field state under study (*7*, *17*).

Figure 3 shows a sequence of reconstructed Wigner functions for increasing values of the seed coherent field amplitude α. The first one (Fig. 3A), obtained with a blocked input, corresponds to the single-photon Fock state (*3*, *4*). Because of the finite efficiency (measured to be about 59% in the present set of measurements) in the detection apparatus, a significant mixture with the vacuum state is present, which clearly allows classically impossible negative values to be reached around the center of the circularly symmetric (because of the undefined value of the phase)

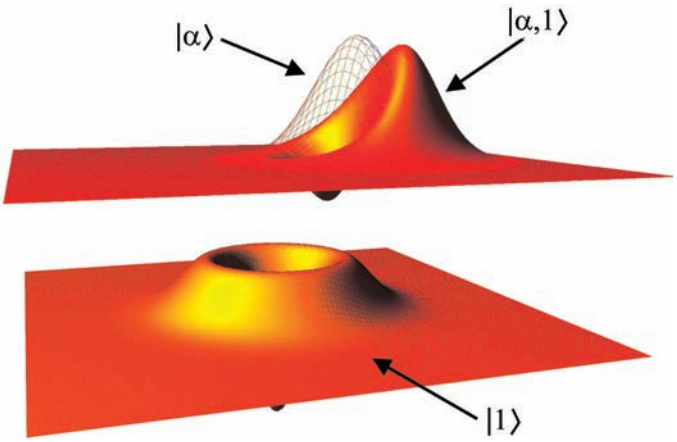

Fig. 1. Theoretical Wigner functions for some of the quantum states of light discussed in the text. Upper surface, SPACS $|\alpha,1\rangle$; wire-frame surface, original unexcited coherent state $|\alpha\rangle$; lower surface, single-photon Fock state $|1\rangle$. The horizontal plane coordinates represent two orthogonal quadratures of the field. The single-photon Wigner function is centered at the origin of the phase space. A value of $|\alpha|^2 = 1$ is used.

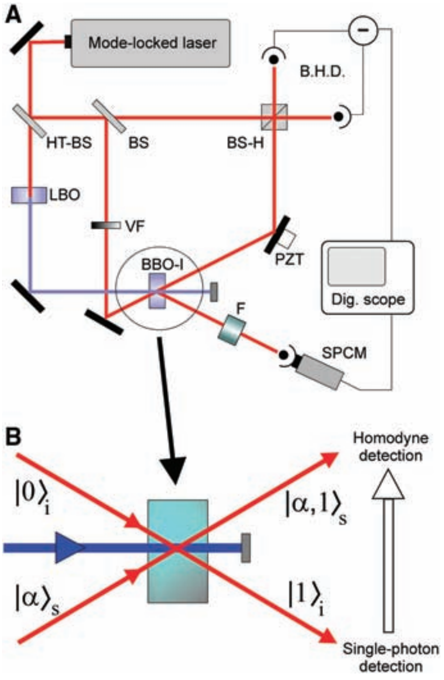

Fig. 2. Experimental apparatus and conceptual scheme for the conditional SPACS preparation. (**A**) Picosecond-duration pulses at 786 nm and at a repetition rate of 82 MHz from a mode-locked Ti:sapphire laser are split by a high-transmission (HT-BS) and a 50% (BS) beam splitter to serve as (i) the pump for spontaneous parametric down-conversion in a 3-mm-thick, type-I BBO crystal after frequency doubling in lithium triborate (LBO) crystal; (ii) the seed coherent field $|\alpha\rangle$, after proper attenuation by variable filters (VF); (iii) the local oscillator field for balanced homodyne detection (B.H.D.) after mixing with the investigated states in another 50% beam splitter (BS-H). F is a combination of spectral and spatial filters constituted by a pair of etalon interference filters with a narrow (50 GHz) spectral width, and by a single-spatial–mode optical fiber directly connected to a single-photon counting module (SPCM). PZT is a piezoelectric transducer used to vary the relative phase between the SPACS and the LO. Additional optics and computer-controlled optical delay lines to adjust the synchronization of the different pulses are not shown here for the sake of clarity. (**B**) The conditional preparation of a SPACS takes place whenever a “click”’ is registered on the single-photon detector placed in the output idler mode. Each of these detection events triggers the acquisition in the balanced homodyne detector analyzing the output signal mode (*17*).

distribution. When the coherent seed is initially switched on at very low intensity ($|\alpha|^2 \approx 0.09$; that is, an average of less than one photon every 10 pulses), the Wigner function starts to lose its circular symmetry while moving away from the origin because of the gradual appearance of a defined phase, but it still exhibits an evident nonclassical nature, as indicated by its partial negativity (Fig. 3B). For increasing seed amplitudes, negativity is gradually lost (Fig. 3C) and the ringlike wings in the distribution start to disappear, making it more and more similar to the Gaussian typical of a classical coherent field (Fig. 3, C and D). Even at relatively high input amplitude, the Wigner distribution for the SPACS $|\alpha,1\rangle$ clearly shows the effect of the one-photon excitation as compared to the corresponding, slightly displaced, unexcited $|\alpha\rangle$ state (Fig. 3D).

Although the SPACS Wigner function eventually becomes entirely positive for sufficiently high values of the seed amplitude, the excitation of an otherwise classical coherent state by a single photon leaves a measurable mark of nonclassicality in the field quadrature statistics (*1*). In particular, whereas the original coherent state has equal fluctuations in the different quadratures independently from its amplitude, the one-photon–excited state exhibits a smaller uncertainty (a squeezing) in one of the quadratures and larger fluctuations in the orthogonal one. One can interpret this as a reduction in the intensity noise associated with the excitation by a perfectly defined number of quanta, which also increases the phase noise because of the lack of phase information intrinsic to Fock states. Whereas Fig. 4 clearly shows the amount of maximum quadrature squeezing for different values of the coherent seed amplitude, the effect on the intensity and phase noise is also evident from Figs. 1 and 3C. Here the reduced intensity fluctuations appear in the decreased width along the radial direction, whereas the increase in the phase noise is indicated by the appearance of the ringlike wings along the tangential direction of the Wigner distribution.

The ability to experimentally investigate the elementary action of the bosonic creation operator on a classical state is of interest both as a tool to take a closer look at such fundamental events in quantum physics and as a starting point for the investigation of the fuzzy border that separates the quantum and classical regimes of light behavior, with natural extensions toward even more "exotic" quantum entities, such as Schroedinger's cat states (*21*).

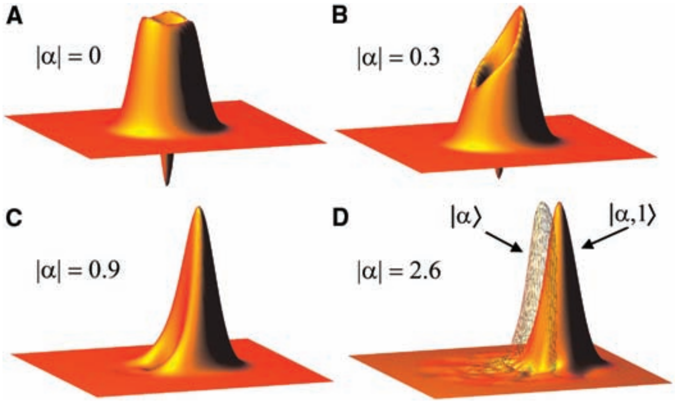

Fig. 3. Experimental Wigner functions for the SPACS. (**A**) Reconstructed Wigner function for the single-photon Fock state obtained without injection. (**B** to **D**) Same, but with an input coherent field of increasing amplitude. In (D), the reconstructed Wigner function for both the SPACS and the unexcited seed coherent state (wire-frame surface) are shown.

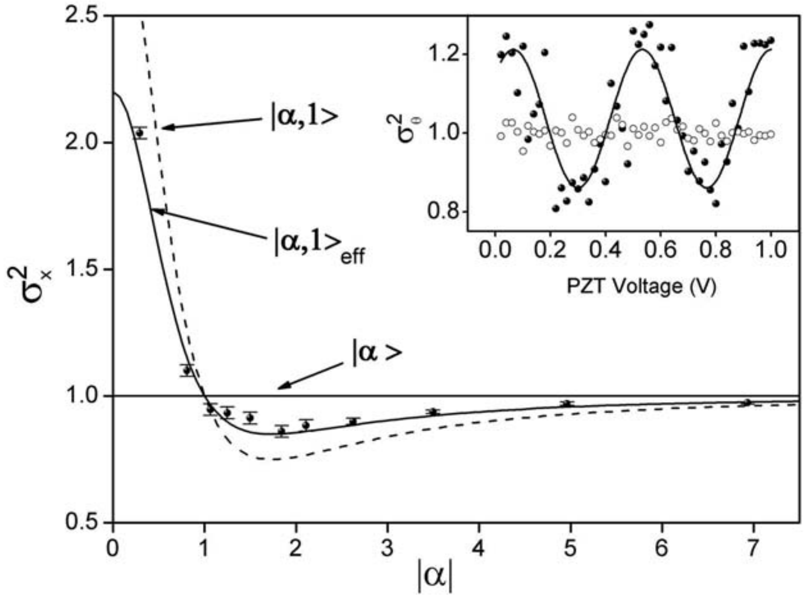

Fig. 4. Experimental squeezing data. Data points represent the variance in the SPACS field quadrature x_θ, which exhibits the maximum squeezing factor (about 15% for $|\alpha|$ between 1.5 and 2) normalized to the fluctuations of the coherent state $|\alpha\rangle$ (horizontal solid line). The dashed curve represents the theoretical prediction for a pure SPACS, whereas the solid one is calculated by taking into account the experimental detection efficiency. The measured variances for the different quadratures as a function of the phase θ (controlled by the PZT voltage) are shown in the inset for the states $|\alpha,1\rangle$ (solid circles) and $|\alpha\rangle$ (open circles) with $|\alpha| \approx 1.8$.

References and Notes

1. G. S. Agarwal, K. Tara, *Phys. Rev. A* **43**, 492 (1991).
2. A. I. Lvovsky, S. A. Babichev, *Phys. Rev. A* **66**, 011801 (2002).
3. A. I. Lvovsky *et al.*, *Phys. Rev. Lett.* **87**, 050402 (2001).
4. A. Zavatta, S. Viciani, M. Bellini, *Phys. Rev. A*, in press (e-print available at http://arxiv.org/abs/quant-ph/0406090).
5. L. Mandel, E. Wolf, *Optical Coherence and Quantum Optics* (Cambridge Univ. Press, Cambridge, 1995).
6. D. F. Walls, G. J. Milburn, *Quantum Optics* (Springer-Verlag, Berlin, 1994).
7. U. Leonhardt, *Measuring the Quantum State of Light* (Cambridge Univ. Press, Cambridge, 1997).
8. K. J. Resch, J. S. Lundeen, A. M. Steinberg, *Phys. Rev. Lett.* **88**, 113601 (2002).
9. Z. Y. Ou, L. J. Wang, L. Mandel, *J. Opt. Soc. Am. B* **7**, 211 (1990).
10. F. De Martini, V. Mussi, F. Bovino, *Opt. Commun.* **179**, 581 (2000).
11. A. Lamas-Linares, C. Simon, J. C. Howell, D. Bouwmeester, *Science* **296**, 712 (2002).
12. Z. Y. Ou, *Quantum Semiclass. Opt.* **9**, 599 (1997).
13. T. Aichele, A. I. Lvovsky, S. Schiller, *Eur. Phys. J. D* **18**, 237 (2002).
14. M. Bellini, F. Marin, S. Viciani, A. Zavatta, F. T. Arecchi, *Phys. Rev. Lett.* **90**, 043602 (2003).
15. S. Viciani, A. Zavatta, M. Bellini, *Phys. Rev. A* **69**, 053801 (2004).
16. A. Zavatta, M. Bellini, P. L. Ramazza, F. Marin, F. T. Arecchi, *J. Opt. Soc. Am. B* **19**, 1189 (2002).
17. Materials and methods are available as supporting material on *Science* Online.
18. S. Reynaud, A. Heidmann, E. Giacobino, C. Fabre, in *Progress in Optics*, E. Wolf, Ed. (Elsevier, Amsterdam, 1992), vol. 30, pp. 1–85.
19. G. Breitenbach, S. Schiller, J. Mlynek, *Nature* **387**, 471 (1997).
20. D. T. Smithey, M. Beck, M. G. Raymer, A. Faridani, *Phys. Rev. Lett.* **70**, 1244 (1993).
21. A. Montina, F. T. Arecchi, *Phys. Rev. A* **58**, 3472 (1998).
22. We thank F. T. Arecchi for helpful comments and for a critical reading of the manuscript. This work was performed in the frame of the "Spettroscopia laser e ottica quantistica" project of the Department of Physics of the University of Florence, with the support of the Italian Ministry of University and Scientific Research (MIUR) under the FIRB contract "Microdispositivi fotonici in Niobato di Litio."

Supporting Online Material

www.sciencemag.org/cgi/content/full/306/5696/660/DC1
Materials and Methods
References

23 July 2004; accepted 15 September 2004

Quantum State Transfer Between Matter and Light

D. N. Matsukevich and A. Kuzmich*

We report on the coherent quantum state transfer from a two-level atomic system to a single photon. Entanglement between a single photon (signal) and a two-component ensemble of cold rubidium atoms is used to project the quantum memory element (the atomic ensemble) onto any desired state by measuring the signal in a suitable basis. The atomic qubit is read out by stimulating directional emission of a single photon (idler) from the (entangled) collective state of the ensemble. Faithful atomic memory preparation and readout are verified by the observed correlations between the signal and the idler photons. These results enable implementation of distributed quantum networking.

The ability to coherently transfer quantum information between photonic- and material-based quantum systems is a prerequisite for all practical distributed quantum computation and scalable quantum communication protocols (*1*). The importance of this process is rooted in the fact that matter-based quantum systems provide excellent long-term quantum memory storage, whereas long-distance communication of quantum information will most certainly be accomplished by coherent propagation of light, often in the form of single photon pulses.

In the microwave domain, coherent quantum control has been obtained with single Rydberg atoms and single photons (*2*); important advances have also been made in ion trapping information processing (*3–5*). Particularly, an entangled state of an ion and a photon has been produced (*6*); however, to convert a single ion (atom) qubit state into a photonic state, strong coupling to a single cavity mode is required. Trapped atoms or ions localized inside high-finesse cavities offer a natural paradigm for coherent, reversible matter-light interactions (*7*, *8*), although technical challenges make these systems difficult to realize in practice.

Optically thick atomic ensembles have emerged recently as an alternative for the light-matter interface (*9*, *10*). Duan, Lukin, Cirac, and Zoller (DLCZ) (*11*) have made a theoretical proposal aimed at long-distance quantum communication that uses the quantum memory capability of atomic ensembles. Important initial steps toward realization of the DLCZ protocol have been made in which nonclassical radiation has been produced from an atomic ensemble, thereby demonstrating the collective enhancement (*12–15*).

Here, we report on the experimental realization of coherent quantum state transfer from a matter qubit onto a photonic qubit, using an optically thick cold atomic cloud. Our experiment involves three steps: (i) An entangled state between a single photon (signal) and a single collective excitation distributed over many atoms in two distinct optically thick atomic samples is generated. (ii) Measurement of the signal photon projects the atomic ensembles into a desired state, conditioned on the choice of the basis and the outcome of the measurement. This atomic state is a nearly maximally entangled state between two distinct atomic ensembles. (iii) This nearly maximally entangled atomic state is converted into a single photon (idler) emitted into a well-defined mode, without using a high-finesse cavity. These three ingredients constitute a complete set of tools required to build an arbitrary large-scale quantum network (*11*).

As illustrated in Fig. 1A, the classical laser pulses used in the generation and verification procedures define the two distinct pencil-shape components of the atomic ensemble that form our memory qubit, L and R. Figure 1B indicates schematically the structure of the four atomic levels involved, $|a\rangle$,$|b\rangle$, $|c\rangle$, and $|d\rangle$. The experimental sequence starts with all of the atoms prepared in state $|a\rangle$. A write pulse tuned to the $|a\rangle \rightarrow |c\rangle$ transition is split into two beams by a polarizing beam splitter (PBS1) and passed through the atomic sample. The light induces spontaneous Raman scattering on the $|c\rangle \rightarrow |b\rangle$ transition. The classical write pulse is so weak that less than one photon is scattered in this manner into the forward direction mode for each pulse in either L or R. The forward scattered mode is dominantly correlated with a distinct collective atomic state (*11*). In the first order of perturbation theory in the atom-light coupling χ, the atom-light state is

$$|\Psi\rangle \sim |a\rangle_1 \ldots |a\rangle_{N_L+N_R} |0_p\rangle_L |0_p\rangle_R + \chi \left(|L_a\rangle |1_p\rangle_L |0_p\rangle_R + |R_a\rangle |0_p\rangle_L |1_p\rangle_R \right) \tag{1}$$

We have defined two effective states of the atomic ensembles

$$|L_a\rangle = \sum_{i=1}^{N_L} g_i |a\rangle_1 \ldots |b\rangle_i \ldots |a\rangle_{N_L} \ldots |a\rangle_{N_L+N_R}$$
$$|R_a\rangle = \sum_{j=N_L+1}^{N_L+N_R} g_j |a\rangle_1 \ldots |a\rangle_{N_L} \ldots |b\rangle_j \ldots |a\rangle_{N_L+N_R} \tag{2}$$

with the weights g_i and g_j determined by the write field intensity distribution, $\sum_{i=1}^{N_L} |g_i|^2 = 1$, $\sum_{j=N_L+1}^{N_L+N_R} |g_j|^2 = 1$ (*16*, *17*). $|L_a\rangle$ and $|R_a\rangle$ have properties of a two-level system (qubit): $\langle L_a|L_a\rangle = 1$, $\langle R_a|R_a\rangle = 1$, and $\langle L_a|R_a\rangle = 0$. Although the interaction of the light with the atoms is nonsymmetric with respect to permutation of atoms, the second term in Eq. 1 in fact describes a strongly entangled atom-photon state in the sense of (*17*). Using PBS4 and a half-wave plate inserted into one of the channels, we map the two spatial modes associated with the two ensembles into a single spatial mode with polarization encoding of the light's origin: $|1_p\rangle_L \rightarrow |H\rangle_s$; $|1_p\rangle_R \rightarrow |V\rangle_s$, where H and V indicate horizontal and vertical polarization, respectively, and s denotes signal. Next, the light is passed through an arbitrary polarization state transformer $R_s(\theta_s,\phi_s)$ and a polarizer PBS5, so that the state at the output of PBS5 is

$$|H'\rangle = \cos(\theta_s) e^{i\phi_s} |H\rangle_s + \sin(\theta_s) |V\rangle_s \tag{3}$$

and is directed onto a single-photon detector D1. When D1 detects a photon, the joint state in Eq. 1 is projected into the desired atomic state

$$|\Psi_a\rangle = \cos(\theta_s)\, e^{-i\phi_s} |L_a\rangle + \sin(\theta_s)\, e^{i\eta_s} |R_a\rangle \tag{4}$$

which is an entangled state of the two atomic samples L and R. Phase η_s is determined by the difference in length of the two paths L and R. After a variable delay time Δt, we convert the atomic excitation into a single photon by illuminating the atomic ensemble with a pulse of light near resonant with the $|b\rangle \rightarrow |d\rangle$ transition. For an optically thick atomic sample, the photon will be emitted with high probability into the spatial mode determined by the write pulse (*11*, *16*), achieving memory read-out.

$$|\Psi_a\rangle = \cos(\theta_s)\, e^{-i\phi_s} |L_a\rangle + \sin(\theta_s)\, e^{i\eta_s} |R_a\rangle \rightarrow |\Psi\rangle_i = \cos(\theta_s)\, e^{-i\phi_s} |H\rangle_i + \sin(\theta_s)\, e^{i(\eta_i+\eta_s)} |V\rangle_i \tag{5}$$

That is, the polarization state of the idler photon i is uniquely determined by the observed state of the signal photon. Alternatively, one could store the signal in a fiber

---

School of Physics, Georgia Institute of Technology, Atlanta, GA 30332, USA.

*To whom correspondence should be addressed. E-mail: alex.kuzmich@physics.gatech.edu.

until after the readout. In that case, the two-photon signal-idler state would be a maximally entangled state:

$$|\Psi_M\rangle = \frac{1}{\sqrt{2}}(|H\rangle_s|H\rangle_i + e^{i(\eta_s+\eta_i)}|V\rangle_s|V\rangle_i) \qquad (6)$$

A magneto-optical trap (MOT) of ^{85}Rb is used to provide an optically thick atomic cloud for our experiment (Fig. 1). The ground states $\{|a\rangle;|b\rangle\}$ correspond to the $5S_{1/2},F = \{3,2\}$ levels of ^{85}Rb, while the excited states $\{|c\rangle;|d\rangle\}$ represent the $\{5P_{3/2},F = 3;5P_{1/2},F = 2\}$ levels of the $\{D_2, D_1\}$ lines at {780;795} nm, respectively. The experimental sequence starts with all of the atoms prepared in state $|a\rangle$ by optical pumping, after shutting off the trapping and cooling light.

A 140-ns-long write pulse tuned to the $|a\rangle \rightarrow |c\rangle$ transition is split into two beams by a polarizing beam splitter PBS1 and focused into two regions of the MOT about 1 mm apart, with Gaussian waists of about 50 μm. PBS2 and PBS3 separate the horizontally polarized component of the forward scattered light from the vertically polarized classical pulse. After being mixed by PBS4, the light goes through the quarter- and the half-wave plates that provide the state transformation $R_s(\theta_s,\phi_s)$. The light continues to another polarizer, PBS5, and is directed to a single photon detector D1. Detection of one photon by D1 prepares the atomic ensemble in any desired state in the basis of $|L_a\rangle$, $|R_a\rangle$ determined by $R_s(\theta_s,\phi_s)$, and thereby concludes the preparation of the quantum memory qubit.

Following memory state preparation, the read-out stage is performed. After a user-programmable delay, Δt, a 115-ns-long read pulse tuned to the $|b\rangle \rightarrow |d\rangle$ transition illuminates the two atomic ensembles. This accomplishes a transfer of the memory state onto the single photon (idler) emitted by the $|d\rangle \rightarrow |a\rangle$ transition. After passing through the state transformer $R_i(\theta_i,\phi_i)$ and PBS6, the two polarization components are directed onto single-photon detectors (D2, D3), thus accomplishing measurement of the idler photon, and hence the memory qubit, on a controllable arbitrary basis.

As in any real experiment, various imperfections prevent the read-out of the quantum memory (idler photon) from being identical to the state that we intended to write into the memory. To quantify the degree to which we faithfully prepare and read out the quantum memory, we measure the polarization correlations between the signal and idler photons.

The observed correlations allow us to characterize the extent to which our procedures are working. To investigate the storage capabilities of our memory qubit quantitatively, we use time-resolved detection of the signal and idler photons for two values of delay Δt between the application of the write and read pulses, 100 ns and 200 ns. The electronic pulses from the detectors are gated, with 250-ns and 140-ns windows centered on the time determined by the write and read light pulses, respectively. Afterward, the electronic pulses are fed into a time-interval analyzer (with $\delta = 2$ ns time resolution). To measure the correlation between the photons produced by the write and read pulses, the output of D1 is fed into the "start" input of a time-interval analyzer, and the outputs of D2 and D3 are fed into two "stop" inputs. A coincidence window imposed by the data acquisition software selects a time interval between the arrival of the idler and signal of (0,80) ns for $\Delta t = 100$ ns and (25,145) ns for $\Delta t = 200$ ns.

We first measure the conditional probabilities of detecting a certain state of the idler (hence, of the quantum memory state) in the basis of $|H\rangle_i$ and $|V\rangle_i$, given the observed state of the signal photon. Varying the angle θ_s produces the correlation patterns shown in

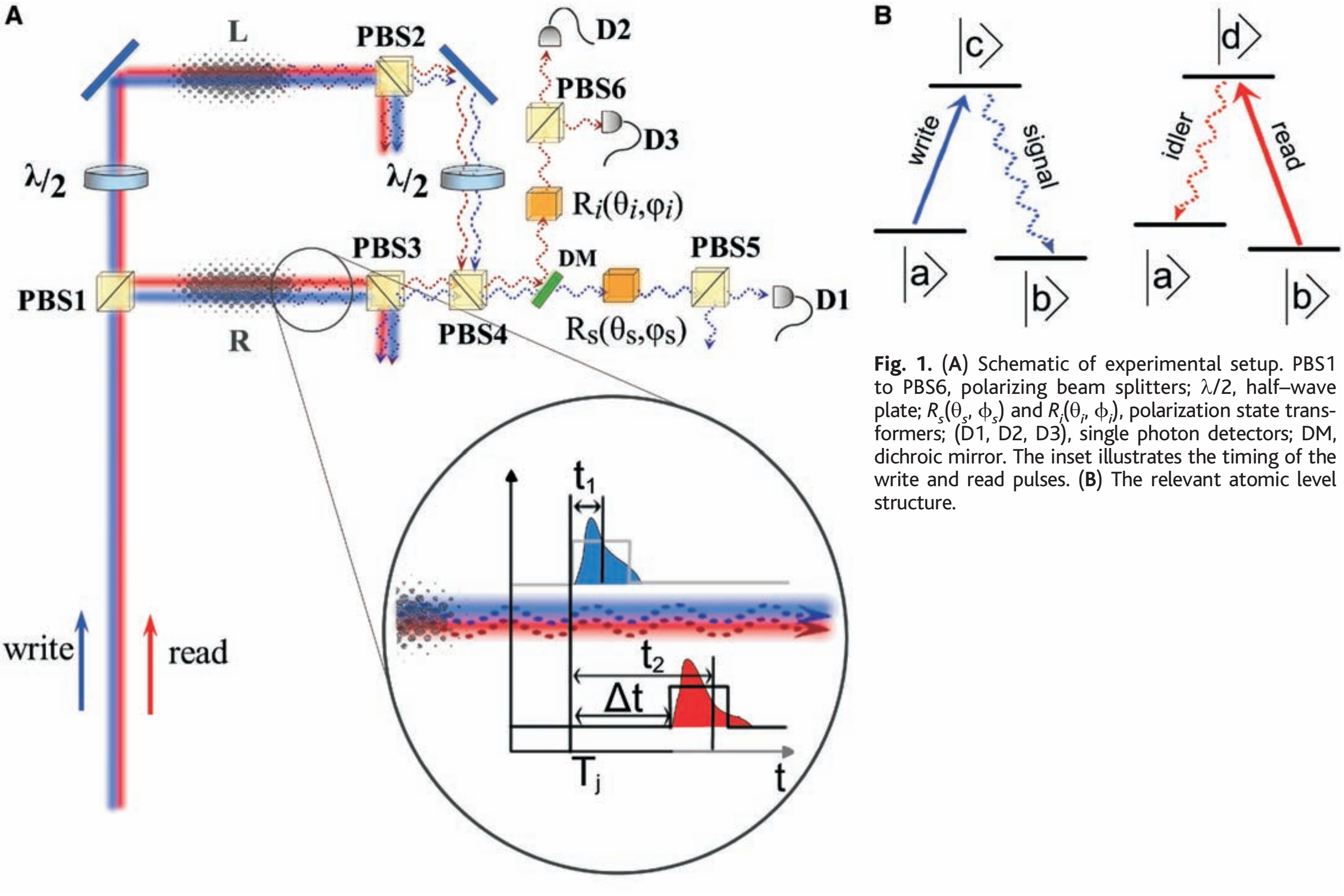

Fig. 1. (**A**) Schematic of experimental setup. PBS1 to PBS6, polarizing beam splitters; λ/2, half–wave plate; $R_s(\theta_s, \phi_s)$ and $R_i(\theta_i, \phi_i)$, polarization state transformers; (D1, D2, D3), single photon detectors; DM, dichroic mirror. The inset illustrates the timing of the write and read pulses. (**B**) The relevant atomic level structure.

Fig. 2A for Δt = 100 ns. Conditional probabilities at the point of maximum correlation are shown in Fig. 2B and the first line of Table 1. To verify faithful memory preparation and readout, we repeat the correlation measurement in a different basis, that of states $(|H\rangle_i \pm |V\rangle_i)/\sqrt{2}$, by choosing $\theta_i = 45°$, $\phi_i = 0°$, and $\phi_s = -(\eta_s + \eta_i)$ in the state transformers R_s and R_i. We vary θ_s, with the measured interference fringes displayed in Fig. 3A. Table 1 (second line) and Fig. 3B show the conditional probabilities at the point of maximum correlations. These probabilities are different from 1/2 only when the phase coherence between the two states of the atomic qubit is preserved in the matter-to-light quantum state mapping.

From these measured correlations, we determine the fidelity of the reconstruction of our intended quantum memory state $|\Psi_I\rangle$ in the idler, $|\langle\Psi_I|\Psi_i\rangle|^2$. The fidelity is given by the value of the corresponding conditional probability at the point of maximum correlation, presented in Table 1 (we choose the lower of the two values as the lower bound). For states in the $\theta_i = 0°$ basis, we find $F_0 = 0.88 \pm 0.03$, clearly exceeding the classical boundary of 2/3 (*18*). For the $\theta_i = 45°$ basis, we found $F_{45} = 0.75 \pm 0.02$, again substantially violating the classical limit. These fidelities give a lower bound for both the fidelities of the memory preparation and the read-out steps, which we do not measure separately.

Another way to quantify the performance of our quantum state transfer is to calculate the fidelity of entanglement between the signal and idler photons F_{si}. The lower bound on F_{si} is given by the overlap of the measured density matrix, with the maximally entangled state we seek to achieve, $|\Psi_M\rangle$, given by Eq. 6: $F_{si} = \langle\Psi_M \mid \rho_{si} \mid\Psi_M\rangle$ (*19*). We calculated $F_{si} = 0.67 \pm 0.02$, substantially greater than the classical limit of 1/2 (*6*, *19*).

At a longer delay of 200 ns, the fidelities in the $\theta_i = 0°$ and $\theta_i = 45°$ bases are $F_0 = 0.79 \pm 0.04$ and $F_{45} = 0.74 \pm 0.04$, while fidelity of entanglement is $F_{si} = 0.63 \pm 0.03$. For both values of Δ*t*, we analyze the fidelity of entanglement as a function of the delay between the detections of the signal and the idler. We split the full coincidence window into four equal intervals and calculated entanglement of formation for each one (Fig. 4). From these results, we conclude that our quantum memory has a useful operational time of about 150 ns. The lifetime of coherence between levels $|a\rangle$ and $|b\rangle$ determines the lifetime of the quantum memory and is limited by the magnetic field of the trapping quadrupole field of the MOT (*12*).

Nonzero coincidence counts in the minima of Fig. 2A are due to transmission losses and nonideal spatial correlations between the signal and idler photons. The residual interferometric drifts in $\eta_s + \eta_i$ further reduce the visibility of Fig. 3A compared with Fig. 2A, resulting in a degradation of the fidelities. Losses also reduce the rate of entanglement generation. The rate of signal photon detections (and hence, atomic qubit preparation) is given by $R_s = \alpha n_s R \cong 300\ s^{-1}$, where $\alpha = 0.05$ is the measured transmission efficiency for the write beam (which includes 0.60 detection efficiency) and $R = 4.7 \times 10^5\ s^{-1}$ is the repetition rate of the experiment. Therefore, the inferred average photon number in the forward scattered mode per pulse is $n_s \cong 1.4 \times 10^{-2}$. The coincident signal-idler detection rate is $R_{si} = \zeta R_s = \zeta\alpha n_s R \cong 0.4\ s^{-1}$, where $\zeta \equiv \beta\xi \cong 1.1 \times 10^{-3}$. The measured transmission and de-

Fig. 2. (**A**) Measured conditional probabilities $P(H_i|H_s)$ and $P(V_i|H_s)$ as the function of the polarization rotation θ_s of the signal photon. The full curves are fits with the visibility as the only adjustable parameter. (**B**) Measured conditional probabilities at the points of highest correlation.

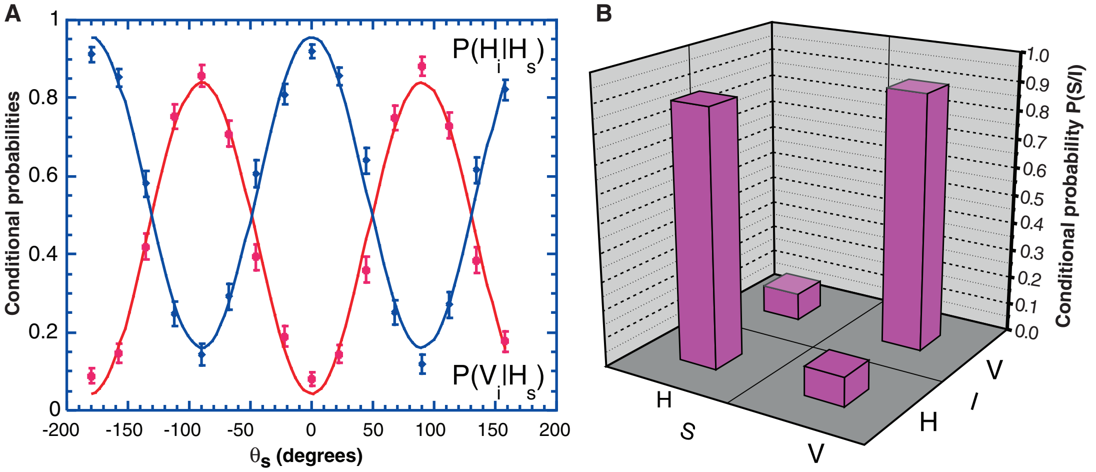

Fig. 3. (**A**) Measured conditional probabilities after $\theta_i = \pi/4$ polarization rotation of the idler photon as the function of θ_s. (**B**) Measured conditional probabilities at the points of highest correlation.

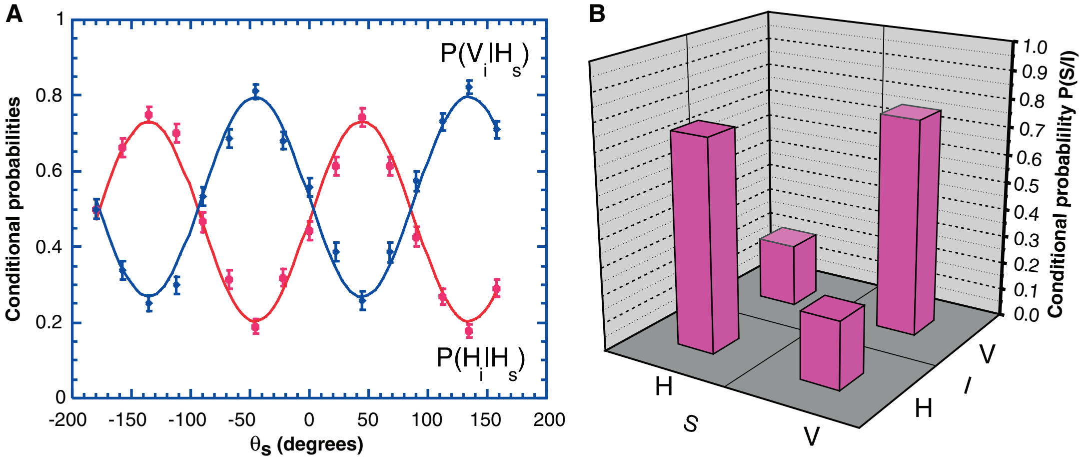

Table 1. Conditional probabilities $P(I|S)$ to detect the idler photon in state I given detection of the signal photon in state S, at the point of maximum correlation for $\Delta t = 100$ ns delay between read and write pulses; all the errors are based on counting statistics of coincidence events.

Basis	$P(H_i\|H_s)$	$P(V_i\|H_s)$	$P(V_i\|V_s)$	$P(H_i\|V_s)$
0°	0.92 ± 0.02	0.08 ± 0.02	0.88 ± 0.03	0.12 ± 0.03
45°	0.75 ± 0.02	0.25 ± 0.02	0.81 ± 0.02	0.19 ± 0.02

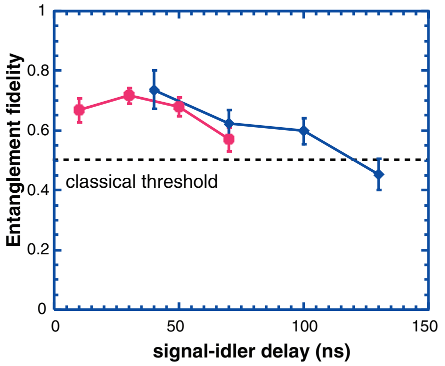

Fig. 4. Time-dependent entanglement fidelity of the signal and the idler F_{si}; circles for Δt = 100 ns, diamonds for Δt = 200 ns.

tection efficiency for the read beam is $\beta \cong 0.04$, so we infer the efficiency of quantum state transfer from the atoms onto the photon, $\xi \cong 0.03$.

We have realized a quantum node by combining the entanglement of atomic and photonic qubits with the atom-photon quantum state transfer. By implementing the second node at a different location and performing a joint detection of the signal photons from the two nodes, the quantum repeater protocol (*11*), as well as distant teleportation of an atomic qubit, may be realized. Based on this work, we estimate the rate for these protocols to be $R_2 \cong (\beta\xi\alpha n_s)^2 R \cong 3 \times 10^{-7} s^{-1}$. However, improvements in ξ that are based on increasing the optical thickness of atomic samples (*16*), as well as elimination of transmission losses, could provide several orders of magnitude increase in R_2. Our results also demonstrate the possibility of realizing quantum nodes consisting of multiple atomic qubits by using multiple beams of light. This approach shows promise for implementation of distributed quantum computation (*20*, *21*).

References and Notes

1. I. Chuang, M. Nielsen, *Quantum Computation and Quantum Information* (Cambridge Univ. Press, Cambridge, 2000).
2. S. Haroche, J. M. Raimond, M. Brune, in *Experimental Quantum Computation and Information*, F. de Martini, C. Monroe, Eds. (Proceedings of the International School of Physics Enrico Fermi, course CXLVIII, IOS Press, Amsterdam, 2002), pp. 37–66.
3. C. A. Sackett *et al.*, *Nature* **404**, 256 (2000).
4. M. D. Barrett *et al.*, *Nature* **429**, 737 (2004).
5. M. Riebe *et al.*, *Nature* **429**, 734 (2004).
6. B. B. Blinov, D. L. Moehring, L.-M. Duan, C. Monroe, *Nature* **428**, 153 (2004).
7. S. Bose, P. L. Knight, M. B. Plenio, V. Vedral, *Phys. Rev. Lett.* **83**, 5158 (1999).
8. H. J. Kimble, *Phys. Scr.* **76**, 127 (1998).
9. A. Kuzmich, E. S. Polzik, in *Quantum Information with Continuous Variables*, S. L. Braunstein, A. K. Pati, Eds. (Kluwer, Dordrecht, 2003).
10. M. D. Lukin, *Rev. Mod. Phys.* **75**, 457 (2003).
11. L.-M. Duan, M. D. Lukin, I. J. Cirac, P. Zoller, *Nature* **414**, 413 (2001).
12. A. Kuzmich *et al.*, *Nature* **423**, 731 (2003).
13. C. H. van der Wal *et al.*, *Science* **301**, 196 (2003).
14. W. Jiang, C. Han, P. Xue, L.-M. Duan, G. C. Guo, *Phys. Rev. A.* **69**, 043819 (2004).
15. C. W. Chou, S. V. Polyakov, A. Kuzmich, H. J. Kimble, *Phys. Rev. Lett.* **92**, 213601 (2004).
16. L.-M. Duan, J. I. Cirac, P. Zoller, *Phys. Rev. A.* **66**, 023818 (2002).
17. A. Kuzmich, T. A. B. Kennedy, *Phys. Rev. Lett.* **92**, 030407 (2004).
18. M. Horodecki, P. Horodecki, R. Horodecki, *Phys. Rev. A.* **60**, 1888 (1994).
19. C. H. Bennett, D. P. DiVincenzo, J. A. Smolin, W. K. Wooters, *Phys. Rev. A.* **54**, 3824 (1996).
20. Y. L. Lim, A. Beige, L. C. Kwek, www.arXiv.org/quant-ph/0408043.
21. S. D. Barrett, P. Kok, www.arXiv.org/quant-ph/0408040.
22. We acknowledge fruitful conversations with T. A. B. Kennedy, J. A. Sauer, L. You, A. Zangwill and, particularly, M. S. Chapman and thank R. Smith and E. T. Neumann for experimental assistance. This work was supported by NASA and the Research Corporation.

28 July 2004; accepted 16 September 2004

Electric Field Effect in Atomically Thin Carbon Films

K. S. Novoselov,[1] A. K. Geim,[1]* S. V. Morozov,[2] D. Jiang,[1]
Y. Zhang,[1] S. V. Dubonos,[2] I. V. Grigorieva,[1] A. A. Firsov[2]

We describe monocrystalline graphitic films, which are a few atoms thick but are nonetheless stable under ambient conditions, metallic, and of remarkably high quality. The films are found to be a two-dimensional semimetal with a tiny overlap between valence and conductance bands, and they exhibit a strong ambipolar electric field effect such that electrons and holes in concentrations up to 10^{13} per square centimeter and with room-temperature mobilities of ~10,000 square centimeters per volt-second can be induced by applying gate voltage.

The ability to control electronic properties of a material by externally applied voltage is at the heart of modern electronics. In many cases, it is the electric field effect that allows one to vary the carrier concentration in a semiconductor device and, consequently, change an electric current through it. As the semiconductor industry is nearing the limits of performance improvements for the current technologies dominated by silicon, there is a constant search for new, nontraditional materials whose properties can be controlled by the electric field. The most notable recent examples of such materials are organic conductors (*1*) and carbon nanotubes (*2*). It has long been tempting to extend the use of the field effect to metals [e.g., to develop all-metallic transistors that could be scaled down to much smaller sizes and would consume less energy and operate at higher frequencies than traditional semiconducting devices (*3*)]. However, this would require atomically thin metal films, because the electric field is screened at extremely short distances (<1 nm) and bulk carrier concentrations in metals are large compared to the surface charge that can be induced by the field effect. Films so thin tend to be thermodynamically unstable, becoming discontinuous at thicknesses of several nanometers; so far, this has proved to be an insurmountable obstacle to metallic electronics, and no metal or semimetal has been shown to exhibit any notable (>1%) field effect (*4*).

We report the observation of the electric field effect in a naturally occurring two-dimensional (2D) material referred to as few-layer graphene (FLG). Graphene is the name given to a single layer of carbon atoms densely packed into a benzene-ring structure, and is widely used to describe properties of many carbon-based materials, including graphite, large fullerenes, nanotubes, etc. (e.g., carbon nanotubes are usually thought of as graphene sheets rolled up into nanometer-sized cylinders) (*5*–*7*). Planar graphene itself has been presumed not to exist in the free state, being unstable with respect to the formation of curved structures such as soot, fullerenes, and nanotubes (*5*–*14*).

---

[1] Department of Physics, University of Manchester, Manchester M13 9PL, UK. [2] Institute for Microelectronics Technology, 142432 Chernogolovka, Russia.

*To whom correspondence should be addressed. E-mail: geim@man.ac.uk

We have been able to prepare graphitic sheets of thicknesses down to a few atomic layers (including single-layer graphene), to fabricate devices from them, and to study their electronic properties. Despite being atomically thin, the films remain of high quality, so that 2D electronic transport is ballistic at submicrometer distances. No other film of similar thickness is known to be even poorly metallic or continuous under ambient conditions. Using FLG, we demonstrate a metallic field-effect transistor in which the conducting channel can be switched between 2D electron and hole gases by changing the gate voltage.

Our graphene films were prepared by mechanical exfoliation (repeated peeling) of small mesas of highly oriented pyrolytic graphite (*15*). This approach was found to be highly reliable and allowed us to prepare FLG films up to 10 μm in size. Thicker films ($d \geq 3$ nm) were up to 100 μm across and visible by the naked eye. Figure 1 shows examples of the prepared films, including single-layer graphene [see also (*15*)]. To study their electronic properties, we processed the films into multiterminal Hall bar devices placed on top of an oxidized Si substrate so that a gate voltage V_g could be applied. We have studied more than 60 devices with $d < 10$ nm. We focus on the electronic properties of our thinnest (FLG) devices, which contained just one, two, or three atomic layers (*15*). All FLG devices exhibited essentially identical electronic properties characteristic for a 2D semimetal, which differed from a more complex (2D plus 3D) behavior observed for thicker, multilayer graphene (*15*) as well as from the properties of 3D graphite.

In FLG, the typical dependence of its sheet resistivity ρ on gate voltage V_g (Fig. 2) exhibits a sharp peak to a value of several kilohms and decays to ~100 ohms at high V_g (note that 2D resistivity is given in units of ohms rather than ohms × cm as in the 3D case). Its conductivity $\sigma = 1/\rho$ increases linearly with V_g on both sides of the resistivity peak (Fig. 2B). At the same V_g where ρ has its peak, the Hall coefficient R_H exhibits a sharp reversal of its sign (Fig. 2C). The observed behavior resembles the ambipolar field effect in semiconductors, but there is no zero-conductance region associated with the Fermi level being pinned inside the band gap.

Our measurements can be explained quantitatively by a model of a 2D metal with a small overlap $\delta\varepsilon$ between conductance and valence bands (*15*). The gate voltage induces a surface charge density $n = \varepsilon_0 \varepsilon V_g/te$ and, accordingly, shifts the position of the Fermi energy ε_F. Here, ε_0 and ε are the permittivities of free space and SiO$_2$, respectively; e is the electron charge; and t is the thickness of our SiO$_2$ layer (300 nm). For typical $V_g = 100$ V, the formula yields $n \approx 7.2 \times 10^{12}$ cm^{-2}. The electric field doping transforms the shallow-overlap semimetal into either completely electron or completely hole conductor through a mixed state where both electrons and holes are present (Fig. 2). The three regions of electric field doping are clearly seen on both experimental and theoretical curves. For the regions with only electrons or holes left, R_H decreases with increasing carrier concentration in the usual way, as $1/ne$. The resistivity also follows the standard dependence $\rho^{-1} = \sigma = ne\mu$ (where μ is carrier mobility). In the mixed state, σ changes little with V_g, indicating the substitution of one type of carrier with another, while the Hall coefficient reverses its sign, reflecting the fact that R_H is proportional to

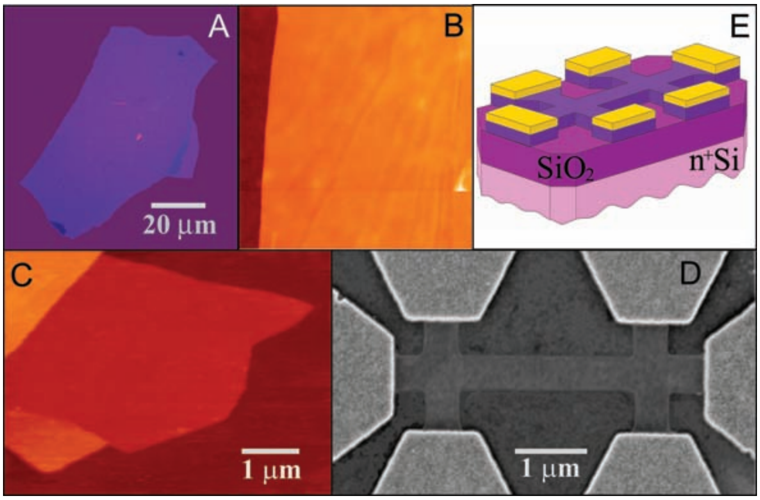

Fig. 1. Graphene films. (**A**) Photograph (in normal white light) of a relatively large multilayer graphene flake with thickness ~3 nm on top of an oxidized Si wafer. (**B**) Atomic force microscope (AFM) image of 2 μm by 2 μm area of this flake near its edge. Colors: dark brown, SiO$_2$ surface; orange, 3 nm height above the SiO$_2$ surface. (**C**) AFM image of single-layer graphene. Colors: dark brown, SiO$_2$ surface; brown-red (central area), 0.8 nm height; yellow-brown (bottom left), 1.2 nm; orange (top left), 2.5 nm. Notice the folded part of the film near the bottom, which exhibits a differential height of ~0.4 nm. For details of AFM imaging of single-layer graphene, see (*15*). (**D**) Scanning electron microscope image of one of our experimental devices prepared from FLG. (**E**) Schematic view of the device in (D).

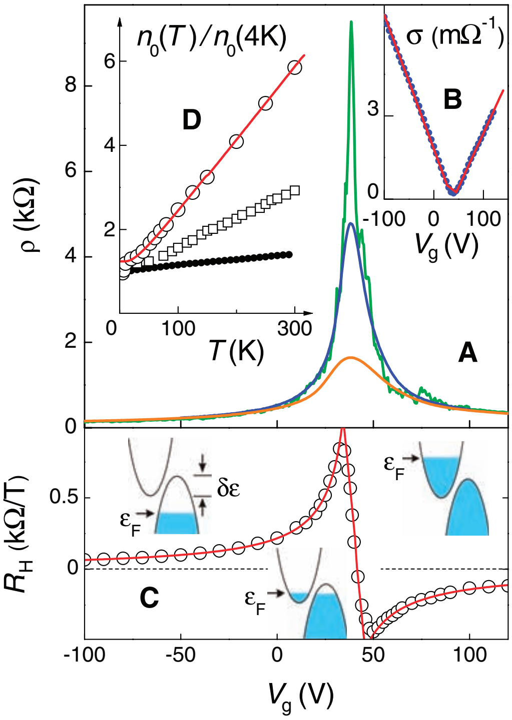

Fig. 2. Field effect in FLG. (**A**) Typical dependences of FLG's resistivity ρ on gate voltage for different temperatures (T = 5, 70, and 300 K for top to bottom curves, respectively). (**B**) Example of changes in the film's conductivity $\sigma = 1/\rho(V_g)$ obtained by inverting the 70 K curve (dots). (**C**) Hall coefficient R_H versus V_g for the same film; T = 5 K. (**D**) Temperature dependence of carrier concentration n_0 in the mixed state for the film in (A) (open circles), a thicker FLG film (squares), and multilayer graphene ($d \approx 5$ nm; solid circles). Red curves in (B) to (D) are the dependences calculated from our model of a 2D semimetal illustrated by insets in (C).

the difference between electron and hole concentrations.

Without electric field doping (at zero V_g), FLG was found to be a hole metal, which is seen as a shift of the peak in ρ to large positive V_g. However, this shift is attributed to an unintentional doping of the films by absorbed water (*16*, *17*). Indeed, we found that it was possible to change the position of the peak by annealing our devices in vacuum, which usually resulted in shifting of the peak close to zero voltages. Exposure of the annealed films to either water vapor or NH_3 led to their p- and n-doping, respectively (*15*). Therefore, we believe that intrinsic FLG is a mixed-carrier material.

Carrier mobilities in FLG were determined from field-effect and magnetoresistance measurements as $\mu = \sigma(V_g)/en(V_g)$ and $\mu = R_H/\rho$, respectively. In both cases, we obtained the same values of μ, which varied from sample to sample between 3000 and 10,000 $cm^2/V{\cdot}s$. The mobilities were practically independent of absolute temperature T, indicating that they were still limited by scattering on defects. For $\mu \approx 10{,}000$ $cm^2/V{\cdot}s$ and our typical $n \approx 5 \times 10^{12}$ cm^{-2}, the mean free path is ~0.4 μm, which is surprising given that the 2D gas is at most a few Å away from the interfaces. However, our findings are in agreement with equally high μ observed for intercalated graphite (*5*), where charged dopants are located next to graphene sheets. Carbon nanotubes also exhibit very high μ, but this is commonly attributed to the suppression of scattering in the 1D case. Note that for multilayer graphene, we observed mobilities up to ~15,000 $cm^2/V{\cdot}s$ at 300 K and ~60,000 $cm^2/V{\cdot}s$ at 4 K.

Despite being essentially gigantic fullerene molecules and unprotected from the environment, FLG films exhibit pronounced Shubnikov–de Haas (ShdH) oscillations in both longitudinal resistivity ρ_{xx} and Hall resistivity ρ_{xy} (Fig. 3A), serving as another indicator of the quality and homogeneity of the experimental system. Studies of ShdH oscillations confirmed that electronic transport in FLG was strictly 2D, as one could reasonably expect, and allowed us to fully characterize its charge carriers. First, we carried out the standard test and measured ShdH oscillations for various angles θ between the magnetic field and the graphene films. The oscillations depended only on the perpendicular component of the magnetic field $B{\cdot}\cos\theta$, as expected for a 2D system. More important, however, we found a linear dependence of ShdH oscillations' frequencies B_F on V_g (Fig. 3B), indicating that the Fermi energies ε_F of holes and electrons were proportional to their concentrations n. This dependence is qualitatively different from the 3D dependence $\varepsilon_F \propto n^{2/3}$ and proves the 2D nature of charge carriers in FLG. Further analysis (*15*) of ShdH oscillations showed that only a single spatially quantized 2D subband was occupied up to the maximum concentrations achieved in our experiments (~3×10^{13} cm^{-2}). It could be populated either by electrons with mass $m_e \approx 0.06m_0$ (where m_0 is the free electron mass) located in two equivalent valleys, or by light and heavy holes with masses of ~$0.03m_0$ and ~$0.1m_0$ and the double-valley degeneracy. These properties were found to be the same for all FLG films studied and are notably different from the electronic structure of both multilayer graphene (*15*) and bulk graphite (*5*–*7*). Note that graphene is expected (*5*–*7*) to have the linear energy dispersion and carriers with zero mass, and the reason why the observed behavior is so well described by the simplest free-electron model remains to be understood (*15*).

We also determined the band overlap $\delta\varepsilon$ in FLG, which varied from 4 to 20 meV for different samples, presumably indicating a different number of graphene layers involved (*18*). To this end, we first used a peak value ρ_m of resistivity to calculate typical carrier concentrations in the mixed state, n_0 (e.g., at low T for the sample in Fig. 2, A to C, with $\mu \approx 4000$ cm^2/V and $\rho_m \approx 8$ kilohms, n_0 was ~2×10^{11} cm^{-2}). Then, $\delta\varepsilon$ can be estimated as n_0/D, where $D = 2m_e/\pi\hbar^2$ is the 2D density of electron states and $\hbar$ is Planck's constant divided by 2π. For the discussed sample, this yields $\delta\varepsilon \approx 4$ meV [i.e., much smaller than the overlap in 3D graphite (~40 meV)]. Alternatively, $\delta\varepsilon$ could be calculated from the temperature dependence of n_0, which characterizes relative contributions of intrinsic and thermally excited carriers. For a 2D semimetal, $n_0(T)$ varies as $n_0(0\ \text{K}){\cdot}f{\cdot}\ln[1 + \exp(1/f)]$, where $f = 2k_BT/\delta\varepsilon$ and k_B is Boltzmann's constant; Fig. 2D shows the best fit to this dependence, which yields $\delta\varepsilon \approx 6$ meV. Different FLG devices were found to exhibit a ratio of $n_0(300\ \text{K})/n_0(0)$ between 2.5 and 7, whereas for multilayer graphene it was only ~1.5 (Fig. 2D). This clearly shows that $\delta\varepsilon$ decreases with decreasing number of graphene layers. The observed major reduction of $\delta\varepsilon$ is in agreement with the fact that single-layer graphene is in theory a zero-gap semiconductor (*5*, *18*).

Graphene may be the best possible metal for metallic transistor applications. In addition to the scalability to true nanometer sizes envisaged for metallic transistors, graphene also offers ballistic transport, linear current-voltage (*I-V*) characteristics, and huge sustainable currents (>10^8 A/cm^2) (*15*). Graphene transistors show a rather modest on-off resistance ratio (less than ~30 at 300 K; limited because

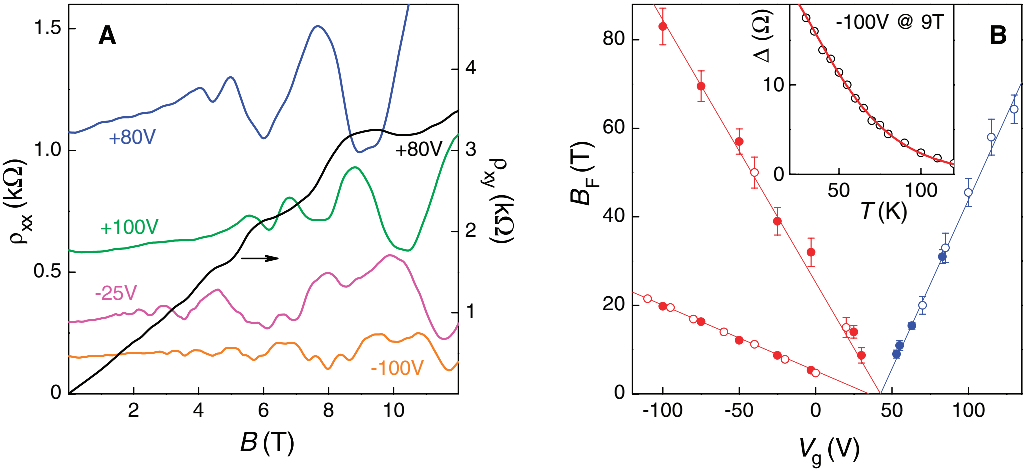

Fig. 3. (**A**) Examples of ShdH oscillations for one of our FLG devices for different gate voltages; T = 3 K, and B is the magnetic field. As the black curve shows, we often observed pronounced plateau-like features in ρ_{xy} at values close to $(h/4e^2)/\nu$ (in this case, ε_F matches the Landau level with filling factor ν = 2 at around 9 T). Such not-fully-developed Hall plateaus are usually viewed as an early indication of the quantum Hall effect in the situations where ρ_{xx} does not yet reach the zero-resistance state. (**B**) Dependence of the frequency of ShdH oscillations B_F on gate voltage. Solid and open symbols are for samples with $\delta\varepsilon \approx 6$ meV and 20 meV, respectively. Solid lines are guides to the eye. The linear dependence $B_F \propto V_g$ indicates a constant (2D) density of states (*15*). The observed slopes (solid lines) account for the entire external charge n induced by gate voltage, confirming that there are no other types of carriers and yielding the double-valley degeneracy for both electrons and holes (*15*). The inset shows an example of the temperature dependence of amplitude Δ of ShdH oscillations (circles), which is fitted by the standard dependence $T/\sinh(2\pi^2k_BT/\hbar\omega_c)$ where ω_c is their cyclotron frequency. The fit (solid curve) yields light holes' mass of $0.03m_0$.

of thermally excited carriers), but this is a fundamental limitation for any material without a band gap exceeding k_BT. Nonetheless, such on-off ratios are considered sufficient for logic circuits (*19*), and it is feasible to increase the ratio further by, for example, using p-n junctions, local gates (*3*), or the point contact geometry. However, by analogy to carbon nanotubes (*2*), other, nontransistor applications of this atomically thin material ultimately may prove to be the most exciting.

References and Notes

1. C. D. Dimitrakopoulos, D. J. Mascaro, *IBM J. Res. Dev.* **45**, 11 (2001).
2. R. H. Baughman, A. A. Zakhidov, W. A. de Heer, *Science* **297**, 787 (2002).
3. S. V. Rotkin, K. Hess, *Appl. Phys. Lett.* **84**, 3139 (2004).
4. A. V. Butenko, D. Shvarts, V. Sandomirsky, Y. Schlesinger, *J. Appl. Phys.* **88**, 2634 (2000).
5. M. S. Dresselhaus, G. Dresselhaus, *Adv. Phys.* **51**, 1 (2002).
6. I. L. Spain, in *Chemistry and Physics of Carbon*, P. L. Walker, P. A. Thrower, Eds. (Dekker, New York, 1981), pp. 119–304.
7. O. A. Shenderova, V. V. Zhirnov, D. W. Brenner, *Crit. Rev. Solid State Mater. Sci.* **27**, 227 (2002).
8. A. Krishnan *et al.*, *Nature* **388**, 451 (1997).
9. E. Dujardin, T. Thio, H. Lezec, T. W. Ebbesen, *Appl. Phys. Lett.* **79**, 2474 (2001).
10. H. Shioyama, *J. Mat. Sci. Lett.* **20**, 499 (2001).
11. Other methods of preparing thin graphitic layers exist. The closest analogs of FLG are nanometer-sized patches of graphene on top of pyrolytic graphite (*12*, *13*), carbon films grown on single-crystal metal substrates (*14*), and mesoscopic graphitic disks with thickness down to ~60 graphene layers (*8*, *9*).
12. A. M. Affoune *et al.*, *Chem. Phys. Lett.* **348**, 17 (2001).
13. K. Harigaya, Y. Kobayashi, K. Takai, J. Ravier, T. Enoki, *J. Phys. Cond. Matter* **14**, L605 (2002).
14. T. A. Land, T. Michely, R. J. Behm, J. C. Hemminger, G. Comsa, *Surf. Sci.* **264**, 261 (1992).
15. See supporting data on *Science* Online.
16. J. Kong *et al.*, *Science* **287**, 622 (2000).
17. M. Krüger, I. Widner, T. Nussbaumer, M. Buitelaar, C. Schönenberger, *N. J. Phys.* **5**, 138 (2003).
18. We believe that our thinnest FLG samples (as in Fig. 2A) are in fact zero-gap semiconductors, because small nonzero values of $\delta\varepsilon$ found experimentally can be attributed to inhomogeneous doping, which smears the zero-gap state over a small range of V_g and leads to finite apparent $\delta\varepsilon$.
19. M. R. Stan, P. D. Franzon, S. C. Goldstein, J. C. Lach, M. M. Zeigler, *Proc. IEEE* **91**, 1940 (2003).

20. Supported by the UK Engineering and Physical Sciences Research Council and the Russian Academy of Sciences (S.V.M., S.V.D.). We thank L. Eaves, E. Hill, and O. Shklyarevskii for discussions and interest.

Supporting Online Material
www.sciencemag.org/cgi/content/full/306/5696/666/DC1
Materials and Methods
SOM Text
Figs. S1 to S11
References and Notes

19 July 2004; accepted 15 September 2004

Hydrated Electron Dynamics: From Clusters to Bulk

A. E. Bragg,[1] J. R. R. Verlet,[1] A. Kammrath,[1] O. Cheshnovsky,[2] D. M. Neumark[1,3]*

The electronic relaxation dynamics of size-selected $(H_2O)_n^-/(D_2O)_n^-$ [$25 \leq n \leq 50$] clusters have been studied with time-resolved photoelectron imaging. The excess electron (e_c^-) was excited through the $e_c^-(p) \leftarrow e_c^-(s)$ transition with an ultrafast laser pulse, with subsequent evolution of the excited state monitored with photodetachment and photoelectron imaging. All clusters exhibited p-state population decay with concomitant s-state repopulation (internal conversion) on time scales ranging from 180 to 130 femtoseconds for $(H_2O)_n^-$ and 400 to 225 femtoseconds for $(D_2O)_n^-$; the lifetimes decrease with increasing cluster sizes. Our results support the "nonadiabatic relaxation" mechanism for the bulk hydrated electron (e_{aq}^-), which invokes a 50-femtosecond $e_{aq}^-(p) \rightarrow e_{aq}^-(s^\dagger)$ internal conversion lifetime.

A free electron introduced into a polar solvent, such as water (*1*) or ammonia (*2*), may be trapped by locally oriented solvent molecules. In water, an "equilibrated" hydrated electron [$e_{aq}^-(s)$] can be transiently confined within a roughly spherical cavity defined by six OH bonds oriented toward the negative charge distribution in the so-called Kevan geometry (*3–5*). The hydrated electron is an important reagent in condensed-phase chemistry and molecular biology, as it participates in radiation chemistry, electron transfer, and charge-induced reactivity. Thus, research investigating the dynamics of this species, whether in the presence or absence of other reagents, has attracted considerable attention in the theoretical and experimental physical chemistry communities. Here, we present time-resolved results on the electronic relaxation dynamics of anionic clusters of water that lend profound insight to the elucidation of hydrated electron dynamics in the bulk.

The electronic energetics of a hydrated electron are characterized by three types of states (Fig. 1A): a localized $e_{aq}^-(s)$ ground state; three localized, near-degenerate $e_{aq}^-(p)$ excited states; and a delocalized conduction band (CB) characterized by a charge distribution spread across hundreds of molecules in the solvent "network." The visible absorption spectrum of the equilibrium hydrated electron, a broad band peaking at 720 nm (*1*), is well understood as an excitation from the occupied $e_{aq}^-(s)$ state to the vacant $e_{aq}^-(p)$ states (*4*, *5*). The electron-solvent dynamics subsequent to $e_{aq}^-(p) \leftarrow e_{aq}^-(s)$ excitation are more controversial, however, in spite of considerable experimental (*6–12*) and theoretical (*13*, *14*) effort devoted to this problem.

Transient absorption measurements made with femtosecond (fs) laser pulses as short as 5 fs (*12*) show a near infrared (NIR) absorption band beyond 900 nm developing on a 40- to 50-fs time scale after $e_{aq}^-(p) \leftarrow e_{aq}^-(s)$ excitation. This broad feature shifts back to shorter wavelengths on a time scale of several hundred fs, with recovery of the original $e_{aq}^-(s)$ absorption spectrum largely complete within ~1 picosecond (ps). Deuteration of the solvent (*8*, *12*) appears only to affect the fastest measured time scale (i.e., the buildup time of the transient NIR absorption), with τ_{D_2O}/τ_{H_2O} = 1.4 to 1.6. As described by Yokoyama *et al.* (*8*), two rather different energy relaxation mechanisms have been proposed to account for these observations. In the "adiabatic solvation" scheme (*13*, *14*), the infrared transient at the earliest times is attributed to absorption of the $e_{aq}^-(p)$ electron, which is solvated on the upper state within 50 fs (process x in Fig. 1A). The excited electron then undergoes internal conversion (IC) to the ground state (y) on a 400-fs time scale, generating ground-state electrons that further relax on the ~1-ps time scale by dissipating energy to the solvent. In contrast, the "nonadiabatic relaxation" mechanism (*7*, *9*, *12*) invokes much more rapid IC, on a 50-fs time scale, and attributes the transient NIR band at early times to absorption of the ground-state electron in a vibrationally excited solvent environment. In this model, subsequent dynamics are assigned to reorganization of the local (~400 fs) and extended (~1 ps) solvent network following the electronic decay.

We present an alternative and complementary approach to assessing the relaxation dynamics of the hydrated electron through time-resolved photoelectron imaging (TRPEI) studies (*15*) of electron dynamics in size-selected water cluster anions, $(H_2O)_n^-$ and $(D_2O)_n^-$, with $25 \leq n \leq 50$. Water cluster anions were first detected mass spectromet-

---

[1] Department of Chemistry, University of California, Berkeley, CA 94720, USA. [2] School of Chemistry, The Sackler Faculty of Exact Sciences, Tel-Aviv University, 69978 Israel. [3] Chemical Sciences Division, Lawrence Berkeley National Laboratory, Berkeley, CA 94720, USA.

*To whom correspondence should be addressed. E-mail: dan@radon.cchem.berkeley.edu

of thermally excited carriers), but this is a fundamental limitation for any material without a band gap exceeding k_BT. Nonetheless, such on-off ratios are considered sufficient for logic circuits (*19*), and it is feasible to increase the ratio further by, for example, using p-n junctions, local gates (*3*), or the point contact geometry. However, by analogy to carbon nanotubes (*2*), other, nontransistor applications of this atomically thin material ultimately may prove to be the most exciting.

References and Notes

1. C. D. Dimitrakopoulos, D. J. Mascaro, *IBM J. Res. Dev.* **45**, 11 (2001).
2. R. H. Baughman, A. A. Zakhidov, W. A. de Heer, *Science* **297**, 787 (2002).
3. S. V. Rotkin, K. Hess, *Appl. Phys. Lett.* **84**, 3139 (2004).
4. A. V. Butenko, D. Shvarts, V. Sandomirsky, Y. Schlesinger, *J. Appl. Phys.* **88**, 2634 (2000).
5. M. S. Dresselhaus, G. Dresselhaus, *Adv. Phys.* **51**, 1 (2002).
6. I. L. Spain, in *Chemistry and Physics of Carbon*, P. L. Walker, P. A. Thrower, Eds. (Dekker, New York, 1981), pp. 119–304.
7. O. A. Shenderova, V. V. Zhirnov, D. W. Brenner, *Crit. Rev. Solid State Mater. Sci.* **27**, 227 (2002).
8. A. Krishnan *et al.*, *Nature* **388**, 451 (1997).
9. E. Dujardin, T. Thio, H. Lezec, T. W. Ebbesen, *Appl. Phys. Lett.* **79**, 2474 (2001).
10. H. Shioyama, *J. Mat. Sci. Lett.* **20**, 499 (2001).
11. Other methods of preparing thin graphitic layers exist. The closest analogs of FLG are nanometer-sized patches of graphene on top of pyrolytic graphite (*12*, *13*), carbon films grown on single-crystal metal substrates (*14*), and mesoscopic graphitic disks with thickness down to ~60 graphene layers (*8*, *9*).
12. A. M. Affoune *et al.*, *Chem. Phys. Lett.* **348**, 17 (2001).
13. K. Harigaya, Y. Kobayashi, K. Takai, J. Ravier, T. Enoki, *J. Phys. Cond. Matter* **14**, L605 (2002).
14. T. A. Land, T. Michely, R. J. Behm, J. C. Hemminger, G. Comsa, *Surf. Sci.* **264**, 261 (1992).
15. See supporting data on *Science* Online.
16. J. Kong *et al.*, *Science* **287**, 622 (2000).
17. M. Krüger, I. Widner, T. Nussbaumer, M. Buitelaar, C. Schönenberger, *N. J. Phys.* **5**, 138 (2003).
18. We believe that our thinnest FLG samples (as in Fig. 2A) are in fact zero-gap semiconductors, because small nonzero values of δε found experimentally can be attributed to inhomogeneous doping, which smears the zero-gap state over a small range of V_g and leads to finite apparent δε.
19. M. R. Stan, P. D. Franzon, S. C. Goldstein, J. C. Lach, M. M. Zeigler, *Proc. IEEE* **91**, 1940 (2003).
20. Supported by the UK Engineering and Physical Sciences Research Council and the Russian Academy of Sciences (S.V.M., S.V.D.). We thank L. Eaves, E. Hill, and O. Shklyarevskii for discussions and interest.

Supporting Online Material
www.sciencemag.org/cgi/content/full/306/5696/666/DC1
Materials and Methods
SOM Text
Figs. S1 to S11
References and Notes

19 July 2004; accepted 15 September 2004

Hydrated Electron Dynamics: From Clusters to Bulk

A. E. Bragg,[1] J. R. R. Verlet,[1] A. Kammrath,[1] O. Cheshnovsky,[2] D. M. Neumark[1,3]*

The electronic relaxation dynamics of size-selected $(H_2O)_n^-/(D_2O)_n^-$ [$25 \leq n \leq 50$] clusters have been studied with time-resolved photoelectron imaging. The excess electron (e_c^-) was excited through the $e_c^-(p) \leftarrow e_c^-(s)$ transition with an ultrafast laser pulse, with subsequent evolution of the excited state monitored with photodetachment and photoelectron imaging. All clusters exhibited p-state population decay with concomitant s-state repopulation (internal conversion) on time scales ranging from 180 to 130 femtoseconds for $(H_2O)_n^-$ and 400 to 225 femtoseconds for $(D_2O)_n^-$; the lifetimes decrease with increasing cluster sizes. Our results support the "nonadiabatic relaxation" mechanism for the bulk hydrated electron (e_{aq}^-), which invokes a 50-femtosecond $e_{aq}^-(p) \rightarrow e_{aq}^-(s^\dagger)$ internal conversion lifetime.

A free electron introduced into a polar solvent, such as water (*1*) or ammonia (*2*), may be trapped by locally oriented solvent molecules. In water, an "equilibrated" hydrated electron [$e_{aq}^-(s)$] can be transiently confined within a roughly spherical cavity defined by six OH bonds oriented toward the negative charge distribution in the so-called Kevan geometry (*3*–*5*). The hydrated electron is an important reagent in condensed-phase chemistry and molecular biology, as it participates in radiation chemistry, electron transfer, and charge-induced reactivity. Thus, research investigating the dynamics of this species, whether in the presence or absence of other reagents, has attracted considerable attention in the theoretical and experimental physical chemistry communities. Here, we present time-resolved results on the electronic relaxation dynamics of anionic clusters of water that lend profound insight to the elucidation of hydrated electron dynamics in the bulk.

The electronic energetics of a hydrated electron are characterized by three types of states (Fig. 1A): a localized $e_{aq}^-(s)$ ground state; three localized, near-degenerate $e_{aq}^-(p)$ excited states; and a delocalized conduction band (CB) characterized by a charge distribution spread across hundreds of molecules in the solvent "network." The visible absorption spectrum of the equilibrium hydrated electron, a broad band peaking at 720 nm (*1*), is well understood as an excitation from the occupied $e_{aq}^-(s)$ state to the vacant $e_{aq}^-(p)$ states (*4*, *5*). The electron-solvent dynamics subsequent to $e_{aq}^-(p) \leftarrow e_{aq}^-(s)$ excitation are more controversial, however, in spite of considerable experimental (*6*–*12*) and theoretical (*13*, *14*) effort devoted to this problem.

Transient absorption measurements made with femtosecond (fs) laser pulses as short as 5 fs (*12*) show a near infrared (NIR) absorption band beyond 900 nm developing on a 40- to 50-fs time scale after $e_{aq}^-(p) \leftarrow e_{aq}^-(s)$ excitation. This broad feature shifts back to shorter wavelengths on a time scale of several hundred fs, with recovery of the original $e_{aq}^-(s)$ absorption spectrum largely complete within ~1 picosecond (ps). Deuteration of the solvent (*8*, *12*) appears only to affect the fastest measured time scale (i.e., the buildup time of the transient NIR absorption), with τ_{D_2O}/τ_{H_2O} = 1.4 to 1.6. As described by Yokoyama *et al.* (*8*), two rather different energy relaxation mechanisms have been proposed to account for these observations. In the "adiabatic solvation" scheme (*13*, *14*), the infrared transient at the earliest times is attributed to absorption of the $e_{aq}^-(p)$ electron, which is solvated on the upper state within 50 fs (process x in Fig. 1A). The excited electron then undergoes internal conversion (IC) to the ground state (y) on a 400-fs time scale, generating ground-state electrons that further relax on the ~1-ps time scale by dissipating energy to the solvent. In contrast, the "nonadiabatic relaxation" mechanism (*7*, *9*, *12*) invokes much more rapid IC, on a 50-fs time scale, and attributes the transient NIR band at early times to absorption of the ground-state electron in a vibrationally excited solvent environment. In this model, subsequent dynamics are assigned to reorganization of the local (~400 fs) and extended (~1 ps) solvent network following the electronic decay.

We present an alternative and complementary approach to assessing the relaxation dynamics of the hydrated electron through time-resolved photoelectron imaging (TRPEI) studies (*15*) of electron dynamics in size-selected water cluster anions, $(H_2O)_n^-$ and $(D_2O)_n^-$, with $25 \leq n \leq 50$. Water cluster anions were first detected mass spectromet-

---

[1] Department of Chemistry, University of California, Berkeley, CA 94720, USA. [2] School of Chemistry, The Sackler Faculty of Exact Sciences, Tel-Aviv University, 69978 Israel. [3] Chemical Sciences Division, Lawrence Berkeley National Laboratory, Berkeley, CA 94720, USA.

*To whom correspondence should be addressed. E-mail: dan@radon.cchem.berkeley.edu

rically (*16*) and have since been studied with photoelectron (*17–19*), vibrational (*20*), and electronic (*21*) spectroscopies. Cluster studies offer access to structural and dynamic details that are often obscured in the larger, more complex bulk water environment. Because insights gleaned from clusters are meant to extrapolate to the bulk, there is keen interest in determining the size at which "bulk-like" behavior of $(H_2O)_n^-$ clusters becomes apparent (*22*), with the excess electron surrounded by water rather than localized on the cluster surface (*23–25*).

In our TRPEI experiment, described in more detail elsewhere (*26*), water cluster anions are generated in an ion source based on a fast, pulsed molecular beam (*27*) and are mass-selected by time of flight. The mass-selected clusters are investigated with the pump-probe scheme illustrated by the right-most arrows in Fig. 1B. Here, the vertical detachment energy (VDE) is the energy required to remove an electron from an anion while maintaining the anion cluster geometry. We use an ~100-fs laser pulse at 1250 nm (1.0 eV) to excite e_c^-, the excess electron in the cluster anion, from the ground s-state to the excited p-state; this energy lies close to the absorption maximum in the cluster size range investigated here (*21*). After a delay, $\Delta\tau$, during which relaxation may occur, the electron is photodetached by an ultraviolet probe pulse (400 nm or 3.1 eV, ~100 fs) and accelerated by a dc field to an imaging detector composed of a 70-mm-diameter microchannel plate assembly coupled to a phosphor screen.

The state of e_c^- prior to detachment is reflected in its residual velocity afterward, which in turn determines the position the electron strikes on the two-dimensional detector plane. This "velocity map image" (*28*) is then analyzed by two- to three-dimensional inversion, radial integration, and radius-to-energy transformation to yield time-dependent photoelectron kinetic energy (eKE) distributions. Thus, we obtain a time-resolved series of snapshots revealing the dynamics of the nonstationary states created by the pump pulse.

A photoelectron image of $(D_2O)_{25}^-$ acquired within the 1250 nm + 400 nm temporal overlap reveals two features of interest (Fig. 2A). The outermost ring, labeled I, corresponds to the signal with the highest eKE and results from two-color (1250 nm + 400 nm) resonant photodetachment via the $e_c^-(p)$ state (right arrows, Fig. 1B). The next ring, II, is from direct 400-nm detachment of the anion ground state (left arrow, Fig. 1B). Additional features are seen from resonant two-photon and direct one-photon detachment at 1250 nm; however, only features I and II of Fig. 2A show any dependence on pump-probe delay.

The time-resolved photoelectron (TRPE) spectra showing eKE($\Delta\tau$) for features I and II (Fig. 2B) highlight the dynamics that ensue after excitation to the $e_c^-(p)$ cluster state. TRPE spectra of $(D_2O)_{25}^-$ and all other clusters studied here are characterized by depletion and partial recovery in intensity of feature II, with simultaneous growth and decay of feature I. Feature I grows as the pump pulse transfers electronic population to the excited state of the cluster, whereas the depletion of feature II results mainly from this same population transfer. The decay of I and the partial recovery of II are unambiguously assigned to direct electronic relaxation, i.e., internal conversion (IC), from the excited state(s) to the ground state of the cluster. We note that direct one-photon detachment at 1250 nm, the innermost feature in Fig. 2A, is seen for all clusters studied here, which indicates that autodetachment from the pump-excited $e_c^-(p)$ state (requiring no probe pulse) is energetically possible and can, in principle, compete with internal conversion as an excited-state decay pathway. However, this feature shows no time dependence, so excited-state autodetachment appears to be at most a minor relaxation channel.

The integrated intensity of features I and II was plotted versus pump-probe delay and fit to single exponential decay functions convoluted with the instrumental temporal-response (pump-probe temporal cross-correlation, ~150 fs) of the experiment (Fig. 2C). These fits give a $e_c^-(p) \rightarrow e_c^-(s^\dagger)$ relaxation lifetime of 398 ± 50 fs in $(D_2O)_{25}^-$, where $e_c^-(s^\dagger)$ denotes the electron in a vibrationally excited ground state. The shape of feature I remains unchanged even as its intensity evolves, indicating the absence of noticeable hydration dynamics in the $e_c^-(p)$ state before $e_c^-(p) \rightarrow e_c^-(s^\dagger)$ relaxation.

The size and isotope dependence of the electronic decay are evident when the decay traces of excited $(D_2O)_{25}^-$, $(D_2O)_{45}^-$, and $(H_2O)_{45}^-$ are plotted together (Fig. 3). These clusters exhibit excited-state lifetimes of 398 ± 50 fs, 240 ± 25 fs, and 132 ± 10 fs, respectively. For all clusters studied, both sets of isotopomers exhibit shortened excited-state lifetimes with increased cluster size (Fig. 4). Size-dependent isotopomer lifetime ratios, τ_{D_2O}/τ_{H_2O}, for n = 25, 35, and 45 have values of 2.1 ± 0.4, 1.8 ± 0.2, and 1.8 ± 0.2, respectively—similar in magnitude to those

Fig. 1. Energetics of an electron in water. (**A**) The bulk hydrated electron. Red arrows illustrate the transient-absorption schema typically used to study bulk dynamics, in which a time-delayed NIR laser pulse probes the change in optical density [$\Delta OD(\Delta\tau)$] of the sample after an initial infrared excitation. (**B**) Water cluster anions. Levels are similar to those of (A), although the photodetachment continuum replaces the conduction band.

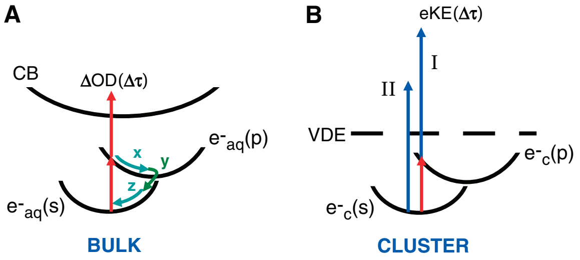

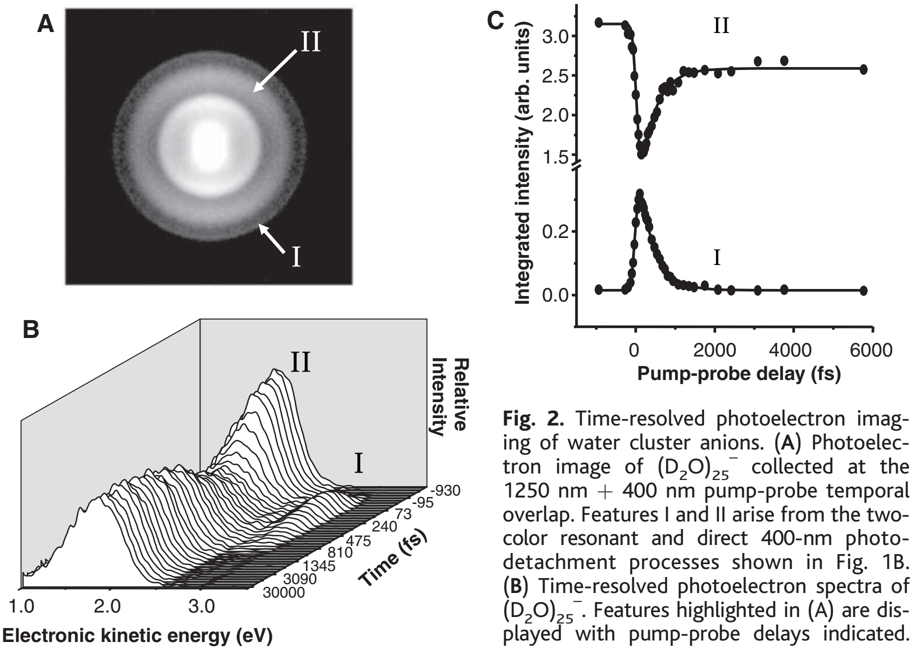

Fig. 2. Time-resolved photoelectron imaging of water cluster anions. (**A**) Photoelectron image of $(D_2O)_{25}^-$ collected at the 1250 nm + 400 nm pump-probe temporal overlap. Features I and II arise from the two-color resonant and direct 400-nm photodetachment processes shown in Fig. 1B. (**B**) Time-resolved photoelectron spectra of $(D_2O)_{25}^-$. Features highlighted in (A) are displayed with pump-probe delays indicated. (**C**) Features I and II. Integrated intensities of features I and II versus pulse delay (experiment, circles; fit, black lines). The fit curves produce a 398 ± 50 fs electronic lifetime for the excited cluster.

observed for the fastest dynamics measured in condensed-phase experiments (*8*, *12*). To test the dependence of the excited-state lifetime on excitation energy, $(H_2O)_{45}^-$ was investigated at a pump energy of 1.57 eV. The lifetime, 117 ± 15 fs, is very close to that found at 1.0 eV and is consistent with the upper bound previously determined by Weber *et al.* (*19*).

These results may be compared and contrasted with the two proposed bulk relaxation mechanisms discussed above. The upper state internal conversion lifetimes decrease markedly with increasing cluster size, approaching 100 fs for the largest $(H_2O)_n^-$ clusters studied here (Fig. 4). This trend suggests even faster IC in bulk water, thereby supporting the nonadiabatic relaxation mechanism in which IC occurs on a 50-fs time scale, rather than the adiabatic solvation model in which a ~400-fs IC has been assigned. Indeed, a plot of IC lifetime versus $1/n$, shown in Fig. 4, is linear and extrapolates to 50 fs in the bulk limit. The significant isotope effect observed for IC in clusters, evident in the $(D_2O)_n^-$ lifetimes plotted in Fig. 4, is likewise consistent with the nonadiabatic mechanism, in which a similar isotope effect is attributed to the IC step (*12*). In contrast, the adiabatic solvation mechanism attributes the isotope effect to faster excited-state hydration in H_2O, whereas the process attributed to IC is insensitive to the identity of the isotopomer (*8*). Finally, the absence of observable upper-state hydration dynamics in our experiment, which would be observed by changes in excited-state spectral features with time, is also in accord with the nonadiabatic mechanism. In this study, all observed dynamical characteristics support the nonadiabatic relaxation model.

A primary motivation for undertaking studies of water cluster anions was to resolve ambiguities regarding the relaxation dynamics of the hydrated electron in solution. We have shown that these ambiguities are directly addressed by investigating the cluster environment, because photoelectron eKE distributions of the excited- and ground-state $(H_2O)_n^-$ are highly distinct (Fig. 2). Thus, internal conversion dynamics from the upper state are cleanly decoupled from solvent relaxation/reorganization processes in the cluster environment, with the rates and nature of relaxation processes free of overlapping spectral signatures that complicate bulk studies. With this in mind, our findings offer important insight into the dynamics of the bulk hydrated electron.

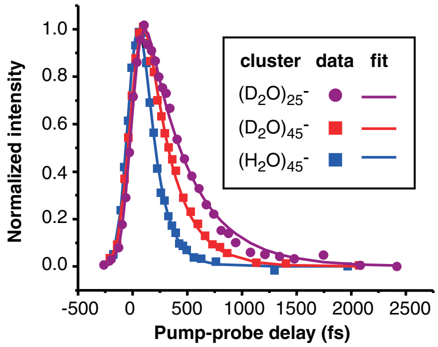

Fig. 3. Size and isotope dependence of excited-state electronic decay traces. Fits (solid lines) to the integrated photoelectron intensities (symbols) versus time yield excited-state lifetimes for $(D_2O)_{25}^-$, $(D_2O)_{45}^-$, and $(H_2O)_{45}^-$ of 398 ± 50 fs, 240 ± 25 fs, and 132 ± 10 fs, respectively.

The above interpretation of our results raises the issue of whether it is appropriate to extrapolate bulk hydrated electron dynamics from those of modest-sized water cluster anions. This issue is particularly important in light of debate regarding whether the excess electron is localized at the cluster surface or within a solvent network cavity. Regardless of which structure holds, it certainly appears more reasonable to extrapolate the cluster relaxation rates to the faster of the two assigned IC time scales for the bulk hydrated electron. Nonetheless, extension of our results to the bulk dynamics is more attractive if the clusters studied here have interior excess electrons, because such structures should be more akin to e_{aq}^-. Coe (*22*) has argued that $n^{-1/3}$-dependent plots of $(H_2O)_n^-$ VDEs, obtained from anion photoelectron spectroscopy (n = 11 to 69) (*17*), and absorption maxima, determined from electronic spectroscopy (n = 11 to 50) (*21*), extrapolate sensibly to bulk values and support the notion that clusters in this size range have internal states. This interpretation disagrees with earlier simulations by Barnett *et al.* (*23*) that predict surface states to be more stable up to n = 32, with the transition to interior states occurring by n = 64. However, Bartels (*25*) has pointed out that the model potentials used in these simulations bind the electron too tightly and that improved model potentials for the e^--H_2O interaction need to be developed to assess the possible role of surface states.

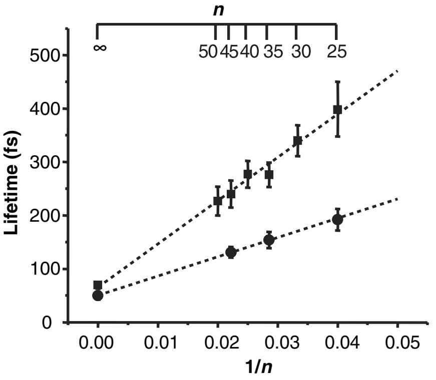

Fig. 4. Size-dependent lifetime trends for $(D_2O)_n^-$ and $(H_2O)_n^-$. Size-dependent decay lifetimes of $(D_2O)_n^-$ (squares) and $(H_2O)_n^-$ (circles) with inverse cluster size ($1/n$). IC lifetimes linearly extrapolate (black dashed lines) to a bulk ($1/n$ = 0) decay time scale of ~50 fs (70 fs) in H_2O (D_2O). Investigated cluster sizes (n) are labeled.

Although our TRPEI measurements do not settle this issue, the IC lifetimes in Fig. 4 vary smoothly with cluster size, casting further doubt on the existence of a structural transition in the n = 25 to 50 range. However, preliminary experiments in our laboratory (*29*) have demonstrated that ion source conditions can be adjusted to generate $(H_2O)_n^-$ ($n \approx 50$) with significantly lower VDEs compared with the clusters discussed here. These newly observed clusters may well represent the long-sought surface states, in which case the cluster dynamics presented in this paper are most likely from structures in which the excess electron has appreciable amplitude within the cluster.

References and Notes

1. E. J. Hart, J. W. Boag, *J. Am. Chem. Soc.* **84**, 4090 (1962).
2. W. Weyl, *Ann. Phys. (Leipzig)* **197**, 601 (1863).
3. L. Kevan, *Acc. Chem. Res.* **14**, 138 (1981).
4. P. J. Rossky, J. Schnitker, *J. Phys. Chem.* **92**, 4277 (1988).
5. M. Boero, M. Parrinello, K. Terakura, T. Ikeshoji, C. C. Liew, *Phys. Rev. Lett.* **90**, 226403 (2003).
6. A. Migus, Y. Gauduel, J. L. Martin, A. Antonetti, *Phys. Rev. Lett.* **58**, 1559 (1987).
7. Y. Kimura, J. C. Alfano, P. K. Walhout, P. F. Barbara, *J. Phys. Chem.* **98**, 3450 (1994).
8. K. Yokoyama, C. Silva, D. H. Son, P. K. Walhout, P. F. Barbara, *J. Phys. Chem. A* **102**, 6957 (1998).
9. A. Hertwig, H. Hippler, A. N. Unterreiner, P. Vohringer, *Ber. Bunsenges. Phys. Chem.* **102**, 805 (1998).
10. M. Assel, R. Laenen, A. Laubereau, *Chem. Phys. Lett.* **317**, 13 (2000).
11. M. J. Tauber, R. A. Mathies, *J. Am. Chem. Soc.* **125**, 1394 (2003).
12. M. S. Pshenichnikov, A. Baltuska, D. A. Wiersma, *Chem. Phys. Lett.* **389**, 171 (2004).
13. B. J. Schwartz, P. J. Rossky, *J. Chem. Phys.* **101**, 6902 (1994).
14. S. Bratos, J. C. Leicknam, D. Borgis, A. Staib, *Phys. Rev. A.* **55**, 7217 (1997).
15. A. Stolow, A. E. Bragg, D. M. Neumark, *Chem. Rev.* **104**, 1719 (2004).
16. M. Armbruster, H. Haberland, H. G. Schindler, *Phys. Rev. Lett.* **47**, 323 (1981).
17. J. V. Coe *et al.*, *J. Chem. Phys.* **92**, 3980 (1990).
18. J. Kim, I. Becker, O. Cheshnovsky, M. A. Johnson, *Chem. Phys. Lett.* **297**, 90 (1998).
19. J. M. Weber *et al.*, *Chem. Phys. Lett.* **339**, 337 (2001).
20. P. Ayotte *et al.*, *J. Chem. Phys.* **110**, 6268 (1999).
21. P. Ayotte, M. A. Johnson, *J. Chem. Phys.* **106**, 811 (1997).
22. J. V. Coe, *Int. Rev. Phys. Chem.* **20**, 33 (2001).
23. R. N. Barnett, U. Landman, C. L. Cleveland, J. Jortner, *J. Chem. Phys.* **88**, 4429 (1988).
24. A. Khan, *J. Chem. Phys.* **118**, 1684 (2003).
25. D. M. Bartels, *J. Chem. Phys.* **115**, 4404 (2001).
26. A. E. Bragg, R. Wester, A. V. Davis, A. Kammrath, D. M. Neumark, *Chem. Phys. Lett.* **376**, 767 (2003).
27. U. Even, J. Jortner, D. Noy, N. Lavie, C. Cossart-Magos, *J. Chem. Phys.* **112**, 8068 (2000).
28. A. T. J. B. Eppink, D. H. Parker, *Rev. Sci. Instrum.* **68**, 3477 (1997).
29. J. R. R. Verlet, A. Kammrath, A. E. Bragg, D. M. Neumark, unpublished data.
30. This research is supported by the National Science Foundation under grant no. CHE-0350585. Additional support from the U.S.-Israel Binational Science Foundation is gratefully acknowledged.

2 August 2004; accepted 27 August 2004
Published online 16 September 2004;
10.1126/science.1103527
Include this information when citing this paper.

Electrons in Finite-Sized Water Cavities: Hydration Dynamics Observed in Real Time

D. Hern Paik, I-Ren Lee, Ding-Shyue Yang, J. Spencer Baskin, Ahmed H. Zewail*

We directly observed the hydration dynamics of an excess electron in the finite-sized water clusters of $(H_2O)_n^-$ with n = 15, 20, 25, 30, and 35. We initiated the solvent motion by exciting the hydrated electron in the cluster. By resolving the binding energy of the excess electron in real time with femtosecond resolution, we captured the ultrafast dynamics of the electron in the presolvated ("wet") and hydrated states and obtained, as a function of cluster size, the subsequent relaxation times. The solvation time (300 femtoseconds) after the internal conversion [140 femtoseconds for $(H_2O)_{35}^-$] was similar to that of bulk water, indicating the dominant role of the local water structure in the dynamics of hydration. In contrast, the relaxation in other nuclear coordinates was on a much longer time scale (2 to 10 picoseconds) and depended critically on cluster size.

The nature of the solvated electron, which was first observed in liquid ammonia in 1864, continues to pose several fundamental problems. When the solvent medium is water, the hydrated electron becomes essential to a myriad of physical, chemical, and biological processes. In a simple picture of an electron in a cavity, the description of the hydrated electron state structure is analogous to that of a hydrogen atom, with a ground state of *s*-type and an excited state of *p*-type character. However, the hydrated electron is far more complex, because of the ultrafast dynamics of structural change, solvation, and recombination. After postulation of the existence of the hydrated electron and the discovery of its absorption, experimental and theoretical efforts have focused on studies in bulk water in which the "cavity" is surrounded by a continuum of other water molecules.

A key issue for understanding electron hydration is knowledge of the time scales involved: the motion of water molecules toward the equilibrium structure and the lifetime of the electron in the different states it occupies. In bulk water, early femtosecond transient absorption studies (*1*, *2*) resolved electron hydration dynamics using excitation by two ultraviolet photons to eject bound electrons from water molecules or solute anions. During the succeeding decade, different research groups have provided a vast amount of experimental data on the time scales of relaxation and the theoretical underpinnings of the hydrated electron system (*3–12*). Among these was the first three-pulse experiment (*3*), in which a population of ground-state hydrated electrons created by an initial laser pulse was subsequently studied using two additional pulses, the first of which excited the electrons from the *s*- to the *p*-state and the second of which probed either state. More recently, studies have been made with pulses as short as 5 fs in order to elucidate the different relaxation pathways (*5*, *9*). In these bulk studies, there remain unanswered questions, especially regarding the microscopic molecular structure and dynamics of hydration.

Mesoscopic clusters (*13*, *14*) are ideal for forming finite-sized nanoscale water cavities for electron hydration, and because of the charge of the electron, it is in principle possible to select a particular size of cluster and study its isolated structure and dynamics. Results from such studies provide insight into the bulk behavior. For example, accurate spectra of neutral water dimers are predictive of the properties of larger clusters and bulk water (*15*). For electrons in water clusters, Haberland and co-workers (*16*) first reported the experimental observation of $(H_2O)_n^-$ clusters, and, in a series of comprehensive studies, the Johnson (*17–19*) and Bowen (*20*, *21*) groups have elucidated the size dependence of spectroscopic properties, examining the role of the core motif in reaching bulk hydration.

The structure of these finite-sized clusters has been studied both experimentally and theoretically, addressing the issue of surface and interior electron binding (*18*, *20*, *22–24*). Theoretical studies (*23*, *24*) of small $(H_2O)_n^-$ clusters, $n \leq 14$, predict that the electron lies at the surface. Earlier calculations by the groups of Landman and Jortner (*22*) indicated that for small clusters ($n \leq 32$), the electron tends to remain on the surface, whereas for the larger ones (n = 64 and 128), the electron is in the interior. Recent work for n = 24 indicates that although three isomers (with the electron inside or outside at the surface) are energetically similar, the vertical detachment energy closest to the experimental value is that of the isomer with the electron inside (*25*). Despite these extensive studies, the only report of real-time dynamics of water cluster anions has been that of a preliminary *p*-state lifetime, limited by laser pulse duration, for a cluster of unspecified size (*19*).

We present here direct observation of the femtosecond dynamics of electrons in water clusters varying in size up to n = 35. We focused our attention on the dynamics in systems with different solvation cavities (n = 15, 20, 25, 30, and 35). The finite-sized clusters were selectively intercepted by femtosecond pulses to promote the electron from the *s*- to the *p*-state (Fig. 1A) (*26*). We followed subsequent relaxation dynamics by monitoring the evolution of the photoelectron (PE) spectrum with kinetic energy resolution (*27*). The latter proved critical, as did the resolution of kinetic energy of ions (*28*), for deciphering different pathways of dynamics. This PE energy resolution allowed us to address whether hydration proceeds while the electron is in the ground (*s*-type) and/or excited (*p*-type) states. For the cavity sizes under study, the behavior observed can be correlated to that of bulk-type hydration.

We generated the negatively charged water clusters by crossing a continuous electron beam (1 keV) with a jet of water vapor, using nitrogen as a carrier gas at 150 to 250 kPa. After ~100 μs of drift time, application of a properly timed voltage pulse accelerated $(H_2O)_n^-$ clusters into the field-free time-of-flight region, where the desired size was intercepted with femtosecond laser pulses (*29*). A typical cluster size distribution is shown in Fig. 1B. The laser pulses (110 fs) were generated from a Ti:sapphire oscillator and amplified by regenerative and multipass amplifiers. The 800-nm laser output was frequency doubled to generate a 400-nm pulse. The residual 800-nm light was used as the excitation pulse, and the 400-nm laser pulse, delayed in time, was used as the probe to photodetach electrons. Photoelectrons were collected by a magnetic-bottle PE spectrometer, and the metastable anions and photofragments were detected by a linear reflectron mass spectrometer. We recorded transients by integrating the PE intensity in selected electron kinetic energy (eKE) windows as a function of the delay time.

A conceptual illustration of our experiments and methodology is shown in Fig. 2.

Arthur Amos Noyes Laboratory of Chemical Physics, Laboratory for Molecular Sciences, California Institute of Technology, Pasadena, CA 91125, USA.

*To whom correspondence should be addressed. E-mail: zewail@caltech.edu

When a particular size of $(H_2O)_n^-$ is selectively excited by the 800-nm femtosecond laser pulse, the excess electron is promoted to the *p*-state (Fig. 2A). The coordinate-labeled solvation represents all nuclear motions of the solvent that strongly affect the electrostatic environment and thus the energy of the electron. As a result of the electronic transition, the electron charge distribution is significantly changed, driving a rearrangement of water molecules around the electron that corresponds to displacement along the solvation coordinate with characteristic time τ_p. Similarly, when the excited state relaxes down to the ground state by internal conversion with characteristic time τ_{ic}, displacement along the solvation coordinate will reverse, and the solvent will move back toward its original configuration with characteristic time τ_s. Because the pump photon energy, which is several times greater than the binding energy of surface water molecules (*30*), is retained in these isolated clusters, the flow of energy from the solvation coordinate into other nuclear coordinates will lead to the eventual evaporation of water molecules (Fig. 2A, left). The fact that 800-nm absorption ultimately leads to evaporation is confirmed by our mass spectra of anionic fragments and has been reported elsewhere (*31*).

The PE spectra were used to follow these dynamics and disentangle the pathways. The energy level diagram (Fig. 2B) shows qualitatively how the energy content in the solvation coordinate of the anion is expected to affect the eKE of the electron ejected upon absorption of the 400-nm probe pulse. Franck-Condon considerations indicate that the eKE distribution broadens asymmetrically as the amount of energy in the solvation coordinate increases in a given electronic state (yellow to red); a change in electronic state causes the spectrum to shift position (yellow to blue). The degree of broadening depends on

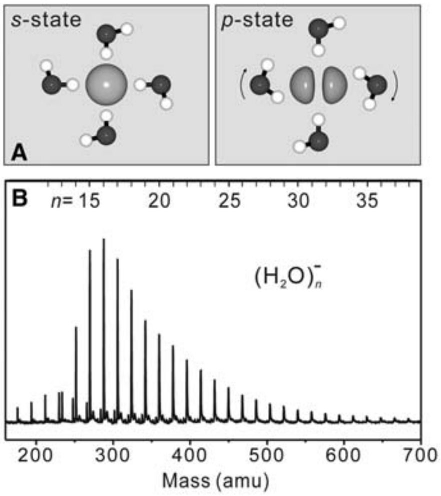

Fig. 1. (**A**) Schematic representation of the *s*- and *p*-states of the hydrated electron, based on fig. 14 of (*5*). (**B**) Experimental mass spectrum of $(H_2O)_n^-$ generated by the ion source in our apparatus. A series of $O_2^-(H_2O)_n$ peaks is seen at low mass. amu, atomic mass units.

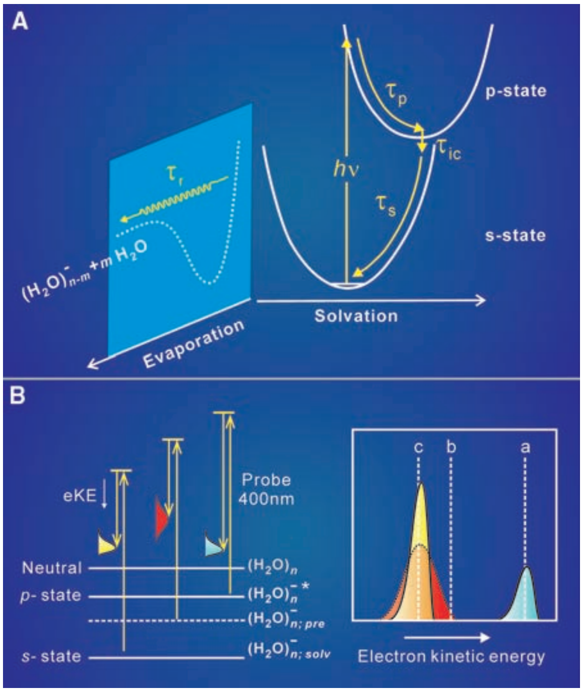

Fig. 2. (**A**) A schematic illustration of the solvation and evaporative dissociation exhibited in the hydrated electron clusters. The upward arrow represents the excitation to the *p*-state. The relaxation and dissociation pathways are depicted and labeled by their characteristic times as follows: τ_p, solvation in *p*-state, τ_{ic}, internal conversion, τ_s, solvation in *s*-state, τ_r, relaxation and evaporation. hν, photon energy. (**B**) Probing of different transient states of the solvated electron by energy and time resolution. Left: An energy-level diagram illustrating the changes in PE distribution originating from anion populations with different electronic and solvation energies. The upward arrows indicate the 400-nm probe pulse that detached the electron, and the downward arrows correspond to the kinetic energy of the detached electron (the eKE). Right: The resulting PE spectra are plotted together on a common energy axis, with *a*, *b*, and *c* indicating points with differing sensitivities to the location of the transient state. The distribution shown is for a moderate weakening of the force constant and displacement of minimum position between the anion and the neutral potentials, as confirmed by Franck-Condon calculation. Asterisk indicates an excited electronic state.

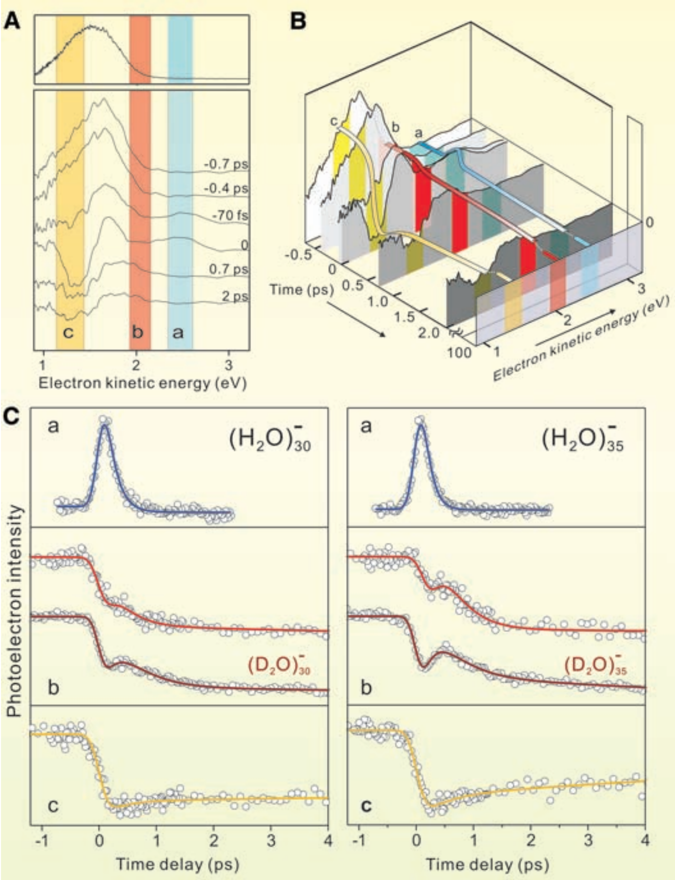

Fig. 3. (**A**) Top: PE spectrum of $(H_2O)_{35}^-$ obtained by irradiation with the 400-nm pulse only. Bottom: Time-dependent PE difference spectra at several time delays of the 400-nm probe pulse relative to the 800-nm excitation pulse. Each spectrum was constructed by subtracting the reference at 100 ps from the PE spectrum at the time specified. Regions *a*, *b*, and *c* indicate the energy windows of interest. (**B**) Three-dimensional representation of the time-dependent PE spectra. The intensity trends in region *a*, *b*, and *c* are indicated by yellow, red, and blue ribbons. (**C**) Femtosecond transients of $(H_2O)_{30}^-$ and $(H_2O)_{35}^-$ obtained by integration of the three different gated regions (*a*, *b*, and *c*) as a function of delay time. The transients of region *b* for $(D_2O)_{30}^-$ and $(D_2O)_{35}^-$ are also shown.

the relative flatness and equilibrium position displacement of the neutral's and anion's solvation coordinate potentials. With this picture in mind, solvation dynamics in both the *p*- and *s*-states can be followed by monitoring the dependence on probe delay time of the production of detached electrons with various values of eKE (e.g., the energies labeled *a*, *b*, and *c* in Fig. 2B).

The PE spectrum of $(H_2O)_{35}^-$ upon irradiation by the 400-nm femtosecond pulse confirmed ejection of the excess electron by vertical detachment, producing the characteristic eKE distribution (Fig. 3A, top). When the clusters were irradiated by both 800-nm and 400-nm pulses, the PE spectrum changed with delay time, as indicated in the difference spectra (Fig. 3A, bottom). The same spectra are also shown in a three-dimensional representation (Fig. 3B). It is apparent that different regions of the PE spectrum exhibit distinct temporal behaviors, and we focused only on the three particular regions labeled *a*, *b*, and *c*. As indicated by the ribbons in Fig. 3B, at high eKE above the onset of the PE spectrum (region *a*), a new peak appeared at time zero and disappeared by 0.7 ps. The PE intensity near the onset (region *b*) decayed with time, whereas the PE signal near the peak of the spectrum (region *c*) displayed an abrupt drop at time zero and a rise at positive time.

To quantify the trends shown by the ribbons in Fig. 3B, we obtained transients by integrating the PE intensity as a function of the delay time for each energy window. The same forms of apparent temporal behaviors were evident for both *n* = 30 and *n* = 35 clusters (Fig. 3C). The greater level of detail provided by the transients revealed that the fast decay for region *a* is not limited by laser pulse duration, as the asymmetry is evident, and there are two distinct time scales of decay for region *b*. We also compared with region *b* results obtained for $(D_2O)_{30}^-$ and $(D_2O)_{35}^-$. For $(H_2O)_n^-$, *n* = 15, 20, and 25, only transients for region *b* were measured (Fig. 4A) (*32*).

The temporal behavior observed in the time-dependent PE spectra of $(H_2O)_{30}^-$ and $(H_2O)_{35}^-$ elucidates the ultrafast dynamics. The instantaneous rise and the fast decay in region *a* (at high eKE) represent vertical excitation to the *p*-state followed by rapid relaxation to the *s*-state. As discussed earlier, an isolated peak of *a*-type character should rise within our pulse duration and decay with the *p*-state lifetime. Moreover, this peak temporally changes at an eKE shift of ~1 eV, which corresponds to the *s*- to *p*-state energy gap (*19*), as predicted conceptually (Fig. 2B). In bulk water (*4*, *5*, *33*), the inertial solvent motions (libration) are expected to occur before the internal conversion. In the clusters, the decay of the *a*-peak gives the time scale for population transfer to the *s*-state, with an effective time constant, τ_{eff}, for inertial motion and internal conversion (τ_p and τ_{ic}). Single exponential fits to the region *a* data give corresponding τ_{eff} values of 170 fs (*n* = 30) and 140 fs (*n* = 35) (Fig. 3C). Given the short time scale of these motions, coherent effects may be present (*4*, *34*), but a kinetic description suffices for the behavior observed here.

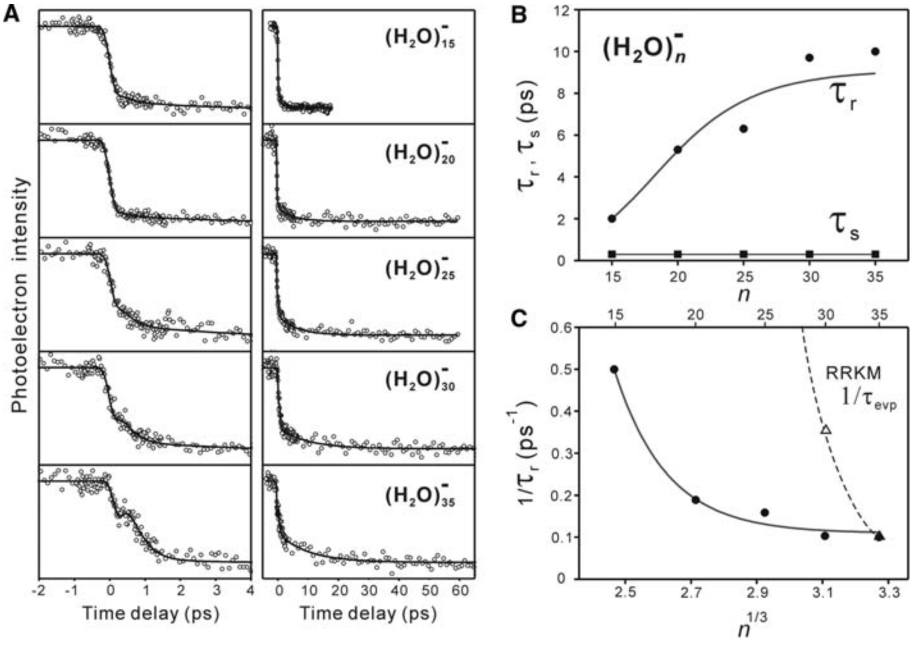

Fig. 4. (**A**) Femtosecond transients of $(H_2O)_n^-$ (where *n* = 15, 20, 25, 30, or 35) obtained by integration of the PE signals in region *b*. The short- and long-range scans are shown in the left and right columns, respectively. (**B**) Time constants τ_s (squares) and τ_r (circles) versus cluster size *n*. The solid curves indicate the observed trends. (**C**) Observed relaxation rate $1/\tau_r$ (circles) and the scaled RRKM rates for the hydrogen-bond breakage $1/\tau_{evp}$ (triangles). The RRKM rate is scaled by ~11,000 to match the observed rate for *n* = 35. The solid curves indicate the observed trend, and the dashed curve indicates the theoretical trend.

After the internal conversion, the electron becomes presolvated in the ground state, and solvation of the electron (τ_s) follows, as revealed by the short time behavior in region *b* and *c*. Relaxation (τ_r) after solvation can be most clearly seen in the long time behavior in region *b* (Fig. 4A, right). To account for the delayed return of population from the *p*- to the *s*-state, a proper kinetic analysis must also include the influence of τ_{eff} on the transients of regions *b* and *c* (*35*). The results (Figs. 3C and 4A) give τ_s values of 300 fs (the range for the clusters studied was ±150 fs with our current analysis) and τ_r values ranging from 2 to 10 ps, depending on cluster size (Fig. 4A). For the different clusters *n* = 15 to *n* = 35 (Fig. 4B), the time scale of solvation was within a factor of two and was similar to that of electrons in bulk water. It was also on the order of the time scale of the diffusive rotational and translational motions of bulk water around molecular probes (*33*). The solvent rearrangement time we obtained here for the *s*-state of these large clusters is about the same as that found for electron hydration after excitation of a charge transfer band of $I^-(H_2O)_n$ for *n* = 5 and *n* = 6 (*36*). Such weak size dependence and the similarity between bulk and clusters indicate that the dynamics of hydration are in large part controlled by the local structure of water molecules in immediate contact with the electron.

The longer relaxation times are determined by the energy content in the *s*-state, the rate of intramolecular vibrational energy redistribution (IVR), and hydrogen-bond breakage (Fig. 4, B and C). Because these times increase with cluster size, we excluded both time-dependent solvation and IVR as rate-determining and considered evaporation. Manifestation of evaporation in the transients was expected because the process alters the PE spectra as a result of change in cluster size and internal energy. We calculated the statistical rate constants for clusters undergoing evaporation by one water molecule ($1/\tau_{evp}$). Using Rice-Ramsperger-Kassel-Marcus theory (*37*), we obtained rate constants that were slower or much slower than the experimental observation, depending on the particular values of frequencies and the reaction barrier; for example, for *n* = 35, τ_{evp} ranged from ~1 ns to 15 μs versus the observed value of 10 ps. The discrepancy would indicate a nonstatistical behavior (*40*). However, there have been reports that such clusters may live for much longer times (*31*), and because the internal energy needs to be determined, the results for the $(H_2O)_n^-$ and $(D_2O)_n^-$ systems should be extended with variation of energy and cluster initial temperature. The experimental time scale for relaxation (2 to 10 ps) of the clusters at finite temperature is not that different from that of hydrogen-bond making/breaking dynamics in bulk at room temperature (*33*).

Our observations demonstrate that solvation dynamics in mesoscopic hydrated electron clusters can be probed directly in real time. From the energy- and time-resolved PE spectra, we were able to follow the ultrafast processes that occur in the presolvated and hydrated states of the electron. With size-selection capability, we also observed the behavior of the rates of solvation and relaxation as a function of cluster size. For the clusters studied, our time-resolved data display solvation dynamics similar to those of the hydrated electron in bulk water, suggesting a local-water-structure model for hydration, and the pathways of electronic relaxation, solvation, and hydrogen-bond breakage have distinctly resolvable time scales. Mesoscopic scale clusters can thus provide the elementary dynamics and, as such, represent simplified model systems to study the behavior of bulk systems.

References and Notes

1. A. Migus, Y. Gauduel, J. L. Martin, A. Antonetti, *Phys. Rev. Lett.* **58**, 1559 (1987).
2. F. H. Long, H. Lu, K. B. Eisenthal, *Phys. Rev. Lett.* **64**, 1469 (1990).
3. J. C. Alfano, P. K. Walhout, Y. Kimura, P. F. Barbara, *J. Chem. Phys.* **98**, 5996 (1993).
4. K. Yokoyama, C. Silva, D. H. Son, P. K. Walhout, P. F. Barbara, *J. Phys. Chem. A* **102**, 6957 (1998).
5. A. Baltuška, M. F. Emde, M. S. Pshenichnikov, D. A. Wiersma, *J. Phys. Chem. A* **103**, 10065 (1999).
6. M. Assel, R. Laenen, A. Laubereau, *Chem. Phys. Lett.* **317**, 13 (2000).
7. N. A. Anderson, K. Hang, J. B. Asbury, T. Lian, *Chem. Phys. Lett.* **329**, 386 (2000).
8. A. Hertwig, H. Hippler, A.-N. Unterreiner, *Phys. Chem. Chem. Phys.* **4**, 4412 (2002).
9. M. S. Pshenichnikov, A. Baltuška, D. A. Wiersma, *Chem. Phys. Lett.* **389**, 171 (2004).
10. E. Neria, A. Nitzan, R. N. Barnett, U. Landman, *Phys. Rev. Lett.* **67**, 1011 (1991).
11. C.-Y. Yang, K. F. Wong, M. S. Skaf, P. J. Rossky, *J. Chem. Phys.* **114**, 3598 (2001).
12. C. Nicolas, A. Boutin, B. Lévy, D. Borgis, *J. Chem. Phys.* **118**, 9689 (2003).
13. A. W. Castleman Jr., K. H. Bowen, *J. Phys. Chem.* **100**, 12911 (1996).
14. M. A. Johnson, W. C. Lineberger, in *Techniques for The Study of Ion-Molecule Reactions*, J. M. Farrar, W. H. Saunders Jr., Eds. (Wiley-Interscience, New York, 1988), vol. 20, pp. 591–635.
15. N. Goldman, R. J. Saykally, *J. Chem. Phys.* **120**, 4777 (2004).
16. M. Armbruster, H. Haberland, H. G. Schindler, *Phys. Rev. Lett.* **47**, 323 (1981).
17. P. Ayotte, M. A. Johnson, *J. Chem. Phys.* **106**, 811 (1997).
18. P. Ayotte *et al.*, *J. Chem. Phys.* **110**, 6268 (1999).
19. J. M. Weber *et al.*, *Chem. Phys. Lett.* **339**, 337 (2001).
20. J. V. Coe *et al.*, *J. Chem. Phys.* **92**, 3980 (1990).
21. J. V. Coe *et al.*, *J. Chem. Phys.* **107**, 6023 (1997).
22. R. N. Barnett, U. Landman, C. L. Cleveland, J. Jortner, *J. Chem. Phys.* **88**, 4429 (1988).
23. A. L. Sobolewski, W. Domcke, *Phys. Chem. Chem. Phys.* **5**, 1130 (2003).
24. J. Kim *et al.*, *J. Chem. Phys.* **106**, 10207 (1997).
25. A. Kahn, *J. Chem. Phys.* **121**, 280 (2004).
26. The Fig. 1A depictions and use of the standard *s* and *p* designations for the solvated electron states in bulk cavities are not meant to imply that, for all clusters, the excess electron must be bound in the interior of the clusters.
27. A. Stolow, A. E. Bragg, D. M. Neumark, *Chem. Rev.* **104**, 1719 (2004).
28. D. P. Zhong, A. H. Zewail, *J. Phys. Chem. A* **102**, 4031 (1998).
29. D. H. Paik, N. J. Kim, A. H. Zewail, *J. Chem. Phys.* **118**, 6923 (2003).
30. S. T. Arnold, R. A. Morris, A. A. Viggiano, M. A. Johnson, *J. Phys. Chem.* **100**, 2900 (1996).
31. P. J. Campagnola, L. A. Posey, M. A. Johnson, *J. Chem. Phys.* **95**, 7998 (1991).
32. Each transient of regions *b* and *c* also includes a fast response-limited negative component due to the vertical detachment by the 800-nm pump pulse the photon energy of which exceeds that of the detachment to the neutral. For small clusters (n = 15, 20, and 25), the photodetachment process is increasingly favored over the transition to the bound *p*-state because of spectral shift (*19*), and this accounts for the small amplitude of the decay component (region *b*) and the fact that neither the peak near time zero in region *a* nor the rise component in region *c* were detected.
33. S. K. Pal, A. H. Zewail, *Chem. Rev.* **104**, 2099 (2004).
34. A. Kummrow, M. F. Emde, A. Baltuška, M. S. Pshenichnikov, D. A. Wiersma, *J. Phys. Chem. A* **102**, 4172 (1998).
35. We employed the scheme of consecutive population flow and selective population window (PE probing) and performed least-squares fitting. With experimentally determined τ_{eff} values for the initial state decay and the rise of the first intermediate of n = 30 and n = 35, the separation in time scales of the femtosecond and picosecond decays allows values of τ_s and τ_r to be extracted by the global fits. The validity of the model was supported by the pronounced dip in the region *b* transients of $(D_2O)_{30}^-$ and $(D_2O)_{35}^-$ (Fig. 3C).
36. L. Lehr, M. T. Zanni, C. Frischkorn, R. Weinkauf, D. M. Neumark, *Science* **284**, 635 (1999).
37. Vibrational frequencies were estimated from those calculated for small clusters (*38*, *39*). Calculation for different size clusters differed only in the number of modes used. Thus, it is assumed that significant structural changes, for instance transition from the surface to interior states (*20*, *22*), do not occur as cluster size increases. The reaction coordinate was taken to be 260 cm^{-1} (*39*), the dissociation energy to be 2700 cm^{-1} (*15*), and the vibrational frequencies to remain the same at the transition state. The initial internal energy of the cluster is assumed to be the highest thermal energy of stable clusters (dissociation energy); the drift time before excitation is ~100 μs, but clusters with higher internal energy may persist during this time. For the degeneracy factor of the reaction coordinate, we take half of the water molecules to be surface-bound and thus subject to dissociation.
38. D. M. A. Smith, J. Smets, Y. Elkadi, L. Adamowicz, *J. Chem. Phys.* **107**, 5788 (1997).
39. J. Kim, S. B. Suh, K. S. Kim, *J. Chem. Phys.* **111**, 10077 (1999).
40. E. W. G. Diau, J. L. Herek, Z. H. Kim, A. H. Zewail, *Science* **279**, 841 (1998).

41. We thank M. A. Johnson and K. H. Bowen for helpful communication. Supported by the National Science Foundation.

16 July 2004; accepted 25 August 2004

10.1126/science.1105018
Include this information when citing this paper.

How Do Small Water Clusters Bind an Excess Electron?

Nathan I. Hammer, Joong-Won Shin, Jeffrey M. Headrick, Eric G. Diken, Joseph R. Roscioli, Gary H. Weddle,* Mark A. Johnson†

The arrangement of water molecules around a hydrated electron has eluded explanation for more than 40 years. Here we report sharp vibrational bands for small gas-phase water cluster anions, $(H_2O)_{4-6}^-$ and $(D_2O)_{4-6}^-$. Analysis of these bands reveals a detailed picture of the diffuse electron-binding site. The electron is closely associated with a single water molecule attached to the supporting network through a double H-bond acceptor motif. The local OH stretching bands of this molecule are dramatically distorted in the pentamer and smaller clusters because the excited vibrational levels are strongly coupled to the electron continuum. The vibration–to–electronic energy transfer rates, as revealed by line shape analysis, are mode-specific and remarkably fast, with the symmetric stretching mode surviving for less than 10 vibrational periods [50 fs in $(H_2O)_4^-$].

In dilute ionic solutions, the negative charge carriers are typically closed-shell molecular species (such as acetate) that capture the extra electron into their molecular orbital networks. Pure dipolar solvents such as ammonia and water do not possess any low-lying valence molecular orbitals to accommodate an extra electron; nonetheless, an electron can become trapped in a cavity within these liquids. The resulting localized charge defect is called a "solvated electron" (*1*–*5*). The aqueous electron, e_{aq}^-, has been subjected to intense study since its discovery in 1962 (*6*), yet impor-

---

Sterling Chemistry Laboratory, Yale University, Post Office Box 208107, New Haven, CT 06520, USA.

*Present address: Department of Chemistry, Fairfield University, Fairfield, CT 06430, USA.

†To whom correspondence should be addressed. E-mail: mark.johnson@yale.edu

tant questions remain regarding the molecular structure of the solvating cavity.

Some of the complexity presented by e_{aq}^- arises from the small spatial extent of the excess electron wavefunction (~2.4 Å radius) (*7*), which is on the same order as the volume occupied by only a few water molecules (*8*, *9*). The relaxation dynamics of photoexcited electrons are still controversial, with reported values ranging from 50 to 300 fs (*10*, *11*). The 50-fs value is particularly interesting because it is on the same order as the time scale for the OH stretching motion, introducing the possibility that the intramolecular vibrations are intrinsically involved in the relaxation. Two of the important outstanding questions to be answered are thus exactly how many water molecules are in direct contact with the excess electron, and to what extent are they perturbed by this interaction? Some workers, for example, have even invoked alternatives to the cavity model (that is, with rearrangements involving the H_3O Rydberg molecule) to explain e_{aq}^- behavior (*12*), although such drastic perturbations appear to be at odds with recent resonant Raman data (*13*).

One approach to resolving these controversies is to focus on a simpler system first. The study of size-selected water clusters in the gas phase isolates local ion-solvent interactions from the background created by the bulk solution (*14*). As such, experimental observables can be directly compared with theoretical calculations that treat the aggregate as a "supermolecule." Anionic water clusters, $(H_2O)_{n\,\geq\,2}^-$, were first isolated in 1984 (*15*–*17*), and their reaction chemistry (*18*, *19*), photophysics (*20*), and spectroscopy (*21*, *22*) have been extensively investigated. Unfortunately, it has not yet been possible to unambiguously invert the available spectral data to reconstruct the geometry and electronic structure of the charged clusters.

The basic problem is that the smallest cluster for which sharp vibrational features have been recovered is the hexamer anion, $(H_2O)_6^-$ (*23*). At that size, the high dimensionality of the neutral cluster is already a challenge for theory (*24*), and the additional complications introduced by the diffuse excess electron have made the calculations too computationally intensive for ab initio methods. Density functional theory (DFT) calculations have recently become the method of choice to calculate $(H_2O)_n^-$ behavior (*25*), although this approach systematically overbinds a diffuse excess electron and does not offer the same convergence guarantee as fully ab initio methods (*26*). Given these theoretical difficulties, it is not surprising that, during the past several years, the observed vibrational bands of the hexamer anion have been rationalized in the context of very different network arrangements and electron-binding motifs.

Kim and co-workers (*25*) have extrapolated the DFT methods used for their hexamer calculation to predict the energies and vibrational spectra for various isomers of the smaller water clusters ($n \leq 5$). Experimental validation of these predictions would afford a high level of confidence in the theoretical method and associated structural assignments. To that end, we exploited very recent advances in size-selected argon nanomatrix spectroscopy (*27*), involving both synthetic methodology (*28*) and wavelength coverage, to establish the network morphologies and intramolecular distortions that occur when the four- to six-membered water clusters bind an excess electron. Our results associate the bound electron most closely with a single water molecule, attached to the cluster through two hydrogen bonds directed toward its O atom. The OH stretches local to this molecule account for a signature doublet feature, previously observed in the spectra of the anionic clusters with $n = 6$ to 9 and 11 (*29*).

Our experimental method probes argon-solvated water cluster anions, for which infrared absorptions can be readily detected in an action mode by mass loss. This nanomatrix spectroscopy (*27*) relies on the fact that a resonantly prepared vibrational level eventually decays, depositing its energy as heat into the argon cluster. This, in turn, causes the evaporation of several argon atoms

$$(H_2O)_{4-6}^- \cdot Ar_n + h\nu \rightarrow (H_2O)_{4-6}^- \cdot Ar_m + n - m\ Ar \qquad (1)$$

The lighter photofragments are easily isolated from the mass-selected parent ions with the use of a double-focusing, tandem time-of-flight photofragmentation mass spectrometer (*30*).

Preparation of the tetramer and, to a lesser extent, pentamer anions has traditionally been hampered by the lack of an efficient pathway for direct electron attachment onto the neutral clusters (*31*). In our approach (*32*), $(H_2O)_{4,5}^- \cdot Ar_m$ clusters are prepared using argon-mediated sequential condensation of water molecules onto the easily generated dimer anion

$$(H_2O)_2^- \cdot Ar_n + 2H_2O \rightarrow (H_2O)_4^- \cdot Ar_m + n - m\ Ar \qquad (2)$$

However, even when the species of interest are successfully captured in an argon cluster, sharp bands will be observed only when the vibrationally excited states are stable with respect to spontaneous electron detachment. We previously determined the vertical electron detachment energy (VDE) of the tetramer anion (dominant isomer) to be 350 ± 20 meV (*32*). The OH stretching frequency of ~420 meV lies above this VDE, and so the associated vibrational transitions are expected to be severely broadened, as reported for the pentamer anion (*29*).

To circumvent the broadening problem, we have probed the ~200-meV intramolecular bending vibrations rather than the OH stretches. These bending bands lie below the VDEs of the $n = 4$ and 5 clusters and therefore should yield sharp features (*33*). As a complementary strategy, we have prepared the deuterated water clusters $(D_2O)_{4,5}^-$. The OD stretches at ~310 meV also lie below the corresponding VDEs (*34*).

The argon predissociation spectra of the $(H_2O)_{4\text{-}6}^-$ clusters in the intramolecular bending region show sharp bands as expected (Fig. 1). The lowest-energy feature appears in almost the same location (1540 ± 5 cm^{-1}) in all three spectra and occurs roughly 50 cm^{-1} below the bend fundamental in the isolated water molecule (arrow in Fig. 1A). This redshift points to a significant influence of the extra electron, because the bending modes have been shown to shift exclusively to higher energy (relative to bare H_2O) in the spectra of the small neutral water clusters (*35*).

We can extract structural information from the way in which the vibrational energies depend on the number of donor and acceptor H-bonds associated with water molecules in particular local environments. For example, molecules in single or double acceptor (A or AA) sites have two nonbonded hydrogen atoms and tend to have the lowest energy

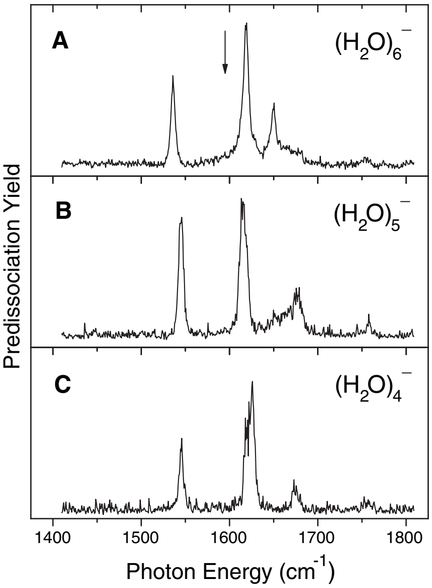

Fig. 1. Argon predissociation spectra of the small $(H_2O)_n^-$ clusters in the intramolecular bending region. Each displayed spectrum is an average of ~20 scans. (**A**) $(H_2O)_6^- \cdot Ar_3$, (**B**) $(H_2O)_5^- \cdot Ar_4$, and (**C**) $(H_2O)_4^- \cdot Ar_5$. The arrow in (A) marks the bend fundamental (ν_2) for isolated H_2O.

bending vibrations. Conversely, double donor (DD) sites provide the largest constraint on the bending motion and are highest in energy. Molecules with AD and D motifs, having one nonbonded hydrogen atom, give rise to bands falling between the two limiting cases.

The three distinct bands in the $n = 4$ spectrum (Fig. 1C) indicate that three binding sites are in play, with the central band appearing somewhat broader, as would be expected from the contribution of two closely related water molecules. The bottom panel of Fig. 2 pairs this bending spectrum (from Fig. 1C) on the left with the spectrum of the deuterated tetramer in the OD stretching region on the right. The recent DFT calculations (*25*) predict that, even for the relatively small tetramer anion, six classes of isomers exist, with small variations available in each class. Of these, however, only the chain (Fig. 2, top panel) and the C_s symmetry cyclic (Fig. 2, middle panel) isomers are consistent with our observed bands in the bending region.

The more symmetrical cyclic form best explains the pattern of bending bands, as two equivalent AD water molecules bridge the other two molecules with DD and AA motifs, respectively. Also, the OD stretching data rule out the linear structure. Even minor details in the experimental spectrum, such as the shoulder on the 2560 cm^{-1} band, are accurately recovered by the calculated spectrum of the cyclic isomer (Fig. 2D). Such agreement indicates that the cyclic isomer is the species formed in the jet, and thus we can rely on this analysis to establish the atomic motions that contribute to the various bands. This form was not calculated to be the lowest energy isomer, but Kim *et al*. (*25*) suspected that it might nonetheless be a dominant species under experimental conditions. An enlarged view of the calculated tetramer anion structure is presented in Fig. 3, which also includes a contour (isosurface at a value of 0.005) for the excess electron orbital. Note that the AA water molecule is completely surrounded by the diffuse electron cloud.

The two strong OD stretching bands (Fig. 2B) appear to match the signature doublet feature common to the OH stretching region of all anionic water clusters from $n =$ 6 to 9 and 11. In the tetramer, the bands can be traced to the symmetric (ν_s) and asymmetric (ν_a) stretching motions of the two deuterium atoms on the AA water molecule. Although these deuterium atoms are slightly inequivalent due to the cis orientation of the neighboring AD water molecules, the splitting between the two normal modes (120 cm^{-1}) is quite close to that found in isolated D_2O (117 cm^{-1}). The retention of this large splitting in the cluster environment indicates that, unlike hydrated anions such as Cl_2^- (*36*), the diffuse electron does not compress the HOH bond angle. The strong redshift of these nominally "free" or nonbonded hydrogen atoms apparently results from the AA arrangement, wherein the acceptor H-bonds act to cooperatively enhance the donor H-bonds to the excess electron (*37*).

The structural assignment for the tetramer anion can be used in characterizing the evolving electron-binding motifs in the larger clusters. The lowest energy bending transition is nearly identical in the $n = 4$ to 6 cluster anions (Fig. 1), which suggests that the AA binding site is preserved in larger clusters. The OD stretching bands for these larger species (Fig. 4) again appear as sharp features, and the ν_s band associated with the AA water molecule in the $n = 4$ spectrum (Fig. 2B) is virtually identical in the spectra of the larger clusters. There is, however, a modest redshift of the $n = 4$ ν_a feature with increasing cluster size.

The $n = 6$ spectrum (Fig. 4B) is particularly useful because the corresponding spectrum in the OH stretching region has also been reported (*23*, *29*), allowing us to link the behavior of the two isotopomers conclusively. The band patterns are remarkably similar for both isotopes; as mentioned earlier, the doublet observed in the OH stretching region was found to persist in larger clusters. In the OH spectra, the band splitting is smaller than in the OD spectra (100 versus 120 cm^{-1}), a finding consistent with the 99 and 117 cm^{-1} splittings measured for isolated H_2O and D_2O, respectively. These observations strongly suggest the continued importance of the AA water molecule.

Using the same level of theory (DFT) that correctly predicted the vibrational bands in the tetramer anion, we have also made structural and band assignments for the pentamer and hexamer. The calculated spectra (Fig. 4, top) accurately reproduce all of the experimentally observed transition energies (Fig. 4, bottom), with the caveat that DFT systematically underestimates the intensities of the most redshifted bands.

The cluster structures giving rise to these patterns are also included above the calcu-

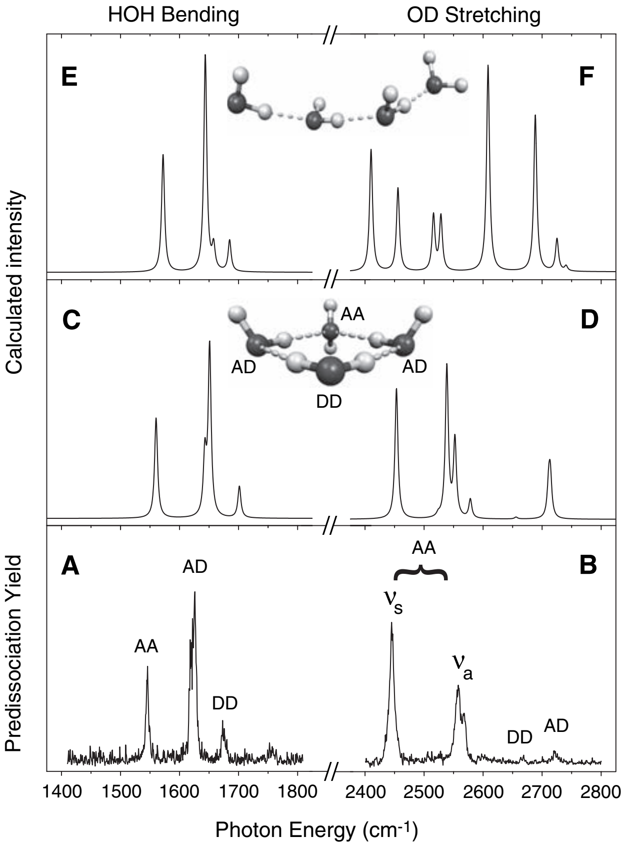

Fig. 2. (Bottom) Argon predissociation spectra of $(H_2O)_4^- \cdot Ar_5$ in the bending region (**A**) and $(D_2O)_4^- \cdot Ar_{10}$ in the OD stretching region (**B**). (Middle) Calculated harmonic spectra of $(H_2O)_4^-$ in the bending region (**C**) and $(D_2O)_4^-$ in the stretching region (**D**) for the cyclic structure shown, with A and D indicating acceptor and donor H-bonds, respectively. (Top) Analogous calculated spectra for the linear structure shown. The calculated spectra [B3LYP/6-311++G**(*sp*)] are scaled by 0.996 and 0.970 in the bend (**E**) and stretch (**F**) regions, respectively, where the factors indicate the corrections required to recover the bands in the isolated water isotopomers.

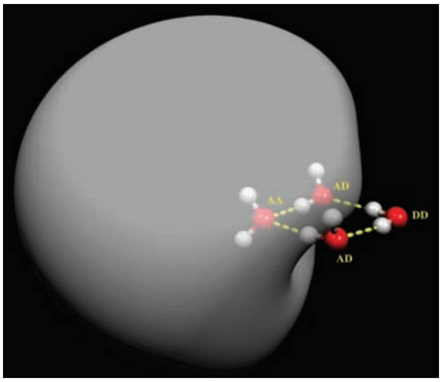

Fig. 3. A contour of the calculated orbital describing the excess electron bound to the cyclic water tetramer anion, $(H_2O)_4^-$.

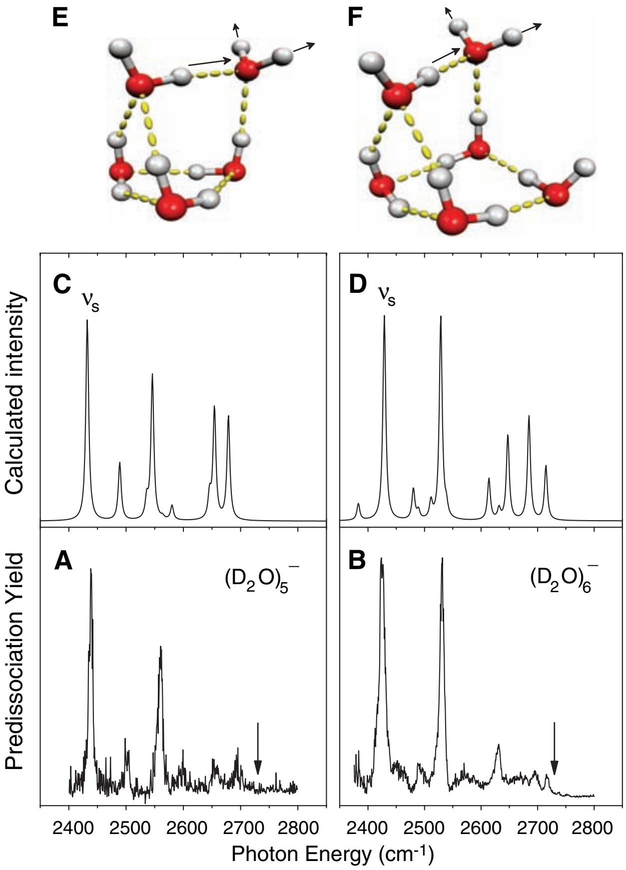

Fig. 4. (Bottom) Argon predissociation spectra of $(D_2O)_5^- \cdot Ar_6$ (**A**) and $(D_2O)_6^- \cdot Ar_7$ (**B**), with arrows indicating ν_{OD} in free D_2O. (Top) Calculated spectra for the corresponding pentamer and hexamer structures shown above (**E** and **F**), with normal mode displacement vectors included for the lowest-energy symmetric stretching vibrations (ν_s) on each structure.

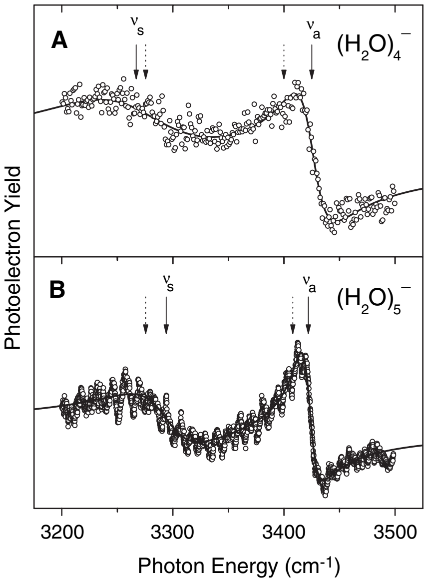

Fig. 5. (**A**) Electron photodetachment spectrum of $(H_2O)_4^- \cdot Ar_6$. (**B**) Electron photodetachment spectrum of $(H_2O)_5^-$, reproduced from (*29*); the sawtooth modulation is an artifact of laser power stabilization. The solid lines are fits as described in the text. The solid arrows indicate the unperturbed locations of the two stretching modes (labeled ν_s and ν_a) of the AA water molecule from the fit, whereas the dotted arrows denote the respective energies extrapolated from the sharper OD bands (Fig. 4).

lated spectra in Fig. 4. The structure calculated for the hexamer anion is the armchair form previously assigned by Kim and coworkers (*25*) on the basis of the OH stretching spectra. In the $n = 5$ and 6 clusters, the AA water molecule, which was associated with a pair of flanking AD molecules in the tetramer, becomes closely associated with only one nearby AD molecule as the cluster grows.

The higher energy vibrational bands shown in Fig. 4 allow us to determine the structures associated with water molecules remote from the excess electron. The bands closest to the free OD stretching frequency (indicated by arrows in the lower traces of Fig. 4) exhibit a discontinuous evolution, first falling toward lower energy in the pentamer and then returning back toward the free OD position in the hexamer. This trend is readily understood in the context of the proposed structures. The $n = 5$ cluster effectively consists of a dimer subcluster mounted on a cyclic trimer base (Fig. 4E). The dimer is supported by three donor H-bonds from the ring, so that the only nonbonded hydrogen atoms are in direct contact with the diffuse electron (*38*). The $n = 6$ structure (Fig. 4F) is closely related to that of the pentamer, but a fourth water molecule is added to the trimer base. This more open arrangement in the hexamer leaves one nonbonded hydrogen atom farther from the excess electron and thus yields a band closer to the free OD location, as is observed in the spectrum.

The emergence of the dimer-subcluster motif is also important because the donor hydrogen atom is calculated to be completely coupled to the stretches of the nonbonded hydrogen atoms on the AA water molecule in the signature doublet. The normal mode vectors for the ν_s vibration are indicated by the arrows on the structures at the top of Fig. 4. Only these three atoms undergo significant displacement. This DAA type of vibration appears to be driving the dimer toward an $OH^- \cdots H_3O^+$ ion pair configuration, which should cause a dramatic increase in the dipole moment, and hence increased coupling to the excess electron.

We can use our spectral assignments to probe the dynamics of vibration-to-electronic coupling in the clusters. In general, when a vibrational level occurs above the electron-binding energy of an anion, the coupling between molecular vibrations and the background electron continuum leads to decay of the vibrational energy via autodetachment

$$(H_2O)_n^- + h\nu \rightarrow (H_2O)_n^- \times (v) \rightarrow (H_2O)_n + e^- \qquad (3)$$

However, in cases where the optical absorption transition moments to the embedded vibrational level and the electron continuum are comparable, the bands become strongly distorted into so-called “Fano” line shapes as a result of interference between the two absorption pathways (*39*).

This phenomenon is observed in the OH stretching region of the $(H_2O)_{4,5}^-$ clusters. The electron photodetachment spectra of both the $(H_2O)_4^- \cdot Ar_6$ cluster and the corresponding pentamer (*29*) (Fig. 5) display the classic derivative-type profiles, indicating very strong coupling to the background electron continuum. These line shapes are known to follow the form (*40*)

$$\sigma(\tilde{\nu}) = \frac{(q + \varepsilon)^2}{1 + \varepsilon^2} \qquad (4)$$

where the q parameter controls the relative absorption strengths of the vibrational level and background continuum, and ε contains information on both the decay rate (τ) and frequency $\tilde{\nu}_0$ of the embedded resonance through the relation

$$\varepsilon = 4\, \tau\, \pi\, c\, (\tilde{\nu} - \tilde{\nu}_0) \qquad (5)$$

To fit the distorted Fano profiles, we iteratively convoluted the independent contributions of the AA symmetric and asymmetric stretching bands, with ε, q, and $\tilde{\nu}_0$ as adjustable parameters. The unperturbed locations of the embedded vibrational levels are indicated by the solid arrows in Fig. 5. The lifetimes extracted from the fits (solid lines in Fig. 5) are remarkably short, with the tetramer symmetric stretch decaying in only about 50 fs and the asymmetric stretch in approximately 150 fs. The pentamer lifetimes are approximately twice as long, with a similar ratio of symmetric to asymmetric decay rates.

This mode-specific relaxation behavior may well be relevant in explaining the ultrashort time scales of the absorption transients observed in the bulk hydrated electron (*41*, *42*). For example, Wiersma and co-workers (*11*) have already noted that their 50-fs electronic relaxation time could only be explained with a model in which the relaxation is mediated by coupling to the vibrational modes of the water molecules. Such a local interaction has also been observed through the resonant Raman spectra of hydrated electrons in the bulk, which reveal that at least one OH bond forms an exceptionally strong donor H-bond either to the electron or to oxygen (*13*). Extension of the ultrafast experiments to the larger clusters will further explore whether the local binding motif uncovered in this work quantitatively recovers the dynamics at work in the bulk environment.

References and Notes

1. W. Weyl, *Ann. Phys.* (*Leipzig*) **197**, 601 (1864).
2. C. A. Kraus, *J. Am. Chem. Soc.* **30**, 1323 (1908).
3. R. A. Ogg Jr., *J. Chem. Phys.* **14**, 114 (1946).
4. R. N. Barnett, U. Landman, C. L. Cleveland, J. Jortner, *J. Chem. Phys.* **88**, 4421 (1988).
5. B. J. Schwartz, P. J. Rossky, *J. Chem. Phys.* **101**, 6917 (1994).
6. E. J. Hart, J. W. Boag, *J. Am. Chem. Soc.* **84**, 4090 (1962).
7. S. Golden, T. R. Tuttle Jr., *J. Chem. Soc. Faraday Trans. II* **75**, 474 (1979).
8. D. M. Bartels, *J. Chem. Phys.* **115**, 4404 (2001).
9. P. Ayotte, thesis, Yale University (1999).
10. P. Kambhampati, D. H. Son, T. W. Kee, P. F. Barbara, *J. Phys. Chem. A* **106**, 2374 (2002).
11. M. S. Pshenichnikov, A. Baltuška, D. A. Wiersma, *Chem. Phys. Lett.* **389**, 171 (2004).
12. A. L. Sobolewski, W. Domcke, *Phys. Chem. Chem. Phys.* **4**, 4 (2002).
13. M. J. Tauber, R. A. Mathies, *J. Am. Chem. Soc.* **125**, 1394 (2003).
14. W. H. Robertson, M. A. Johnson, *Annu. Rev. Phys. Chem.* **54**, 173 (2003).
15. H. Haberland, H.-G. Schindler, D. R. Worsnop, *Ber. Bunsenges. Phys. Chem.* **88**, 271 (1984).
16. H. Haberland, H. Langosh, H.-G. Schindler, D. R. Worsnop, *J. Phys. Chem.* **88**, 3903 (1984).
17. H. Haberland, C. Ludewigt, H.-G. Schindler, D. R. Worsnop, *J. Chem. Phys.* **81**, 3742 (1984).
18. S. T. Arnold, R. A. Morris, A. A. Viggiano, M. A. Johnson, *J. Phys. Chem.* **100**, 2900 (1996).
19. M. K. Beyer, B. S. Fox, B. M. Reinhard, V. E. Bondybey, *J. Chem. Phys.* **115**, 9288 (2001).
20. P. J. Campagnola, D. J. Lavrich, M. J. Deluca, M. A. Johnson, *J. Chem. Phys.* **94**, 5240 (1991).
21. C. G. Bailey, J. Kim, M. A. Johnson, *J. Phys. Chem.* **100**, 16782 (1996).
22. J. V. Coe *et al.*, *J. Chem. Phys.* **92**, 3980 (1990).
23. P. Ayotte, C. G. Bailey, J. Kim, M. A. Johnson, *J. Chem. Phys.* **108**, 444 (1998).
24. C. J. Tsai, K. D. Jordan, *Chem. Phys. Lett.* **213**, 181 (1993).
25. H. M. Lee, S. Lee, K. S. Kim, *J. Chem. Phys.* **119**, 187 (2003).
26. F. Wang, K. D. Jordan, *Annu. Rev. Phys. Chem.* **54**, 367 (2003).
27. S. A. Corcelli, J. A. Kelley, J. C. Tully, M. A. Johnson, *J. Phys. Chem. A* **106**, 4872 (2002).
28. W. H. Robertson, J. A. Kelley, M. A. Johnson, *Rev. Sci. Instrum.* **71**, 4431 (2000).
29. P. Ayotte *et al.*, *J. Chem. Phys.* **110**, 6268 (1999).
30. L. A. Posey, M. A. Johnson, *J. Chem. Phys.* **89**, 4807 (1988).
31. J. Kim, I. Becker, O. Cheshnovsky, M. A. Johnson, *Chem. Phys. Lett.* **297**, 90 (1998).
32. J.-W. Shin, N. I. Hammer, J. M. Headrick, M. A. Johnson, *Chem. Phys. Lett.*, in press.
33. Accessing the lower wavelength region of the bending modes (~1500 cm^{-1}) required modification of our pulsed infrared laser (LaserVision) by addition of a third nonlinear mixing stage based on a AgGaSe$_2$ crystal. This arrangement provides about 100 μJ of energy in the bending region.
34. Because of the near mass degeneracy between Ar and $(D_2O)_2$, we verified that the dimer and trimer clusters exhibit no photofragmentation or sharp bands, consistent with their low VDEs. Thus, the $(D_2O)_4^- \cdot Ar_m$ spectrum could be selectively monitored by detecting the photofragment anions that arise only from this species.
35. J. B. Paul *et al.*, *J. Phys. Chem. A* **103**, 2972 (1999).
36. E. A. Price, N. I. Hammer, M. A. Johnson, *J. Phys. Chem. A* **108**, 3910 (2004).
37. W. H. Robertson, K. Karapetian, P. Ayotte, K. D. Jordan, M. A. Johnson, *J. Chem. Phys.* **116**, 4853 (2002).
38. T. Tsurusawa, S. Iwata, *Chem. Phys. Lett.* **315**, 433 (1999).
39. U. Fano, *Phys. Rev.* **124**, 1866 (1961).
40. A. R. P. Rau, *Phys. Scrip.* **69**, C10 (2004).
41. C. Silva, P. K. Walhout, K. Yokoyama, P. F. Barbara, *Phys. Rev. Lett.* **80**, 1086 (1998).
42. A. Baltuška, M. F. Emde, M. S. Pshenichnikov, D. A. Wiersma, *J. Phys. Chem. A* **103**, 10065 (1999).
43. We thank the U.S. Department of Energy (grant DR-FG02-00ER15066) for support of this research direction, as well as NSF, which provided the equipment used in this study. We also thank K. D. Jordan for valuable discussions regarding the formation mechanisms at work in these clusters and T. Zwier and J. Stearns for help with the wavelength extension of the laser.

15 July 2004; accepted 20 August 2004

Reconstructing Past Climate from Noisy Data

Hans von Storch,[1]* Eduardo Zorita,[1] Julie M. Jones,[1] Yegor Dimitriev,[1] Fidel González-Rouco,[2] Simon F. B. Tett[3]

Empirical reconstructions of the Northern Hemisphere (NH) temperature in the past millennium based on multiproxy records depict small-amplitude variations followed by a clear warming trend in the past two centuries. We use a coupled atmosphere-ocean model simulation of the past 1000 years as a surrogate climate to test the skill of these methods, particularly at multidecadal and centennial time scales. Idealized proxy records are represented by simulated grid-point temperature, degraded with statistical noise. The centennial variability of the NH temperature is underestimated by the regression-based methods applied here, suggesting that past variations may have been at least a factor of 2 larger than indicated by empirical reconstructions.

Reconstruction of past climate from palaeoclimate proxy data is important for the detection of anthropogenic climate change. A number of studies have attempted to reconstruct variations in global or NH temperature within the past millennium by regressing proxy indicators and early instrumental time series on recent instrumental climate variables with high spatial resolution (*1*–*3*). Regression models are developed during the period of common instrumental and proxy data and are then applied to longer proxy records to reconstruct past climates. Similar methods have been applied for the reconstruction of atmospheric circulation indices, such as the North Atlantic Oscillation (*4*) or the Antarctic Oscillation (*5*). A number of reconstructions show that the temperatures in the last millennium were characterized by geographically varying warm values in the 11th and 12th centuries, followed by a secular cooling trend punctuated by decadal-scale colder periods in the mid-16th, early 17th, and early 19th centuries (*6*). These cooler intervals were followed by the marked warming experienced until today. Although the amplitude of these preindustrial variations is still debated, according to the most quoted NH temperature reconstruction [Mann, Bradley, Hughes, 1998 (MBH98) (*1*) and Mann, Bradley, Hughes, 1999 (MBH99) (*2*)] and the most recent Intergovernmental Panel on Climate Change (IPCC) report (*7*), these variations were of small amplitude. However, recent studies with general circulation models suggest that these centennial variations may have been larger (*8*–*10*). We used a coupled atmosphere-ocean model simulation of the past 1000 years as surrogate climate to test whether

---

[1] Institute for Coastal Research, GKSS Research Centre, Geesthacht 21502, Germany. [2] Department of Astrophysics and Atmospheric Physics, Universidad Complutense, Madrid 28040, Spain. [3] UK Meteorological Office, Hadley Centre (Reading Unit), Meteorology Building, University of Reading, Reading, RG6 6BB, UK.

*To whom correspondence should be addressed. E-mail: storch@gkss.de

the reconstruction method of MBH98 and MBH99 and a much simpler regression method can yield realistic estimates of the multidecadal and secular temperature variations.

A number of modeling studies of the evolution of the climate in the past centuries (*11–14*) pose some questions about the reliability of empirical reconstructions based on regression methods. For instance, concerning the cooling around 1700, the reconstructions by MBH98 have agreed with the results obtained with the the Goddard Institute for Space Studies model only in the model version with a low climate sensitivity ($0.4 K/W/m^2$) (*10*). Similarly, the agreement between an energy-balance model (*11*) and reconstructions has been achieved by prescribing a model sensitivity to changes in radiative forcing of $0.5 K/W/m^2$. These values of climate sensitivity are at the low end of the range of the models included in the IPCC analysis (*7*). Other reconstructions that indicate markedly stronger cooling in the 16th to 18th centuries are, for instance, the result of empirical methods that explicitly aim to preserve low-frequency variability (*15*) and the borehole-based reconstructions (*16*). Interestingly, the latter is not based on empirical regression methods. This apparent discrepancy poses a question as to whether model simulations overestimate secular climate variability or regression-based reconstructions underestimate it.

The reliability of these empirical methods at centennial time scales can be tested in the surrogate climate simulated by three-dimensional climate models driven by plausibly estimated historical external forcing. The results of the reconstruction process can then be validated against the climate fields simulated by the climate model. The data representing the proxy records are climate variables simulated at grid-box resolution, which can be degraded with statistical noise to mimic more realistic data [so-called pseudoproxies (*17*)]. Here, we follow this strategy with the output of a climate simulation of the past millennium with the coupled atmosphere-ocean general circulation model European Centre Hamburg 4–Hamburg Ocean Primitive Equation–G (ECHO-G) (*18*), driven by estimations of historical climate forcing. This simulation provides a data set in which the potential nonstationarity of the covariances and the length of the time series are similar to those found in applications of the empirical reconstruction methods.

This simulation reproduces warming around 1100 and extended coolings over the Spörer, Maunder, and Dalton Minima as near-global events, as well as the recent anthropogenic warming. Compared with the reconstructions of MBH99, however, the variations are stronger. For the purpose of this paper, it is not critical if the simulation is not absolutely realistic because of model limitations (e.g., coarse resolution or deficient representation of processes) or uncertainties in external forcings. The crucial point is that the model simulates a reasonable, internally consistent climate, and the external forcing lies within the envelope of possible values. In this case, it will be used as a virtual world to determine the skill of regression-based reconstruction methods like MBH98 to estimate its temperature variations.

Here, we focus on the reconstruction of NH temperature. For this analysis, we applied as realistically as possible the statistical method of MBH98. However, when arbitrary choices were required, the a priori most favorable for the statistical method were implemented, thus probably minimizing the loss of variance in the statistical reconstructions. For instance, the proxy network in MBH98 gets coarser backward in time, but the pseudoproxy network in this study was not decimated to avoid loss of skill. Also, only temperature pseudoproxies were used to reconstruct the temperature evolution. The pseudoproxies were generated by adding a statistical white noise to the simulated temperatures in grid points colocated to the MBH98 proxy network (*1*). Several tests with varying amounts of noise were carried out.

The loss of variance resulting from a regression-type method may be simply conceptualized (*18*). The proxy data P are thought to blend local temperature T_l and unrelated variability ε: $P = \alpha T_l + \varepsilon$. The temperature variations are essentially estimated as $T_l^* = \beta P$, where $\beta = \rho\sigma_T/\sigma_P < 1$ and ρ is the correlation between T_l and P. Therefore, $\mathrm{Variance}(T^*) = \rho^2 \mathrm{Variance}(T_l) < \mathrm{Variance}(T_l)$. In case of proxy data, the correlation ρ is mostly on the order of 0.4 to 0.7 (*8*), resulting in a leakage or variance on the order of 50 to 80%. In particular, if T_l has a red spectrum and ε has a white spectrum, T^* will underestimate the low-frequency variance of T_l. In the case of MBH98 and other reconstructions, the methodological process is more sophisticated, but the fundamental problem of the loss of variance resulting from noisy proxy data may also exist in these studies (*19*). This loss of variance, also known in areas such as regionalization and long-term forecasting (*20*), is sometimes accounted for by artificially inflating the parameter ρ. For paleoclimate reconstructions, ρ should be made time-scale dependent, and this dependency is unknown.

To implement the method of MBH98, we selected model grid boxes colocated with their proxy data network (Fig. 1, red pixels) and added white noise (*21*) to the grid-point temperatures T_g, so that the pseudoproxy data are $P = T_g + \varepsilon$. The variance of ε varies between $m = 0$ and $m = 4 \times \mathrm{Var}(T_g)$. The correlation between the T_g and P is then $(1 + m)^{-1/2}$. Thus, with $m = 0$, the local P variance described by T_g is 100%; for $m = 1$, when noise with the same variance as that of the local temperature is added, the percentage of described variance is 50%. For $m = 4$, the described variance is only 20%. Ideally, the reconstructions would coincide with the simulated NH temperature, but actually they do not, even for $m = 0$ (Fig. 2A, illustrating the loss of variance induced by the method alone). The short-term variations are reasonably reproduced, at least for $m < 4$. For instance, on an interannual time scale, the fit between simulated and reconstructed NH temperature is good, with a calibration reduction-of-error statistics of 0.7 for perfect pseudoproxies and 0.30 for pseudoproxies with $\varepsilon = 0.5$. The substantial underestimation of low-frequency temperature variations is evident from Fig. 2B. For example, only 20% of the 100-year variability is recovered when the noise level is 50%. For time scales of 20 years, about three-quarters of the variability is lost. Similar results are obtained with a simulation with the third Hadley Centre coupled model (HadCM3), demonstrating that the results obtained here are not dependent on the particular climate characteristics of the ECHO-G simulation (*18*). Also a spatially varying level of noise does not essentially modify these conclusions (*18*).

Our setup allowed the test of a number of hypotheses. The first hypothesis is that the inclusion of more instrumental data would improve the estimate, as the multiproxy data used by MBH99 contained a number of long instrumental temperature data, which start

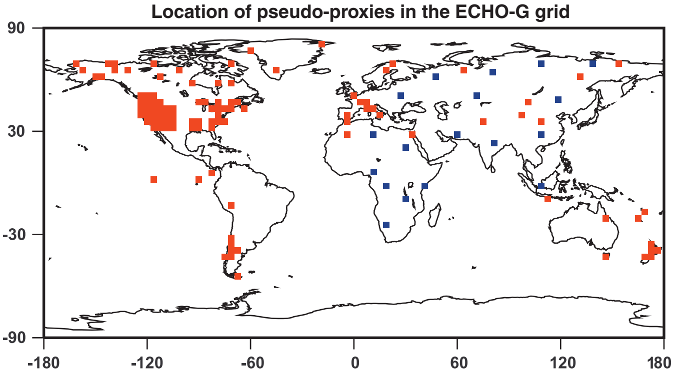

Fig. 1. Grid boxes in the ECHO-G model, from which simulated temperatures are used to estimate NH temperatures. The red pixels are used for the basic reconstruction; the blue pixels are added in a test of whether a better spatial coverage would improve the reconstruction.

typically at the end of the 18th century. To test the influence of such instrumental data, we included grid-box temperatures without adding noise (*18*). The effect of this modification on the hemispheric temperature was small; the differences in the reconstructed temperature anomalies were within a range of 2%. This can be explained by the relatively low number of perfect pseudoproxies included in comparison with the total number of pseudoproxies and by the built-in robustness against local influences of the inverse regression method used by MBH98, because the signal is extracted nonlocally from the whole proxy data set simultaneously (*18*). Other direct regression methods, aimed at more regionally limited temperature reconstructions, do show an improvement when instrumental records are included in the proxy network (*22*).

The second hypothesis is related to the sparseness of the proxy locations (Fig. 1, red pixels). The proxy data set was enlarged by adding 18 locations in Asia and Africa (Fig. 1, blue pixels) to increase the spatial coverage. This leads to a minor improvement in the NH temperature reconstruction (Fig. 3), which was largely independent of the inclusion or exclusion of Southern Hemisphere pseudoproxies.

Finally, we tested whether the range of variability present in the instrumental period is sufficient to reconstruct the climate of past centuries. To test this hypothesis, 40 years were taken from the Late Maunder Minimum (1680 to 1720) and 40 years from the early part of the 20th century (1900 to 1940) to calibrate the statistical model, thereby expanding the range of temperature variability present in the pseudoproxies. When the proxies are free of noise, the reconstruction of the simulated NH temperature is greatly improved (Fig. 3). With 50% local noise included, the reconstruction is also improved, although the loss of low-frequency variance is still large. Therefore, augmenting the variability in the calibration period improves the skill, but obviously this is limited by the available observational record.

A further question is whether the limitations we have found are common to regression methods in general. Thus, two further approaches were tested. In the first, local temperatures were estimated by a linear regression from pseudoproxies, and the local temperature estimations were spatially averaged to derive the NH temperature. This method mimics the situation in which, for example, local dendrochronologies calibrated in terms of local temperature are just arithmetically averaged. In the second approach, the pseudoproxies at the various locations were directly simply averaged. This is more similar to the borehole methodology (*16*). For the first method, we found qualitatively similar but quantitatively even worse problems than with the MBH98 method; that is, the underestimation of low-frequency variability for a given amount of noise is greater than for MBH98, whereas the second method returns good estimates of NH temperature, with very little loss of variance with 75% variance noise (Fig. 4). This result is not surprising given that the first method suffers from the variance loss related to regression, whereas in the second, the noise contributions are simply averaged out.

Hints of the underestimation of low-frequency variability by empirical reconstruction methods have been found in previous studies, based either on short data sets (*17*) or climate simulations with fixed external forcing (*23*). In a study based entirely on an instrumental data set (*17*), the spectrum of the difference between the reconstructed and observed global mean annual temperature is, albeit consistent with a white noise assumption, slightly red. In a further analysis of an instrumental data set and data from a long control simulation with the Geophysical Fluid Dynamics Laboratory climate model (with constant external forcing) and a relatively short simulation of 143 years driven by varying external forcing (*23*), the spectra of the temperature differences from the analysis of control simulation are red (although again statistically compatible with white noise assumption). In this externally forced simulation, it was found that the temperature reconstructions are biased if the external forcing leads to nonstationary behavior in the verification period. In a long control simulation (1000 years) with the model ECHO-G (*24*), the spectrum of the reconstructed annual global temperature underestimates the spectrum of the simulated global temperature at very low frequencies.

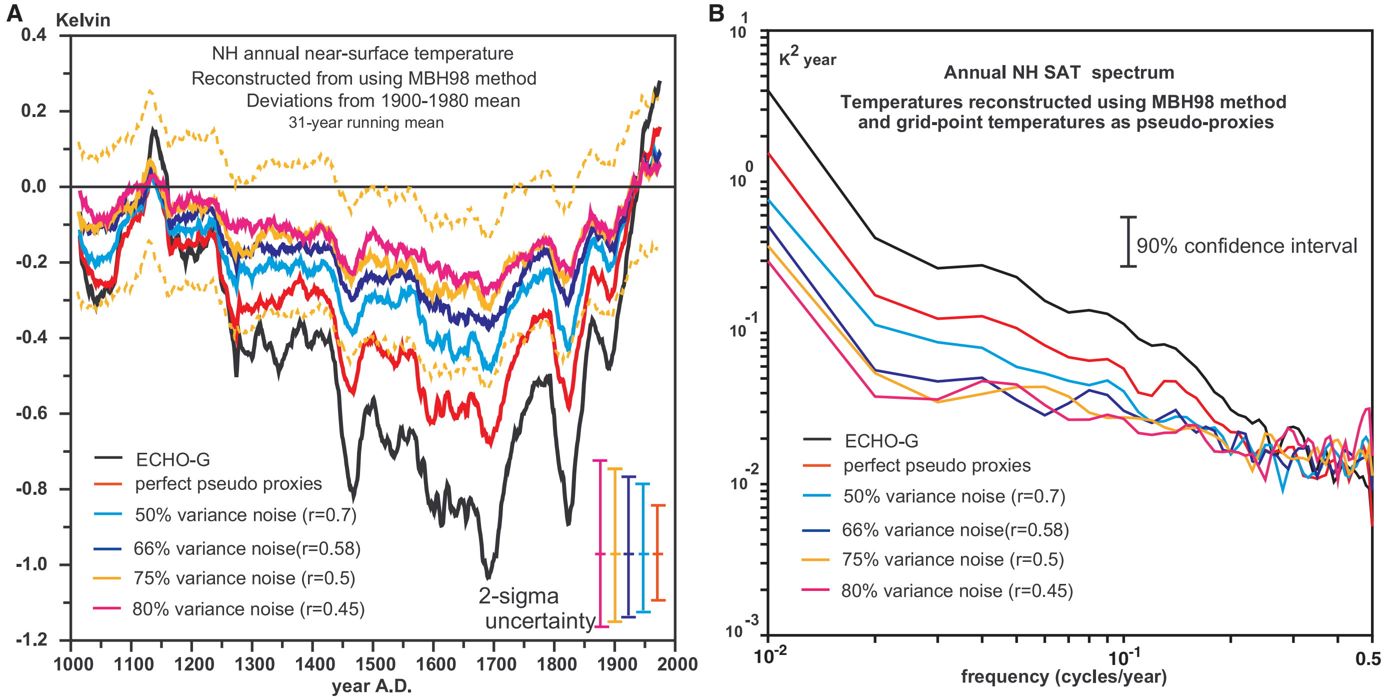

Fig. 2. (**A**) The NH annual temperature evolution over the past 1000 years. The NH annual temperature simulated by the model ECHO-G and MBH98 reconstructions of this temperature from 105 model grid points mimicking the multiproxy network of MBH98. Increasing amounts of noise have been added to the grid-point temperatures to mimic the presence of other than temperature signals in the proxies. The corresponding local correlation is also indicated. The 2σ uncertainty range (derived as in MBH98 from the variance of the interannual residuals) for the different noise levels is indicated. The reconstruction with $\rho = 0.5$ is shown with its 2σ uncertainty range. (**B**) The spectra of the NH annual temperatures shown in (A).

Climate simulations of the past millennium are burdened by model limitations and uncertainties in the external forcing, and therefore their output must be considered with care. However, they provide a surrogate climate realistic enough to conclude that the use of the regression methods considered here, which exploit short-term cross-correlations to reconstruct past climates, suffer from marked losses of centennial and multidecadal variations. This conclusion probably applies to most other regression-based methods. Other methods that estimate past temperatures with physical, as opposed to statistical, methods [e.g., borehole temperature profiles (*16*)], or regression methods that address retention of the information of the low-frequency variability contained in the proxy indicators (*25*), may be in theory free from this specific caveat. Our results indicate that a detailed testing of these reconstruction methods in simulated climates should be an essential part in the reconstruction process and may help in the design of better reconstruction methods.

Fig. 3. Simulated (black) and estimated NH temperature (purple, blue, orange, yellow, and pink) showing the effect of noise. Different setups for the estimation were used: the standard method with 50% noise added (pink); with additional pixels in Africa and Asia (locations, Fig. 1) with 50% noise (blue) and without noise (purple); with a different fitting period, namely 1680 to 1720 plus 1900 to 1940 (instead of the standard 1900 to 1980) with 50% noise (yellow) and without noise (orange).

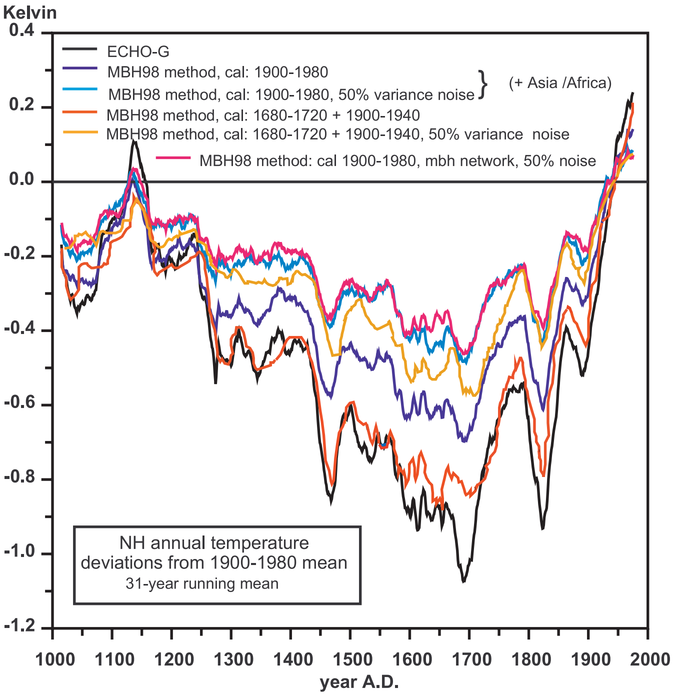

Fig. 4. Simulated NH temperature compared with an estimate with a simple local linear regression on the pseudoproxies used in Fig. 2. The local temperature is estimated from each pseudoproxy and the result is simply averaged over all pseudoproxy locations to obtain the NH estimate. Also shown is the arithmetic mean of the perfect pseudoproxies and of the pseudoproxies containing 50% noise.

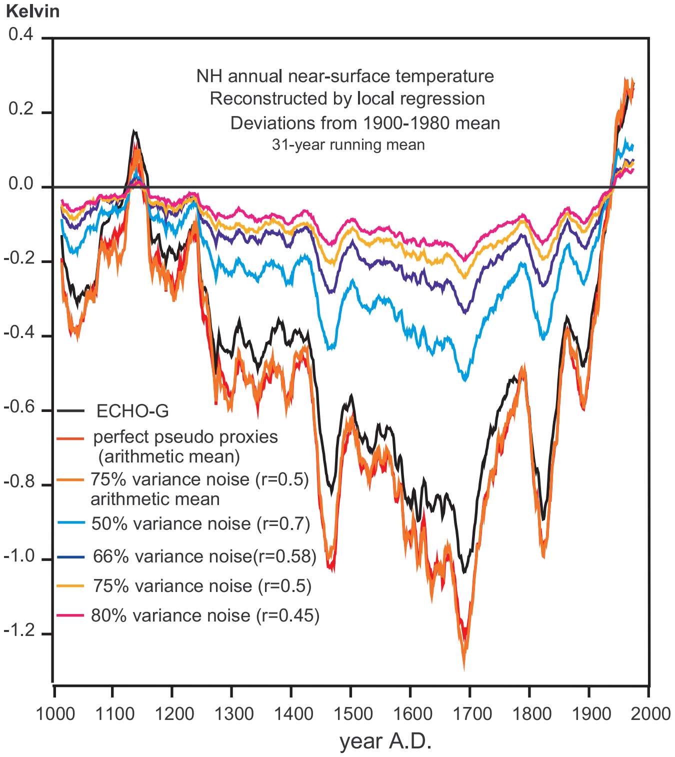

References and Notes

1. M. E. Mann, R. S. Bradley, M. K. Hughes, *Nature* **392**, 779 (1998).
2. M. E. Mann, R. S. Bradley, M. K. Hughes, *Geophys. Res. Lett.* **26**, 759 (1999).
3. P. D. Jones, K. R. Briffa, T. P. Barnett, S. F. B. Tett, *Holocene* **8**, 455 (1998).
4. J. Luterbacher, C. Schmutz, D. Gyalistras, E. Xoplaki, H. Wanner, *Geophys. Res. Lett.* **26**, 2745 (1999).
5. J. M. Jones, M. Widmann, *J. Clim.* **16**, 3511 (2003).
6. P. D. Jones, T. J. Osborn, K. R. Briffa, *Science* **292**, 662 (2001).
7. J. T. Houghton *et al.*, *Climate Change 2001: The Scientific Basis* (Cambridge Univ. Press, Cambridge, 2001).
8. P. D. Jones, M. E. Mann, *Rev. Geophys.* **42**, RG2002, 10.1029/2003RG000143 (2004).
9. E. Zorita *et al.*, *Meteorol. Z.* **13**, 271 (2004).
10. D. Rind *et al.*, *J. Clim.* **17**, 906 (2004).
11. T. J. Crowley, *Science* **289**, 270 (2000).
12. S. Gerber *et al.*, *Clim. Dyn.* **20**, 281 (2003).
13. H. Goosse *et al.*, *Geophys. Res. Lett.* **31**, L06203, 10.1029/2003GL019140 (2004).
14. E. Bauer, M. Claussen, V. Brovkin, A. Huenerbein, *Geophys. Res. Lett.* **30**, 1276, 10.1029/2002GL016639 (2003).
15. J. Esper, E. R. Cook, F. H. Schweingruber, *Science* **295**, 2250 (2002).
16. S. H. Huang, H. N. Pollack, P. Y. Shen, *Nature* **403**, 756 (2000).
17. M. E. Mann, S. Rutherford, *Geophys. Res. Lett.* **29**, 139, 10.1029/2001GL014554 (2002).
18. Materials and Methods are available as supporting material on *Science* Online.
19. For instance, the standard deviation of the MBH99 reconstructed NH temperature in the period of 1948 to 1980 is 0.9K, compared with 1.4K derived from the National Centers for Environmental Protection reanalysis or from the Jones *et al.* (*26*) NH gridded instrumental data.
20. H. von Storch, *J. Clim.* **12**, 3505 (1999).
21. Local noise could in many cases be expected to be either white or red. In any case, red noise degrades the reconstructions, as in (*17*).
22. J. Luterbacher, D. Dietrich, E. Xoplaki, M. Grosjean, H. Wanner, *Science* **303**, 1499 (2004).
23. S. Rutherford, M. E. Mann, T. L. Delworth, R. J. Stouffer, *J. Clim.* **16**, 462 (2003).
24. E. Zorita, F. González-Rouco, S. Legutke, *J. Clim.* **16**, 1378 (2003).
25. T. J. Osborn, K. R. Briffa, *Dendrochronologia* **18**, 9 (2000).
26. P. D. Jones, M. New, D. E. Parker, S. Martin, I. G. Rigor, *Rev. Geophys.* **37**, 173 (1999).
27. This work was carried out within the projects German Climate Research Program (DEKLIM) [German Federal Ministry for Education and Research (BMBF)]; Simulations, Observations, and Palaeoclimate data (SOAP) (European Union, EVK2-CT-2002-00160); and REN-2000-0786cli (Comisión Interministerial de Ciencia y Tecnologia). S.F.B.T. was supported by a UK Government Meteorological Research contract and SOAP. Computer time for HadCM3 simulations was funded by Defra under contract PECD/7/12. Data distribution was through SOAP. Three anonymous reviewers greatly contributed to the improvement of the original manuscript. We acknowledge fruitful suggestions by T. Stocker.

Supporting Online Material
www.sciencemag.org/cgi/content/full/1096109/DC1
SOM Text
Figs. S1 and S2
References

27 January 2004; accepted 23 August 2004
Published online 30 September 2004;
10.1126/science.1096109
Include this information when citing this paper.

Mycobacterial Ku and Ligase Proteins Constitute a Two-Component NHEJ Repair Machine

**Marina Della,[1]*† Phillip L. Palmbos,[2]† Hui-Min Tseng,[3]†
Louise M. Tonkin,[1,4] James M. Daley,[2] Leana M. Topper,[2]
Robert S. Pitcher,[4] Alan E. Tomkinson,[5] Thomas E. Wilson,[2]
Aidan J. Doherty[4]‡**

In mammalian cells, repair of DNA double-strand breaks (DSBs) by nonhomologous end-joining (NHEJ) is critical for genome stability. Although the end-bridging and ligation steps of NHEJ have been reconstituted in vitro, little is known about the end-processing reactions that occur before ligation. Recently, functionally homologous end-bridging and ligation activities have been identified in prokarya. Consistent with its homology to polymerases and nucleases, we demonstrate that DNA ligase D from *Mycobacterium tuberculosis* (Mt-Lig) possesses a unique variety of nucleotidyl transferase activities, including gap-filling polymerase, terminal transferase, and primase, and is also a 3′ to 5′ exonuclease. These enzyme activities allow the Mt-Ku and Mt-Lig proteins to join incompatible DSB ends in vitro, as well as to reconstitute NHEJ in vivo in yeast. These results demonstrate that prokaryotic Ku and ligase form a bona fide NHEJ system that encodes all the recognition, processing, and ligation activities required for DSB repair.

Nonhomologous end-joining (NHEJ) is the major pathway for repairing DNA double-strand breaks (DSBs) in mammalian cells (*1*). Key factors in eukaryotic NHEJ are the Ku70/Ku80 heterodimer (Ku) and DNA ligase IV (*2*), which have functional homologs in prokaryotes (*3*). Ku binds directly to the termini of DSBs and has end-bridging activity (*4*, *5*), as has the yeast Mre11/Rad50/Xrs2 (MRX) complex (*6*). These factors interact with ligase IV/XRCC4 to achieve repair (*6*–*8*). Many DSBs generated in vivo have damaged or noncomplementary termini that require processing by nucleases and polymerases to generate ligatable termini. The molecular mechanisms of these reactions are poorly understood.

The *Mycobacterium tuberculosis* DNA repair ligase, Mt-Lig (*Rv0938* and *LigD*), which is specifically stimulated by Mt-Ku homodimer (*3*), contains domains that exhibit significant homology with polymerases (*9*–*12*) and possibly nucleases (*10*–*12*), suggesting that Mt-Lig might process and then join incompatible DNA ends. Mt-Lig is most homologous to eukaryotic primase (*9*–*12*); however, a requirement for primase during NHEJ is not obvious. Eukaryotic primases share significant sequence homology with the Pol X family of nucleotidyl transferases active in NHEJ (*13*–*17*). Purified recombinant Mt-Lig (*3*, *18*) was an efficient DNA-dependent DNA polymerase in template-dependent primer extension assays (fig. S1). Mt-Lig similarly acted as a DNA-dependent RNA polymerase (fig. S1). Mutating predicted catalytic aspartate residues abolished all polymerase activities, confirming that they are intrinsic properties of Mt-Lig (fig. S1). Terminal transferase (TdT), a Pol X family member, has also been implicated in V(D)J recombination and NHEJ (*14*, *15*). Mt-Lig used adenosine triphosphate (ATP) and, to a lesser extent, dATP to extend single-strand (ss) DNA, demonstrating terminal transferase activity (fig. S2). Finally, Mt-Lig synthesized 10- to 25–nucleotide (nt) oligomers on unprimed circular M13 ssDNA using nucleotide triphosphates (NTPs) but not dNTPs (fig. S3). Thus, Mt-Lig has DNA-dependent RNA primase activity.

To examine microhomology-mediated joints typical of NHEJ, we performed polymerization assays with oligonucleotides that generate a nonligatable 1-nt gap upon alignment (Fig. 1A). Mt-Lig efficiently filled in the gap with no detectable strand displacement synthesis (Fig. 1A, left). Addition of a phosphate group to the 5′ terminus of the 1-nt gap resulted in gap filling and ligation (Fig. 1A, right), indicating the concerted action of Mt-Lig polymerase and ligase activities.

Mt-Lig is also predicted to contain a distinct nuclease domain (*10*, *11*). Indeed, Mt-Lig progressively digested the 3′ but not the 5′ ss tails of partial duplexes (*18*) until reaching the double-strand (ds) region (Fig. 1B). Thus, Mt-Lig possesses 3′ to 5′ ssDNA exonuclease activity. Using DNA substrates that generate a 3′-flap adjacent to a nick, Mt-Lig removed the flap by exonucleolytic digestion, generating a base-paired linear duplex (Fig. 1C). At higher concentrations, the nuclease progressed through the microhomology re-

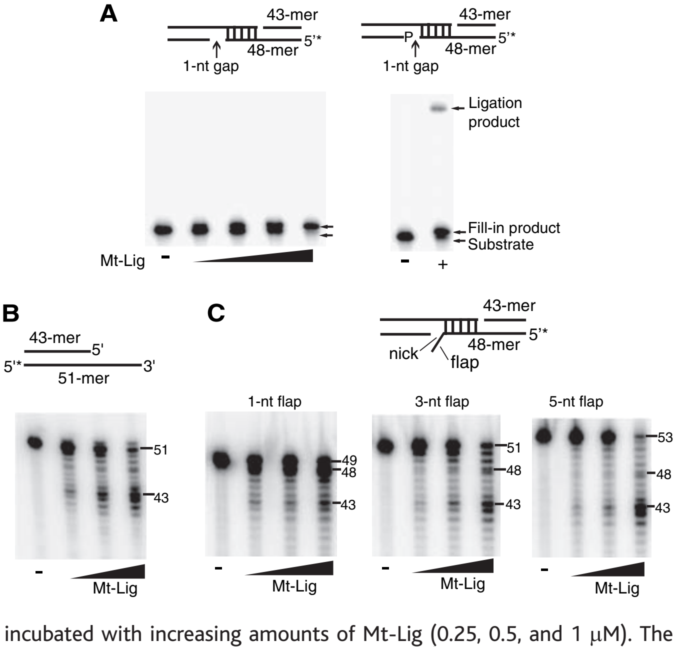

Fig. 1. Mt-Ligase is a multidomain enzyme with polymerase, nuclease, and ligase activities. (**A**) Left: In assays with DNA duplexes that form a nonligatable 1-nt gap, Mt-Lig (0.125, 0.25, 0.5, or 1 μM) efficiently filled in the gap. Right: When a phosphate group was added to the 5′ terminus, Mt-Lig (1 μM) ligated the filled intermediate. (**B**) DNA duplexes with 3′-overhangs were incubated with increasing amounts of Mt-Lig (0.25, 0.5, and 1 μM). The positions of the 51-nt oligomer substrate and 43-nt oligomer degradation products are indicated. (**C**) DNA substrates were incubated with increasing amounts of Mt-Lig (0.25, 0.5, and 1 μM). The positions of the 51-nt oligomer substrate and 48- and 43-nt oligomer 3′ degradation products are indicated.

---

[1] Cambridge Institute for Medical Research, University of Cambridge, Department of Haematology, Hills Road, Cambridge CB2 2XY, UK. [2] Department of Pathology, University of Michigan Medical School, Ann Arbor, Michigan 48109–0602, USA. [3] Molecular Medicine Graduate Program, Institute of Biotechnology, The University of Texas Health Science Center at San Antonio, San Antonio, TX 78245–3207, USA. [4] Genome Damage and Stability Centre, University of Sussex, Falmer, Brighton BN1 9RQ, UK. [5] Department of Radiation Oncology and Greenebaum Cancer Center, University of Maryland School of Medicine, Baltimore, MD 21201–1559, USA.

*Present address: The Institute of Cancer Research, Chester Beatty Laboratories, London SW3 6JB, UK.
†These authors contributed equally to this work.
‡To whom correspondence should be addressed. E-mail: AJD21@sussex.ac.uk

gion and into the duplex (Fig. 1C and fig. S4). Nuclease activity required the presence of magnesium or manganese. Mutation of a conserved histidine residue abolished this exonuclease activity, confirming that it is also an intrinsic property of Mt-Lig (fig. S5).

We thus asked whether this single polypeptide could repair a DSB that requires 3′ resection, gap filling, and ligation. In the presence of NTPs, Mt-Lig joined aligned DNA duplexes possessing a 1-nt 3′ flap adjacent to a 3-nt gap (Fig. 2A and fig. S6). A similar, albeit less efficient, reaction was observed in the presence of dNTPs (fig. S6). Neither the nuclease nor polymerase mutants were able to repair this junction, confirming that both activities were required to process the DSB (fig. S7). Sequencing of ligated junctions in equivalent assays with substrates with a 3-nt flap adjacent to a 5-nt gap revealed that the microhomology sequence was retained and that the mismatched flap was replaced by nucleotides complementary to the template strand (*18*).

Mt-Ku stimulates joining of fully complementary ends by Mt-Lig (*3*). At incompatible ends, Mt-Ku did not have a significant effect on the removal of mismatched flaps, but it did inhibit further digestion into the microhomology region (Fig. 2B), suggesting that Mt-Ku remains physically associated with this region during repair. Using an in vitro polymerase chain reaction (PCR)–based plasmid repair assay (*19*), we observed that Mt-Ku markedly stimulated the joining of long linear DNA molecules with different incompatible ends (Fig. 2C). This occurred in the presence of either dNTPs or NTPs (Fig. 2C). In contrast, we observed no rejoining by T4 ligase in the presence or absence of Mt-Ku (Fig. 2C). Joining of partially complementary 5′ (Hind III–Nhe I) and 3′ (Pst I–Kpn I) overhangs appeared to require microhomology-mediated alignments that need gap filling and, in some instances, 3′ flap removal on one strand (Fig. 2D). Joining of a blunt end–3′ ss overhang (Sma I–Aat II) appeared to require the addition of one nucleotide by the terminal transferase activity, followed by microhomology pairing with the 3′ overhang, flap resection, gap filling, and ligation (Fig. 2D). In all cases, gap filling accurately copied the template strand (*18*).

To examine the rejoining of chromosome breaks in vivo, we exploited a variant of the yeast-based "suicide deletion" assay (*20*, *21*), which allows the simultaneous determination of NHEJ and recombination frequencies (fig. S8A). Consistent with prior observations (*20*, *21*), ~75% of wild-type yeast cells repaired an I-SceI endonuclease-induced DSB by recombination and ~2% by NHEJ, with the remainder dying (Fig. 3A). NHEJ occurred predominantly by simple religation [resulting in Ade$^+$ colonies (fig. S8)] and was decreased 99% by *yku70* (Ku) deletion. Introducing plasmids that express Mt-Ku and Mt-Lig restored NHEJ to about half its level in wild-type yeast (Fig. 3A and fig. S9A). Combinations of Mt-Ku, Mt-Lig, and *yku70* and *dnl4* (yeast ligase IV) mutations demonstrated that Mt NHEJ was truly reconstituted by a concerted species-specific Ku-ligase interaction (Fig. 3B).

In *Saccharomyces cerevisiae*, NHEJ is also dependent on the MRX complex (*21*, *22*). MRX may act as an end-bridging factor and/or functionally interact with yeast Ku and Dnl4 (*6*, *23*). Expression of the Mt NHEJ proteins in yeast *rad50* mutants substantially recovered NHEJ (Fig. 3C), although to a lesser extent than seen with *yku70* or *dnl4* mutants. Thus, Mt NHEJ can occur in the absence of both MRX and its bacterial ortholog SbcCD (*23*).

As with NHEJ mediated by yeast proteins (*20*, *21*, *24*), Mt NHEJ reconstituted in yeast occasionally resulted in imperfect repair, evident as Ade$^-$ colonies in the absence of the gene conversion donor. Sequencing of these colonies revealed a variety of junctions that occurred predominantly through mispairing of the I-SceI 3′ overhangs (fig. S9A). To create a suicide deletion system that selected specifically for such NHEJ events, we substituted HO (endonuclease) for I-SceI so that joints with a relative reading frame of +2 nucleotides yielded Ade$^+$ colonies (fig. S8). Again consistent with previous results (*16*, *25*), ~0.75% of all NHEJ events in wild-type yeast were Ade$^+$ (Fig. 4A), and >50% of these were HO(+2) joints (fig. S9). With Mt NHEJ reconstituted, the overall frequency of NHEJ remained high (*18*), but the percentage of Ade$^+$ events was substantially decreased (Fig. 4A). Although some HO(+2) processed joints were formed, the HO(−1) joint now predominated (Fig. 4B), providing a signature for Mt NHEJ (Fig. 4C and fig. S9). Mt NHEJ proteins shifted the NHEJ profile even in wild-type yeast (Fig. 4, A and C, and fig. S9). Mt-Ku and Mt-Lig proteins can there-

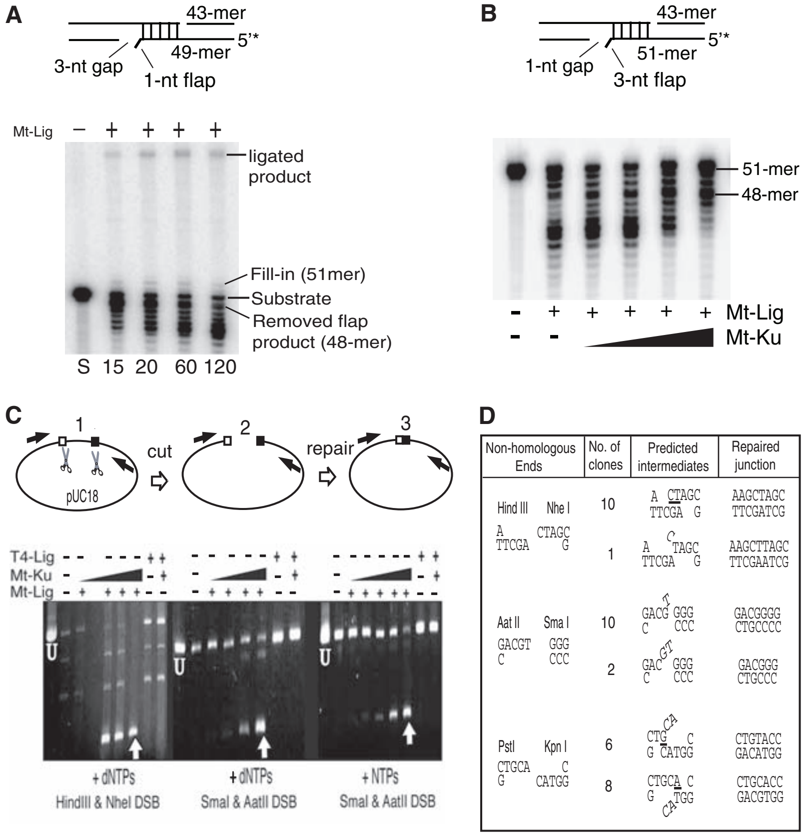

Fig. 2. Joining of DNA molecules with incompatible ends by Mt NHEJ. (**A**) Mt-Lig (1 μM) and the indicated DNA duplex were incubated with $MgCl_2$, NTPs, and ATP for increasing times (minutes). S, DNA substrate alone. The positions of the 49-nt oligomer (substrate), 48-nt oligomer (removal of flap), 51-nt oligomer (gap fill-in product), and 92-nt oligomer (ligated product) are indicated. Asterisks denote labeled strands. (**B**) Effect of Mt-Ku on the nuclease activity of Mt-Lig. DNA duplexes were incubated with 1 μM Mt-Lig and increasing amounts of Mt-Ku (0.8, 1.6, 3.2, and 6.4 μM) without ATP. (**C**) Plasmid DNA cut with two restriction enzymes was incubated with Mt-Lig (4 pmol) and increasing amounts of Mt-Ku (0.05, 0.1, 0.5, and 1 pmol), with either dNTPs or NTPs, followed by PCR to monitor the rate of repair (bottom). Slower migrating products correspond to uncut plasmid, and the fastest migrating products (white arrows) correspond to successfully repaired junctions that have lost ~500 base pairs between the restriction sites. pUC18, plasmid DNA. (**D**) Plasmids from experiments similar to (C) were transformed into bacteria and sequenced. The starting ends, final products, and inferred alignment intermediates are shown.

fore catalyze processed NHEJ in chromosomes, but despite this ability, repair is highly accurate at compatible DSB ends.

With the exception of 5′ trimming, Mt-Ku and Mt-Lig thus encode a self-sufficient NHEJ repair machine. The accuracy of this machine suggests that its different activities must be highly regulated to correctly handle different end configurations. Eukaryotic NHEJ involves many more proteins (*1*, *2*), but we suggest that the mechanisms of end-processing will be fundamentally similar, although coordinated by protein-protein interactions rather than linkage in a single polypeptide. Indeed, the variety of nucleotidyl transferase activities in Mt-Lig suggests a reduced dependence on template similar to that of mammalian Pol μ and Pol λ (*26*–*28*), which likely accommodates the limited base pairing inherent to NHEJ. As with Pol μ, Mt-Lig also appears most likely to incorporate NTPs in vivo, which has been suggested to be beneficial given the relative concentrations of NTPs and dNTPs outside of S phase (*17*). Incorporated ribonucleotides could be replaced by described mechanisms (*29*). Finally, Mt proteins catalyze NHEJ in yeast even though prokaryotes lack histones. This might suggest that a specific histone interaction is not required during NHEJ.

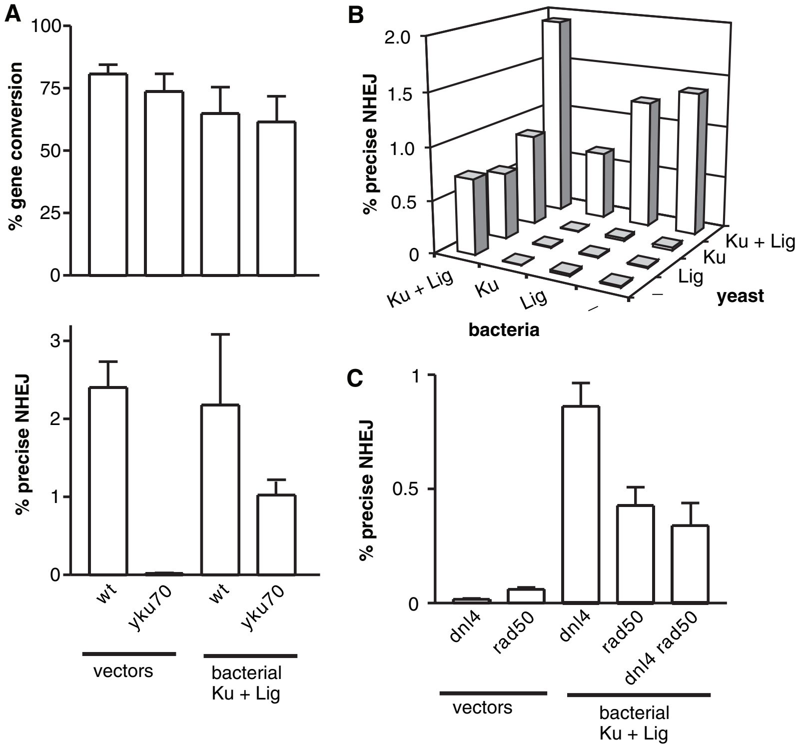

Fig. 3. Reconstitution of NHEJ in yeast by Mt proteins. (**A**) Frequencies of gene conversion and simple religation NHEJ in wild-type and *yku70* mutant yeast demonstrate reconstitution of NHEJ by combined expression of Mt-Ku and Mt-Lig. wt, wild-type. (**B**) All combinations of yeast and bacterial Ku and ligase genes were tested for NHEJ function. Labels indicate those proteins that were present in the cell. (**C**) NHEJ catalyzed by Mt proteins is only partially dependent on an intact MRX complex. No Ade$^+$ colonies were recovered from *dnl4 rad50* yeast with vectors only.

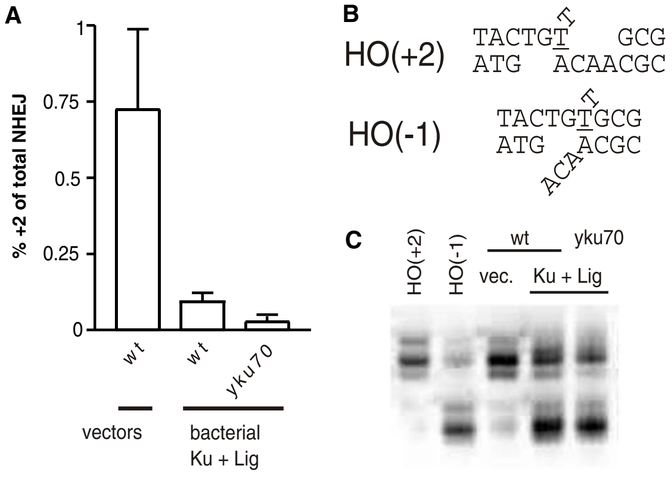

Fig. 4. Mt NHEJ exhibits a different pattern of imprecise NHEJ than yeast NHEJ. (**A**) The extent of +2 frameshifted NHEJ was determined as a fraction of all NHEJ events. Mt NHEJ showed a markedly lower +2 frequency than yeast NHEJ. No Ade$^+$ colonies recovered from *yku70* yeast with vectors only. (**B**) Inferred NHEJ intermediates for the HO(+2) and HO(−1) events that give a +2 reading frame. (**C**) Genomic DNA was prepared from bulk cultures of the indicated yeast bearing the HO suicide deletion system after outgrowth in adenine-selective medium. Flanking PCR was performed, and products were electrophoresed alongside standards derived from colonies of known joint types.

References and Notes

1. L. Krejci, L. Chen, S. Van Komen, P. Sung, A. E. Tomkinson, *Prog. Nucleic Acid Res. Mol. Biol.* **74**, 159 (2003).
2. S. E. Critchlow, S. P. Jackson, *Trends Biochem. Sci.* **23**, 394 (1998).
3. G. R. Weller *et al.*, *Science* **297**, 1686 (2002).
4. L. G. DeFazio, R. M. Stansel, J. D. Griffith, G. Chu, *EMBO J.* **21**, 3192 (2002).
5. D. Ramsden, M. Gellert, *EMBO J.* **17**, 609 (1998).
6. L. Chen, K. Trujillo, W. Ramos, P. Sung, A. E. Tomkinson, *Mol. Cell* **8**, 1105 (2001).
7. L. Chen, K. Trujillo, P. Sung, A. E. Tomkinson, *J. Biol. Chem.* **275**, 26196 (2000).
8. S. A. Nick McElhinny, C. M. Snowden, J. McCarville, D. Ramsden, *Mol. Cell. Biol.* **20**, 2996 (2000).
9. L. Aravind, E. V. Koonin, *Genome Res.* **11**, 1365 (2001).
10. E. V. Koonin, Y. I. Wolf, A. S. Kondrashov, L. Aravind, *J. Mol. Microbiol. Biotechnol.* **2**, 509 (2000).
11. G. R Weller, A. J. Doherty, *FEBS Lett.* **505**, 340 (2001).
12. T. E. Wilson, L. M. Topper, P. L. Palmbos, *Trends Biochem. Sci.* **28**, 62 (2003).
13. B. Arezi, R. Kuchta, *Trends Biochem. Sci.* **11**, 572 (2000).
14. K. N. Mahajan, S. A. Nick McElhinney, B. S. Mitchell, D. A. Ramsden, *Mol. Cell. Biol.* **22**, 5194 (2002).
15. H.-M. Tseng, A. E. Tomkinson, *J. Biol. Chem.* **277**, 45630 (2002).
16. T. E. Wilson, M. R. Lieber, *J. Biol. Chem.* **274**, 23599 (1999).
17. S. A. Nick McElhinney, D. Ramsden, *Mol. Cell. Biol.* **23**, 2309 (2003).
18. M. Della *et al.*, unpublished data.
19. D. A. Ramsden, T. T. Paull, M. Gellert, *Nature* **388**, 488 (1997).
20. E. Karathanasis, T. E. Wilson, *Genetics* **161**, 1015 (2002).
21. T. E. Wilson, *Genetics* **162**, 677 (2002).
22. S. J. Boulton, S. P. Jackson, *EMBO J.* **17**, 1819 (1998).
23. J. C. Connelly, D. R. Leach, *Trends Biochem. Sci.* **27**, 410 (2002).
24. T. E. Wilson, U. Grawunder, M. R. Lieber, *Nature* **388**, 495 (1997).
25. J. K. Moore, J. E. Haber, *Mol. Cell. Biol.* **16**, 2164 (1996).
26. K. Bebenek, M. Garcia-Diaz, L. Blanco, T. A. Kunkel, *J. Biol. Chem.* **278**, 34685 (2003).
27. M. Garcia-Diaz *et al.*, *Mol. Cell* **13**, 561 (2004).
28. S. Covo, L. Blanco, Z. Livneh, *J. Biol. Chem.* **279**, 859 (2004).
29. B. Rydberg, J. Game, *Proc. Natl. Acad. Sci. U.S.A.* **99**, 16654 (2002).

30. We thank S. Bell and E. Koonin for discussions, S. Bell for assistance with assays, and T. Carr, P. Jeggo, and K. Caldecott for comments on the manuscript. A.J.D. is a Royal Society University Research Fellow and L.T. is supported by a Biotechnology and Biological Sciences Research Council (BBSRC) studentship. Supported by grants from the BBSRC, the Association for International Cancer Research, the Royal Society, the U.S. Public Health Service, and the Pew Charitable Trusts. Molecular interaction data have been deposited in the Biomolecular Interaction Network Database with accession code 153967.

Supporting Online Material
www.sciencemag.org/cgi/content/full/306/5696/683/DC1
Materials and Methods
Figs. S1 to S9
References and Notes

3 May 2004; accepted 3 September 2004

Elemental and Redox Analysis of Single Bacterial Cells by X-ray Microbeam Analysis

Kenneth M. Kemner,[1]* Shelly D. Kelly,[1] Barry Lai,[1] Joerg Maser,[1]
Edward J. O'Loughlin,[1] Deirdre Sholto-Douglas,[1] Zhonghou Cai,[1]
Mark A. Schneegurt,[2] Charles F. Kulpa Jr.,[3] Kenneth H. Nealson[4]

High-energy x-ray fluorescence measurements were used to make elemental maps and qualitative chemical analyses of individual *Pseudomonas fluorescens* strain NCIMB 11764 cells. Marked differences between planktonic and adhered cells were seen in the morphology, elemental composition, and sensitivity to Cr(VI) of hydrated cells at spatial scales of 150 nm. This technology can be applied to natural geomicrobiological systems.

Attachment of prokaryotic cells to surfaces during biofilm formation not only leads to major changes in metabolism, resistance, and survivability (*1*), but the substrates metabolized by such communities (such as iron or manganese oxides) and their products (such as uraninite or chromium oxides) often are insoluble and associated with the attached bacteria (*2–4*). Thus, quantifying and specifying the locations of cellular components, metabolic reactants, and metabolic products of prokaryotes is technologically challenging.

There are no techniques currently available that use noninvasive, nondestructive analytical techniques with the spatial resolution to examine living and hydrated samples at the nanometer scale and that are capable of both imaging and chemical determinations. In particular, most analytical methods with high spatial resolution (typically with electron or proton microprobes) use high-vacuum systems, almost certain to alter the cellular material itself and the locations of key associated elements.

To address this issue, we have used high-energy x-ray fluorescence (XRF) methods with a spatial resolution of 150 nm to examine elemental compositions of single hydrated bacterial cells (*5*). We determined elemental compositions of single cells of *P. fluorescens* NCIMB 11764, an aquatic Gram-negative bacterium that exists naturally both in planktonic form and in surface-adhered biofilms. We saw changes in cell morphology and elemental composition of single cells when attached to a solid substrate. Many studies have investigated the interactions of metals and ions with bacteria (*6–8*) and aquatic protists (*9*), but not with hydrated bacteria at the single-cell level.

Zone plate fabrication technology for the production of high-energy x-ray microprobes (*10*) combines high spatial resolution with high elemental sensitivity (better than 1 × 10^4 atoms within a spot size of 150 nm) (*11*) and x-ray absorption spectroscopy to probe chemical interactions at this scale (*12*). The high-energy x-ray microprobe has better elemental sensitivity than most charged-particle probes and allows the investigation of heterogeneous hydrated samples. The x-ray microprobe also allows investigation of structures tens of microns beneath solid-phase surfaces.

High-energy XRF microscopy showed planktonic cells were rod shaped and contained high concentrations of virtually all elements expected in living cells (Fig. 1, table S1); the attached cells were rounded and had notable excesses of Ca and P associated with them (Fig. 2, table S1). With surface adherence, [P] associated with the cells increased from ~16,000 to ~650,000 ppm, and [Ca] increased from ~4,000 to ~550,000 ppm, yielding ~1:1 stoichiometry for these two elements (table S1). Other elements showed only minor changes in the attached cells.

The greater [Ca] and [P] in the adhered cells versus the planktonic cells remains un-

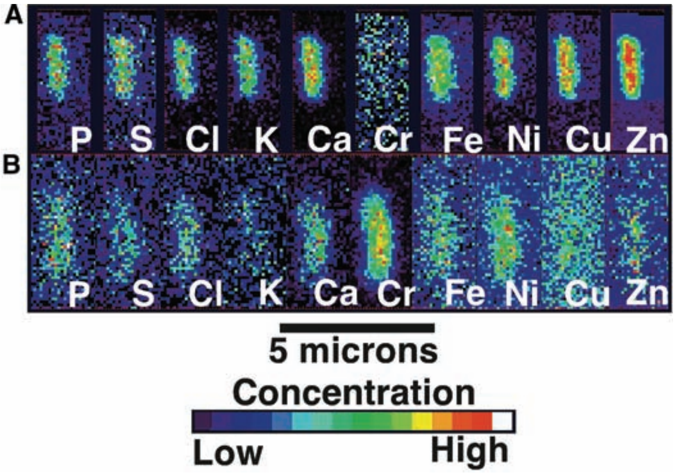

Fig. 1. False-color micro-XRF maps of qualitative spatial distributions and concentration gradients of elements in and around planktonic *P. fluorescens* microbes harvested before (**A**) and after (**B**) exposure to potassium dichromate [Cr(VI)] solution (1000 ppm) for 6 hours.

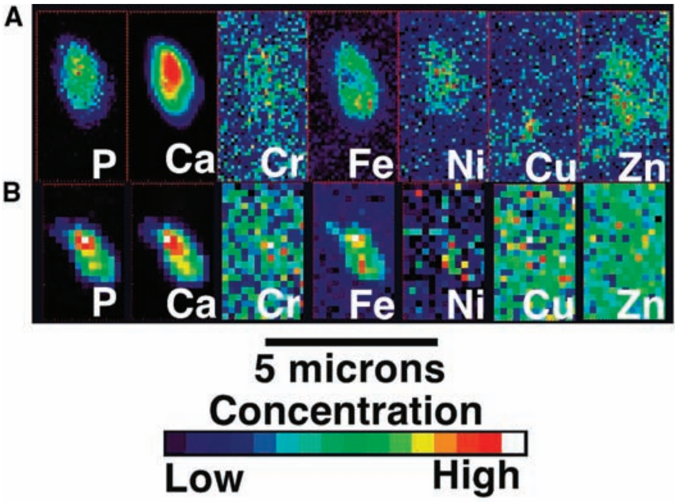

Fig. 2. False-color micro-XRF maps of qualitative spatial distributions and concentration gradients of elements in and around surface-adhered *P. fluorescens* microbes harvested before (**A**) and after (**B**) exposure to potassium dichromate [Cr(VI)] solution (1000 ppm) for 6 hours. Because of the extremely high concentrations of Ca and P in the surface-adherent microbes, the intensities of neighboring XRF signals from S, Cl, and K could not be determined accurately. Therefore, spatial distributions for these elements are not illustrated.

---

[1] Environmental Research Division and Advanced Photon Source, Argonne National Laboratory, Argonne, IL 60439–4843, USA. [2] Department of Biological Sciences, Wichita State University, Wichita, KS 67260, USA. [3] Department of Biological Sciences, University of Notre Dame, Notre Dame, IN 46556, USA. [4] Department of Earth Sciences, Mail Code 0740, University of Southern California, Los Angeles, CA 90089–0740, USA.

*To whom correspondence should be addressed. E-mail: kemner@anl.gov

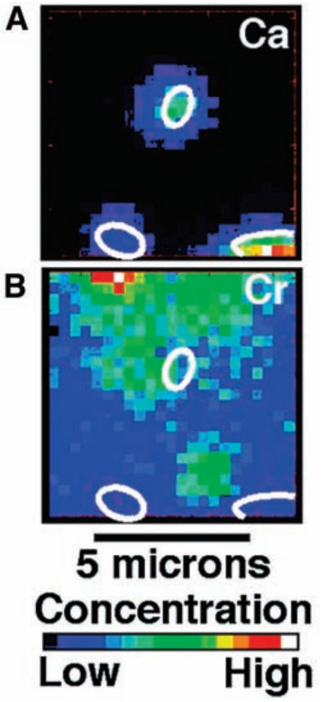

Fig. 3. False-color micro-XRF maps of Ca (**A**), identifying the locations of surface-adherent microbes exposed to Cr(VI) solution (1000 ppm), and Cr (**B**), depicting the locations of elevated concentrations of Cr within 1 to 3 μm of surface-adherent *P. fluorescens*. Cell positions [determined from Ca distribution in (A)] are drawn in white.

explained, but it probably involves the extracellular polysaccharide (EPS) matrix laid down by the *P. fluorescens* cells and the precipitation of apatite (*5*). Strains of this species produce various acidic EPSs (*13–16*) that can bind calcium ions preferentially from solution (*17–19*). SEM imaging of the cells from our experiments indicated the formation of an extracellular matrix.

Because attached cells are thought to have enhanced resistance to stress, we challenged the planktonic cells with Cr(VI) at 1000 and 25 ppm for 6 hours and the attached cells with Cr(VI) at 1000 ppm for 6 hours. After this treatment, planktonic *P. fluorescens* cells were markedly altered; they stained as dead cells in the live or dead stain reaction (*5*), lost almost all of their cellular transition elements, and accumulated substantial amounts of Cr (Fig. 1). In contrast, the attached cells showed virtually no change in elemental composition and no uptake of Cr into the cells (Fig. 2), and living cells were abundant.

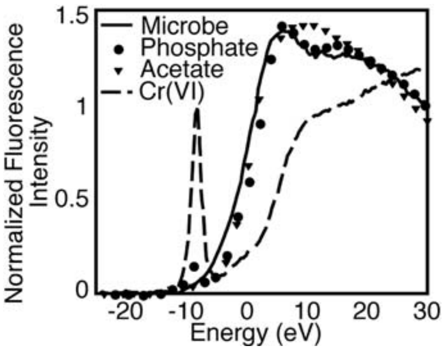

Fig. 4. Cr K-edge micro-XANES spectra representing potassium dichromate [Cr(VI)] solution added to growth medium; a chromium phosphate dihydrate [Cr(III)] standard; a chromium acetate [Cr(III)] standard; and the elevated microbe-associated Cr concentrations illustrated in Fig. 3B.

Finally, we used the XRF microscopy system to measure x-ray absorption near edge spectra (XANES) (*12*) to determine the redox state of the Cr in this system. With micro-XANES we investigated the chemical speciation of Cr in the Cr-enriched areas seen in Fig. 3. Comparison of these Cr K-edge spectra to standards (Fig. 4) indicates reduced Cr [i.e., Cr(III)], consistent with association of Cr with a phosphoryl functional group.

The XRF approach also revealed that, when attached to a surface, the cells changed shape slightly, lost some transition elements (Co, Cu, Ni, and Zn), gained others (Fe and Mn), and became resistant to exposure to high levels of Cr(VI), which shows the utility of this technique for investigating a cell's metabolic state. Combining elemental analysis with the ability to measure redox state and local chemistry is advantageous for dissecting the activity of metal-active bacteria in geomicrobiological systems.

References and Notes

1. J. W. Costerton *et al.*, *Annu. Rev. Microbiol.* **41**, 435 (1987).
2. D. R. Lovley, *Microbiol. Rev.* **55**, 259 (1991).
3. K. H. Nealson, D. Saffarini, *Annu. Rev. Microbiol.* **48**, 311 (1994).
4. J. W. Costerton, Z. Lewandowski, D. E. Caldwell, D. R. Korber, H. M. Lappin-Scott, *Annu. Rev. Microbiol.* **49**, 711 (1995).
5. Materials and methods are available as supporting material on *Science* Online.
6. T. J. Beveridge, *Annu. Rev. Microbiol.* **43**, 147 (1989).
7. G. Winkelmann, C. J. Carrano, *Transition Metals in Microbial Metabolism* (Harwood Academic Publishers, Amsterdam, 1997).
8. S. Langley, T. J. Beveridge, *Can. J. Microbiol.* **45**, 616 (1999).
9. B. S. Twinning *et al.*, *Anal. Chem.* **75**, 3806 (2003).
10. W. Yun *et al.*, *Rev. Sci. Instrum.* **70**, 2238 (1999).
11. Z. Cai *et al.*, in *X-ray Microscopy: Proceedings of the Sixth International Conference*, W. Meyer-Ilse, T. Warwick, D. Attwood, Eds. (American Institute of Physics, New York, 2000), pp. 472–477.
12. K. M. Kemner *et al.*, *J. Synchrotron Radiat.* **6**, 639 (1999).
13. G. Skjak-Braek, H. Grasdalen, B. Larsen, *Carbohydr. Res.* **154**, 239 (1986).
14. R. R. Read, J. W. Costerton, *Can. J. Microbiol.* **33**, 1080 (1987).
15. W. F. Fett, S. F. Osman, M. F. Dunn, *Appl. Environ. Microbiol.* **55**, 579 (1989).
16. E. Conti, A. Flaibani, M. O'Regan, I. W. Sutherland, *Microbiology* **140**, 1125 (1994).
17. G. T. Grant, E. R. Morris, D. A. Rees, P. J. C. Smith, D. Thom, *FEBS Lett.* **32**, 195 (1973).
18. J. E. Gregor, E. Fenton, G. Brokenshire, P. Van den Brink, B. O'Sullivan, *Water Res.* **30**, 1319 (1996).
19. I. Braccini, R. P. Grasso, S. Perez, *Carbohydr. Res.* **317**, 119 (1999).
20. We thank M. Boyanov, K. Germino, P. Illinski, D. Legnini, M. Mundo, S. T. Pratt, W. Rodrigues, and W. Yun for earlier contributions to this project. This work is supported by the Natural and Accelerated Bioremediation (NABIR) Research Program, Office of Biological and Environmental Research, Office of Science, U.S. Department of Energy (DOE). Additional support for K.M.K. was provided by the DOE-Office of Science Early Career Scientist and Engineer Award. Work at the Advanced Photon Source is supported by the DOE Office of Science, Office of Basic Energy Sciences.

Supporting Online Material
www.sciencemag.org/cgi/content/full/306/5696/686/DC1
Materials and Methods
SOM Text
Table S1

2 August 2004; accepted 26 August 2004

A Chromosome 21 Critical Region Does Not Cause Specific Down Syndrome Phenotypes

L. E. Olson,[1]* J. T. Richtsmeier,[2] J. Leszl,[2] R. H. Reeves[1]†

The "Down syndrome critical region" (DSCR) is a chromosome 21 segment purported to contain genes responsible for many features of Down syndrome (DS), including craniofacial dysmorphology. We used chromosome engineering to create mice that were trisomic or monosomic for only the mouse chromosome segment orthologous to the DSCR and assessed dysmorphologies of the craniofacial skeleton that show direct parallels with DS in mice with a larger segmental trisomy. The DSCR genes were not sufficient and were largely not necessary to produce the facial phenotype. These results refute specific predictions of the prevailing hypothesis of gene action in DS.

Trisomy 21 is among the most complex genetic insults compatible with human survival past term. The genetic complexity and individual variability of DS phenotypes pose a considerable challenge to understanding mechanisms by which development is disrupted in trisomy. The DSCR concept suggesting that most phenotypes are the product of a few dosage-sensitive genes has dominated the field of DS research for three decades, but until now there has been no method for definitive testing of this hypothesis.

DS occurs in 1 out of 700 live births. The disorder is the leading cause of congenital heart disease and the most frequent genetic cause of mental retardation. Characteristic dysmorphology of the face and underlying skeleton, alterations in brain structure, and early onset Alzheimer pathology occur in all individuals with DS, though with variable severity and onset. The occurrence of Hirschsprung's disease, testicular cancer, and childhood onset leukemia is elevated, and many additional clinical features occur with varying frequency in DS (*1*).

Rare individuals have chromosome rearrangements resulting in triplication of a subset of HSA21 genes (segmental trisomy 21) (*2*, *3*). Correspondence of the smallest region of overlap among individuals with the same DS features led to the concept that a critical chromosomal region (DSCR) delimited a dosage-sensitive gene or genes that are responsible for various features of DS. The most precise description of the DSCR extends about 5.4 Mb on HSA21 from a proximal boundary between markers *D21S17* and *D21S55* to a distal boundary between *MX1* and *BCEI* (*4*, *5*). This region has been associated with several major DS phenotypes including facial features that result from dysmorphology of the craniofacial skeleton (*6*, *7*) (fig. S1). The DSCR hypothesis predicts that a gene or genes in this region are sufficient to produce this phenotype.

Several recent developments enable direct testing of the genetic basis for disrupted development in trisomy. Annotation of the finished sequence of HSA21 provides a complete gene catalog (*8*). Manipulation of the mouse germ line through embryonic stem (ES) cells supports the creation of defined segmental aneuploidies (*9*). Quantitative assessments of phenotypes with direct parallels between DS and trisomic mice provide readouts for these genetic experiments and suggest that these features arise from perturbations of common evolutionarily derived developmental pathways (*10*).

Whereas some differences between mouse and human gene content have been reported for HSA21 predicted genes (*11*), established genes are nearly perfectly conserved in content and order between species (*12*) (table S1). Ts65Dn mice contain a marker chromosome resulting in segmental trisomy for orthologs of about half of the genes on HSA21. These mice have been used widely in studies relevant to DS and display a variety of phenotypes that parallel or predict those in DS (*10*).

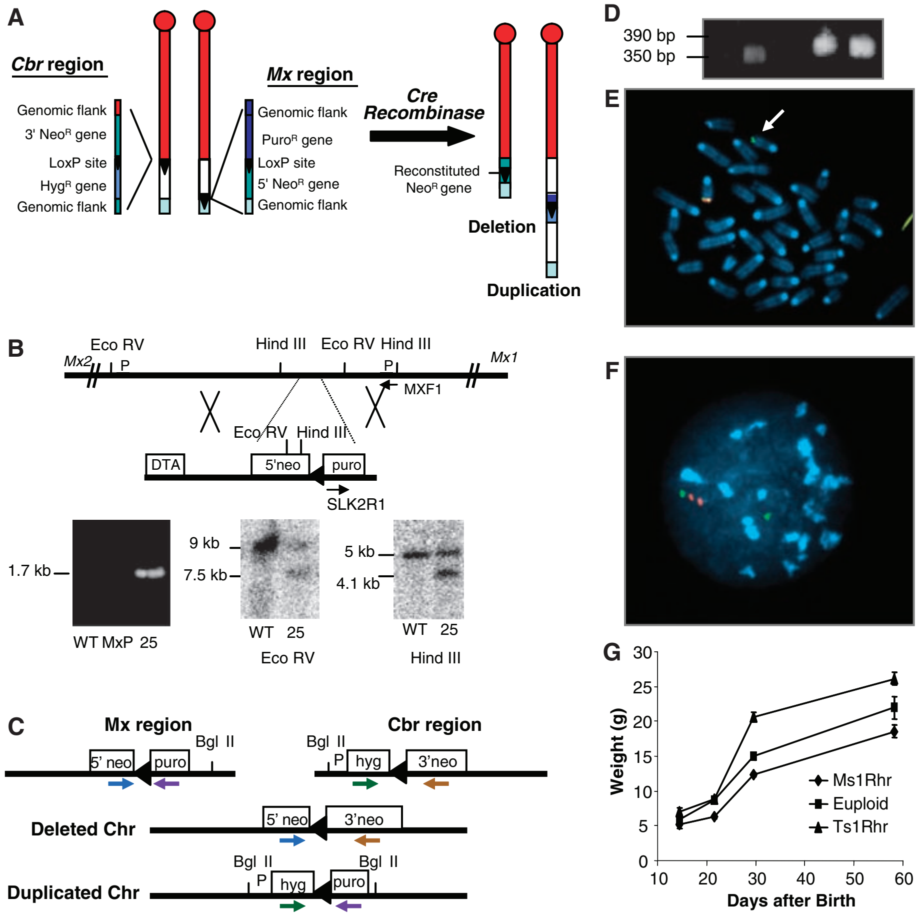

Fig. 1. Construction of a duplication or deletion of the MMU16 region orthologous to the DSCR. **(A)** LoxP sites were targeted to asymmetrical positions on MMU16 at *Cbr1* (*13*) and adjacent to *Mx2*. Each targeting vector contained a LoxP site (triangle), a selectable antibiotic resistance gene (hyg or puro), and half of the neomycin resistance gene (5′ or 3′ neo). **(B)** The Mx-Lox vector produced a 1.7-kb PCR product from the targeted allele in line MxP25. Wild-type (WT) and targeted alleles produced 9.0- and 7.5-kb restriction fragments with *Eco*RV and 5.0- and 4.1-kb fragments with *Hin*dIII. Arrows identify PCR primers; P designates probes. **(C)** PCR primers used to screen vector sequences for recombination after Cre-mediated translocation. **(D)** PCR products from *neo*^{r} ES lines produced the 350– and 390–base pair (bp) fragments expected for deletion and duplication, respectively. **(E)** Metaphase FISH with one bacterial artificial chromosome (BAC) that maps to the DSCR (red) and a second BAC proximal to it (green) shows one chromosome with a single green signal (arrow) and a second with green and red plus a yellow signal, indicating overlap. **(F)** Interphase FISH shows a green signal by itself representing the deleted MMU16 and a green signal with two adjacent red signals representing the duplication. **(G)** Body weights of Ts1Rhr mice are significantly larger than controls. Standard errors (bars) are indicated.

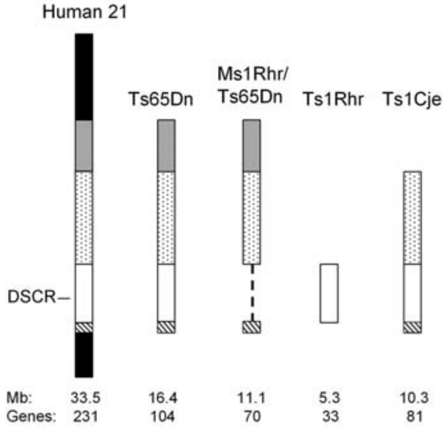

Fig. 2. Trisomic segments represented in mouse models relative to HSA21. The DSCR is indicated as an open box where it is present and by a dashed line where it is deleted. Approximate size in megabases of triplicated information is based on genomic sequence; gene number is from Gardiner *et al.* (*11*). Gene content for each segment is given in table S1.

---

[1]Department of Physiology, Johns Hopkins University School of Medicine, Baltimore, MD 21205, USA. [2]Department of Anthropology and Program in Genetics, Pennsylvania State University, University Park, PA 16802, USA.

*Present address: Department of Biology, University of Redlands, Redlands, CA 92373, USA.
†To whom correspondence should be addressed. E-mail: rreeves@jhmi.edu

To assess the contribution of DSCR genes to DS facial features that have been mapped to this region, we generated ES cells carrying a 3.9-Mb reciprocal duplication or deletion (Fig. 1A). This segment contains mouse orthologs of the 33 conserved and minimally conserved genes in the human DSCR (Fig. 2). Cre-mediated recombination between LoxP sites located on different chromosomes was used to produce the duplication and deletion (*9*) (Fig. 1A).

Consecutive targeting with homologous recombination vectors containing LoxP sequences established the boundaries for the translocation at *Cbr1* (*13*) and at a site adjacent to the *Mx2* gene (Fig. 1B). The targeting vectors were designed so that Cre-mediated recombination between LoxP sites would make cells resistant to G418 (neo^r). The CAGGS-Cre expression vector was electroporated into doubly targeted ES cells and two neo^r clones were recovered. The presence of both recombined chromosomes was confirmed by Southern blotting and polymerase chain reaction (PCR) followed by sequencing (Fig. 1, C and D). Metaphase and interphase fluorescence in situ hybridization (FISH) demonstrated the predicted association of signals from the duplicated and deleted chromosomes (Fig. 1, E and F). These karyotypically normal ES lines were injected into blastocysts and one of the resulting chimeras exhibited germline transmission when bred to C57BL/6J (B6) mice. Mice with segmental monosomy due to the deleted MMU16 (Ms1Rhr mice) and with segmental trisomy due to the duplication (Ts1Rhr) were born, and both were fertile.

Ms1Rhr mice were smaller than (B6 × 129)F_1 controls from birth to adulthood (Fig. 1G). However, adult Ts1Rhr mice were significantly larger than euploid mice, in contrast to Ts65Dn mice, which were smaller than their euploid littermates (*14*). Femur length, a commonly used index of body size, was shorter in Ts65Dn mice than in controls, whereas femurs were longer in Ts1Rhr mice than in controls. Short stature in DS is a feature attributed to the DSCR (*4*, *5*). Thus, whereas trisomy for orthologs of about half of the genes on HSA21 produces an effect similar to that in DS in Ts65Dn mice, the opposite effect occurred in Ts1Rhr mice, which were trisomic only for the DSCR.

Anomalies of the skull contribute to the distinctive face in DS. The mandible is small (*7*), contributing to the characteristic open mouth and protruding tongue, features that have been attributed to trisomy for genes within the DSCR (*4*, *5*). The DS skull shows a compact midface with reduced maxilla and zygomatic bones, and brachycephaly. Ts65Dn mice show specific abnormalities in the mandible and in bones of the face and neurocranium that directly parallel these patterns in DS (*6*).

These parameters were assessed quantitatively and compared in four mouse models. The Ts1Rhr skull was larger than that of euploid littermates (Fig. 3). These differences were not localized to specific bones of the face or neurocranium but instead demonstrated an overall rostrocaudal elongation of the skull. There was no significant difference between Ts1Rhr and euploid littermates along the mediolateral axis local to the face or neurocranium.

These differences contrast sharply with the findings of previous studies of Ts65Dn mice (*6*). Skulls of Ts65Dn were significantly smaller than euploid littermates. Differences were most pronounced along the rostrocaudal axis local to the bones of the face corresponding with reduced facial dimensions in humans with DS. The reduced rostrocaudal dimension coupled with increased cranial vault width local to the parietal bones produced a brachycephalic skull corresponding with the human condition (Fig. 3).

The mandibles of Ts1Rhr mice were larger overall than mandibles of their euploid littermates. Out of 21 linear distances, 5 were significantly larger in Ts1Rhr, and these converged on the condyle, inferior ramus, and incisive alveolar of the murine mandible (Fig. 4). As was the case for face and skull, this pattern in Ts1Rhr mandibles was in marked contrast to that in Ts65Dn mice, which were significantly smaller overall. Further, differences in Ts65Dn were centered on the coronoid and angular processes (*6*). The DS mandible is significantly reduced in size as well (*7*). Direct comparisons between mouse and human mandibles are available for a few dimensions; these show a DS-like pattern in Ts65Dn but not in Ts1Rhr mice (Fig. 4).

Morphological assessment of the neurocranium, face, and mandible demonstrate that trisomy of only critical region genes is not sufficient to produce the anomalies seen in Ts65Dn mice that parallel those assigned to the DSCR. To determine whether critical region genes are necessary to produce phenotypes mapped to this region, we examined

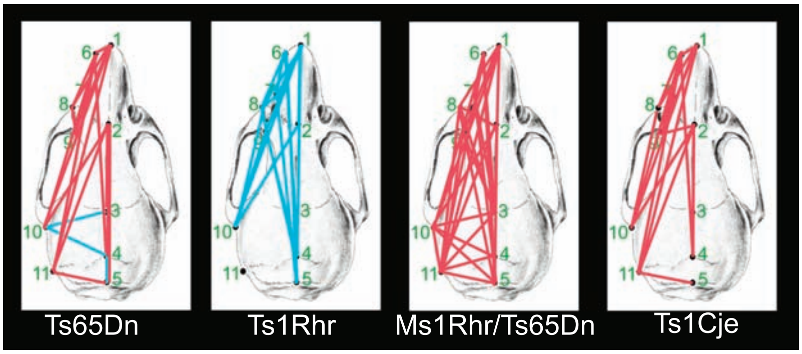

Fig. 3. Linear measurements that contribute to dysmorphology in Ts65Dn, Ts1Cje, and Ms1Rhr/Ts65Dn form a closely related set, whereas trisomy for the DSCR alone produces a distinct dysmorphology in Ts1Rhr. Red lines indicate linear distances between landmarks that were significantly smaller in trisomic mice relative to euploid mice; blue lines indicate distances that were larger. Statistical significance was determined using Euclidean Distance Matrix Analysis confidence intervals (*17*). This is not a simple scaling difference because the magnitude of the differences varies from one measure to another and the set of differences contributing to dysmorphology in Ts1Rhr is different from that in the other models. Landmarks are defined in fig. S3.

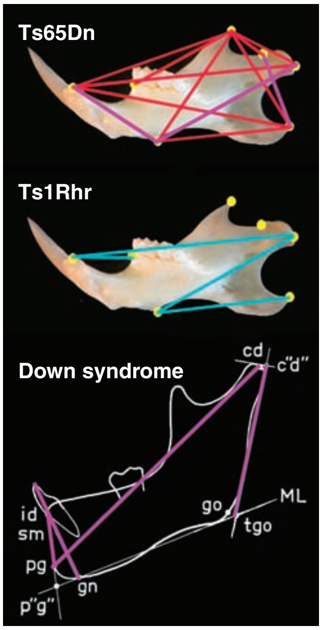

Fig. 4. The Ts1Rhr mandible is larger overall and has a distinctly different shape than Ts65Dn. Results of three-dimensional comparative analysis of mandibular shape show those distances between landmarks that are significantly smaller in trisomic mice as red lines, whereas blue lines indicate distances that are larger. Purple lines drawn on the DS and Ts65Dn mandibles are measures that are significantly smaller than those for euploid in both (*6*, *7*). Landmarks are described in fig. S3.

skull morphology of the Ms1Rhr/Ts65Dn mouse. Crossing the Ms1Rhr deletion onto the Ts65Dn background produced mice that were trisomic for about 70% of the genes trisomic in Ts65Dn but had the normal two copies of genes in the critical region (Fig. 2). Similar to Ts65Dn mice and in contrast to Ts1Rhr mice, the skull was significantly smaller than that of euploid littermates in these mice (Fig. 3). Ms1Rhr/Ts65Dn mice did not show disproportionate changes along the rostrocaudal and mediolateral axis (i.e., they did not have brachycephaly). Overall, however, the pattern of dysmorphology in the Ms1Rhr/Ts65Dn craniofacial skeleton was similar to Ts65Dn, whereas the anomalies seen in Ts1Rhr mice were distinctly different. Thus, although genes in the critical region may contribute to skull development, the Ts65Dn pattern is produced substantially without their contribution.

One alternative to the critical region concept suggests that anomalies in DS occur primarily because of disruption of genetic homeostasis and, therefore, the number of triplicated genes rather than their specific functions explain DS phenotypes (*15*). Thus, Ts1Rhr mice, with only 32% of the trisomic genes in Ts65Dn, should have a mild form of the Ts65Dn phenotype. This was not the case. Furthermore, we compared the craniofacial dysmorphology in Ms1Rhr/Ts65Dn mice, which are trisomic for about 70% of the genes triplicated in Ts65Dn, with that in Ts1Cje segmental trisomic mice (*16*), which are trisomic for 78% of Ts65Dn genes (Fig. 2). Ts65Dn, Ts1Cje, and Ms1Rhr/Ts65Dn mice showed expansion, no change, and reduction in measures of the middle aspect of the cranial vault, respectively, but the models shared reductions of the face and rostrocaudal aspects of the cranial vault (Fig. 3).

Overall, the Ts65Dn, Ts1Cje, and Ms1Rhr/Ts65Dn face and skull are affected similarly, whereas the pattern produced by three copies of the DSCR alone in Ts1Rhr mice is very different. Statistical analyses of cranial shape in these precisely constructed genetic models show that DSCR genes alone are not sufficient and are largely unnecessary to produce the facial dysmorphology attributed to this region. This result points to interactions among noncontiguous genes that could not have been predicted from or observed in human studies. The critical region concept proposes that a small number of dosage-sensitive genes have large effects on phenotypes when present in three copies. The developmental instability hypothesis considers that nonspecific, small effects of many genes perturb genetic homeostasis. We favor a synthesis of these two hypotheses, which acknowledges that a triplicated gene, the solitary effect of which is inconspicuous, could contribute to a trisomic phenotype in combination with other genes based on the specificity of effects and interactions of these genes.

References and Notes

1. W. I. Cohen, *Down Syndrome Q.* **4**, 3 (September, 1999).
2. E. Niebuhr, *Humangenetik* **21**, 99 (1974).
3. M. K. McCormick *et al.*, *Genomics* **5**, 325 (1989).
4. J. M. Delabar *et al.*, *Eur. J. Hum. Genet.* **1**, 114 (1993).
5. J. R. Korenberg *et al.*, *Proc. Natl. Acad. Sci. U.S.A.* **91**, 4997 (1994).
6. J. Richtsmeier, L. Baxter, R. Reeves, *Dev. Dyn.* **217**, 137 (2000).
7. E. Kisling, *Cranial Morphology in Down's Syndrome: A Comparative Roentgencephalometric Study in Adult Males* (Munksgaard, Copenhagen, 1966).
8. M. Hattori *et al.*, *Nature* **405**, 311 (2000).
9. R. Ramirez-Solis, P. Liu, A. Bradley, *Nature* **378**, 720 (1995).
10. R. Reeves, L. Baxter, J. Richtsmeier, *Trends Genet.* **17**, 83 (2001).
11. K. Gardiner, A. Fortna, L. Bechtel, M. T. Davisson, *Gene* **318**, 137 (2003).
12. R. J. Mural *et al.*, *Science* **296**, 1661 (2002).
13. L. E. Olson *et al.*, *Cancer Res.* **63**, 6602 (2003).
14. M. T. Davisson, personal communication.
15. B. Shapiro, *Am. J. Med. Genet.* **14**, 241 (1983).
16. H. Sago *et al.*, *Proc. Natl. Acad. Sci. U.S.A.* **95**, 6256 (1998).
17. S. R. Lele, J. T. Richtsmeier, *An Invariant Approach to Statistical Analysis of Shapes* (Chapman & Hall/CRC, Boca Raton, FL, 2001).

18. We thank J. D. Gearhart for insightful comments, M. Cowan for ES cells and chimeras, and S. South for FISH analysis. This work was supported by a Howard Hughes Predoctoral Fellowship to L.E.O. and by a Public Health Service awards HD38384 and HD24605 (R.H.R.).

Supporting Online Material

www.sciencemag.org/cgi/content/full/306/5696/687/DC1

Materials and Methods

Figs. S1 to S3

Table S1

References

9 April 2004; accepted 23 August 2004

In Silico Genetics: Identification of a Functional Element Regulating *H2-E*α Gene Expression

Guochun Liao,[1]* Jianmei Wang,[1]* Jingshu Guo,[1] John Allard,[1]
Janet Cheng,[1] Anh Ng,[1] Steve Shafer,[2] Anne Puech,[3]
John D. McPherson,[4] Dorothee Foernzler,[5]
Gary Peltz,[1]† Jonathan Usuka[1]

Computational tools can markedly accelerate the rate at which murine genetic models can be analyzed. We developed a computational method for mapping phenotypic traits that vary among inbred strains onto haplotypic blocks. This method correctly predicted the genetic basis for strain-specific differences in several biologically important traits. It was also used to identify an allele-specific functional genomic element regulating *H2-E*α gene expression. This functional element, which contained the binding sites for YY1 and a second transcription factor that is probably serum response factor, is located within the first intron of the *H2-E*α gene. This computational method will greatly improve our ability to identify the genetic basis for a variety of phenotypic traits, ranging from qualitative trait information to quantitative gene expression data, which vary among inbred mouse strains.

Commonly available inbred mouse strains can be used to genetically model many traits that vary in the human population, including those associated with disease susceptibility. We have previously shown that chromosomal regions regulating phenotypic traits could be computationally predicted by correlative analysis of phenotypic data obtained from inbred mouse strains and the extent of allele sharing within genomic regions (*1*). However, this computational method had several limitations. It identified 60-Mb chromosomal regions that contained hundreds of genes, and the predictions were assessed by relative (percentile ranking), rather than absolute (*P*-value), statistical criteria.

Single-nucleotide polymorphism (SNP) and allelic information in our mouse SNP database (*2*) were used to produce a high-resolution map of the haplotypic block structure of the mouse genome covering 16 commonly used inbred mouse strains (*3*). This

---

[1]Department of Genetics and Genomics, Roche Palo Alto, 3431 Hillview Avenue, Palo Alto, CA 94304–1397, USA. [2]Department of Anesthesia, Stanford University Medical Center, Stanford, CA 94305, USA. [3]Centre National de Génotypage, 2 rue Gaston Crémieux, CP 5721, 91057 Evry Cedex, France. [4]Department of Genetics and Genome Sequencing Center, Washington University School of Medicine, St. Louis, MO 63108, USA. [5]Roche Center for Medical Genomics F. Hoffmann–La Roche, RCMG, Bau 93/4.26, CH-4070 Basel, Switzerland.

*These authors contributed equally to this work.

†To whom correspondence should be addressed. E-mail: gary.peltz@roche.com

haplotype map was used to develop a computational method for genetic analysis of phenotypic traits in mice (*4*). Haplotypic blocks that best correlate with phenotypic trait data obtained from inbred strains were identified. As a first example, we tested the ability of the haplotype-based computational mapping method to predict the chromosomal location of the *K* locus of the major histocompatibility complex (MHC) located on murine chromosome 17 (~33 Mb). The known properties of the MHC *K* locus of 16 inbred strains were used as input phenotypic data for this analysis (*5*) (Table 1). The categorical *K* locus data (b, k, d, u, v) were transformed into points in multidimensional metric space, such that each *K* locus category was equidistant from any other category, and then computationally analyzed for correlation with the haplotypic blocks (Fig. 1A). One haplotypic block best correlated with the phenotypic data. The predicted haplotypic block was on chromosome 17 [32.778 to 32.805 Mb, NCBI (National Center for Biotechnology Information) Build 30] and contained five genes (*H2-Dma*, *Psmb9*, *Tap1*, *Psmb8*, and *Tap2*). These genes are known to determine the MHC class I and class II phenotypes (*6*, *7*). Consistent with this prediction, the *K*, *A*β, *A*α, and *E*β phenotypes were identical among the 16 mouse strains tested (Table 1). The same computational prediction profile was obtained when any of the other class II phenotypes were used as input phenotypic data (computational profile identical to that in Fig. 1A).

We next determined if the computational method could correctly identify haplotypic blocks associated with two other MHC phenotypes, the MHC class III *S* locus and the class Ib *Qa2* locus (*5*). In both cases, the computationally identified haplotypic block with the highest correlation contained the MHC gene that corresponded with the phenotype analyzed (Fig. 1, B and C, and Table 2). The correct identification of *Qa2* locus by the computational method was particularly encouraging, because there were only two different categorical phenotypes (a and b) at this locus (Table 1). This analysis of four MHC phenotypes demonstrates that the computational method can analyze input phenotypic data and accurately discriminate among colinear, neighboring haplotypic blocks in the mouse genome.

We next tested the ability of the computational mapping method to identify genetic loci regulating the aromatic hydrocarbon (AH) response among inbred mouse strains. Genetic variation in this metabolic response pathway can affect the response to drugs and environmental toxins and is also likely to affect cancer susceptibility (*8*, *9*). The aromatic hydrocarbon receptor (AHR) is the ligand-binding component of the intracellular protein complex that regulates this response. After ligand binding, this receptor translocates to the nucleus where it forms a heterodimeric protein complex that stimulates the expression of genes involved in drug and xenobiotic metabolism. The AH response was previously characterized by measuring the amount of hepatic aromatic hydrocarbon hydroxylase activity induced after intraperitoneal injection of 3-methylcholanthrene in 42 inbred mouse strains (*10*). Thirteen of these strains were characterized in our mouse SNP database (*2*). The AKR/J, 129/SvlmJ, LP/J, NZB/BinJ, NZW/LacJ, and DBA/2J strains were AH

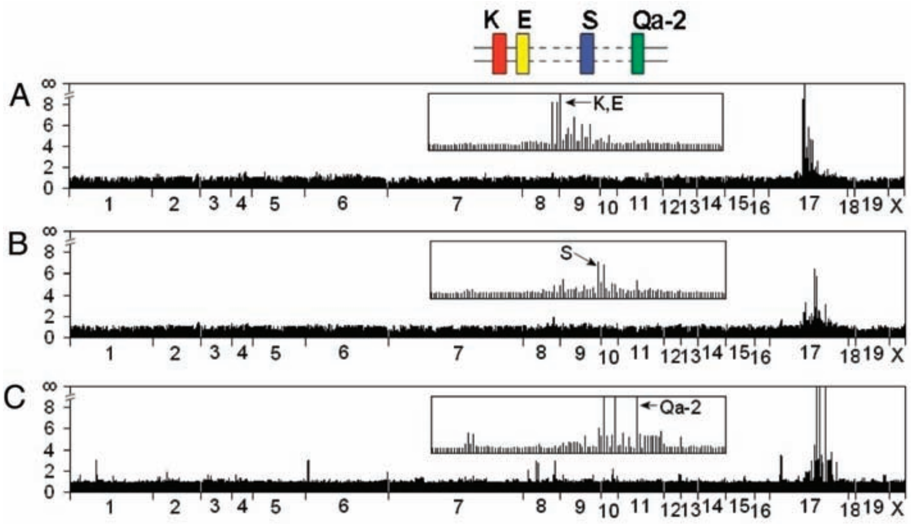

Fig. 1. Computational mapping of MHC phenotypic data onto haplotypic blocks. The correlation for each haplotypic block is represented as a bar, and the haplotypic blocks are arranged from proximal (centromeric) to distal (telomeric) for all 20 chromosomes. The variable width of each chromosome indicates the number of haplotypic blocks on that chromosome. The height of each bar is the inverse of the score measuring the correlation between the phenotypic data and the haplotypic block. The insets show predictions for haplotypic blocks on chromosome 17 for each phenotype. The relative location of the MHC genes on chromosome 17 is shown in the block diagram at the top of the figure. (**A**) Computational prediction of the location of the MHC class I-*K* locus. The MHC class I-*K* phenotypic data were analyzed for correlation with strain groupings within haplotypic blocks. The predicted haplotypic block was located in the MHC region on chromosome 17 at 33.78 to 32.81 Mb and contained both the MHC *K* and class II genes. (**B**) Computational analysis of MHC class III *S* locus phenotypic data. The predicted haplotypic block is located within the MHC region and contains the *S*-locus gene. (**C**) Computational analysis of the MHC class Ib *Qa2* locus phenotypic data. The three predicted haplotypic blocks are all located on chromosome 17 within the region 33.32 to 33.82 Mb. They contain the *Qa2* locus.

Table 1. Phenotypic data used for computational haplotype-based genetic analysis. The MHC class Ia, Ib, II, and III phenotypes; hepatic AH response; and pulmonary *H2-E*α gene expression data are shown. n/a, not available.

Strain	H2 Haplotypes					*H2-E*α gene expression	AH response
	Class Ia	Class II		Class III	Class Ib		
	K	Aβ Aα Eβ	Eα	S	Qa-2		
129/SvJ	b	b	Null	b	a	5	−
A/J	k	k	k	d	a	42	+
A/HeJ	k	k	k	d	a	23	+
AKR/J	k	k	k	k	b	44	−
B10.D2-H2/oSnJ	d	d	d	d	b	1055	+
BALB/cJ	d	d	d	d	b	1063	+
BALB/cByJ	d	d	d	d	b	n/a	n/a
C3H/HeJ	k	k	k	k	b	36	+
C57/6J	b	b	Null	b	a	8	+
DBA/2J	d	d	d	d	b	1343	−
LG/J	d	d	d	d	b	n/a	n/a
LP/J	b	b	Null	b	a	n/a	−
MRL/MpJ	k	k	k	k	b	38	n/a
NZB/BinJ	d	d	d	d	b	n/a	−
NZW/LacJ	u	u	u	z	b	n/a	−
SM/J	v	v	v	v	a	n/a	+

nonresponsive, whereas the A/J, A/HeJ, C57BL/6J, BALB/cJ, B10.D2-H2/oSnJ, SM/J, and C3H/HeJ strains were AH responsive. The AH response phenotypes were treated as a qualitative binary phenotype (either + or −) for the computational analysis. The pattern of genetic variation within only two haplotype blocks exactly matched the pattern of AH responsiveness (calculated score = 0) among the inbred strains (Fig. 2, A and B). Within these two blocks, all six nonresponsive strains shared one haplotype, whereas the seven responder strains had one of two other haplotypes. Both of these haplotypic blocks were within the *Ahr* locus on mouse chromosome 12 (29.7 Mb). None of the other haplotypic blocks exactly matched the AH response pattern among the inbred strains. Furthermore, because the AH phenotype was measured in liver tissue, identification of the computationally predicted genes that were expressed in liver would also help to identify the causative genetic locus. Analysis of gene expression data indicated that only three of the nine haplotypic blocks whose strain groupings were best correlated with the phenotypic response were within genes (*Ahr* and *Dnpep*) expressed in liver tissue (Fig. 2B). In summary, haplotypic blocks within the *Ahr* locus were the only blocks having a perfect correlation with AH response phenotype, and the *Ahr* gene was expressed in liver tissue. Therefore, *Ahr* was the computationally predicted gene candidate selected for further analysis.

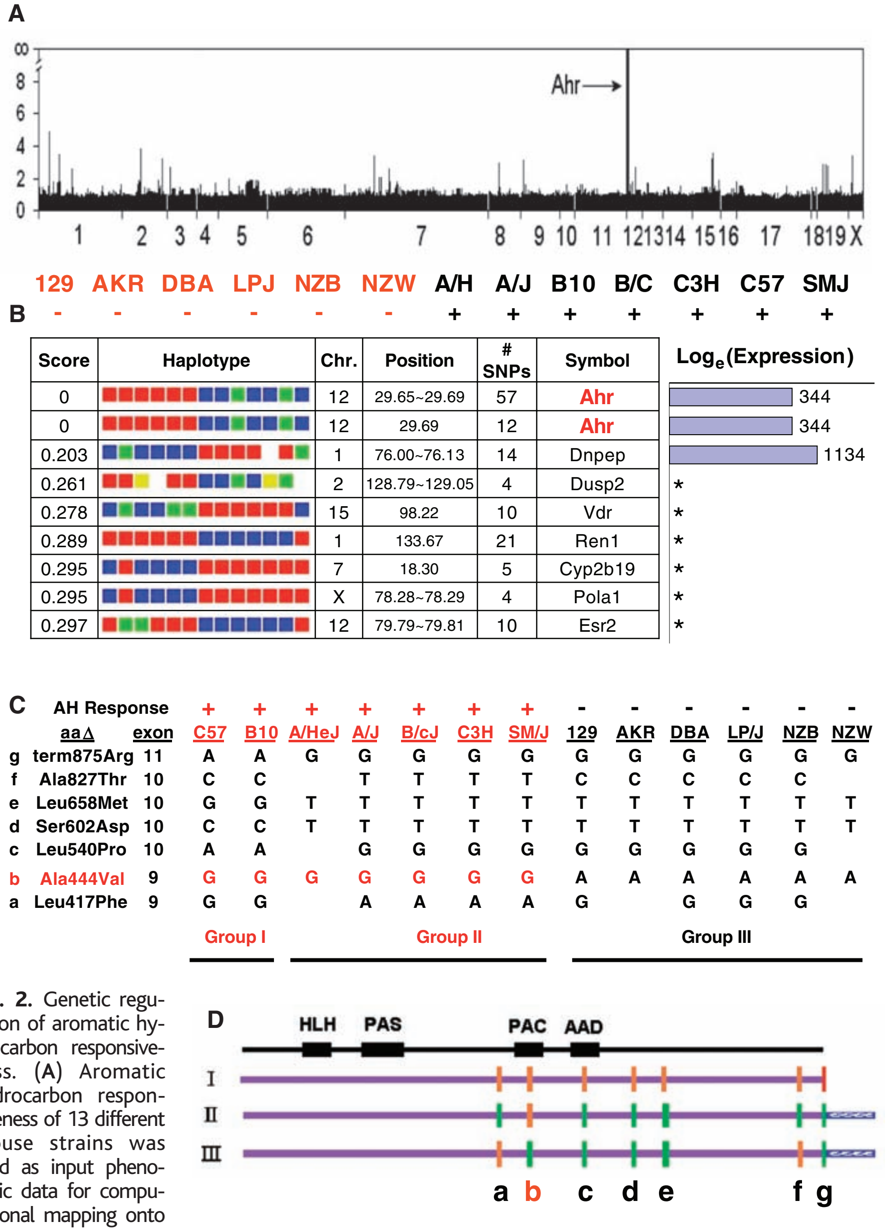

129	AKR	DBA	LPJ	NZB	NZW	A/H	A/J	B10	B/C	C3H	C57	SMJ
-	-	-	-	-	-	+	+	+	+	+	+	+

Score	Haplotype	Chr.	Position	# SNPs	Symbol	Log$_e$(Expression)
0	🟥🟥🟥🟥🟥🟥🟦🟦🟩🟦🟦🟩🟦	12	29.65~29.69	57	Ahr	344
0	🟥🟥🟥🟥🟥🟥🟦🟦🟩🟦🟦🟩🟦	12	29.69	12	Ahr	344
0.203	🟦🟩🟦🟦🟦🟦🟥🟥🟥🟥 🟥🟩	1	76.00~76.13	14	Dnpep	1134
0.261	🟥🟥🟨 🟥🟥🟦🟦🟩🟦🟨🟩	2	128.79~129.05	4	Dusp2	*
0.278	🟦🟩🟦🟦🟩🟩🟥🟥🟥🟥🟥🟥🟦	15	98.22	10	Vdr	*
0.289	🟥🟥🟥🟥🟥🟥🟦🟦🟦🟦🟦🟦🟥	1	133.67	21	Ren1	*
0.295	🟦🟥🟦🟦🟦🟦🟥🟥🟥🟥🟥🟥🟥	7	18.30	5	Cyp2b19	*
0.295	🟦🟥🟦🟦🟦🟦🟥🟥🟥🟥🟥🟥🟥	X	78.28~78.29	4	Pola1	*
0.297	🟥🟩🟩🟥🟥🟥🟦🟦🟦🟦🟦🟦🟥	12	79.79~79.81	10	Esr2	*

	AH Response		+	+	+	+	+	+	+	-	-	-	-	-	-
	aaΔ	exon	C57	B10	A/HeJ	A/J	B/cJ	C3H	SM/J	129	AKR	DBA	LP/J	NZB	NZW
g	term875Arg	11	A	A	G	G	G	G	G	G	G	G	G	G	G
f	Ala827Thr	10	C	C		T	T	T	T	C	C	C	C	C	
e	Leu658Met	10	G	G	T	T	T	T	T	T	T	T	T	T	T
d	Ser602Asp	10	C	C	T	T	T	T	T	T	T	T	T	T	T
c	Leu540Pro	10	A	A		G	G	G	G	G	G	G	G	G	
b	Ala444Val	9	G	G	G	G	G	G	G	A	A	A	A	A	A
a	Leu417Phe	9	G	G		A	A	A	A	G		G	G	G	
			Group I		Group II					Group III					

Fig. 2. Genetic regulation of aromatic hydrocarbon responsiveness. (**A**) Aromatic hydrocarbon responsiveness of 13 different mouse strains was used as input phenotypic data for computational mapping onto haplotypic blocks. Two haplotypic blocks had a perfect correlation with the AHR response phenotype, and both were within the *Ahr* locus on chromosome 12 (indicated by the arrow). (**B**) The AH response phenotype for the 13 strains and a list of haplotypic blocks with the best correlation with the pattern of AH response among the inbred strains are shown. For each predicted block, the calculated score for partitioning of the phenotypic data, chromosomal location, and the number of SNPs within a block and its gene symbol are shown. The haplotypes for each strain are represented by colored blocks that are presented in the same order as shown for the strain phenotypes. Strains sharing the same haplotype have the same colored block. A calculated partition score of 0 indicates an exact match between the distribution of phenotypic responses and haplotypic groupings among the inbred strains. An asterisk (*) indicates that the gene was not expressed in liver tissue. (**C**) Three haplotypes within the *Ahr* locus on chromosome 12 (29.7 Mb). Of 211 SNPs within the *Ahr* locus, the seven exonic SNPs (labeled as a to g) that change an amino acid are shown. (**D**) The relative location of amino acid changes in the AHR protein for the three haplotypic groups. Four of the amino acid changes (c, d, e, and g) distinguish group I from the other two haplotypic groups, including an amino acid change (g) that converts a stop codon in the group I protein to an Arg in group II and III. Three other amino acid changes (a, b, and f) differentiate the group II and group III proteins. However, only a single SNP (b), which converts an Ala (group I and II) to Val (group III) and is located within the PAC domain, distinguishes the responder and nonresponder strains.

Analysis of genetic variation within the *Ahr* locus identified the precise molecular basis for the differential AH response among inbred strains. The 211 SNPs within the *Ahr* locus (*2*) divided the inbred mouse strains into three haplotypic groups (Fig. 2C). The AH-responsive strains were in haplotypic groups I and II, whereas the nonresponsive strains were in group III. Sixteen SNPs were located in exons, and 7 (labeled a to g in Fig. 2, C and D) altered the amino acid sequence of the encoded protein. One polymorphism converted a stop codon in the group I strains (B10 and C57BL/6) to an Arg in all other strains, adding 43 C-terminal amino acids to the AHR protein expressed by the group II and III strains. Three amino acid changes differentiated the group II from the group III strains. Although these polymorphisms induced amino acid changes and were previously thought to be of importance to this phenotype (*11*), their strain distribution indicated that they were not responsible for differences in AH response phenotype. The precision of these computational predictions is demonstrated by the fact that only one SNP distinguished the AH responsive and nonresponsive strains. This polymorphism (labeled b in Fig. 2, C and D) converted Ala^{444} in the AH-responsive (group I and II) strains to Val^{444} in the AH-unresponsive (group III) strains. This SNP was located within a PAS Associated C-terminal (PAC) motif that contributes to the folding of the ligand binding and dimerization region of this protein (*12*, *13*). Consistent with the prediction of this computational genetic method, an Ala^{444} → Val substitution in an expressed recombinant AHR protein shifted the in vitro AH response from a responder to a nonresponder state (*11*, *14*).

Gene expression profiles across inbred mouse strains provide a useful intermediate phenotype that can be analyzed to understand how phenotypic traits are genetically regulated. In the same manner as phenotypic trait information, strain-specific gene expression data can be computationally mapped onto haplotypic blocks to identify genetic loci that potentially regulate differential gene expression. For example, the level of *H2-Eα* gene expression in mouse lung, which is an MHC class II gene, differed by more than 20-fold across 10 inbred mouse strains examined using oligonucleotide microarrays (Fig. 3). Logarithm-transformed *H2-Eα* gene expression data were computationally analyzed using our haplotype-based computational mapping method. The haplotypic block within the first intron of the *H2-Eα* gene had the strongest correlation with *H2-Eα* gene expression. A Bonferroni-adjusted *P*-value of 0.001 for this prediction (table S1) supported the possibility that a cis-acting functional element within the *H2-Eα* gene could regulate its basal expression.

To identify the cis-acting element, we analyzed 23 SNPs within this 1.0-kb haplotypic block (Fig. 4A). The nucleotide sequence within this haplotypic block was scanned to identify known recognition elements for transcription factors in the TRANSFAC database (*15*). Then, combinations of SNPs that were located within or near transcription factor recognition elements and that distinguished haplotypes within this block were selected. By this method, three haplotype-determining SNPs within this block, all located within a 30–base pair (bp) sequence at nucleotide positions +974, +975, and +999 downstream from the *H2-Eα* transcription start site, were selected for analysis. We examined the effect of these polymorphisms on reporter gene expression in a B lymphoma cell line. Two constructs with insertion of the *H2-Eα* promoter, first exon segments, and first intron segments were prepared (Fig. 4B). Construct II has the 10- to 1029-bp region of *H2-Eα* inserted, with the intronic region between positions +475 and +925 deleted. Genomic segments for construct II were amplified from three different inbred strains; each strain had a different haplotype resulting from the three polymorphisms discussed above. The intronic region containing these three polymorphic sites is not contained in construct I. Though similar to construct II, construct I contains only the 10- to 957-bp region of *H2-Eα*, with the intronic region between positions +475 and +925 deleted. The BALB/cJ haplotype in the first intron sequence resulted in a threefold enhancement of reporter gene expression, relative to plasmids containing the same regions amplified from the other two haplotypes (Fig. 4C). In fact, the AKR- and C57/BL6-derived intronic sequences did not enhance expression of construct II plasmids relative to the *H2-Eα* promoter and exonic sequence present in construct I. These results demonstrate that an allele-specific regulatory element is located between nucleotides +958 and +1029 in the first intron of the *H2-Eα* gene.

To further characterize the regulatory element within this intronic region, we performed electrophoretic mobility–shift assay (EMSA) experiments using three 45-bp oligonucleotides. Each oligonucleotide had a different SNP allele combination that corresponded to one of the three *H2-Eα* haplotypes at positions +974, +975, and +999 (Fig. 4A). The EMSA experiments demonstrated that DNA-protein complexes were formed after incubation of two different (CA…T and CA…G) oligonucleotides with nuclear extracts prepared from lung tissue. In contrast, the (TG…G) oligonucleotide did not form detectable protein complexes (Fig. 4D). The adjacent SNPs (CA/TG) were located within a Yin Yang 1 (YY1) transcription factor binding site, whereas the third SNP (T/G) was within a serum response factor (SRF) binding site. The CA-to-TG conversion eliminated the YY1 binding site, whereas the G-to-T change converts an SRF binding site to a potential recognition element for another Activator Protein 1 (AP1) transcription factor. YY1 binding to the CA-allele oligonucleotide was confirmed by "supershift" experiments performed by preincubation of the nuclear lysate proteins with an antibody to YY1. The mobility of the upper band was altered in the presence of the antibody, indicating that it was a complex of YY1 bound to the oligonucleotide (Fig. 4E). YY1 has been shown to be required for association of SRF with its serum response element (SRE) (*16*). Of note, only mouse strains with the CA…G haplotype exhibited high *H2-Eα* gene expression in the lung. Taken together, the EMSA, reporter gene, and gene expression results indicate that a 45-bp functional element within the *H2-Eα* gene locus regulates its basal expression level in an allele-specific manner. Within this functional element, alleles that enable the

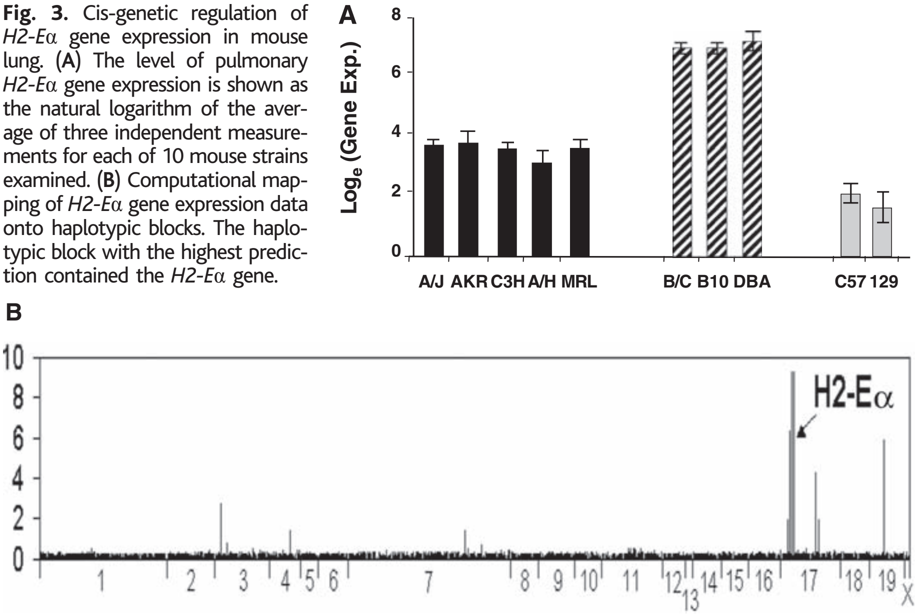

Fig. 3. Cis-genetic regulation of *H2-Eα* gene expression in mouse lung. (**A**) The level of pulmonary *H2-Eα* gene expression is shown as the natural logarithm of the average of three independent measurements for each of 10 mouse strains examined. (**B**) Computational mapping of *H2-Eα* gene expression data onto haplotypic blocks. The haplotypic block with the highest prediction contained the *H2-Eα* gene.

Table 2. Haplotype-based computational predictions generated for five phenotypic data sets. For each phenotype, the location of the haplotypic block, which contains the gene determining the phenotype, along with its computational score are shown. The score for each haplotypic block was calculated as a function of the correlation between the phenotypic data and strain grouping within the haplotypic block. A smaller score indicates a better match, and 0 indicates a perfect match.

Phenotype	Predicted locus	Score	Chr.	MB
H2 K	*H2-K*	0	17	32.78–32.81
H2 A α/β, E α/β	*H2-A α/β*, *H2-E α/β*	0	17	32.94–32.94
H2 S	*H2-S*	0.16	17	33.26–33.32
H2 Qa-2	*H2-Qa2*	0	17	33.32–33.42
H2-Eα gene expression	*H2-Eα*	0.11	17	32.57–33.26
AH response	*Ahr*	0	12	29.66–29.69

binding of YY1 and a second transcription factor, which is probably SRF, are required for high *H2-Eα* gene expression in the lung.

These examples demonstrate that a variety of genetically regulated phenotypic traits, ranging from qualitative trait information to quantitative gene expression data that vary among inbred strains, can be computationally analyzed by this method. The haplotypic blocks exhibiting a strong correlation with phenotypic data provide a valuable starting point that enables pathway analysis or mechanistic studies to be performed. As shown in the analysis of the *H2-Eα* gene expression and AH response data, a very precise hypothesis about the genetic basis for the phenotypic difference among mouse strains can be generated using this computational method. In these examples, the SNPs responsible for the phenotypic differences were predicted.

A number of factors affect the performance of this method. As shown here, it performs extremely well when the phenotypic data reflect the genetic variation within a haplotypic block in our SNP database. However, if haplotypic information for a key genetic locus or phenotypic information for a sufficient number of strains is not available, its performance is substantially reduced. When phenotypic data for only a few inbred strains are available, this method usually produces a large number of top predictions with comparable scores, and most are false-positives. We have empirically determined that phenotypic data from eight or more strains are needed to produce statistically significant predictions (table S1). The statistical power and SNP coverage issues will diminish as the numbers of inbred strains and SNPs in the database increase. A haplotypic map with more than 300,000 SNPs covering between 40 and 50 commonly used inbred mouse strains should be available within 2 years. At present, it is unlikely that this computational method can analyze traits controlled by multiple genetic loci, each with a small effect size. However, coverage of additional inbred strains should enable this computational method to

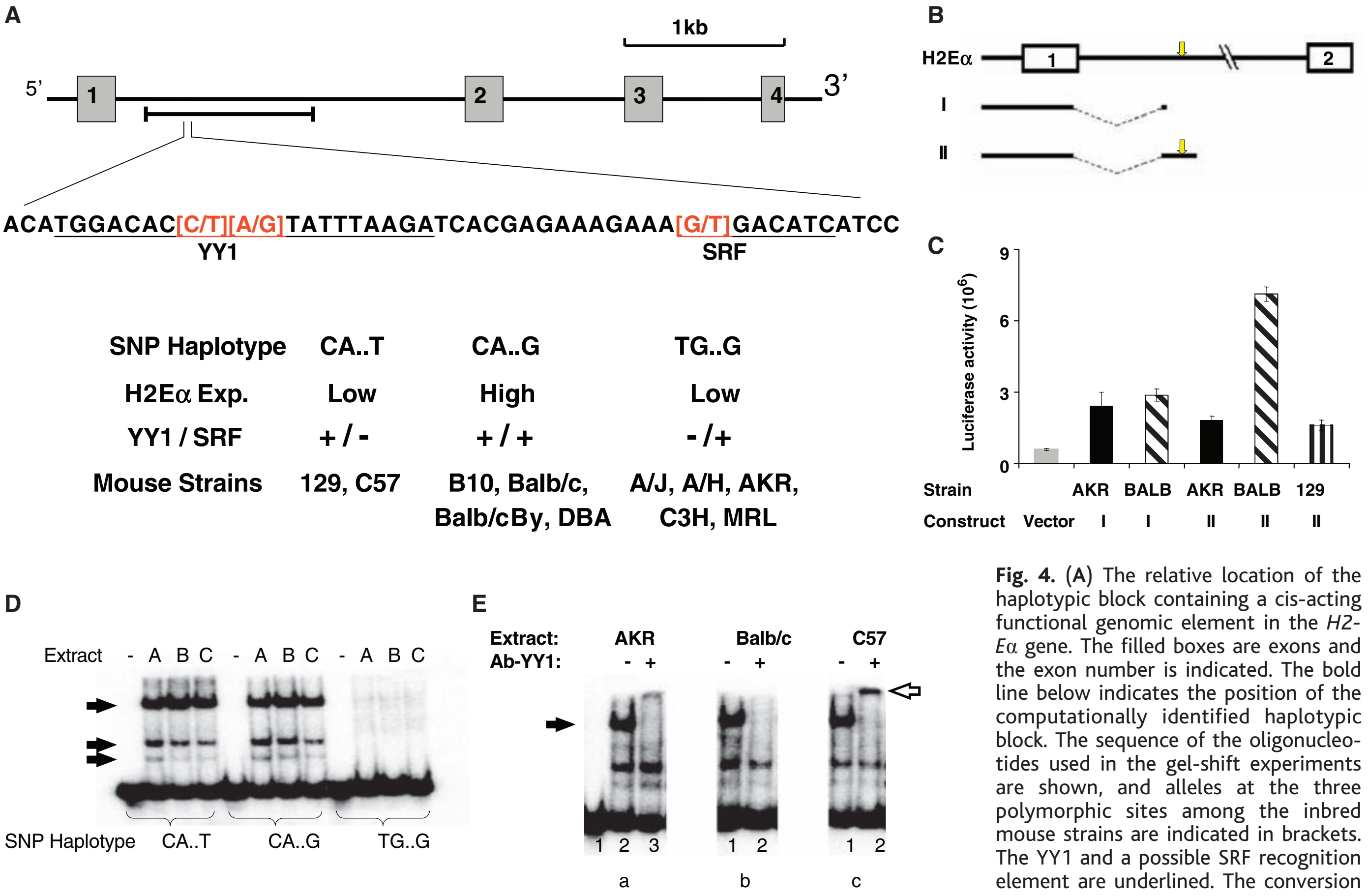

Fig. 4. (**A**) The relative location of the haplotypic block containing a cis-acting functional genomic element in the *H2-Eα* gene. The filled boxes are exons and the exon number is indicated. The bold line below indicates the position of the computationally identified haplotypic block. The sequence of the oligonucleotides used in the gel-shift experiments are shown, and alleles at the three polymorphic sites among the inbred mouse strains are indicated in brackets. The YY1 and a possible SRF recognition element are underlined. The conversion of the CA to TG alleles eliminates the YY1 binding site. The CA..G allele–containing haplotype has the YY1 and SRF binding sites and also had high *H2-Eα* gene expression. (**B**) *H2-Eα* gene structure and reporter gene constructs. Construct II contains the 10- to 1029-bp region of *H2-Eα*, with a deletion of the 475- to 925-bp region. The shorter construct (I) contains the 10- to 925-bp region of *H2-Eα*, with deletion of the region between 475 and 925 bp. The yellow arrow indicates the location of the polymorphic regulatory element containing YY1 and SRF binding sites. (**C**) The haplotype-specific effect of the *H2-Eα* cis-acting element on reporter gene expression. The level of luciferase reporter gene expression in the A20 B lymphoma cell line after transfection of the indicated plasmids is shown. Luciferase assays were performed using two different construct I plasmids, which had genomic DNA obtained from either the AKR or Balb/cJ strains. Three construct II plasmids were prepared, and each had genomic DNA obtained from AKR, Balb/c, or 129 mice. These three strains represent each of the three different haplotypes identified within the first intron of the *H2-Eα* gene. The luciferase expression level was normalized for transfection efficiency by cotransfection with a β-galactosidase plasmid. (**D**) Allele-specific formation of protein-DNA complexes requires a YY1 recognition element. Three different ^{32}P-labeled oligonucleotides, each with different alleles at three polymorphic sites, were incubated with nuclear extracts from lung tissue obtained from AKR (lane A), Balb/c (lane B), or C57 (lane C) mice. The arrowheads indicate the protein-DNA complexes. (**E**) YY1 is part of the allele-specific protein-DNA complex. EMSAs were performed using a ^{32}P-labeled 45-bp CA..G oligonucleotide, containing a YY1 recognition element, and nuclear extracts of lung tissue were prepared as in (D). The extracts were preincubated with an antibody to YY1. The filled arrow indicates the position of the YY1 DNA complex, and the open arrow indicates the position of this complex after incubation with the antibody to YY1.

have substantial power to identify genetic loci for a wider range of phenotypic traits, including those with increased underlying genetic complexity, than is currently possible.

References and Notes

1. A. Grupe *et al.*, *Science* **292**, 1915 (2001).
2. See http://mouseSNP.Roche.com.
3. J. Wang *et al.*, in *Computational Genetics and Genomics: New Tools for Understanding Disease*, G. Peltz, Ed. (Humana, Totowa, NJ, 2004).
4. Materials and methods are provided as supporting online material in *Science* Online. The haplotype maps used in this study are available at http://mouseSNP.Roche.com.
5. Jackson Laboratory, *Jackson Lab. Notes* **475** (1998).
6. Y. Yang *et al.*, *J. Biol. Chem.* **267**, 11669 (1992).
7. S. G. Cho, M. Attaya, J. J. Monaco, *Nature* **353**, 573 (1991).
8. D. W. Nebert, A. Puga, V. Vasiliou, *Ann. N. Y. Acad. Sci.* **685**, 624 (1993).
9. A. B. Okey, D. S. Riddick, P. A. Harper, *Toxicol. Lett.* **70**, 1 (1994).
10. D. W. Nebert, N. M. Jensen, H. Shinozuka, H. W. Kunz, T. J. Gill III, *Genetics* **100**, 79 (1982).
11. M. Ema *et al.*, *J. Biol. Chem.* **269**, 27337 (1994).
12. C. P. Ponting, L. Aravind, *Curr. Biol.* **7**, R674 (1997).
13. K. M. Burbach, A. Poland, C. A. Bradfield, *Proc. Natl. Acad. Sci. U.S.A.* **89**, 8185 (1992).
14. A. Maier *et al.*, *Environ. Health Perspect.* **106**, 421 (1998).
15. V. Matys *et al.*, *Nucleic Acids Res.* **31**, 374 (2003).
16. S. Natesan, M. Gilman, *Mol. Cell. Biol.* **15**, 5975 (1995).
17. J.C., A.N., and J.W. were supported by an NIH Genome Research Institute grant (1 R01 HG02322-01) awarded to G.P. We also thank M. Ott (Roche Center for Medical Genomics) for his help with DNA sequencing.

Supporting Online Material

www.sciencemag.org/cgi/content/full/306/5696/690/DC1

Materials and Methods

Table S1

References

24 May 2004; accepted 14 September 2004

The PP2A-Associated Protein α4 Is an Essential Inhibitor of Apoptosis

Mei Kong,[1,3] Casey J. Fox,[1,3] James Mu,[2] Laura Solt,[1] Anne Xu,[1,3] Ryan M. Cinalli,[1,3] Morris J. Birnbaum,[2] Tullia Lindsten,[1,5] Craig B. Thompson[1,3,4]*

Despite evidence that protein kinases are regulators of apoptosis, a specific role for phosphatases in regulating cell survival has not been established. Here we show that α4, a noncatalytic subunit of protein phosphatase 2A (PP2A), is required to repress apoptosis in murine cells. α4 is a nonredundant regulator of the dephosphorylation of the transcription factors c-Jun and p53. As a result of *α4* deletion, multiple proapoptotic genes were transcribed. Either inhibition of new protein synthesis or Bcl-x_L overexpression suppressed apoptosis initiated by *α4* deletion. Thus, mammalian cell viability depends on repression of transcription-initiated apoptosis mediated by a component of PP2A.

The α4 protein was initially identified as a component of receptor signal transduction complexes in mammalian B and T lymphocytes (*1*, *2*) and was later determined to be broadly expressed (*1*, *3*). It interacts with the catalytic subunit of protein phosphatase PP2A (PP2Ac) as well as those of PP4 and PP6 (*4*, *5*). Binding of α4 to PP2Ac displaces PP2Ac from a dimeric regulatory complex composed of the core A subunit and any of more than 12 variable B components (*6*). Interaction of α4 with PP2Ac both enhances PP2Ac catalytic activity and alters its substrate specificity (*4*, *7*). Its yeast homolog, Tap42, is a PP2A regulatory subunit that functions in TOR-dependent nutrient sensing (*8*). In mammalian cells, the association of α4 with PP2Ac is regulated by growth factor signals and modulators of the TOR pathway such as rapamycin (*4*, *7*) (Fig. 1A). However, rapamycin potentiates apoptosis in growth factor–deprived cells (*9*), so it is difficult to determine whether the decline in association of α4 with PP2Ac contributes to the cellular response to such treatments or occurs as a consequence of the decrease in cell viability.

To determine whether α4 contributes to the regulation of cell survival, we generated mice deficient in α4. Two constructs were created that each deleted exon I and adjacent sequences of the *α4* gene. These were introduced into an embryonic stem (ES) cell line, but a homologous recombinant was not recovered in either case. Because the *α4* gene is located on the X chromosome, this result raised the possibility that *α4* was an essential gene in the male ES cells. Hence, we prepared a construct containing the *α4* gene in which exons III to V were flanked by *lox*P (Fig. 1B). After electroporation, 4 of 192 clones showed homologous recombination. Introduction of recombinant Cre into these clones failed to yield ES cell clones carrying a deleted *α4* gene (*10*). Next, we generated mice carrying a germline-transmitted *α4*-floxed allele ($\alpha4^{\mathrm{fl}}$) integrated by homologous recombination. These mice were bred to Lck-Cre transgenic mice to determine the effect of *α4* deletion on developing T cells, a nonessential lineage. In $\alpha4^{\mathrm{fl}}$/Lck-Cre male mice, the thymi were depleted of developing T cells (Fig. 1C) and the residual cells were enriched in immature thymocytes (*10*). Although the Cre-deleted form of the *α4* allele was present in the residual thymocytes, these cells died in the thymus, as no T cells with a deleted *α4* allele appeared in the periphery (Fig. 1D). Thus, α4 is required for either T cell development or survival.

In female heterozygotes carrying one wild-type and one $\alpha4^{\mathrm{fl}}$ allele, thymocyte numbers were reduced by about 60% relative to wild-type mice, but peripheral T cell numbers were normal (Fig. 1C) (*10*). Most peripheral T cells in female heterozygotes carried a Cre-deleted form of $\alpha4^{\mathrm{fl}}$ (Fig. 1D). Because T cell precursors have undergone random X-chromosome inactivation, this finding suggests that the decreased number of thymocytes resulted from the death of cells in which *α4* was deleted on the active X chromosome.

To further analyze the consequences of *α4* deletion, we generated immortalized mouse embryonic fibroblasts (MEFs) from male $\alpha4^{\mathrm{fl}}$ embryos and compared them to littermate $\alpha4^{\mathrm{wt}}$ MEFs (fig. S1) (*11*). Retroviruses encoding either green fluorescent protein (GFP) expressed from an internal ribosome entry site (IRES) alone (vector) or both a Cre recombinase and an IRES-GFP (Cre) were introduced into $\alpha4^{\mathrm{fl}}$ or $\alpha4^{\mathrm{wt}}$ MEFs, and GFP-positive cells were isolated. Immunoblot analysis of lysates from GFP-positive cells 48 hours and 72 hours after Cre infection showed a decrease and absence of α4 protein, respectively, in $\alpha4^{\mathrm{fl}}$ MEFs but not in $\alpha4^{\mathrm{wt}}$ MEFs (Fig. 2A). Cell death was observed beginning 48 hours after Cre infection in the $\alpha4^{\mathrm{fl}}$ MEFs, and nearly all cells were dead by 120 hours after infection (Fig. 2B). In contrast, the viability of $\alpha4^{\mathrm{wt}}$ cells infected with Cre or $\alpha4^{\mathrm{fl}}$ infected with vector was not affected (Fig. 2B). Reconstitution of α4 into $\alpha4^{\mathrm{fl}}$

---

[1]Abramson Family Cancer Research Institute, [2]Howard Hughes Medical Institute, University of Pennsylvania, Philadelphia, PA 19104, USA. [3]Department of Cancer Biology, [4]Department of Medicine, [5]Department of Pathology and Laboratory Medicine, University of Pennsylvania School of Medicine, Philadelphia, PA 19104, USA.

*To whom correspondence should be addressed. E-mail: craig@mail.med.upenn.edu

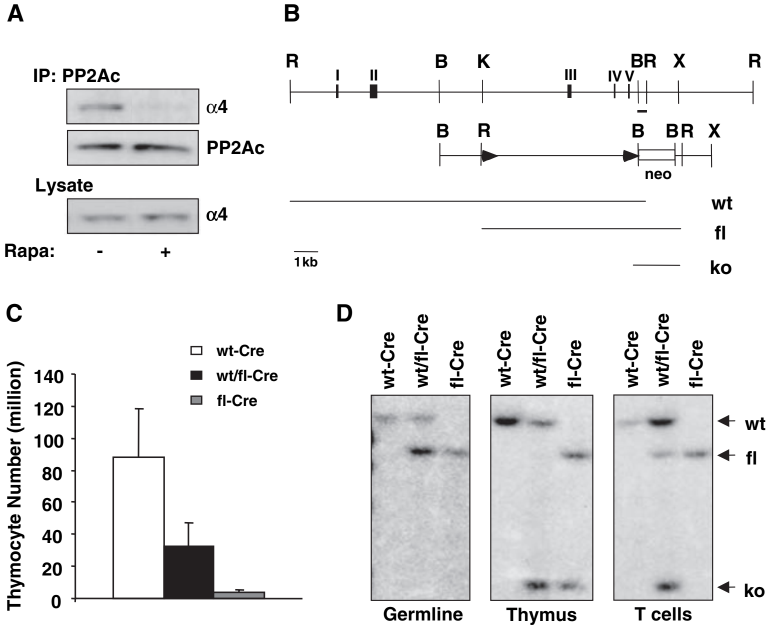

Fig. 1. Conditional deletion of the PP2A-associated protein α4 in thymocytes. (**A**) Association of α4 with PP2Ac is inhibited by rapamycin. The lymphoid progenitor cell line FL5.12 was cultured overnight in growth factor–deficient medium in the presence (+) or absence (−) of 20 nM rapamycin (Rapa) as indicated. Cell lysates were immunoprecipitated (IP) with antibody to PP2Ac followed by immunoblotting with antibodies to α4 or PP2Ac. As a control, an equivalent amount of lysate was immunoblotted with antibody to α4 to detect total α4. (**B**) Generation of an *α4* allele containing *lox*P sites. Upper panel: Genomic organization of the *α4* gene locus. R, Eco RI; B, Bam HI; K, Kpn I; X, Xba I. The bar indicates the probe used for the Southern blots. Lower panel: Targeting construct and different Eco RI fragments generated from different genotypes (wt, *α4* wild-type genotype; fl, floxed *α4* allele; ko, Cre-deleted *α4* allele). (**C**) Thymocyte cell number was determined in $\alpha4^{\mathrm{wt}}$/Lck-Cre male (wt-Cre), $\alpha4^{\mathrm{wt/fl}}$/Lck-Cre female (wt/fl-Cre), and $\alpha4^{\mathrm{fl}}$/Lck-Cre male (fl-Cre) mice. Values are means ± SD of three mice. (**D**) Southern blots of DNA prepared from tail (germline), thymus, and purified splenic T cells of different genotypes as described in (C).

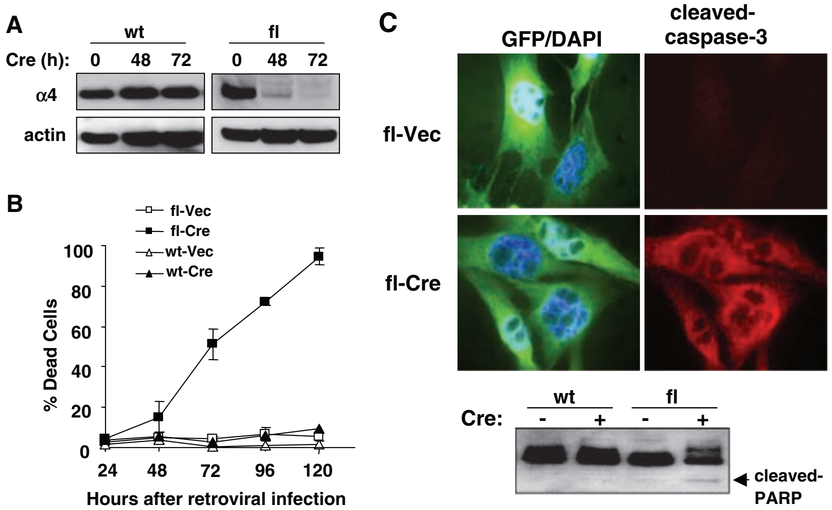

Fig. 2. *α4* deletion induces cell death in MEFs. (**A**) Depletion of α4 protein in $\alpha4^{\mathrm{fl}}$ male MEFs after Cre introduction. $\alpha4^{\mathrm{wt}}$ (wt) or $\alpha4^{\mathrm{fl}}$ (fl) MEFs were infected with MIGR1-GFP-Cre (Cre), and the resulting GFP-positive cells were isolated and analyzed at the time points indicated. Immunoblotting was performed with antibodies to α4 or actin. (**B**) The percentage of dead cells was determined by the ratio of 4′,6′-diamidino-2-phenylindole (DAPI)–positive cells to GFP-positive cells isolated after infection of $\alpha4^{\mathrm{fl}}$ MEFs with MIGR1-GFP-Cre (fl-Cre) or MIGR1-GFP (fl-Vec) or after infection of $\alpha4^{\mathrm{wt}}$ MEFs with MIGR1-GFP-Cre (wt-Cre) or MIGR1-GFP (wt-Vec). (**C**) After 48 hours of Cre infection, cells were fixed and the presence of cleaved caspase-3 was determined with a specific antibody (red). GFP expression of the cells in the same field was visualized with a fluorescein isothiocyanate (FITC) filter (green) and overlapped with DAPI staining (blue). Lower panel: Cell lysates were analyzed by immunoblotting with a PARP-specific antibody.

cells by stable transfection rescued cell death in response to Cre infection (*10*). The dying *α4*-deleted cells displayed the typical features of apoptosis, including cleavage of caspase-3 and cleavage of the caspase substrate PARP [poly(ADP-ribose) polymerase] (Fig. 2C).

Apoptosis can be initiated either through biochemical modulation of existing apoptotic regulatory proteins or through transcription and translation–dependent changes in apoptotic regulatory proteins (*12–14*). To distinguish between these two possibilities, we investigated the effect of protein synthesis inhibition on *α4* deletion–induced cell death. Addition of the protein synthesis inhibitor cycloheximide (CHX) 48 hours after Cre infection rescued $\alpha4^{\mathrm{fl}}$ cells from apoptosis, despite a decrease of α4 protein expression in the presence or absence of CHX (Fig. 3A) (fig. S2).

The transcription factor c-Jun is a PP2A substrate and has been implicated in transcription-dependent apoptotic death in response to diverse cellular stresses, including ultraviolet irradiation, heat and osmotic shock, and growth factor withdrawal (*15*). Its activation involves phosphorylation followed by nuclear translocation. At 72 hours after Cre-mediated *α4* deletion, c-Jun phosphorylation on Ser^{63} increased (Fig. 3B) and accumulated in the nucleus (Fig. 3C). However, no changes in the expression or activation status of the Jun kinases were detected, as measured by their phosphorylation status (Fig. 3B).

To examine the transcriptional changes that occur after *α4* deletion, we performed RNA microarray analysis with RNA from $\alpha4^{\mathrm{fl}}$ MEFs 48 hours after infection with Cre or vector. Isolated RNA was hybridized to Affymetrix mouse expression microarrays containing more than 39,000 transcripts and variants. Pairwise analysis of the hybridization profiles revealed that among the 20 genes whose expression was most highly increased in the Cre-infected sample (relative to the vector-infected control), six were established p53-dependent targets: p21, Noxa, MDM2, cyclin G, Stk11, and SIP (table S1). Several genes implicated in the intrinsic mitochondrial apoptotic pathway were also induced, including those encoding mDAP-3, Siva, and endonuclease G (*10*). The up-regulation of p53-dependent transcripts was associated with the accumulation of p53 that was phosphorylated on Ser^{18} as α4 expression declined (Fig. 3D). In addition to p53 Ser^{18} phosphorylation, α4-depleted cells accumulated p21 and Noxa proteins.

Because induction of p53 activity is a potent inducer of apoptosis, we made $\alpha4^{\mathrm{fl}}$ cells deficient in p53 by stimulating the ubiquitin-dependent proteolysis of p53 (*16*).

Expression of a papilloma virus E6 protein repressed p53 expression (fig. S3) and partially inhibited apoptosis in response to α4 loss (Fig. 3E). Like the proapoptotic p53 gene targets induced in *α4*-deleted cells, the other proapoptotic genes transcriptionally induced in *α4*-deleted cells also regulate the intrinsic apoptotic pathway. Overexpression of Bcl-x_L, an inhibitor of the intrinsic apoptotic pathway, protected $\alpha4^{fl}$-deleted cells from cell death; this result indicates that the transcriptional initiation of apoptosis repressed by α4 is mediated through the intrinsic apoptotic pathway (Fig. 3F).

To determine whether the requirement for α4 is restricted to developing and proliferating cells, we assessed the effect of *α4* deletion on differentiated adipocytes. Expression of PPARγ (peroxisome proliferator-activated receptor γ), a nuclear hormone receptor that is critical for adipogenesis (*17*), caused the $\alpha4^{fl}$ MEFs to differentiate into adipocytes, as confirmed by the intracellular accumulation of lipid droplets (Fig. 4A) and by lipid staining with Oil Red O (*10*). Cells were then infected at high multiplicity with either an adenovirus encoding Cre recombinase or a control adenovirus. Seven days after infection, fewer adipocytes were observed among the Cre-infected cells, most of which were dead or dying (Fig. 4A) (fig. S4). This Cre-induced death resulted in caspase-3 activation (fig. S4). As in proliferating cells, increased phosphorylation of p53 and c-Jun was detected in response to deletion of *α4* (Fig. 4A).

Next, we assessed the role of α4 in maintaining the viability of differentiated cells in vivo. Three adult $\alpha4^{fl}$ mice and three $\alpha4^{wt}$ mice were injected with an adenovirus encoding Cre through the tail vein, a technique that selectively infects the liver parenchyma (*18*). At day 5 after injection, all $\alpha4^{fl}$ mice showed signs of illness, with ruffled fur, hunched posture, and rapid breathing. Over the next 24 hours, their condition deteriorated while the $\alpha4^{wt}$ mice remained healthy. All six mice were killed and their livers removed for histological and biochemical analysis (Fig. 4B). Immunoblot analysis of liver lysates revealed that α4 was absent in the $\alpha4^{fl}$ mice and present in the $\alpha4^{wt}$ mice. The lysates from the α4-depleted liver revealed increased phosphorylation of p53 and c-Jun and induction of p21 expression. Liver sections from Cre-infected $\alpha4^{fl}$ mice revealed multiple apoptotic cells, as determined by terminal deoxynucleotidyl transferase–mediated deoxyuridine triphosphate nick end labeling (TUNEL) staining. In contrast, TUNEL analysis revealed an absence of apoptotic cells in Cre-infected $\alpha4^{wt}$ mice.

It is surprising that the deletion of a single PP2A regulatory subunit could have such a profound phenotype. Previous studies of *α4* deletion in lymphocytes had concluded that *α4* is not an essential gene because mature lymphocytes were observed (*19*, *20*). However, our data show that the peripheral T cells that arose in $\alpha4^{fl}$/Lck-Cre mice failed to delete the $\alpha4^{fl}$ allele, a possibility not addressed in the prior work. The α4 homolog in yeast, Tap42, plays an essential role in suppressing stress response genes in yeast by either repressing PP2Ac/Sit4 activity or altering their substrate specificity (*21*). Similarly, α4 appears to suppress the stress response factor c-Jun by maintaining it in a more dephosphorylated state. However, because yeast lack both p53 and an apoptotic response, α4 has also been evolutionarily adapted to repress p53-dependent transcription and apoptosis. It is likely that, in addition to its effect on c-Jun and p53, *α4* deletion alters the phosphorylation status of more specialized substrates such as Mid1, a protein involved in midline pattern formation that is also a substrate of the α4/PP2Ac complex (*22*). Moreover, PP2Ac may play an additional role in apoptosis through interaction with other regulatory subunits (*23*). Nonetheless, the observation that *α4* deletion leads rapidly to apoptosis in all cell types tested demonstrates that specific phosphatase complexes play nonredundant and essential roles in the regulation of transcription-induced apoptosis. The data support the hypothesis that in animal cells, apoptosis is a default cell fate (*24*). In the absence of specific and regulated inhibition, cells initiate new transcription and translation to actively initiate their apoptotic demise.

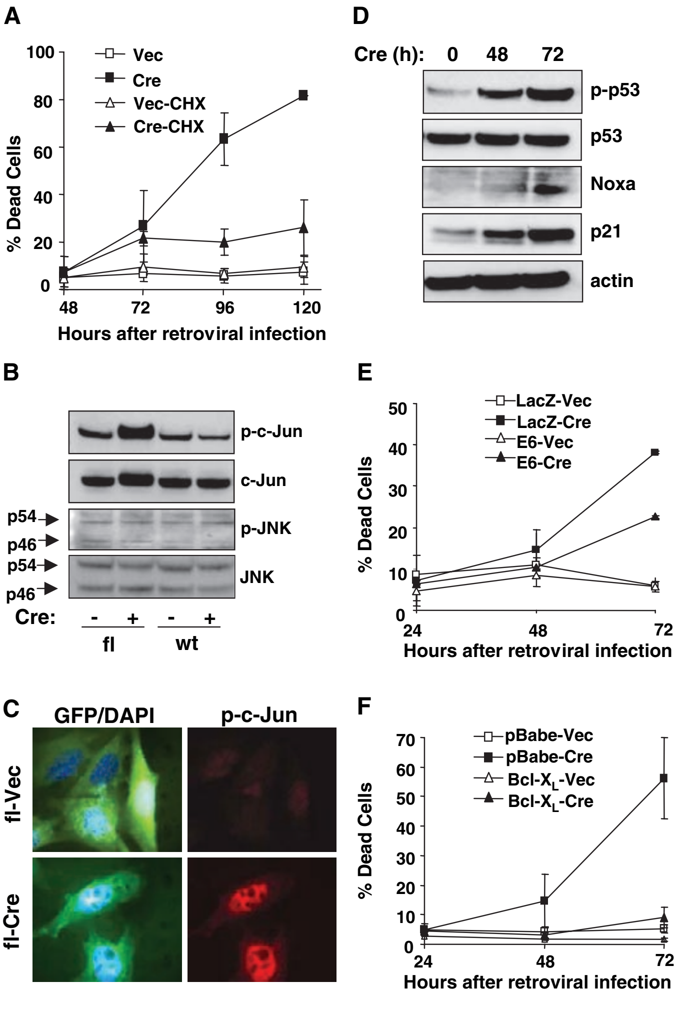

Fig. 3. p53 and c-Jun are phosphorylated after *α4* deletion. (**A**) Cycloheximide treatment rescues *α4*-deleted cells from death. $\alpha4^{fl}$ MEFs were infected with MIGR1-GFP (Vec) or MIGR1-GFP-Cre (Cre). Duplicate cultures were prepared, and after 48 hours of retroviral infection, CHX was added to one of the paired samples. The percentage of dead cells was determined by the ratio of DAPI-positive cells to GFP-positive cells. (**B**) $\alpha4^{fl}$ (fl) or $\alpha4^{wt}$ (wt) MEFs were infected with MIGR1-GFP (−) or MIGR1-GFP-Cre (+). GFP-positive cells were sorted by flow cytometry after 24 hours of infection and collected at 72 hours after retroviral infection. Immunoblotting was performed with different antibodies as indicated. (**C**) $\alpha4^{fl}$ (fl) MEFs were infected with MIGR1-GFP (Vec) or MIGR1-GFP-Cre (Cre). After 72 hours, cells were fixed and c-Jun phosphorylation was visualized with an antibody to phosphorylated c-Jun Ser^{63} (red). GFP expression of the cells in the same field was visualized with a FITC filter (green) and overlapped with DAPI staining (blue). (**D**) $\alpha4^{fl}$ MEFs were infected with MIGR1-GFP-Cre (Cre), and GFP-positive cells were isolated and analyzed at 48 and 72 hours after Cre introduction. Immunoblotting was performed with antibodies as indicated (*11*). (**E**) $\alpha4^{fl}$ MEFs were infected with adeno-LacZ (LacZ) or adeno-E6 (E6) followed by either MIGR1-GFP (Vec) or MIGR1-GFP-Cre (Cre) and cell death was quantitated over time. (**F**) $\alpha4^{fl}$ MEFs were stably transfected with pBabe-Bcl-x_L (Bcl-x_L) or pBabe (pBabe) retrovirus vector. The selected clones were infected with either MIGR1-GFP (Vec) or MIGR1-GFP-Cre (Cre) and cell death was quantitated over time (means ± SD).

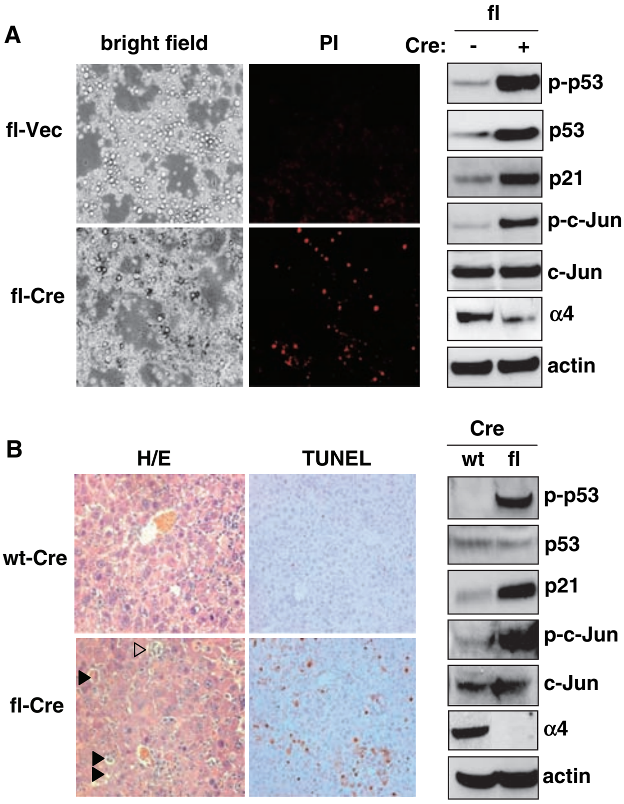

Fig. 4. *α4* deletion induces cell death in nonproliferating tissues. (**A**) Adipocytes generated from $\alpha 4^{fl}$ MEFs (fl) as described in (*11*) were infected with adeno-LacZ (Vec) or adeno-Cre (Cre). Seven days after infection, cells were stained with propidium iodide (PI) and photographed with a tetramethyl rhodamine isothiocyanate (TRITC) filter or bright field (left panel) or analyzed for alterations in protein expression or phosphorylation by immunoblotting with the indicated antibodies (right panel). (**B**) $\alpha 4^{wt}$ (wt) or $\alpha 4^{fl}$ (fl) mice were injected with adeno-Cre (Cre). After 6 days, the mice were killed, livers were removed, and liver sections were analyzed by hematoxylin and eosin (H/E) or TUNEL staining. Solid arrowheads indicate apoptotic cells; open arrowheads indicate macrophages with ingested apoptotic cells (left panel). Immunoblotting was performed with liver lysates from $\alpha 4^{wt}$ (wt) or $\alpha 4^{fl}$ (fl) mice after infection with adeno-Cre (Cre) using antibodies as indicated (right panel).

References and Notes

1. S. Inui *et al.*, *J. Immunol.* **154**, 2714 (1995).
2. E. Chuang *et al.*, *Immunity* **13**, 313 (2000).
3. A. D. Everett, D. L. Brautigan, *Dev. Dyn.* **224**, 461 (2002).
4. K. Murata, J. Wu, D. L. Brautigan, *Proc. Natl. Acad. Sci. U.S.A.* **94**, 10624 (1997).
5. J. Chen, R. T. Peterson, S. L. Schreiber, *Biochem. Biophys. Res. Commun.* **247**, 827 (1998).
6. S. Zolnierowicz, *Biochem. Pharmacol.* **60**, 1225 (2000).
7. S. Inui *et al.*, *Blood* **92**, 539 (1998).
8. C. J. Di Como, K. T. Arndt, *Genes Dev.* **10**, 1904 (1996).
9. A. L. Edinger, C. B. Thompson, *Mol. Biol. Cell* **13**, 2276 (2002).
10. T. Lindsten, M. Kong, J. Mu, unpublished data.
11. See supporting data on *Science* Online.
12. K. Polyak, Y. Xia, J. L. Zweier, K. W. Kinzler, B. Vogelstein, *Nature* **389**, 300 (1997).
13. K. Nakano, K. H. Vousden, *Mol. Cell* **7**, 683 (2001).
14. L. R. Devireddy, J. G. Teodoro, F. A. Richard, M. R. Green, *Science* **293**, 829 (2001).
15. R. J. Davis, *Cell* **103**, 239 (2000).
16. A. Storey *et al.*, *Nature* **393**, 229 (1998).
17. D. Shao, M. A. Lazar, *J. Biol. Chem.* **272**, 21473 (1997).
18. A. Rohlmann, M. Gotthardt, T. E. Willnow, R. E. Hammer, J. Herz, *Nature Biotechnol.* **14**, 1562 (1996).
19. D. R. Hua *et al.*, *Eur. J. Immunol.* **33**, 1899 (2003).
20. S. Inui *et al.*, *Int. Immunol.* **14**, 177 (2002).
21. K. Duvel, A. Santhanam, S. Garrett, L. Schneper, J. R. Broach, *Mol. Cell* **11**, 1467 (2003).
22. J. Liu, T. D. Prickett, E. Elliott, G. Meroni, D. L. Brautigan, *Proc. Natl. Acad. Sci. U.S.A.* **98**, 6650 (2001).
23. A. M. Silverstein, C. A. Barrow, A. J. Davis, M. C. Mumby, *Proc. Natl. Acad. Sci. U.S.A.* **99**, 4221 (2002).
24. M. C. Raff, *Nature* **356**, 397 (1992).
25. We thank M. A. Lazar and W. El-Deiry for providing the PPARγ and E6 constructs, and B. Keith, S. Reiner, and members of the Thompson laboratory for helpful discussions. Supported by a postdoctoral fellowship from the Lymphoma Research Foundation (M.K.) and by grants from the National Cancer Institute.

Supporting Online Material
www.sciencemag.org/cgi/content/full/306/5696/695/DC1
Materials and Methods
Figs. S1 to S4
Table S1
References

20 May 2004; accepted 2 September 2004

A Network of Control Mediated by Regulator of Calcium/ Calmodulin-Dependent Signaling

S. V. Rakhilin,[1] P. A. Olson,[2] A. Nishi,[1,3] N. N. Starkova,[1] A. A. Fienberg,[1,4] A. C. Nairn,[1,5]* D. J. Surmeier,[2]* P. Greengard[1]*

Calmodulin (CaM) is a major effector for the intracellular actions of Ca^{2+} in nearly all cell types. We identified a CaM-binding protein, designated regulator of calmodulin signaling (RCS). G protein–coupled receptor (GPCR)–dependent activation of protein kinase A (PKA) led to phosphorylation of RCS at Ser^{55} and increased its binding to CaM. Phospho-RCS acted as a competitive inhibitor of CaM-dependent enzymes, including protein phosphatase 2B (PP2B, also called calcineurin). Increasing RCS phosphorylation blocked GPCR- and PP2B-mediated suppression of L-type Ca^{2+} currents in striatal neurons. Conversely, genetic deletion of RCS significantly increased this modulation. Through a molecular mechanism that amplifies GPCR- and PKA-mediated signaling and attenuates GPCR- and PP2B-mediated signaling, RCS synergistically increases the phosphorylation of key proteins whose phosphorylation is regulated by PKA and PP2B.

The regulator of calmodulin signaling (RCS), previously referred to as ARPP-21, is a small (9600 dalton), acidic (pI = 4.6) neuronal phosphoprotein that is highly expressed in regions of the mammalian brain innervated by dopamine-releasing neurons (*1*, *2*). RCS contains no obvious conserved domains and displays no similarity to any known protein except for the N terminus of TARPP (thymus-specific cyclic adenosine monophosphate–regulated phospho-protein), a splice variant that is not expressed in brain (*3*). RCS is phosphorylated by protein kinase A (PKA) at Ser^{55} in neostriatal slices (*4*, *5*). However, the function of RCS or of its phosphorylation has remained unknown.

We used the LexA yeast two-hybrid system to study protein-protein interactions and identified CaM as a binding partner for RCS (fig. S1A). The RCS-CaM protein interaction was confirmed by co-immunoprecipitation of endogenous CaM from bovine striatal extract with antibody to RCS (Fig. 1A). In the presence but not the absence of Ca^{2+}, CaM from bovine brain extract bound immobilized recombinant RCS (fig. S1B), and RCS also bound to CaM-Sepharose (fig. S1C).

---

[1]Laboratory of Molecular and Cellular Neuroscience, Rockefeller University, New York, NY 10021, USA. [2]Department of Physiology, Feinberg School of Medicine, Northwestern University, Chicago, IL 60611, USA. [3]Department of Pharmacology, Kurume University School of Medicine, Kurume, Fukuoka 830-0011, Japan. [4]Intra-Cellular Therapies Incorporated, Audubon Biomedical Science and Technology Park, New York, NY 10032, USA. [5]Department of Psychiatry, Yale University School of Medicine, New Haven, CT 06508, USA.

*To whom correspondence should be addressed. E-mail: angus.nairn@yale.edu; j-surmeier@northwestern.edu; greengard@rockefeller.edu

Thus, the interaction between RCS and CaM has high affinity and is Ca^{2+}-dependent.

To assess the role of phosphorylation in modulating the interaction of RCS and CaM, we phosphorylated glutathione *S*-transferase (GST)–RCS stoichiometrically at Ser^{55} with PKA. Phospho-GST-RCS bound to CaM with higher affinity than did dephospho-GST-RCS (Fig. 1B) (apparent K_d = 826 ± 60 nM). In support of this result, mutation of Ser^{55} of RCS to alanine greatly decreased yeast growth, whereas substitution of Ser^{55} with aspartic acid sustained yeast growth, dependent on the RCS-CaM interaction (fig. S1D). Notably, phosphorylated but not dephosphorylated RCS effectively inhibited the activities of CaM-dependent kinase I (CaMKI) and CaM-dependent protein phosphatase 2B (PP2B), with median inhibitory concentration (IC_{50}) values of 1 and 1.2 μM, respectively (Fig. 1, C and D). Considering the dissimilar structural properties of CaMKI and PP2B, the inhibitory activity of phospho-RCS can be attributed to sequestration of CaM, thereby preventing CaM binding to its targets.

Although CaM is expressed in very high concentrations (possibly >100 μM) in most cell types, growing evidence suggests that the level of CaM is substantially lower than that of all of its targets (*6*). Thus, the amount of free CaM is limited, and phosphorylation of RCS would be expected to influence CaM-dependent signaling by regulating its availability. A recent study in nonneuronal cells has indicated that under resting conditions (low intracellular Ca^{2+}) the available free CaM concentration is only ~9 μM (*7*). Moreover, after elevation of intracellular Ca^{2+} by using methods similar to those in this study, the available concentration of CaM is <200 nM. The concentration of RCS in medium spiny neurons is very high [estimated to be in the range of 10 to 20 μM (*1*, *8*)]. Assuming free CaM in neurons is also <10 μM, regulation of RCS phosphorylation would therefore be expected to influence the CaM available for activation of PP2B and other CaM targets.

In medium spiny neurons, PP2B is a potent regulator of L-type Ca^{2+} channels (*9*, *10*). Mobilization of intracellular Ca^{2+} stores by activation of either M_1 muscarinic or D_2 dopaminergic receptors leads to activation of PP2B and suppression of L-type Ca^{2+} channel currents. PP2B-dependent modulation of the L-type Ca^{2+} current was examined in medium spiny neurons from wild-type mice or RCS knock-out mice (fig. S2). Application of the M_1 muscarinic receptor agonist muscarine (2 μM) or the D_2 dopamine receptor agonist R(–)-propylnorapomorphine hydrochloride (NPA, 10 μM) reduced L-type Ca^{2+} channel current by roughly 20% in wild-type medium spiny neurons (Fig. 2). However, in neurons from RCS knock-out mice, the ability of both M_1 and D_2 receptor activation to modulate L-type current was enhanced roughly twofold.

Our biochemical results suggested that increased RCS phosphorylation should suppress the ability of G protein–coupled receptors (GPCRs) to activate PP2B and thereby modulate L-type Ca^{2+} channels. In neurons from RCS knock-out mice, dialysis with phospho-RCS diminished the ability of M_1 receptor stimulation to reduce L-type Ca^{2+} currents (IC_{50} = 13%, $n = 5$, $P < 0.01$, Kruskal Wallis), whereas dialysis with dephospho-RCS had no effect on the modulation (*8*). Activation of PKA to phosphorylate endogenous RCS in wild-type neurons nearly eliminated the muscarinic receptor modulation of L-type Ca^{2+} channel currents ($n = 8$ and median modulation of 0%) (fig. S3). In contrast, PKA activation in neurons from RCS knock-out mice had no significant effect on the muscarinic receptor modulation ($n = 9$ and median modulation = 32%; untreated control, $n = 8$ and median modulation = 42%; $P > 0.05$, Kruskal Wallis) (compare fig. S3D with Fig. 2F).

PP2B also has an important role in dephosphorylation of Thr^{34} of DARPP-32 (dopamine and cyclic adenosine monophosphate–regulated phospho-protein, 32,000 daltons), a key component of dopaminergic signaling in medium spiny neurons (*11*). Treatment of neostriatal slices with the D_1 receptor agonist SKF 81297 increased phosphorylation of Ser^{55} of RCS by ~threefold, reaching a peak within 1 min and continuing for at least 30 min (Fig. 3A). Treatment with SKF81297 also increased phosphorylation of Thr^{34} of DARPP-32 by ~sevenfold in slices obtained from wild-type mice, an effect that was sustained for up to 30 min (Fig. 3B). In slices from RCS knock-out mice, SKF 81297–stimulated phosphorylation of DARPP-32 was similar over the first 5 min. However, DARPP-32 phosphorylation was transient, and dephosphorylation occurred rapidly in slices from RCS knock-out mice (Fig. 3B).

Application of D_2 receptor agonists activates PP2B and leads to dephosphorylation of Thr^{34} of DARPP-32 (*11*). Treatment

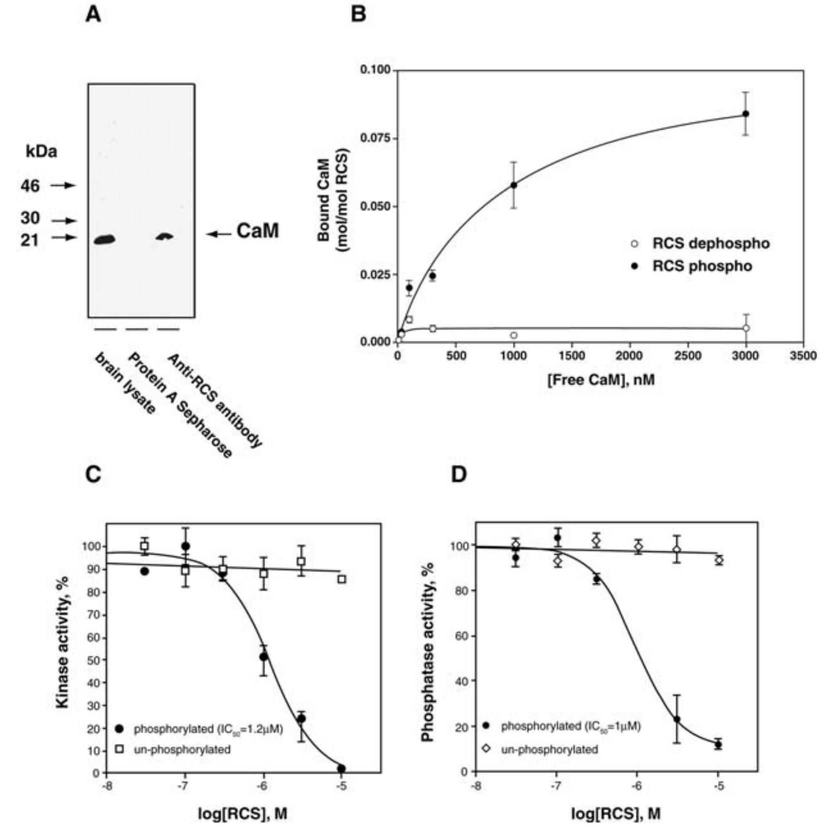

Fig. 1. Phosphorylation-dependent interaction of RCS and CaM. (**A**) Co-immunoprecipitation of CaM using an antibody against RCS. Striatal extract (lane 1 shows CaM in 10 μg lysate) was incubated without (lane 2) or with (lane 3) rabbit polyclonal antibody against RCS followed by protein A Sepharose beads. Co-immunoprecipitated proteins were separated by SDS–polyacrylamide gel electrophoresis and immunoblotted with the use of mouse antibody against CaM. (**B**) Binding of CaM to phospho- and dephospho-RCS. Increasing concentrations of CaM were incubated with either dephospho-GST-RCS or phospho-Ser^{55}-GST-RCS (90% phosphorylated). Results shown are means ± SEM from three independent experiments. Phosphorylated RCS inhibits CaMKI (**C**) and PP2B (**D**). Increasing concentrations of unphosphorylated RCS or RCS phosphorylated by PKA (90% phosphorylated) were incubated with CaM, either CaMKI or PP2B, and the respective substrate. Data represent means ± SEM of three independent experiments.

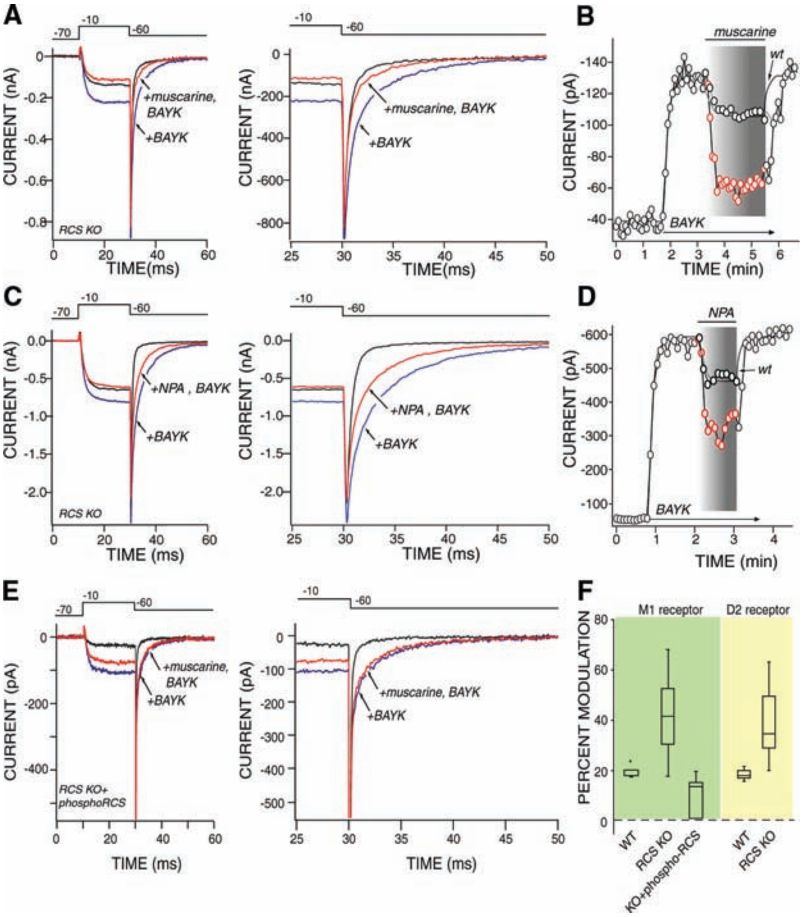

Fig. 2. Knock-out of RCS increases modulation of L-type calcium currents by GPCRs. [(A), (C), and (E)] Current traces from dorsal striatal medium spiny neurons. (Left) The complete trace throughout the voltage step protocol; (right) currents during the repolarizing step. (**A**) Neuron from an RCS knock-out mouse. Control current (black) and tail currents elicited in the presence of 1 μM S(–)-BAY K 8644 (BayK), either alone (blue) or with 2 μM (+)-muscarine chloride (red). (**B**) Time course of current isolated from cell in (A). Muscarine inhibited L-type current by 55% 5 ms after initiation of the repolarization. The black trace shows the normalized time course from a typical wild-type (wt) dorsal striatal medium spiny neuron in which median inhibition of current by 2 μM muscarine was 20%. (**C**) Neuron from an RCS knock-out mouse. Control current (black) and tail currents elicited in the presence of 1 μM BayK, either alone (blue) or with 10 μM R(–)-propylnorapomorphine hydrochloride (red). (**D**) Time course of current isolated from cell in (C). NPA inhibited L-type current by 44%. The black trace represents the normalized time course from a typical wild-type neuron, in which median inhibition of current by 10 μM NPA in wild-type neurons was 18%. (**E**) Neuron from an RCS knock-out mouse dialyzed with 20 μM thio-phospho-RCS. Control current (black) and tail currents elicited in the presence of 1 μM BayK, either alone (blue) or with 2 μM muscarine (red). (**F**) Box plot (green) illustrates differences in percent inhibition by M_1 receptor activation of L-type current in medium spiny neurons from wild-type mice (n = 5 and median of 20%), RCS knock-out (KO) mice (n = 8 and median of 41%, $P < 0.02$, compared to wild-type, Kruskal Wallis test) and RCS knock-out mice dialyzed with thio-phospho-RCS (n = 5 and median of 13%, $P < 0.01$ compared with RCS knock-out mice). Box plot (yellow) illustrates differences in percent inhibition by D_2 receptor activation of L-type current in medium spiny neurons from wild-type mice (n = 3 and median of 18%) and RCS knock-out mice (n = 6 and median of 34%, $P < 0.05$).

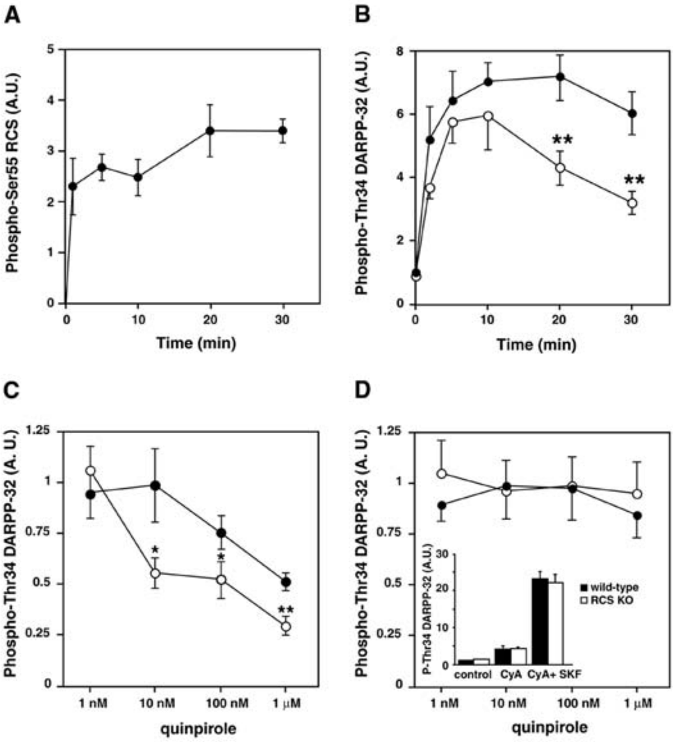

Fig. 3. PP2B-dependent dephosphorylation of DARPP-32 in striatal neurons from wild-type and RCS knock-out mice. (**A**) Effect of SKF81297 (1 μM) on RCS Ser^{55} phosphorylation in neostriatal slices. The levels of phospho-Ser^{55} RCS were analyzed by immunoblotting, and results were normalized to values obtained with untreated slices from wild-type mice. Data represent means ± SEM for five experiments. A.U., arbitrary units. (**B**) Effect of D1 receptor agonist on DARPP-32 Thr^{34} phosphorylation in neostriatal slices. Slices from wild-type mice (solid) or RCS knock-out mice (open) were incubated with SKF81297 (1 μM) for the indicated times. Data were normalized to values obtained with untreated slices from wild-type mice and represent means ± SEM for 13 experiments. $^{**}P < 0.01$ compared with wild-type mice; two-way analysis of variance (ANOVA) followed by Bonferroni posthoc test. (**C**) Effect of D2 receptor agonist on dephosphorylation of DARPP-32 Thr^{34} in neostriatal slices. Slices from wild-type mice (solid) or RCS knock-out mice (open) were incubated for a total of 10 min in the absence or presence of quinpirole (1 nM to 1 μM). SKF81297 (1 μM) was added after 5 min of incubation. Data were normalized to values obtained from slices treated with SKF81297 alone. The SKF81297-stimulated levels of phospho-Thr^{34} DARPP-32 were similar in slices from wild-type and RCS knock-out mice. Data represent means ± SEM for five to seven experiments. $^{*}P < 0.05$ and $^{**}P < 0.01$ compared with wild-type mice; Student's t test. (**D**) Effect of quinpirole on dephosphorylation of DARPP-32 Thr^{34}, using slices prepared from wild-type mice (solid), and RCS knock-out mice (open) was examined in the presence of the PP2B inhibitor cyclosporin A (CyA, 10 μM for 70 min). Data were normalized to values obtained from slices treated with CyA plus SKF81297. Data represent means ± SEM for four experiments. (Insert) Neostriatal slices prepared from wild-type mice (black) and RCS knock-out mice (white) were incubated with no drug (control), CyA (10 μM for 70 min), or CyA (10 μM for 70 min) plus SKF81297 (1 μM for last 5 min). Data were normalized to values obtained with untreated slices from wild-type mice. Data represent means ± SEM for four to five experiments. The effects of CyA and CyA plus SKF on DARPP-32 Thr^{34} phosphorylation were similar in slices from wild-type and RCS knock-out mice.

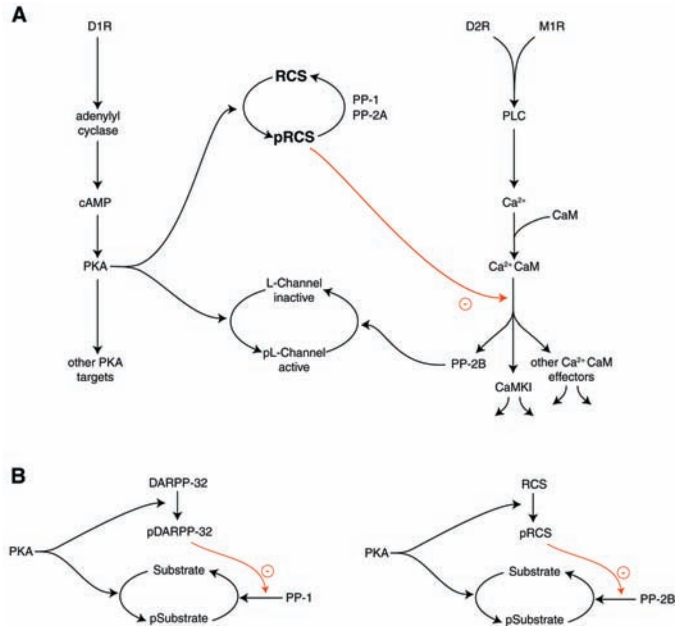

Fig. 4. Role of RCS in neuronal signaling. (**A**) Regulation by RCS of phosphorylation and dephosphorylation of PKA/PP2B substrates. Stimulation of dopamine D_1 receptors activates PKA. Stimulation of muscarinic M_1 and dopamine D_2 receptors mobilizes intracellular Ca^{2+} stores, resulting in stimulation of PP2B, which dephosphorylates a large number of substrates. Many proteins, including, for example, L-type channels (illustrated here) and DARPP-32, are substrates for both PKA and PP2B (*23*). RCS regulates the state of phosphorylation of this major class of substrates. The phosphorylated form of RCS inhibits the activation by free Ca^{2+}/CaM of PP2B (red arrow) and other Ca^{2+}/CaM effectors that are likely to include CaM kinases, CaM-dependent phosphodiesterase, and adenylyl cyclase (not shown in the figure). [Effects dependent upon bound CaM, like Ca^{2+}-dependent inactivation of Ca^{2+} channels (*24*, *25*), are less likely to be affected by phosphorylation of soluble RCS.] As shown in the figure, phosphorylation of RCS amplifies the effects of PKA by turning off the dephosphorylation of these PKA substrates by PP2B. Conversely, dephosphorylation of RCS by PP1 and PP2A (*14*), through activation of PP2B, promotes Ca^{2+}/CaM signaling with a consequent dampening of PKA signal transduction pathways. Thus, the state of phosphorylation of RCS may regulate the balance between adenylyl cyclase–mediated versus PP2B-mediated GPCR signaling pathways. (**B**) Parallel roles of DARPP-32 and RCS in regulation of signal transduction. The efficacy of phosphorylation by PKA of numerous PKA/PP1 substrates is increased by PKA phosphorylation of DARPP-32, which inhibits PP1 (*23*). In an analogous manner, the efficacy of phosphorylation by PKA of numerous PKA/PP2B substrates is increased by PKA phosphorylation of RCS, which inhibits PP2B. Thus, parallel signal transduction mechanisms have evolved, with the use of DARPP-32 and RCS, to amplify PKA phosphorylation of two major and distinct classes of substrates.

of neostriatal slices from wild-type mice with the D_2 receptor agonist quinpirole resulted in a dose-dependent decrease in phosphorylation of Thr^{34} of DARPP-32 (Fig. 3C). The effect of quinpirole was greater in slices from RCS knock-out mice. Half-maximal inhibition of phosphorylation required 1 μM quinpirole in slices from wild-type mice but 10 nM in slices from RCS-knock-out mice. The effect of quinpirole was abolished when slices from either wild-type or RCS knock-out mice were pretreated with cyclosporin A (10 μM), a specific PP2B inhibitor (Fig. 3D).

The present study indicates that RCS plays a central role in integration of key neurotransmitter inputs into medium spiny neurons, placing it in a potentially pivotal position to regulate striatal function in health and disease through binding to CaM and affecting the activation of multiple CaM targets. For example, RCS levels are reduced in a presymptomatic transgenic mouse model of Huntington's disease (*12*). CaM is known to regulate transglutaminase-mediated cross-linking of the huntingtin protein (*13*), a process that would be increased in the absence of the inhibitory actions of phospho-RCS. Administration of methamphetamine or cocaine results in an increased phosphorylation of RCS (*14*), suggesting that RCS-mediated suppression of CaM signaling may be an important mechanism underlying the effects of psychomotor stimulants. Alterations in RCS regulation of CaM and PP2B also may be an important contributing factor in the pathogenesis of schizophrenia, where there are clear dopaminergic determinants (*15*, *16*). Lastly, RCS is positioned to arbitrate the interaction between cholinergic and dopaminergic signaling. The balance between these two transmitters is critical for normal striatal function. In Parkinson's disease, the loss of striatal dopamine and the concomitant elevation of cholinergic tone is thought to be responsible for the emergence of bradykinesia, rigidity, and tremor (*17–19*). Our work demonstrates that RCS plays a central role in determining the physiological impact of acetylcholine on the principal neurons of the striatum and shows how this regulation should change with dopamine depletion (*20–22*). The identification of RCS and the determination of its importance in striatal physiology creates a therapeutic entry point for diseases of the basal ganglia.

By binding CaM and inhibiting PP2B, phospho-RCS has the ability to amplify signaling mediated by D_1 dopamine receptors and other PKA-mediated GPCRs and to attenuate signaling mediated by competing D_2 dopamine receptors, M1 muscarinic receptors, and other phospholipase C–activating GPCRs (Fig. 4A). The ability of phospho-RCS to inhibit PP2B is analogous to that of phospho-DARPP-32 to inhibit PP1 (Fig. 4B). Working in concert, these two signal transduction mechanisms serve to amplify the cellular consequences of PKA activation in medium spiny neurons.

References and Notes

1. C. C. Ouimet, H. C. Hemmings Jr., P. Greengard, *J. Neurosci.* **9**, 865 (1989).
2. S. Brene *et al.*, *J. Neurosci.* **14**, 985 (1994).
3. J. Kisielow, A. C. Nairn, K. Karjalainen, *Eur. J. Immunol.* **31**, 1141 (2001).
4. H. C. Hemmings Jr., J. A. Girault, K. R. Williams, M. B. LoPresti, P. Greengard, *J. Biol. Chem.* **264**, 7726 (1989).
5. J. A. Girault, S. I. Walaas, H. C. Hemmings Jr., P. Greengard, *Neuroscience* **37**, 317 (1990).
6. A. Persechini, P. M. Stemmer, *Trends Cardiovasc. Med.* **12**, 32 (2002).
7. D. J. Black, Q.-K. Tran, A. Persechini, *Cell Calcium* **35**, 415 (2004).
8. S. V. Rakhilin *et al.*, unpublished data.
9. A. R. Howe, D. J. Surmeier, *J. Neurosci.* **15**, 458 (1995).
10. S. Hernandez-Lopez *et al.*, *J. Neurosci.* **20**, 8987 (2000).
11. A. Nishi, G. L. Snyder, P. Greengard, *J. Neurosci.* **17**, 8147 (1997).
12. J. A. Bibb *et al.*, *Proc. Natl. Acad. Sci. U.S.A.* **97**, 6809 (2000).
13. G. M. Zainelli, C. A. Ross, J. C. Troncoso, J. K. Fitzgerald, N. A. Muma, *J. Neurosci.* **24**, 1954 (2004).
14. G. L. Caporaso *et al.*, *Neuropharmacology* **39**, 1637 (2000).
15. D. J. Gerber *et al.*, *Proc. Natl. Acad. Sci. U.S.A.* **100**, 8993 (2003).
16. T. Miyakawa *et al.*, *Proc. Natl. Acad. Sci. U.S.A.* **100**, 8987 (2003).
17. A. Barbeau, *Can. Med. Assoc. J.* **87**, 802 (1962).
18. R. C. Duvoisin, *Arch. Neurol.* **17**, 124 (1967).
19. O. Hornykiewicz, S. J. Kish, *Adv. Neurol.* **45**, 19 (1987).
20. V. Bernard, E. Normand, B. Bloch, *J. Neurosci.* **12**, 3591 (1992).
21. S. M. Hersch, C. A. Gutekunst, H. D. Rees, C. J. Heilman, A. I. Levey, *J. Neurosci.* **14**, 3351 (1994).
22. D. J. Surmeier, W. J. Song, Z. Yan, *J. Neurosci.* **16**, 6579 (1996).
23. P. Svenningsson *et al.*, *Annu. Rev. Pharmacol. Toxicol.* **44**, 269 (2004).
24. B. Z. Peterson *et al.*, *Neuron* **22**, 549 (1999).
25. J. Kim, S. Ghosh, D. A. Nunziato, G. S. Pitt, *Neuron* **41**, 745 (2004).
26. We thank P. Ingrassia, A. Horiuchi, F. Liu, and E. Griggs for technical support. Work described in this paper was supported by U.S. Public Health Service grants MH40899 and DA10044 (A.C.N. and P.G.) and NS34696 and DA12958 (D.J.S.), the Picower Foundation, the Peter Jay Sharp Foundation, and the Simons Foundation (P.G.), and a Grant-in-Aid for Scientific Research from the Japan Society for the Promotion of Science (A.N.). Molecular interaction data have been deposited in the Biomolecular Interaction Network Database with accession codes 169429 to 169431.

Supporting Online Material
www.sciencemag.org/cgi/content/full/306/5696/698/DC1
Materials and Methods
SOM Text
Figs. S1 to S3

5 May 2004; accepted 3 September 2004

Plant Cuticular Lipid Export Requires an ABC Transporter

Jamie A. Pighin,[1]* Huanquan Zheng,[1]* Laura J. Balakshin,[1]
Ian P. Goodman,[1] Tamara L. Western,[1] Reinhard Jetter,[1,2]
Ljerka Kunst,[1] A. Lacey Samuels[1]†

A waxy protective cuticle coats all primary aerial plant tissues. Its synthesis requires extensive export of lipids from epidermal cells to the plant surface. *Arabidopsis cer5* mutants had reduced stem cuticular wax loads and accumulated sheetlike inclusions in the cytoplasm of wax-secreting cells. These inclusions represented abnormal deposits of cuticular wax and resembled inclusions found in a human disorder caused by a defective peroxisomal adenosine triphosphate binding cassette (ABC) transporter. We found that the *CER5* gene encodes an ABC transporter localized in the plasma membrane of epidermal cells and conclude that it is required for wax export to the cuticle.

All primary aerial organs of land plants are covered with a waxy cuticle that is essential for their protection and interaction with the environment. The cuticle is composed of very-long-chain fatty acids and their derivatives, collectively termed cuticular wax, embedded within and encasing the cutin matrix (*1*). Cuticle synthesis requires extensive transport of lipids out of the epidermal cells to the plant surface. The mechanism of export of the cuticular lipids is unknown.

To identify mutants defective in lipid transport to the cuticle, we examined a collection of *Arabidopsis thaliana eceriferum* (or *cer*) lines for changes in wax-secreting epidermal cells by transmission electron microscopy (TEM). *Cer* mutants have a glossy, bright green stem phenotype because of a reduction or altered composition of cuticular wax (*2*). TEM study (*3*) of the stem epidermis of the *cer5* mutant revealed an unusual cellular phenotype. Similar to the wild type, *cer5* cells were entirely filled with a central vacuole with the cytoplasm present in a thin rim around the edge of the cell (Fig. 1A), but they also contained large protrusions of cytoplasm into the vacuole (Fig. 1B). Within these protrusions, loose bundles of linear inclusions, distinct from the endoplasmic reticulum, Golgi, and cytoskeletal elements, were found (Fig. 1C). These inclusions were found only in the epidermis; they were never observed in other cell types. Morphologically similar trilamellar inclusions had been described in the cells of patients with X-linked adrenoleukodystrophy (ALD), a neurodegenerative disease caused by a defect in an ABC transporter involved in transport of saturated very-long-chain fatty acids into the peroxisome for β-oxidation (*4*).

The *cer5* stem epidermis was further examined by cryo–scanning electron microscopy (SEM) (Fig. 1D) (*3*). The stem surface was sparsely covered with epicuticular wax crystals, consistent with reports that the wax load on *cer5* stems is merely reduced, not eliminated (*5*). The *cer5* epidermal cells contained large sheetlike structures, which corresponded in size and arrangement with the rod-shaped inclusion profiles seen in TEM sections (Fig. 1, E and F). Nile red staining and examination by light microscopy demonstrated that these inclusions were lipidic in nature (fig. S1).

Morphological similarities between the *cer5* inclusions and those found in ALD cells raised the question of whether both structures had similar composition. Because the *cer5* inclusions could not be prepared selectively, we inferred their composition from comparisons between isolated epidermal cells with and without inclusions (*3*). The total fatty acid profiles of *cer5* and wild-type epidermal peels did not differ significantly. Thus, it is unlikely that the *cer5* inclusions consist of fatty acids, distinguishing them from the corresponding structures in ALD cells.

When cuticular wax components were quantified (*3*), wild-type plants showed a wax load of 0.24 μg/mm^2, whereas the mutant had only 0.11 μg/mm^2 of wax (Fig. 2A). The amounts of all wax components (e.g., alkanes, ketones, and primary and secondary alcohols) on the *cer5* surface were significantly reduced (Fig. 2B). In contrast, the amounts of total epidermal wax (surface plus intracellular) extracted from isolated epidermal peels of wild type (0.31 μg/mm^2) and *cer5* (0.28 μg/mm^2), did not differ significantly. Thus, wax biosynthesis was not compromised in *cer5*, but wax components were retained within epidermal cells.

To determine the molecular basis of the *cer5* defect, we isolated the *CER5* gene by using a combination of positional cloning and insertional mutagenesis (*3*). Complementation of the *cer5* mutant with the wild-type *CER5* gene (At1g51500) rescued the wax-deficient phenotype (Fig. 2A). Thus, *CER5* is the At1g51500 gene encoding an ABC transporter. During cloning, we identified an additional allele of *CER5* in the Salk transfer-DNA (T-DNA) insertional mutation collection (Salk 036776) (Fig. 2A). We designated the original mutant allele *cer5-1* and the Salk 036776 allele *cer5-2*. Sequencing of the At1g51500 gene in *cer5-1* identified a point

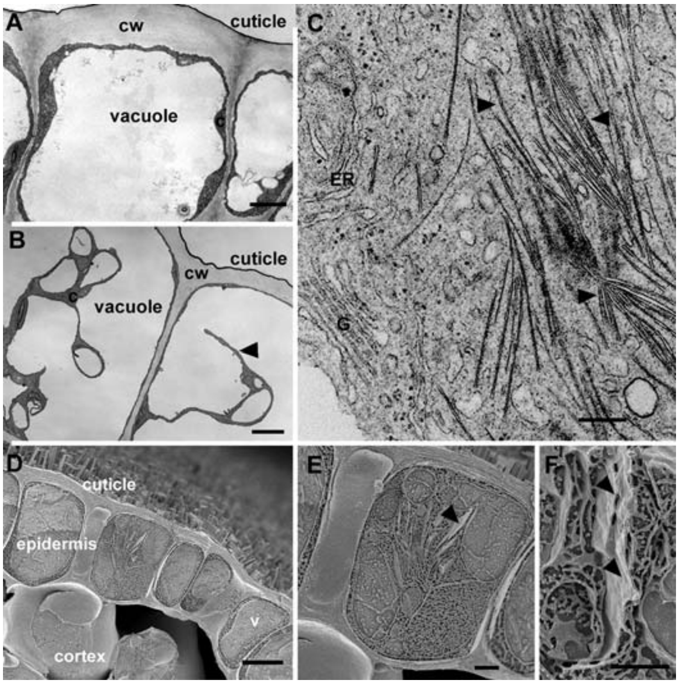

Fig. 1. Epidermal wax-secreting cells of *Arabidopsis* stems in transverse section. (**A**) Wild-type cells. c indicates cytoplasm; cw, cell wall. Scale bar, 2 μm. (**B**) *cer5* cells with intrusions of cytoplasm in vacuoles (arrowhead). Scale bar, 2 μm. (**C**) *cer5* cytoplasm contains unusual linear inclusions (arrowheads). ER, endoplasmic reticulum; G, Golgi. Scale bar, 200 nm. (**D**) Cryo-SEM of *cer5* epidermis, covered with cuticle. Scale bar, 5 μm. (**E**) *cer5* epidermal cell with inclusions (arrow). Scale bar, 2 μm. (**F**) High-magnification view showing sheetlike nature of inclusions. Scale bar, 2 μm.

---

[1]Department of Botany, University of British Columbia (UBC), 6270 University Boulevard, Vancouver, BC V6T 1Z4, Canada. [2]Department of Chemistry, UBC, 2036 Main Mall, Vancouver, BC V6T 1Z1, Canada.

*These authors contributed equally to this work.

†To whom correspondence should be addressed. E-mail: lsamuels@interchange.ubc.ca

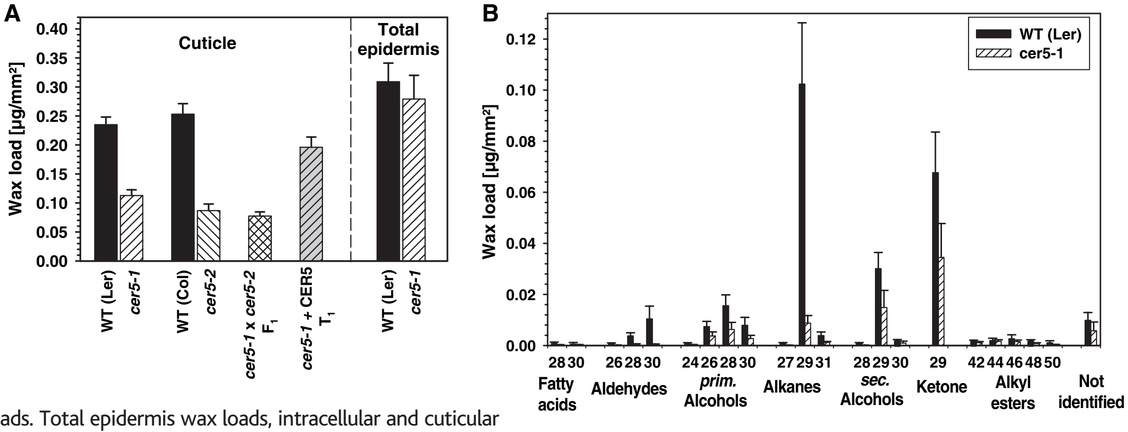

Fig. 2. Wax analyses of *Arabidopsis* stem surface (cuticle) or epidermal peel extracts (total epidermis). (**A**) Cuticular wax loads of WT ecotypes are significantly different from the corresponding mutants: Landsberg *erecta* (Ler) vs. *cer5-1*; Columbia-2 (Col) vs. *cer5-2* (*t* test, $P = 0.05$). F_1 progeny of a *cer5-1* and *cer5-2* cross had a reduced wax load similar to both parents. *Cer5-1* plants, complemented with the At1g51500 gene, showed significantly increased wax loads. Total epidermis wax loads, intracellular and cuticular (right), are not significantly different in WT and *cer5-1*. (**B**) Cuticular wax analysis, including chain lengths of aliphatic compounds, revealed reductions of all major wax components of *cer5-1* (Error bars represent means ± SE).

mutation that, in the predicted CER5 protein, would cause the replacement of a glycine with an aspartate within the consensus ABC C motif (*6*) (fig. S2). The T-DNA insertion in the *cer5-2* allele was located in an exon encoding the region after the predicted fifth transmembrane domain of the CER5 protein. We examined *CER5* transcript levels in the *cer5* mutants to determine the extent of gene disruption in each line. Whereas the abundance of the *CER5* transcript in *cer5-1* was comparable to the wild type, no transcript could be detected in *cer5-2*, indicating that it is a transcriptional knockout (fig. S3).

Analysis of the predicted CER5 protein sequence revealed the presence of the characteristic ABC transporter domains near the N terminus, including the Walker A and B boxes and C motif for nucleotide binding and six transmembrane domains (TMD) near the C terminus (fig. S2). When compared with prototype ABC transporters, which have the TMD near the N terminus followed by the ABC domain, the ABC-TMD orientation found in CER5 would be considered a reverse arrangement. Known ABC transporters consist of two (ABC-TMD) units (*7*) either within one polypeptide or as two "half-transporters" making up homo- or heterodimers. *CER5* sequence predicts that it would encode a half-transporter, so presumably CER5 would require dimerization to function.

The *CER5* sequence has been designated WBC12, a member of the *white-brown complex* subfamily, in an analysis of the 129 putative ABC transporters of the *Arabidopsis* genome (*8*). This is the largest subfamily of ABC transporters in *Arabidopsis*, and, although some have been cloned (*9*), CER5 is the only member of the subfamily that has been characterized functionally. Two other putative *Arabidopsis* ABC transporters have high similarity to CER5, At3g21090 (WBC 15) and At1g51460 (WBC 13) (*10*). Furthermore, there is similarity to two human ABC transporters from the WBC/ABCG subfamily: breast cancer resistance protein and a placental ABCG2, which are localized to the plasma membrane (*11*) and believed to function in lipid and xenobiotic export (*12*). The simplest hypothesis is that CER5, like other WBC subfamily members, acts as a primary transporter of lipids. However, it cannot be ruled out that it acts indirectly by regulating the activities of other transporters.

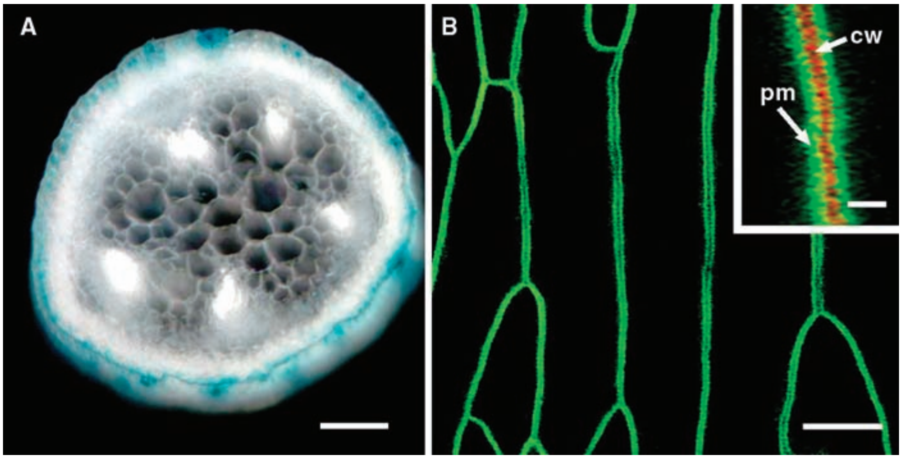

Fig. 3. Expression of CER5 in the plasma membrane of the stem epidermis. (**A**) *CER5* promoter directed epidermis-specific expression of GUS in stem. Scale bar, 100 µm. (**B**) GFP-CER5 fusion protein was localized to the plasma membrane (pm) of epidermal cells. Scale bar, 10 µm. (Inset) High magnification of GFP-CER5 expressing cells labeled with propidium iodide, which stains the cell wall red between adjacent GFP-labeled plasma membranes. Scale bar, 1 µm.

CER5 was expressed exclusively in the epidermal cells, as shown by GUS activity assays in plants transformed with the *CER5* promoter::*GUS* construct (Fig. 3A) (*3*). *CER5* transcript was found in all examined plant organs, including stems, leaves, siliques, flowers, and roots (fig. S4). This was unexpected, because the *cer5* phenotype is only apparent in stems or detectable by gas chromatography in stems and leaves (85% of wild-type wax load) (*5*). It suggests that additional transporters must be involved in delivering wax components to the cuticle in other tissues.

To investigate the subcellular localization of CER5 in *Arabidopsis*, we introduced a *GFP-CER5* (where GFP indicates green fluorescent protein) construct driven by the native *CER5* promoter into *cer5-1* plants (*3*). The wild-type phenotype was restored in 42 of 43 transgenic plants expressing the GFP-CER5 fusion protein, indicating that the protein was fully functional. The GFP-tagged CER5 was localized in the plasma membrane of epidermal cells (Fig. 3B). When the cell wall was stained with propidium iodide, the GFP-CER5 plasma membrane fluorescence was clearly separated by the red propidium iodide signal (Fig. 3B, inset).

We identified the plasma membrane-localized ABC transporter, CER5, involved in wax export to the plant cuticle. CER5 must be an important component of the export machinery in the *Arabidopsis* stem, because disruption of this transporter results in striking accumulations of wax inside the epidermal cells. The absence of a detectable phenotype in tissues other than the stem and leaf and accumulation of residual surface wax on the stem of *cer5-2* knockout line suggest that additional wax export mechanisms must exist in plants. Chemical analysis of the mutant wax demonstrated that CER5, like many ABC transporters, has broad substrate specificity and is capable of transporting a variety of wax substrates. We conclude that in plants, as in other eukaryotes, proteins of the WBC/ABCG subfamily are key components of lipid transport systems.

References and Notes

1. L. Kunst, A. L. Samuels, *Prog. Lipid Res.* **42**, 51 (2003).
2. M. Koornneef, C. J. Hanhart, F. Thiel, *J. Hered.* **80**, 118 (1989).
3. Materials and methods are presented as supporting material on *Science* Online.
4. H. Powell, R. Tindall, P. Schultz, *Arch. Neurol.* **32**, 250 (1975).
5. A. M. Rashotte, M. A. Jenks, K. A. Feldmann, *Phytochemistry* **57**, 115 (2001).
6. ABC transporter motifs were predicted by PROSITE as referenced in (*13*).
7. M. Jasinski, E. Ducos, E. Martinoia, M. Boutry, *Plant Physiol.* **131**, 1169 (2003).
8. R. Sánchez-Fernández, T. G. E. Davies, J. O. D. Coleman, P. A. Rea, *J. Biol. Chem.* **276**, 30231 (2001).
9. C. T. Otsu *et al.*, *J. Exp. Bot.* **55**, 1643 (2004).
10. The analyses of R. Sánchez-Fernández *et al.* (*8*) agree with these relationships; however, they erroneously duplicated WBC15/WBC22 in their 2001 work. This was corrected in (*14*).
11. G. L. Scheffer *et al.*, *Cancer Res.* **60**, 2589 (2000).
12. J. W. Jonker *et al.*, *Proc. Natl. Acad. Sci. U.S.A.* **99**, 15649 (2002).
13. L. Falquet *et al.*, *Nucleic Acids Res.* **30**, 235 (2002).
14. P. A. Rea *et al.*, in *ABC Transporters from Bacteria to Man*, I. B. Holland, S. P. C. Cole, K. Kuchler, C. F. Higgins, Eds. (Academic Press, London, 2003), pp. 335–355.

15. Thanks to G. Haughn, M. Smith, T. Hooker, and O. Rowland for their insightful comments. The financial support of the Natural Sciences and Engineering Research Council of Canada, Canadian Foundation for Innovation, BC Knowledge Development Foundation, and the UBC Blusson fund are gratefully acknowledged. We thank the Salk Institute for Genomic Analysis Laboratory for providing sequence-indexed *Arabidopsis* T-DNA insertion mutants (project funded by NSF). The *CER5* gene has been submitted to Genbank, and the accession no. is AY734542.

Supporting Online Material

www.sciencemag.org/cgi/content/full/306/5696/702/DC1
Materials and Methods
Figs. S1 to S4

5 July 2004; accepted 3 September 2004

Oscillations in NF-κB Signaling Control the Dynamics of Gene Expression

D. E. Nelson,[1] A. E. C. Ihekwaba,[2] M. Elliott,[1] J. R. Johnson,[1] C. A. Gibney,[1] B. E. Foreman,[1] G. Nelson,[1] V. See,[1] C. A. Horton,[1] D. G. Spiller,[1] S. W. Edwards,[1] H. P. McDowell,[4] J. F. Unitt,[5] E. Sullivan,[6] R. Grimley,[7] N. Benson,[7] D. Broomhead,[3] D. B. Kell,[2] M. R. H. White[1]*

Signaling by the transcription factor nuclear factor kappa B (NF-κB) involves its release from inhibitor kappa B (IκB) in the cytosol, followed by translocation into the nucleus. NF-κB regulation of IκBα transcription represents a delayed negative feedback loop that drives oscillations in NF-κB translocation. Single-cell time-lapse imaging and computational modeling of NF-κB (RelA) localization showed asynchronous oscillations following cell stimulation that decreased in frequency with increased IκBα transcription. Transcription of target genes depended on oscillation persistence, involving cycles of RelA phosphorylation and dephosphorylation. The functional consequences of NF-κB signaling may thus depend on number, period, and amplitude of oscillations.

NF-κB is a family of dimeric transcription factors (usually RelA/p65:p50) that regulates cell division, apoptosis, and inflammation (*1*). NF-κB dimers are sequestered in the cytoplasm of unstimulated cells by binding to IκB proteins. NF-κB–activating stimuli activate the inhibitor kappa B kinase (IKK) signalosome that phosphorylates IκB [at Ser32 and Ser36 on IκBα (*2*)] and NF-κB [at Ser536 in RelA (*3*, *4*)]. Phosphorylated IκB proteins are then ubiquitinated and degraded by the proteasome, liberating NF-κB dimers to translocate to the nucleus and regulate target gene transcription.

IκBα is a transcriptional target for NF-κB (*5*), creating a negative feedback loop (Fig. 1A) in which its delayed expression gives the system similar characteristics to the circadian clock (*6*) and to ultradian oscillators such as p53 (*7*, *8*) and the segmentation clock (*8*, *9*). IκBα contains both nuclear localization and export sequences, enabling its nuclear-cytoplasmic (N-C) shuttling. Newly synthesized free IκBα binds to nuclear NF-κB, leading to export of the complex to the cytoplasm (*10*). This complex, but not free IκBα, is the target for IκBα phosphorylation by IKK (*11*, *12*).

Oscillations in the temporal response of NF-κB activity have been observed by electromobility shift assay (EMSA) only in studies of IκBβ and ε knockout mouse embryonic fibroblast cell populations and have been simulated in a computational model (*13*). In the absence of time-lapse single-cell analysis, it has remained unclear whether asynchronous single-cell oscillations occur in single cells following NF-κB stimulation (*8*, *14*). Like calcium signaling (*15*), NF-κB could be a complex dynamic oscillator using period and/or amplitude to regulate transcription of target genes.

We have used fluorescence imaging of NF-κB (RelA) and IκBα fluorescent fusion proteins (*11*, *16*) to study oscillations in RelA N-C localization (N-C oscillations) in HeLa (human cervical carcinoma) cells and SK-N-AS cells [human S-type neuroblastoma cells that have been associated with deregulated NF-κB signaling (*17*)]. In SK-N-AS cells expressing RelA fused at the C terminus to the red fluorescent protein DsRed (RelA-DsRed) and IκBα fused at the C terminus to the enhanced green fluorescent protein EGFP (IκBα-EGFP) (Fig. 1B and Fig. 2A), 96% showed an NF-κB nuclear translocation response to tumor necrosis factor alpha (TNFα) stimulation and 72% showed long-term N-C oscillations in RelA-DsRed localization. Oscillations with a typical period of ∼100 min continued for >20 hours after continuous TNFα stimulation, damping slowly. In transfected cells expressing RelA-DsRed and control EGFP (Fig. 2C), 97% responded and 91% of cells showed N-C oscillations. These oscillations appeared more synchronous between cells in the first three cycles

---

[1] Centre for Cell Imaging, School of Biological Sciences, Bioscience Research Building, Crown Street, Liverpool, L69 7ZB, UK. [2] Department of Chemistry, [3] Department of Mathematics, University of Manchester Institute of Science and Technology, P.O. Box 88, Sackville Street, Manchester, M60 1QD, UK. [4] Royal Liverpool Children's National Health Service Trust, Alder Hey Hospital, Eaton Road, Liverpool, L12 2AP, UK. [5] Molecular Biology Department, [6] Advanced Science and Technology Laboratory, AstraZeneca Research and Development Charnwood, Bakewell Road, Loughborough, Leicestershire, LE11 5RH, UK. [7] Pfizer Central Research, Ramsgate Road, Sandwich, Kent, CT13 9NJ, UK.

*To whom correspondence should be addressed. E-mail: mwhite@liv.ac.uk

compared with cells that also expressed IκBα-EGFP, which suggests that the system was sensitive to variation in IκBα levels, thus contributing to the degree of cell-to-cell asynchrony. When HeLa cells were continually stimulated with TNFα (Fig. 2D), 86% of the cells responded and 30% exhibited up to three detectable N-C oscillations that were markedly damped. However, when TNFα was added to SK-N-AS cells (Fig. 2B) or HeLa cells (Fig. 2E) as a 5-min pulse, a single peak of nuclear occupancy was observed with no subsequent cycles of RelA movement.

TNFα treatment induced endogenous RelA localization patterns in cells, consistent with increasingly asynchronous N-C oscillations (fig. S3). Western blot analysis (figs. S4 and S5) showed that SK-N-AS and HeLa cells continually treated with TNFα gave biphasic dynamics of total IκBα, phosphorylated IκBα (Ser32 phospho-IκBα), and phosphorylated RelA (Ser536 phospho-RelA). In HeLa cells, phosphoprotein expression levels diminished more rapidly than in the SK-N-AS cells (fig. S5). A 5-min TNFα pulse directed transient accumulation of Ser32 phospho-IκBα and Ser536 phospho-RelA (fig. S4B). These data support the hypothesis that loss of IKK activity (due to TNFα removal) results in loss of N-C oscillations and that dephosphorylation of RelA occurs rapidly without persistent IKK activity. When SK-N-AS cells were treated with an alternative stimulus, the topoisomerase II inhibitor etoposide (VP16), 37% of the cells responded and 24% showed N-C oscillations. Etoposide-induced N-C oscillations had lower amplitude than those induced by TNFα, peaking after 300 min and then diminishing (Fig. 2F). The IκBα and RelA phosphoprotein expression levels after etoposide treatment (fig. S4C) corresponded to the timing of N-C oscillations.

We investigated whether N-C oscillation persistence influenced the dynamics of NF-κB–regulated gene expression using real-time imaging of firefly luciferase activity (*18*) driven by a κB (5× consensus site) promoter. SK-N-AS cells exhibited stable luminescence for more than 25 hours in the continual presence of TNFα (Fig. 2G). HeLa cells showed a transient peak 10 hours after TNFα treatment that decayed by 20 hours (Fig. 2I). In SK-N-AS (Fig. 2H) or HeLa cells (Fig. 2J) treated with a 5-min TNFα pulse, a more transient peak of luminescence occurred after 5 hours, which decayed by 10 hours. Etoposide treatment of SK-N-AS cells elicited a lower luminescence signal, reaching a peak at ~15 hours after treatment (Fig. 2K). With each stimulus, the kinetics of NF-κB oscillations and maintenance of phosphoprotein levels appeared closely related to the kinetics of gene expression. Thus, persistent NF-κB oscillations appear to maintain NF-κB–dependent gene expression.

Analysis of successive peaks of RelA nuclear occupancy (figs. S13 and S14 and Fig. 3, E and F) showed that N-C oscillation damping and successive peak timing were highly reproducible, but because of phase differences, this was not apparent at the population level. However, the pattern of peak timing and amplitudes was different between HeLa and SK-N-AS cells. The expression of IκBα–EGFP affected the amplitude and peak timing of the N-C oscillations (fig. S14). To study the role of IκBα synthesis rate on N-C oscillations, the rate of NF-κB–regulated IκBα transcription was modulated. IκBα-EGFP expression was driven by the κB (5× consensus site) promoter and expressed in HeLa cells together with a fusion protein between RelA and the modified red fluorescent protein DsRed-Express (RelA-DsRed-Express). Continual TNFα stimulation elicited oscillations in IκBα-EGFP expression out of phase with the RelA N-C oscillations (Fig. 3, A and B). This caused a statistically significant delay in the timing of nuclear RelA peaks 1, 2, and 3 (Fig. 3F). The amplitude was also slightly reduced for peaks 2 and 3 in the presence of the κB-IκBα-EGFP expression vector (Fig. 3E).

To investigate parameters affecting the oscillation dynamics, we used a computational model (*13*) that predicted NF-κB oscillations with a similar period and damping as those observed here. From this model, we noted that changes in just two molecular species (variables), free IKK and IκBα, were intimately coupled to the oscillation dynamics of nuclear NF-κB (fig. S16). Transfection with the κB-IκBα-EGFP expression vector (Fig. 3, A, B, E, and F) was equivalent to increasing the rate of NF-κB–dependent IκBα transcription; thus, we chose to study the effect of this parameter in the model (reaction 28 in table S1; Fig. 3, C and D; and fig. S17).

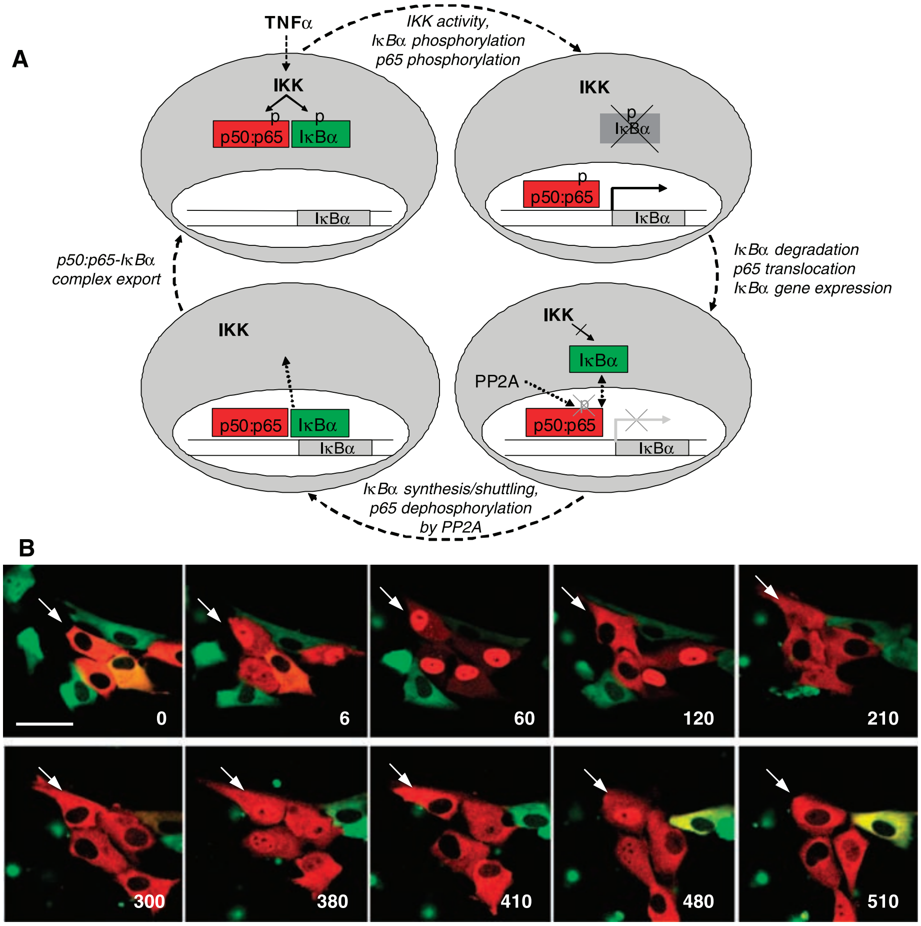

Fig. 1. Oscillations in NF-κB localization. (**A**) Schematic diagram illustrating the potential mechanism for repeated oscillations in NF-κB (p65/RelA) N-C localization. (**B**) Time-lapse confocal images of SK-N-AS cells expressing RelA-DsRed (red) and IκBα-EGFP (green) showing single-cell asynchronous N:C oscillations in RelA-DsRed localization after stimulation with 10 ng/ml TNFα. The arrow marks one oscillating cell. Times, min; scale bar, 50 μm.

Fig. 2. Analysis of the dynamics of NF-κB localization and κB-dependent reporter gene expression. (**A** to **F**) Time course of N:C localization of RelA-DsRed in cells co-expressing IκBα-EGFP [(A), (B), (D), (E), and (F)] or EGFP control (C). N:C ratio in RelA-DsRed fluorescence was normalized to highest peak intensity. The peak N:C ratio was expressed as the average value for each set of four cells. Data from each cell is represented by a different colored line. (**G** to **K**) Luminescence imaging (RLU, relative light units) of the dynamics of κB-dependent luciferase reporter activity represented as a different colored line for each of four different cells. The black line represents the average of the cells. [(A), (C), and (G)] SK-N-AS cells treated with continual 10 ng/ml TNFα. [(D) and (I)] HeLa cells treated with continual 10 ng/ml TNFα. [(B) and (H)] SK-N-AS cells treated with a 5-min TNFα pulse. [(E) and (J)] HeLa cells treated with a 5-min TNFα pulse. [(F) and (K)] SK-N-AS cells treated with 20 μM of etoposide. The black bar above each graph is a representation of the duration of TNFα treatment. For images of data in [(B) to (F)], (G), and (I), see figs. S6 to S11.

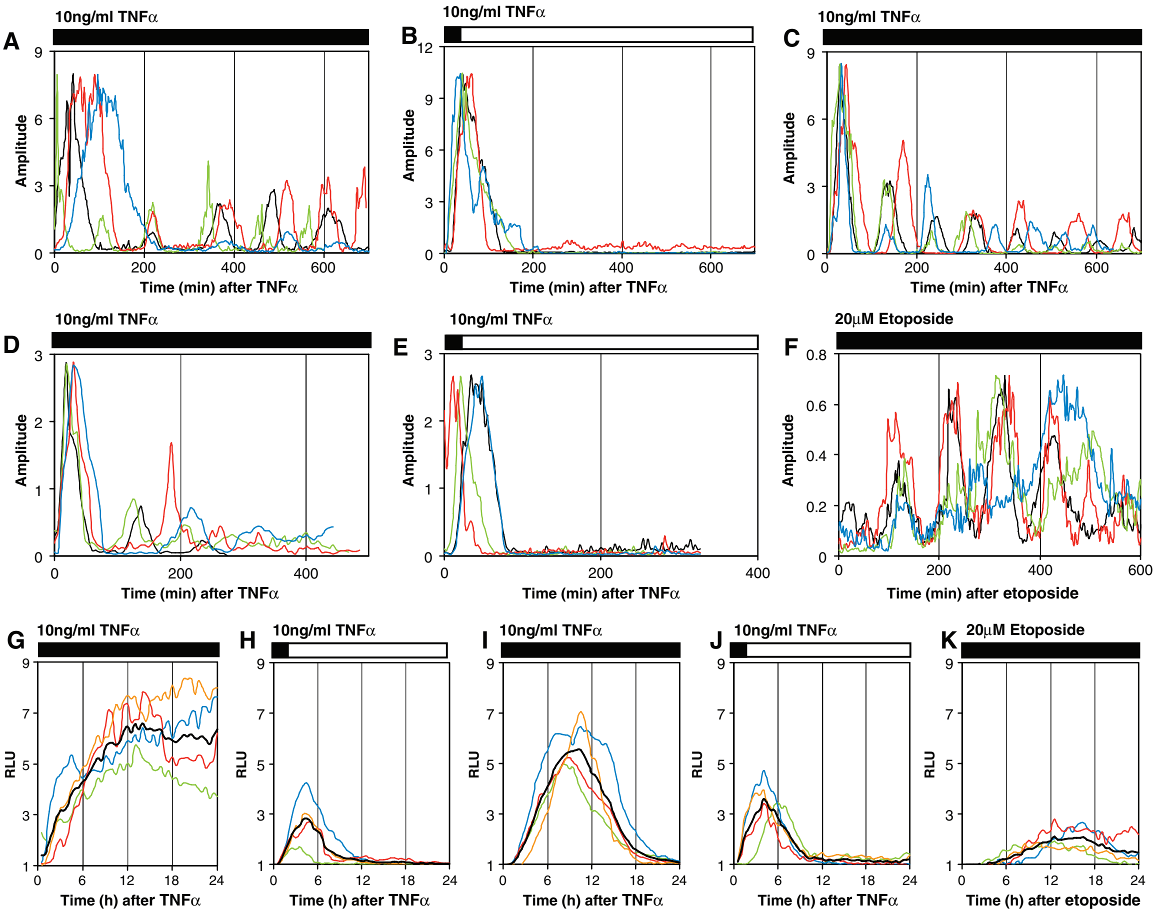

See (*19*) for analysis of some other related parameters (figs. S18 and S19). As the rate of this reaction was increased, there was a delay in simulated peaks 2 and onward (Fig. 3, C, D, and G). Thus, the computational analysis showed the effects of this reaction rate to be similar to those seen in the experimental studies. One discrepancy between the computational model and the experimental data was the unpredicted delay in experimentally observed peak 1 caused by κB-IκBα-EGFP transfection (Fig. 3, F and G). It is unclear how the two cell types studied differ with respect to the values of the parameters used in the model. Given that the oscillations are naturally asynchronous between cells and that this might be associated with varying levels of IκB proteins (*13*) or a lack of optimization of the pre-equilibration step in the model, this may explain why the timing of peak 1 was imperfectly predicted.

The amplitude of oscillations in IκBα-EGFP when expressed under the control of the κB promoter was not directly related to the amplitude of the preceding peak in RelA nuclear localization. In many HeLa cells, peak 2 or 3 in RelA localization was small in amplitude (Fig. 3B) compared with peak 1 (and would not have been observed in asynchronous populations). Nevertheless, these oscillations led to easily observable IκBα-EGFP responses. Thus, persistence of NF-κB oscillations maintains NF-κB–dependent transcription. However, NF-κB translocation cannot be the only factor regulating transcriptional activation (a property of the whole system), and further NF-κB activating and inactivating reactions, including modifications of RelA by phosphorylation (*3*, *4*, *20*), acetylation (*21*), or prolyl isomerization/targeted degradation (*22*), have also been described. The cessation of NF-κB–dependent transcription in the nucleus, independent of nuclear export (*11*), might occur as a consequence of RelA inactivation. Thus, NF-κB oscillations could repeatedly deliver newly activated NF-κB into the nucleus, maintaining a high nuclear ratio of active:inactive NF-κB. To investigate this hypothesis, we used the CRM1-dependent nuclear export inhibitor leptomycin B (LMB) to trap RelA in the nucleus of SK-N-AS cells (Fig. 4, A and B). This resulted in transitory κB-dependent luciferase reporter gene expression (*11*) that peaked after ~5 hours (Fig. 4C). Western blot analysis indicated a transient increase in Ser32 phospho-IκBα expression after 5 min, with no subsequent recovery (Fig. 4E). Ser536 phospho-RelA expression was maximal at 5 min after stimulation and decayed to the threshold of detection by 180 min (in contrast to cells treated with constant TNFα, Fig. 4D). These data support the hypothesis (*23*) that rapid dephosphorylation of NF-κB in the nucleus [by PP2A activity (*24*)] may be a key factor in the switch-off of NF-κB–dependent gene expression.

We propose that oscillations in NF-κB localization coupled to cycles of RelA and IκBα phosphorylation maintain NF-κB–dependent gene expression. Calcium spikes at intervals as long as 30 min have been shown to maintain NF-κB activity in T cells (*25*). The decoding of this [Ca^{2+}] spike frequency might be related to the observed kinetics of oscillatory transcription factor shuttling and regulation (*26*). Specific, non-

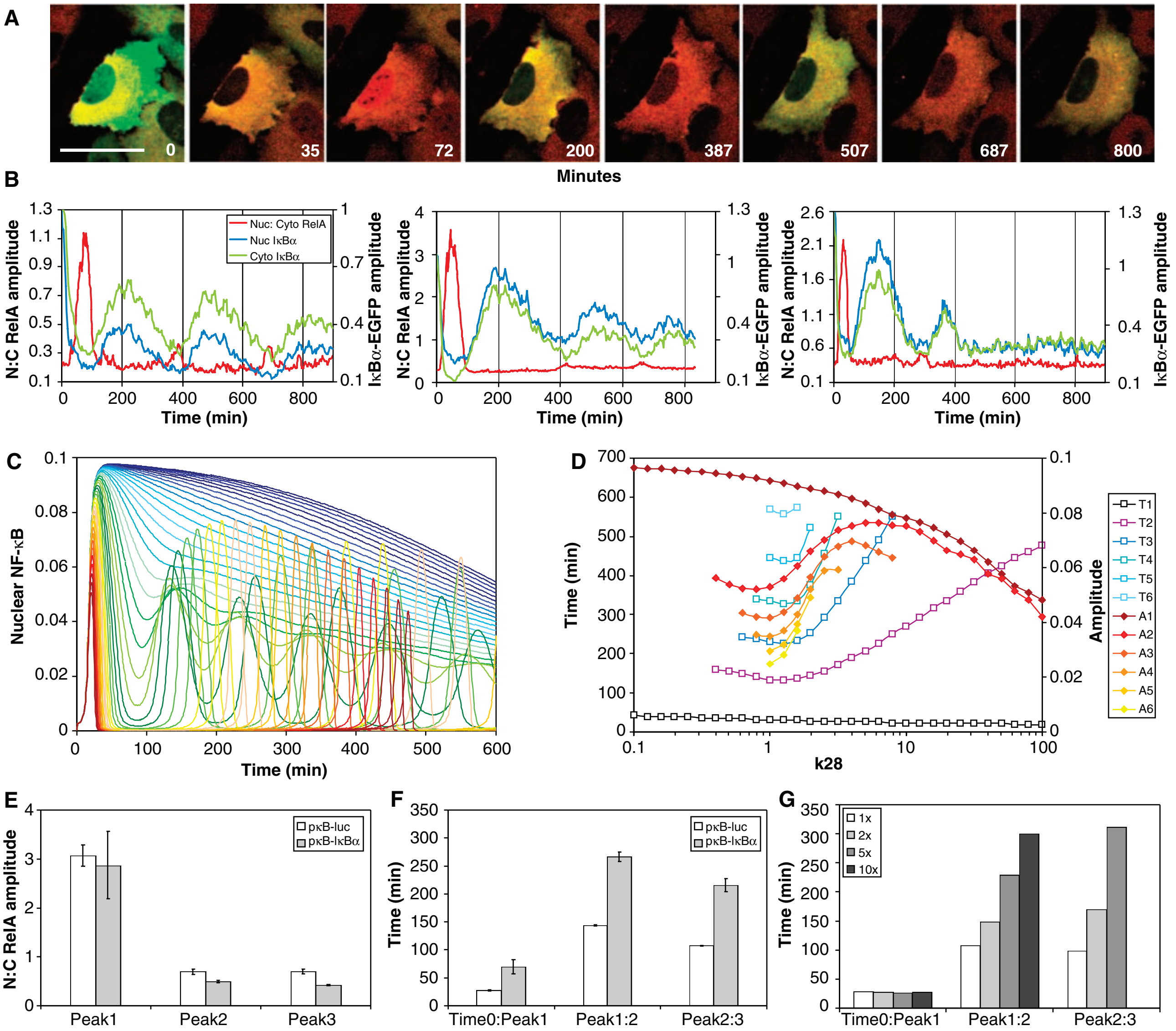

Fig. 3. NF-κB–directed oscillations in IκBα expression. Experimental and computational analysis of factors affecting the amplitude and period of oscillations. (A, B, E, and F) HeLa cells were transfected to express RelA-DsRed-Express and IκBα-EGFP under the control of either the consensus κB promoter or a control κB promoter vector. Cells were stimulated with continual 10 ng/ml TNFα. (**A**) Confocal time course of one typical cell showing oscillations in both RelA-DsRed-Express (red) localization and IκBα-EGFP (green) expression. Scale bar, 50 μm. (**B**) Analysis of three typical cells showing RelA-DsRed-Express N:C ratio and cytoplasmic and nuclear IκBα-EGFP levels. (**C**) The simulated time-dependent nuclear localization of NF-κB for successively increasing the NF-κB–regulated IκBα transcription rate constant by two orders of magnitude on either side of the standard rate constant (reaction 28 in the computational model, table S1) is shown by 41 lines changing in regularly increasing log intervals from blue to green to yellow to red (scanned after equilibration). (**D**) The peak amplitudes (A1 to A6) and timings (T1 to T6) of the first six simulated peaks for different rate constant values for NF-κB regulated IκBα transcription [as determined from data in (C)]. (**E**) Experimentally determined relative amplitude (N:C ratio) of successive RelA-DsRed-Express oscillations in HeLa cells continually stimulated with TNFα. Peak 1 set to 100%; subsequent peaks show relative amplitude ±SEM). (**F**) Average timing between successive peaks (±SEM) of successive N-C oscillations in RelA-DsRed-Express. (**G**) Simulated peak timings for 1x, 2x, 5x, and 10x standard reaction rate constant for NF-κB–regulated IκBα transcription (reaction 28 in computational model, table S1). The parameter was changed before the equilibration period.

linear "network motifs" can decode frequencies rather than amplitudes (*27*). Therefore, the signal-processing elements of the NF-κB signaling pathway, and its interaction with other dynamic signaling systems, may involve the encoding and decoding of specific time-varying signals. Such temporal encoding could avoid undesirable cross talk between cellular signaling pathways that share common components. Furthermore, oscillatory phosphorylation of RelA at Ser536 appears to be a consequence of its shuttling between the cytoplasm and the nucleus. Oscillatory modifications at other regulatory amino acids in RelA (*21*, *28*) might also occur as a consequence of N-C oscillations, whereas changes in N-C oscillation frequency and persistence might explain differential regulation of cell fate in response to different stimuli. Thus, in common, and perhaps in combination, with other oscillatory transcription factor pathways such as p53 (*7*, *8*), NF-κB may constitute a complex analog-to-digital coding system that regulates cell fate.

References and Notes

1. S. Ghosh, M. J. May, E. B. Kopp, *Annu. Rev. Immunol.* **16**, 225 (1998).
2. J. A. DiDonato, M. Hayakawa, D. M. Rothwarf, E. Zandi, M. Karin, *Nature* **388**, 548 (1997).

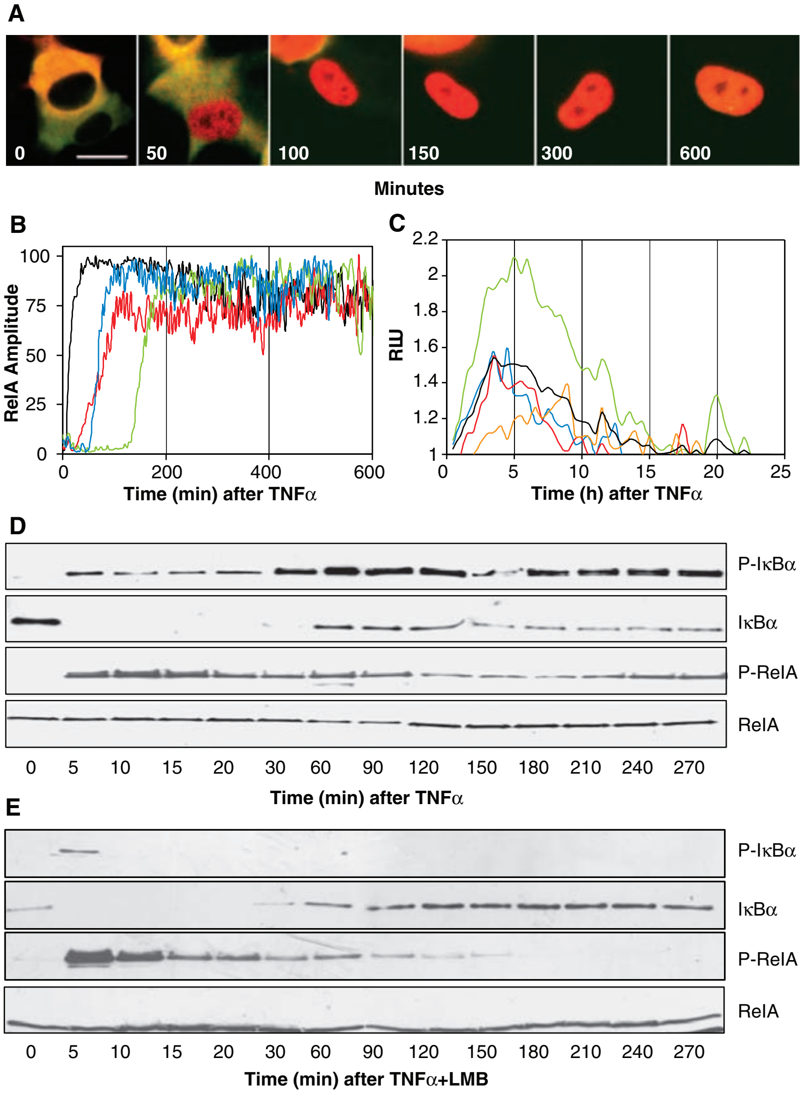

Fig. 4. Effect of nuclear export inhibition on the dynamics of RelA localization, κB-dependent reporter gene expression, and NF-κB phosphoprotein expression. SK-N-AS cells were treated with continuous 10 ng/ml TNFα and 10 ng/ml LMB (unless stated). (**A**) Time-lapse confocal images of RelA-EGFP localization. (**B**) Time course of RelA-EGFP localization expressed as N:C fluorescence ratio (each colored line represents data from one of four single cells). (**C**) κB-dependent luciferase reporter gene expression (each colored line represents data from one of four single cells, and the black line represents the average). (**D**) Western blot analysis of Ser32 phospho-IκBα (P-IκBα), total IκBα (IκBα), Ser536 phospho-RelA (P-RelA), and total RelA (RelA) protein levels in SK-N-AS cells stimulated with continual 10 ng/ml TNFα for the indicated times before analysis. (**E**) Western blot analysis of SK-N-AS cells stimulated with continual 10 ng/ml TNFα and 18 nM LMB for the indicated times before analysis.

3. H. Sakurai, H. Chiba, H. Miyoshi, T. Sugita, W. Toriumi, *J. Biol. Chem.* **274**, 30353 (1999).
4. X. Jiang, N. Takahashi, N. Matsui, T. Tetsuka, T. Okamoto, *J. Biol. Chem.* **278**, 919 (2003).
5. S. C. Sun, P. A. Ganchi, D. W. Ballard, W. C. Greene, *Science* **259**, 1912 (1993).
6. M. W. Young, S. A. Kay, *Nature Rev. Genet.* **2**, 702 (2001).
7. G. Lahav *et al.*, *Nature Genet.* **36**, 147 (2004).
8. N. A. Monk, *Curr. Biol.* **13**, 1409 (2003).
9. O. Pourquié, *Science* **301**, 328 (2003).
10. F. Arenzana-Seisdedos *et al.*, *Mol. Cell. Biol.* **15**, 2689 (1995).
11. G. Nelson *et al.*, *J. Cell Sci.* **115**, 1137 (2002).
12. E. Zandi, Y. Chen, M. Karin, *Science* **281**, 1360 (1998).
13. A. Hoffmann, A. Levchenko, M. L. Scott, D. Baltimore, *Science* **298**, 1241 (2002).
14. A. Y. Ting, D. Endy, *Science* **298**, 1189 (2002).
15. M. J. Berridge, *Nature* **386**, 759 (1997).
16. G. Nelson *et al.*, *J. Cell Sci.* **116**, 2495 (2003).
17. X. Bian *et al.*, *J. Biol. Chem.* **277**, 42144 (2002).
18. D. W. McFerran *et al.*, *Endocrinology* **142**, 3255 (2001).
19. Materials and methods are available as supporting material on *Science* Online.
20. L. Vermeulen, G. De Wilde, S. Notebaert, W. Vanden Berghe, G. Haegeman, *Biochem. Pharmacol.* **64**, 963 (2002).
21. L. Chen, W. Fischle, E. Verdin, W. C. Greene, *Science* **293**, 1653 (2001).
22. A. Ryo *et al.*, *Mol. Cell* **12**, 1413 (2003).
23. H. Sakurai *et al.*, *J. Biol. Chem.* **278**, 36916 (2003).
24. J. Yang, G. H. Fan, B. E. Wadzinski, H. Sakurai, A. Richmond, *J. Biol. Chem.* **276**, 47828 (2001).
25. R. E. Dolmetsch, R. S. Lewis, C. C. Goodnow, J. I. Healy, *Nature* **386**, 855 (1997).
26. R. S. Lewis, *Biochem. Soc. Trans.* **31**, 925 (2003).
27. D. B. Kell, *Curr. Opin. Microbiol.* **7**, 296 (2004).
28. L. F. Chen, W. C. Greene, *J. Mol. Med.* **81**, 549 (2003).
29. This work was supported by the Merseyside Neuroblastoma Research Fund, Alder Hey Oncology Fund, North West Cancer Research Fund, AstraZeneca, Medical Research Council, Department of Trade and Industry, Engineering and Physical Sciences Research Council, Royal Society of Chemistry, Biotechnology and Biological Sciences Research Council, and Pfizer UK. Carl Zeiss, Hamamatsu Photonics, and Kinetic Imaging provided technical support. We thank A. Hoffmann and A. Levchenko for assistance with the NF-κB model and M. Begon, A. Hall, A. Loudon, A. Millar, H. Rees, J. Turnbull, and the late Ray Paton for helpful discussions.

Supporting Online Material

www.sciencemag.org/cgi/content/full/306/5696/704/DC1
Materials and Methods
Figs. S1 to S19
Movies S1 to S4
References

5 May 2004; accepted 11 August 2004

NEW PRODUCTS

T CELL KIT

Miltenyi Biotec
For more information
+49 2204-8306-0
www.MiltenyiBiotec.com
http://science.labvelocity.com

The T Cell Activation/Expansion Kit consists of Anti-Biotin MACSiBead particles and biotinylated antibodies against human CD2, CD3, and CD28. Anti-Biotin MACSiBead particles loaded with biotinylated antibodies are used to mimic antigen-presenting cells and activate resting T cells from peripheral blood mononuclear cells as well as purified T cells. T cell expansion is achieved by culturing and reactivation at day 14 of culture. Activated T cells can be used for any downstream processing such as cytokine analysis or immunoprecipitation, and can be efficiently transfected. The kit is also suitable for the expansion of antigen-specific T cell lines and clones.

GENE EXPRESSION ASSAYS

BD Biosciences
For more information
650-424-8222
www.bdbiosciences.com/clontech
http://science.labvelocity.com

The BD ProLabel Screening and Detection Kits provide sensitive chemiluminescence assays for measuring the expression levels of any gene of interest in total cell lysates. These fast, quantitative assay kits were designed to provide a functional assay for protein knockdown RNA interference studies. The assay provides an excellent dynamic range, high sensitivity, and a low threshold of detection. Crude cell lysates can be tested without any purification. These assays can be easily run in a high-throughput screen.

NMR SAMPLE RAIL

Bruker
For more information
978-667-9580
www.bruker-biospin.com
http://science.labvelocity.com

The Sample Rail enables fully automated sample preparation and delivery for 24-hour, hands-off, high-throughput nuclear magnetic resonance (NMR) operation. The system interfaces with a liquid handling robot, which prepares samples in NMR tubes and then transports them on a rail system to the magnet. The liquid handler is synchronized with the NMR experiments for just-in-time sample preparation, suitable for samples requiring analysis immediately after preparation. The Sample Rail increases the utility of NMR in various high-throughput applications, such as metabolic studies, structure activity relations, protein-ligand binding detection, and other drug discovery methods. The Sample Rail is compatible with all Bruker BioSpin Avance NMR spectrometers.

RNA INTERFERENCE STUDIES

Genetix
For more information
+44 1425 624600
www.genetix.com
http://science.labvelocity.com

The QArrayMini microarrayer and aQuire microarray scanner with blue laser option combine to carry out RNA interference optimization experiments. RNA interference is a powerful molecular biology tool to achieve targeted gene silencing in cells. Double-stranded small-interfering RNA (siRNA) molecules can be introduced to silence genes. It is usually necessary to test a variety of oligonucleotide sequences for their efficacy in silencing a given gene, that can be done in a parallel and high-throughput manner by microarraying. The synthetic siRNA duplexes or the plasmids which are eventually processed into siRNA molecules in the cell can be arrayed with a matrix of lipid transfection regents onto a microarray slide using the QArrayMini or QArray2. The slide is then overcoated with a monolayer of adherent cells that subsequently become transfected upon contact with the arrayed spots. In the case of an RNAi screen in which the cell line is expressing a green fluorescent protein (GFP) fusion protein to the target gene, the efficacy of each siRNA molecule is assessed by the formation of plaques (nonfluorescent regions) in the lawn of fluorescent GFP-expressing cells. Images of GFP fusion protein expressing cells can be acquired and analyzed using the Genetix aQuire scanner with optional blue laser.

PCR PRODUCT PURIFICATION

Millipore
For more information
800-MILLIPORE
www.millipore.com/montage
http://science.labvelocity.com

The 96-well Montage PCRμ96 cleanup plates are for small-volume polymerase chain reaction (PCR) product purification. The plates incorporate Millipore's patent-pending size-exclusion technology to process PCR reaction volumes from 1 to 150 μl. The microwell plate design is optimized to purify, concentrate, and recover PCR products in as little as 20 μl. The 15-min, vacuum-driven protocol removes more than 99% of primers and deoxynucleotide triphosphates (dNTPs) in one step. The plates yield purified PCR product suitable for sensitive genotyping applications, direct sequencing, and microarray spotting.

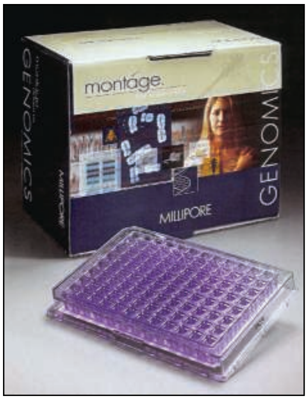

GENE SILENCING REAGENTS

Mirus
For more information
608-441-2824
www.mirusbio.com
http://science.labvelocity.com

Two new small-interfering RNA (siRNA) delivery reagents, TransIT-siQuest and TransIT-TKO, are designed to achieve optimal delivery and high-efficiency target knockdown in a broad range of cell types, including primary cells. They are serum-compatible, one-step transfection reagents.

ENGINEERED M-MLV RT

Ambion
For more information
800-888-8804
www.ambion.com
http://science.labvelocity.com

ArrayScript reverse transcriptase is a modified enzyme that produces up to twice as much complementary RNA compared with wild-type Moloney murine leukemia virus (M-MLV) and other engineered M-MLV reverse transcriptases when low amounts of total RNA are used (~100 ng). It is suitable for applications such as complementary DNA (cDNA) library construction, RNA ligase mediated-rapid amplification of cDNA ends, and RNA amplification in which high yields of full-length cDNA are critical.

Newly offered instrumentation, apparatus, and laboratory materials of interest to researchers in all disciplines in academic, industrial, and government organizations are featured in this space. Emphasis is given to purpose, chief characteristics, and availability of products and materials. Endorsement by *Science* or AAAS of any products or materials mentioned is not implied. Additional information may be obtained from the manufacturer or supplier by visiting http://science.labvelocity.com on the Web, where you can request that the information be sent to you by e-mail, fax, mail, or telephone.